August 2019

Performance Analysis for 5G cellular networks: Millimeter Wave and UAV Assisted Communications

Esma Turgut
Syracuse University

Recommended Citation

Turgut, Esma, "Performance Analysis for 5G cellular networks: Millimeter Wave and UAV Assisted Communications" (2019). *Dissertations - ALL*. 1082.
https://surface.syr.edu/etd/1082

Abstract

Recent years have witnessed exponential growth in mobile data and traffic. Limited available spectrum in microwave (μWave) bands does not seem to be capable of meeting this demand in the near future, motivating the move to new frequency bands. Therefore, operating with large available bandwidth at millimeter wave (mmWave) frequency bands, between 30 and 300 GHz, has become an appealing choice for the fifth generation (5G) cellular networks. In addition to mmWave cellular networks, the deployment of unmanned aerial vehicle (UAV) base stations (BSs), also known as drone BSs, has attracted considerable attention recently as a possible solution to meet the increasing data demand. UAV BSs are expected to be deployed in a variety of scenarios including public safety communications, data collection in Internet of Things (IoT) applications, disasters, accidents, and other emergencies and also temporary events requiring substantial network resources in the short-term. In these scenarios, UAVs can provide wireless connectivity rapidly.

In this thesis, analytical frameworks are developed to analyze and evaluate the performance of mmWave cellular networks and UAV assisted cellular networks. First, the analysis of average symbol error probability (ASEP) in mmWave cellular networks with Poisson Point Process (PPP) distributed BSs is conducted using tools from stochastic geometry. Secondly, we analyze the energy efficiency of relay-assisted downlink mmWave cellular networks. Then, we provide an stochastic geometry framework to study heterogeneous downlink mmWave cellular networks consisting of K tiers of randomly located BSs, assuming that each tier operates in a mmWave frequency band. We further study the uplink performance of the mmWave cellular networks by considering the coexistence of cellular and potential D2D user equipments (UEs) in the same band. In addition to mmWave cellular networks, the performance of UAV assisted cellular networks is also studied. Signal-to-interference-plus-noise ratio (SINR) coverage performance analysis for UAV assisted networks with clustered users is provided. Finally, we study the energy coverage performance of UAV energy harvesting networks with clustered users.

PERFORMANCE ANALYSIS FOR 5G CELLULAR NETWORKS: MILLIMETER WAVE AND UAV ASSISTED COMMUNICATIONS

By

Esma Turgut

B.S., Middle East Technical University, Ankara, Turkey, 2010

M.S., Bilkent University, Ankara, Turkey, 2012

DISSERTATION

Submitted in partial fulfillment of the requirements for the degree of

Doctor of Philosophy in Electrical and Computer Engineering

Syracuse University

August 2019

Dedicated to Zeynep and Hasan...

Acknowledgements

First and foremost I would like to express my sincere gratitude to my advisor, Prof. M. Cenk Gursoy, for his invaluable guidance, continuous encouragement, enduring patience, immense knowledge and constant support throughout my doctoral study. I appreciate his consistent support from the first day I applied to graduate program to these concluding moments. I also sincerely thanks for the time spent listening my questions, asking challenging questions, giving critical comments, and proofreading my research papers. I am truly fortunate to work under his guidance.

I also would like to thank the other members of my Ph.D. thesis committee, Prof. Pramod Varshney, Prof. Biao Chen, Prof. Senem Velipasalar Gursoy, Prof. Qinru Qui and Prof. Lixin Shen for their time, carefully reading my dissertation, and their insightful comments.

I thank my fellow labmates in Wireless Communication and Networking Lab., Gozde, Teddy, Yi, Mustafa, Chuang, Sharon, Hani, Chen, Yang and Mangqing for their friendship and motivating discussions. I feel lucky to have such a great work environment. I have learned a lot from their research in our weekly group meetings with our advisor.

It is my fortune to gratefully acknowledge the support of my friends, Fatmagul, Selvihan and Onur for their support and generous care throughout my Ph. D. journey. They were always beside me during the happy and hard moments to push me and motivate me. Special thank is extended to my friend Sumeyra for her support and help whenever I need during my thesis writing.

Also, I would like to express my deepest appreciation to my mother and father for their unconditional love, devotion and support throughout my life. I also want to thank to my brother and sister for their support and being my best friends since childhood. I also would like to thank to my mother in law, father in law, sister in law and brother in law for their encouragement throughout my study.

Most importantly, this thesis would not have been possible without the love of my kids, Zeynep and Hasan. I appreciate them for their patience throughout my doctoral study. I want to express my deepest love and special thanks to my husband, for his unconditional love, support, patience, and encouragement during my pursuit of Ph.D degree that made the completion of this thesis possible. I consider myself the luckiest person in the world to have such a great family.

Table of Contents

List of Figures **ix**

List of Tables **xv**

1 Introduction **1**

1.1 Main Contributions 3

1.2 List of Publications 7

2 Average Error Probability Analysis in Millimeter Wave Cellular Networks **9**

2.1 Introduction 10

2.1.1 Main Contributions 10

2.2 System Model 11

2.3 Average Error Probability Analysis 14

2.3.1 Derivation of Pairwise Error Probability 15

2.3.2 Characteristic Function of the Aggregate Interference I_{agg} . . . 16

2.3.3 Average Pairwise Error Probability 19

2.3.4 Average Symbol Error Probability 20

2.4 ASEP in the Presence of Beamsteering Errors 21

2.5 Numerical Results 22

2.6 Conclusion 25

3 Energy Efficiency in Relay-Assisted Millimeter Wave Cellular Networks 26

3.1 Introduction 27

3.2 System Model 27

3.3 Coverage Probability 30

3.3.1 Signal-to-Interference-plus-Noise Ratio (SINR) 30

3.3.2 SINR Coverage Probability 31

3.4 Energy Efficiency Analysis 35

3.4.1 Power Model 35

3.4.2 Energy Efficiency Metric 36

3.4.3 Coverage and Energy Efficiency In the Presence of Beamsteering Errors 37

3.5 Numerical Results 38

3.6 Conclusion 42

4 Coverage in Heterogeneous Downlink Millimeter Wave Cellular Networks 43

4.1 Introduction 44

4.1.1 Main Contributions 46

4.2 System Model 47

4.2.1 Statistical Characterization of the Path Loss 50

4.2.2 Cell Association 52

4.3 SINR Coverage Analysis 55

4.3.1 Signal-to-Interference-plus-Noise Ratio (SINR) 55

4.3.2 SINR Coverage Probability 56

4.3.3 Special Case: Noise-limited Network 57

4.3.4 SINR Coverage Probability Analysis In the Presence of Beamsteering Errors 60

4.4 Extensions to Other Performance Metrics and Hybrid Scenario 61

4.4.1 Rate Coverage Probability 61

4.4.2 Energy Efficiency Analysis 62

4.4.3 Analysis of Hybrid Cellular Network Scenario 64

4.5 Simulation and Numerical Results 65

4.6 Conclusion 74

5 Uplink Performance Analysis in D2D-Enabled Millimeter Wave Cellular Networks 77

5.1 Introduction 77

5.1.1 Main Contributions 78

5.2 System Model 79

5.2.1 Spectrum Sharing 82

5.2.2 Interference Modeling 82

5.2.3 Mode Selection 83

5.3 Analysis of Uplink SINR Outage Probability 84

5.3.1 SINR Analysis 84

5.4 Simulation and Numerical Results 89

5.5 Conclusion 91

6 Uplink Performance Analysis in D2D-Enabled Millimeter Wave Cellular Networks with Clustered Users 93

6.1 Introduction 94

6.1.1 Main Contributions 96

6.2 System Model 97

6.3 Transmission Strategies and Interference Characterizations 99

6.3.1 Spectrum Sharing 100

6.3.2 Interference Modeling 100

6.3.3 Path-loss exponents and link distance modeling 102

6.3.4 Mode Selection 106

6.3.5 Directional beamforming 107

6.4 Analysis of Uplink SINR Outage Probability 108

6.4.1 Signal-to-Interference-plus-Noise Ratio (SINR) 108

6.4.2 Laplace Transform of Interferences 110

6.4.3 Uplink SINR Outage Probability 114

6.4.4 Uplink SINR Outage Probability Analysis with Power Control 115

6.4.5 Uplink SINR Outage Probability Analysis In the Presence of Beamsteering Errors 116

6.5 Analysis of Area Spectral Efficiency 118

6.6 Simulation and Numerical Results 120

6.7 Conclusion 126

7 Downlink Analysis in Unmanned Aerial Vehicle (UAV) Assisted Cellular Networks with Clustered Users 129

7.1 Introduction 130

7.1.1 Main Contributions 132

7.2 System Model 134

7.2.1 Statistical Characterization of the Path Loss 136

7.2.2 Cell Association 138

7.3 SINR Coverage Analysis 140

7.3.1 Signal-to-Interference-plus-Noise Ratio (SINR) 140

7.3.2 SINR Coverage Probability 141

7.4 Area Spectral Efficiency 142

7.5 Extension to a Model with UAVs at Different Heights 143

7.6 Simulation and Numerical Results 146

7.7 Conclusion 152

8 Energy Harvesting in Unmanned Aerial Vehicle Networks with 3D Antenna Radiation Patterns 154

8.1 Introduction 155

8.2 System Model 159

8.2.1 Path Loss and Blockage Modeling 160

8.2.2 3D Antenna Modeling 162

8.3 Path Loss and UAV Association 165

8.3.1 Statistical Characterization of the Path Loss 165

8.3.2 Cell Association 166

8.4 Energy Coverage Probability Analysis 167

8.4.1 Downlink Power Transfer 168

8.4.2 Energy Coverage Probability 168

8.5 Simulation and Numerical Results 170

8.5.1 Impact of Cluster Size 171

8.5.2 Impact of UAV Height 173

8.5.3 Impact of Antenna Orientation 176

8.5.4 Impact of Energy Outage Threshold 179

8.6 Conclusion 180

9 Conclusion 181

9.1 Summary 181

9.2 Future Research Directions 186

9.2.1 Simultaneous Information and Energy Transfer in UAV Networks with 3D Antenna Radiation Patterns 186

9.2.2 Visible Light Communication Energy Harvesting 186

A Proof of Lemma 4.1 188

B Proof of Lemma 4.3 190

C Proof of Theorem 4.1 191

D Proof of Lemma 6.1 194

E Proof of Lemma 6.2 195

F Proof of Lemma 6.3 196

G Proof of Lemma 6.5 199

H Proof of Theorem 6.1 202

I Proof of Lemma 7.1 203

J Proof of Lemma 7.2 204

K Proof of Lemma 7.3 205

L Proof of Theorem 7.1 207

M Proof of Lemma 8.1 209

N Proof of Lemma 8.2 210

O Proof of Lemma 8.3 211

P Proof of Theorem 8.1 213

List of Figures

2.1 ASEP as a function of the SNR = $E_0\sigma_0/4$ for different BS densities λ ($\alpha_L = 2.1$, $\alpha_N = 4$, $M = 10$ dB, $m = -10$ dB, $\theta = 15$, BPSK) 23

2.2 ASEP as a function of the SNR = $E_0\sigma_0/4$ for different antenna main lobe gains M and BS densities λ ($\alpha_L = 2.1$, $\alpha_N = 4$, $m = -10$ dB, $\theta = 15$, BPSK) 24

2.3 ASEP as a function of the SNR = $E_0\sigma_0/4$ for different modulation orders Mo ($\alpha_L = 2.1$, $\alpha_N = 4$, $M = 20$, dB $m = -10$ dB, $\theta = 15$, $\lambda = 10^{-4}$) 24

2.4 ASEP as a function of the SNR = $E_0\sigma_0/4$ in the presence of beamsteering error for different standard deviations of alignment error ($\alpha_L = 2.1$, $\alpha_N = 4$, $M = 20$, dB $m = -10$ dB, $\theta = 15$, $\lambda = 10^{-5}$, BPSK) 25

3.1 Relay-assisted mmWave Cellular Network Frame Structure 29

3.2 EE as a function of the BS density λ_B for different antenna patterns (M,m,θ). 39

3.3 EE as a function of the BS density λ_B for different LOS ball radiuses R_B and LOS path-loss exponents α_L. 40

3.4 EE, ASE and ANPC as a function of the BS density λ_B for different RS densities λ_R. 41

3.5 EE as a function of the BS density λ_B for different alignment errors σ_{BE}. 41

4.1 LOS ball model 50

4.2 Coverage Probability as a function of the threshold in dB comparison between SINR and SNR. 67

4.3 SNR Coverage Probability as a function of the threshold in dB for different values of antenna main lobe gain M. 68

4.4 Coverage Probability as a function of the threshold in dB for different values of D-ball model parameters R and β. 69

4.5 SNR Coverage Probability as a function of the biasing factor of picocells and femtocells in dB ($B_1 = 0dB$). 70

4.6 SNR Coverage Probability as a function of the threshold in dB for different alignment errors σ_{BE}. 70

4.7 Rate Coverage Probability as a function of the threshold in Gbps. 71

4.8 Energy Efficiency as a function of the biasing factor of femtocells in dB ($B_1 = B_2 = 0dB$). 72

4.9 Cell Association Probability for all-mmWave network as a function of the biasing factor of picocells and femtocells in dB ($B_1 = 0$dB). 73

4.10 Cell Association Probability for hybrid network as a function of the biasing factor of picocells and femtocells in dB ($B_1 = 0$dB). 74

4.11 SINR Coverage Probability as a function of the threshold in dB for hybrid network for different biasing factor of picocells and femtocells in dB ($B_1 = 0dB$). 75

4.12 SINR Coverage Probability as a function of the threshold in dB for hybrid network for different density of microcells λ_1. 75

5.1 Probability of selecting D2D mode as a function of the D2D biasing factor T_d. 90

5.2 SINR outage probability as a function of the threshold in dB for different antenna parameters. Simulation results are also plotted with markers. . . 90

5.3 SINR outage probability as a function of the threshold in dB for different β values. 91

6.1 BSs (red squares) and cellular UEs (pink circles) are distributed as independent PPPs, potential D2D UEs (blue dots) are normally distributed around PPP distributed cluster centers (black plus signs). The average number of potential D2D UEs per cluster is set to 10. 98

6.2 Illustration of the distances r_{d0} and r_{d1} in the representative cluster. The typical D2D UE is assumed to be located at the origin. Cluster center is located at x_0 with respect to (w.r.t.) the origin. Transmitting D2D UE is located at y_0 w.r.t. the cluster center. Intra-cluster interfering D2D UEs are located at $\{y\}$ w.r.t. the cluster center (Only one of them is shown in the figure). Arrows represent the coordinate vectors (and do not indicate the direction of communication). 104

6.3 Probability of selecting D2D mode as a function of UE distribution's standard deviation σ_d for different values of $p_{L,c}$ and $p_{L,d}$. Simulation results are also plotted with markers. 121

6.4 SINR outage probability as a function of average number of simultaneously active D2D links $\bar{n}$ for different values of cluster center density λ_C ($\Gamma = 40dB$). Simulation results are also plotted with markers. 122

6.5 SINR outage probability as a function of UE distribution's standard deviation σ_d for different values of LOS ball radius $R_{B,d}$ ($\Gamma = 20dB$). Simulation results are also plotted with markers. 123

6.6 SINR outage probability as a function of the threshold in dB for different antenna parameters. Simulation results are also plotted with markers. . . 124

6.7 SINR outage probability as a function of the threshold in dB for different alignment errors σ_{BE}. Simulation results are also plotted with markers. . 125

6.8 Area Spectral Efficiency (ASE) for underlay type of sharing for (a) cellular network, (b) D2D network as a function of average number of simultaneously active D2D links $\bar{n}$ for different values of cluster center density λ_C ($\Gamma = 40dB$). 126

6.9 Area Spectral Efficiency (ASE) for overlay type of sharing for (a) cellular network, (b) D2D network as a function of average number of simultaneously active D2D links $\bar{n}$ for different values of spectrum partition factor δ ($\Gamma = 40dB$). 127

6.10 Objective function in (6.31) as a function of spectrum partition factor δ ($\Gamma = 40dB$). 127

7.1 UAVs (black plus signs) and BSs (red squares) are distributed as independent PPPs, UEs (blue dots) are normally distributed around projections of UAVs on the ground. 135

7.2 Association probability as a function of UE distribution's standard deviation σ_c for different values of UAV height H. Simulation results are also plotted with markers. 147

7.3 SINR Coverage probability as a function of the threshold in dB for different values of UAV height H. Simulation results are also plotted with markers. 148

7.4 SINR coverage probability as a function of the path-loss exponents $\alpha_{\text{LOS}} = \alpha_{\text{NLOS}} = \alpha_B$ for different values of UAV height H. Simulation results are also plotted with markers. 149

7.5 SINR coverage probability as a function of the threshold in dB for different values of UAV density λ_U. Simulation results are also plotted with markers. 150

7.6 Area spectral efficiency (ASE) as a function of UAV density λ_U for different values of UE distribution's standard deviation σ_c. Simulation results are also plotted with markers. 151

7.7 SINR coverage probability as a function of the threshold in dB for two different values of the UE distribution's standard deviation σ_c. Solid lines show the coverage probabilities when half of the UAVs are located at height $H_1 = 10$m and the other half are located at height $H_2 = 20$m, and the typical UE is clustered around a UAV at either height H_1 or H_2. 153

8.1 Network model for a UAV energy harvesting network. BSs are distributed as a PPP, while UEs are normally distributed around the cluster centers (projections of UAVs on the ground). Both BS and UEs are equipped with UWB antennas with different antenna orientations. 160

8.2 LOS probability function for high-altitude and low-altitude models as a function of (a) UAV height H and (b) 2D distance to the cluster center UAV d. 162

8.3 Approximated antenna radiation pattern for HH antenna orientation. . . 164

8.4 (a) Association probability and (b) energy coverage probability as a function of UE distribution's standard deviation σ_c for LOS probability functions of high-altitude and low-altitude models when $H = 50$ m. Simulation results are plotted with markers while dashed/solid curves show theoretical results. 172

8.5 (a) Association probability and (b) energy coverage probability as a function of UAV height H for LOS probability functions of high-altitude and low-altitude models when $\sigma_c = 10$. Simulation results are plotted with markers while dashed/solid curves show theoretical results. 174

8.6 Association probability as a function of UAV height H for different values of UAV density λ_U for (a) HH, (b) VV and (c) HV antenna orientations when $\sigma_c = 10$. 175

8.7 Energy coverage probability as a function of UAV height H for different values of UAV density λ_U for different antenna orientations when $\sigma_c = 10$. 176

8.8 Energy coverage probability as a function of UAV density λ_U. 178

8.9 Energy coverage probability as a function of energy outage threshold in dB for LOS probability functions of high-altitude and low-altitude models when $\sigma_c = 10$ and $H = 50$ m. Simulation results are plotted with markers while dashed/solid curves show theoretical results. 179

List of Tables

3.1 System Parameters 38

4.1 System Parameters 66

5.1 System Parameters 89

6.1 System Parameters 120

7.1 System Parameters 146

8.1 System Parameters 171

Chapter 1

Introduction

Recent years have witnessed exponential growth in mobile data and traffic due to, e.g., ever increasing use of smart phones, portable devices, and data-hungry multimedia applications. According to the UMTS traffic forecasts, 1000 fold increase in mobile data traffic is predicted by the year 2020 [1]. In another estimate, more than 50 billion devices may be connected wirelessly by 2020 which may cause a capacity crisis [2]. Limited available spectrum in microwave (μWave) bands does not seem to be capable of meeting this demand in the near future, motivating the move to new frequency bands. Therefore, the large available bandwidth at millimeter wave (mmWave) frequency bands, between 30 and 300 GHz, becomes a good candidate for the fifth generation (5G) cellular networks and has attracted considerable attention recently [3] – [8].

Despite the great potential of mmWave bands, they have been considered attractive only for short range-indoor communication due to increase in free-space path loss with increasing frequency, and poor penetration through solid materials such as concrete and brick. However, these high frequencies may also be used for outdoor communication over a transmission range of about 150-200 meters as demonstrated by recent channel measurements [3], [4], [7], [8]. Also, comparable coverage area and much higher data rates than μWave networks can be achieved provided that the base station density is sufficiently high and highly directional antennas are used [9]. With the employment of directional antennas, mmWave cellular networks can be considered as noise-limited rather than interference-limited [5], [10], [11], [12], [13].

Evaluating the system performance of mmWave cellular networks is a crucial task in order to understand the network behavior. Stochastic geometry has been identified as a powerful mathematical tool to analyze the system performance of mmWave cellular networks due to its tractability and accuracy. Therefore, in most of the recent studies on mmWave cellular networks, spatial distribution of the BSs is assumed to follow a point process and the most commonly used distribution is the Poisson point process (PPP) due to its tractability and accuracy in approximating the actual cellular network topology [14], [15]. In [15], authors provide a comprehensive tutorial on stochastic geometry based analysis for cellular networks. Additionally, a detailed overview of mathematical models and analytical techniques for mmWave cellular systems are provided in [16]. Since the path loss and blockage models for mmWave communications are significantly different from μWave communications, three different states, namely line-of-sight (LOS), non-line-of-sight (NLOS) and outage states, are considered for mmWave frequencies [12], [13].

In addition to mmWave cellular networks, there are other new technologies and designs under consideration for 5G cellular networks in order to meet the increasing data demand. One of them is expected to be the deployment of dense low-power small-cell BSs to assist the congested lower-density high-power large-cell BSs by offloading some percentage of their user equipments (UEs), resulting in a better quality of service per UE [5], [14]. Additionally, in the case of unexpected scenarios such as disasters, accidents, and other emergencies or temporary events requiring the excessive need for network resources such as concerts and sporting events, it is important to provide wireless connectivity rapidly [17]–[19]. In such scenarios, the deployment of unmanned aerial vehicle (UAV) BSs, also known as drone BSs, has attracted considerable attention recently as a possible solution.

These aforementioned considerations motive us to conduct the current and proposed research, which will be described later in more detail in this thesis. Firstly, the analysis of average symbol error probability (ASEP) in mmWave cellular networks with Poisson Point Process (PPP) distributed base stations (BSs) is conducted using tools from stochastic geometry. Secondly, we employ stochastic geometry to analyze the energy efficiency of relay-assisted downlink mmWave cellular networks. Then, we provide an analytical framework to analyze heterogeneous downlink mmWave cellular networks consisting of K tiers of randomly located BSs where each tier operates in a mmWave frequency band. We further study the uplink performance of the mmWave cellular networks by considering the coexistence of cellular and potential D2D UEs in the same band. In addition to mmWave cellular networks, we also study the performance of UAV assisted cellular networks.

1.1 Main Contributions

We summarize the main contributions of the thesis below:

In Chapter 2, we develop a mathematical framework for the analysis of average symbol error probability (ASEP) in mmWave cellular networks with PPP distributed BSs using tools from stochastic geometry. We incorporate the distinguishing features of mmWave communications such as directional beamforming and having different path loss laws for LOS and NLOS links in the average error probability analysis. First, we obtain average pairwise error probability (APEP) expression by averaging pairwise error probability (PEP) over fading and random shortest distance from mobile user (MU) to its serving BS. Subsequently, we approximate average symbol error probability from APEP using the nearest neighbor (NN) approximation. We analyze

ASEP for different antenna gains and base station densities. Finally, we investigate the effect of beamforming alignment errors on ASEP to get insight on more realistic cases. This chapter, as a conference paper, appeared in the Proceedings of the IEEE Vehicular Technology Conference (VTC)-Fall in 2015 [20].

In Chapter 3, we analyze the energy efficiency of relay-assisted mmWave cellular networks with PPP distributed BSs and relay stations (RSs) using tools from stochastic geometry. Following the description of the system model for mmWave cellular networks, we compute the coverage probabilities for each link. Subsequently, we model the average power consumption of BSs and RSs and determine the energy efficiency in terms of system parameters. We also investigate the energy efficiency in the presence of beamforming alignment errors to get insight on the performance in practical scenarios. Finally, we analyze the impact of BS and RS densities, antenna gains, main lobe beam widths, LOS interference range, and alignment errors on the energy efficiency via numerical results. This chapter, as a conference paper, appeared in the Proceedings of the IEEE Vehicular Technology Conference (VTC)-Fall in 2016 [21].

In Chapter 4, we provide an analytical framework to analyze heterogeneous downlink mmWave cellular networks consisting of K tiers of randomly located BSs where each tier operates in a mmWave frequency band. We derive the Signal-to-interference-plus-noise ratio (SINR) coverage probability for the entire network using tools from stochastic geometry. We take into account the distinguishing features of mmWave communications such as directional beamforming and having different path loss laws for LOS and NLOS links in the coverage analysis by assuming averaged biased-received power association and Nakagami fading. We obtain a simpler expression requiring the computation of only one numerical integral for coverage probability by using the noise-limited assumption for mmWave networks. Also, we investigate the effect of beamforming alignment errors on the coverage probability analysis to get insight on the performance in practical scenarios. We also derive the downlink rate coverage probability to get more insights on the performance of the network. Moreover, we analyze the effect of deploying low-power smaller cells and the impact of biasing factor on energy efficiency. Finally, we address a hybrid cellular network operating in both mmWave and μWave frequency bands. This chapter, as a journal paper, appeared in IEEE Transactions on Communications in 2017 [22], and, as a conference paper, appeared in the Proceedings of the IEEE Global Communications Conference (Globecom) in 2016 [23].

In Chapter 5, we provide an analytical framework to analyze the uplink performance of device-to-device (D2D)-enabled mmWave cellular networks. We derive the SINR outage probabilities for both cellular and D2D links using tools from stochastic geometry. We employ the distinguishing features of mmWave communications such as directional beamforming and having different path loss laws for LOS and NLOS links in the outage analysis by considering a flexible mode selection scheme and Nakagami fading. This chapter, as a conference paper, appeared in the Proceedings of the IEEE Vehicular Technology Conference (VTC)-Fall in 2017 [24].

In Chapter 6, we provide an analytical framework to analyze the uplink performance of D2D-enabled mmWave cellular networks with clustered D2D user UEs. Locations of cellular UEs are modeled as a PPP, while locations of potential D2D UEs are modeled as a Poisson Cluster Process (PCP). SINR outage probabilities are derived for both cellular and D2D links using tools from stochastic geometry. The distinguishing features of mmWave communications such as directional beamforming and having different path loss laws for LOS and NLOS links are incorporated into the outage analysis by employing a flexible mode selection scheme and Nakagami fading. Also, the effect of beamforming alignment errors on the outage probability is investigated to get insight on the performance in practical scenarios. Moreover, area spectral efficiency (ASE) of the cellular and D2D networks are determined for both underlay and overlay types of sharing. Optimal spectrum partition factor is determined for overlay sharing by considering the optimal weighted proportional fair spectrum partition. This chapter , as a journal paper, appeared in IEEE Transactions on Wireless Communications in 2019 [25], and, as a conference paper, appeared in the Proceedings of the IEEE Vehicular Technology Conference (VTC)-Fall in 2018 [26].

In Chapter 7, we provide an analytical framework to analyze the SINR coverage probability of unmanned aerial vehicle (UAV) assisted cellular networks with clustered UEs. Locations of UAVs and ground BSs are modeled as PPPs, and UEs are assumed to be distributed according to a PCP around the projections of UAVs on the ground. Initially, the complementary cumulative distribution function (CCDF) and probability density function (PDF) of path losses for both UAV and ground BS tiers are derived. Subsequently, association probabilities with each tier are obtained. SINR coverage probability is derived for the entire network using tools from stochastic geometry. Finally, ASE of the entire network is determined, and SINR coverage probability expression for a more general model is presented by considering that UAVs are located at different heights. Via numerical results, we have shown that UAV height and path-loss exponents play important roles on the coverage performance. Moreover, coverage probability can be improved with smaller number of UAVs, while better area spectral efficiency is achieved by employing more UAVs and having UEs more compactly clustered around the UAVs. This chapter, as a journal paper, appeared in the IEEE Access in 2018 [27].

In Chapter 8, we provide an analytical framework to analyze the energy coverage performance of UAV energy harvesting networks with clustered UEs. Locations of UAVs are modeled as a PPP, while locations of UEs are modeled as a PCP. Two different models are considered for the LOS probability function to compare their effect on the network performance. Moreover, ultra-wideband (UWB) antennas with doughnut-shaped radiation patterns are employed in both UAVs and UEs, and the impact of practical 3D antenna radiation patterns on the network performance is also investigated. Initially, the CCDF and PDF of path losses for each tier are derived. Subsequently, association probabilities with each tier are obtained. Energy coverage probability is derived for the entire network using tools from stochastic geometry. Via numerical results, we have shown that cluster size and UAV height play crucial roles on the energy coverage performance. Furthermore, energy coverage probability is significantly affected by the antenna orientation and number of UAVs in the network. This chapter is submitted for journal publication.

In Chapter 9, we conclude this thesis and discuss future research directions.

1.2 List of Publications

Journals

[J5] **E. Turgut**, M. C. Gursoy, and I. Guvenc, "Energy Harvesting in Unmanned Aerial Vehicle Networks with 3D Antenna Radiation Patterns," submitted for journal publication.

[J4] X. Wang, **E. Turgut**, and M. Cenk Gursoy, "Coverage in downlink heterogeneous mmWave cellular networks with user-centric small cell deployment," *IEEE Transactions on Vehicular Technology*, vol. 68, no. 4, pp. 3513-3533, Apr. 2019.

[J3] **E. Turgut**, and M. C. Gursoy, "Uplink performance analysis in D2D-enabled mmwave cellular networks with clustered users," *IEEE Transactions on Wireless Communications*, *IEEE Trans. Wireless Commun.*, vol. 18, no. 2, pp. 1085-1100, Feb. 2019.

[J2] **E. Turgut**, and M. C. Gursoy, "Downlink analysis in unmanned aerial vehicle (UAV) assisted cellular networks with clustered users," *IEEE Access*, vol. 6, 2018.

[J1] **E. Turgut**, and M. Cenk Gursoy, "Coverage in heterogeneous downlink millimeter wave cellular networks," *IEEE Transactions on Communications*, vol. 65, no. 10, Oct. 2017.

Conferences

[**C7**] **E. Turgut**, M. C. Gursoy, and I. Guvenc, "Energy harvesting in unmanned aerial vehicle networks with 3D antenna radiation patterns," *Proc. IEEE Veh. Technol. Conf. (VTC-Fall)*, Sep. 2019.

[**C6**] **E. Turgut**, and M. C. Gursoy, "Outage probability analysis in D2D-enabled mmwave cellular networks with clustered users," *Proc. IEEE Veh. Technol. Conf. (VTC-Fall)*, pp. 1-5, Aug. 2018.

[**C5**] X. Wang, **E. Turgut**, and M. C. Gursoy, "Coverage in downlink heterogeneous mmWave cellular networks with user-centric small cell deployment," *Proc. IEEE Personal, Indoor, and Mobile Radio Commun. (PIMRC)*, pp. 1-7, Oct. 2017.

[**C4**] **E. Turgut**, and M. C. Gursoy," Uplink performance analysis in D2D-enabled millimeter wave cellular networks," *Proc. IEEE Veh. Technol. Conf. (VTC-Fall)*, pp. 1-5, Sep. 2017.

[**C3**] **E. Turgut**, and M. C. Gursoy, "Coverage in heterogeneous downlink millimeter wave cellular networks," *Proc. of IEEE Global Commun. Conf. (Globecom)*, pp. 1-6, Dec. 2016.

[**C2**] **E. Turgut**, and M. C. Gursoy, "Energy efficiency in relay-assisted mmwave cellular networks," *Proc. IEEE Veh. Technol. Conf. (VTC-Fall)*, pp. 1-5, Sep. 2016.

[**C1**] **E. Turgut**, and M. C. Gursoy, "Average error probability analysis in mmWave cellular networks," *Proc. IEEE Veh. Technol. Conf. (VTC-Fall)*, pp. 1-5, Sep. 2015.

Chapter 2

Average Error Probability Analysis in Millimeter Wave Cellular Networks

In this chapter, a mathematical framework for the analysis of average symbol error probability (ASEP) in mmWave cellular networks with PPP distributed BSs is developed using tools from stochastic geometry. The distinguishing features of mmWave communications such as directional beamforming and having different path loss laws for LOS and NLOS links are incorporated in the average error probability analysis. First, average pairwise error probability (APEP) expression is obtained by averaging pairwise error probability (PEP) over fading and random shortest distance from mobile user (MU) to its serving BS. Subsequently, average symbol error probability is approximated from APEP using the nearest neighbor (NN) approximation. ASEP is analyzed for different antenna gains and base station densities. Finally, the effect of beamforming alignment errors on ASEP is investigated to get insight on more realistic cases.

2.1 Introduction

Evaluating the system performance of mmWave cellular networks is a crucial task in order to understand the network behavior. There are several recent studies which analyze the coverage probability and average rate in mmWave cellular networks using results from stochastic geometry and the theory of point processes for different BS-user associations [9], [13], [28]. Stochastic geometry is a commonly used powerful mathematical tool to evaluate the average network performance of spatially distributed nodes [29]. Poisson point process (PPP) is a widely used model in wireless networks in general and in cellular networks in particular due to its analytical tractability. However, average error probability in PPP-based cellular networks has only been barely analyzed in the literature. For instance, there is work focusing on the computation of ASEP in the presence of Poisson field interferers (see e.g., [30]). However, none of them are applicable to cellular networks since the BS to MU cell association is generally not considered. In [31], a mathematical framework to compute the ASEP in cellular networks, where the BS locations are modeled as independent homogeneous PPPs, is established for the first time. Their approach is based on the shortest BS-to-MU distance cell association criterion, which guarantees that the interfering BSs are located farther than the serving BS, so it is applicable to cellular networks. However, to the best of our knowledge, average error probability analysis has not been conducted for mmWave cellular networks yet.

2.1.1 Main Contributions

We follow a similar approach as in [31] to develop a mathematical framework for the computation of ASEP in downlink mmWave cellular networks. First, APEP is calculated by averaging PEP over fading and random shortest distance from MU to serving BS. Then, ASEP is found using the NN approximation. Our main contribution is the combination of the characteristic features of mmWave communications with the proposed mathematical framework in [31]. One distinguishing feature of mmWave cellular communication is the directional beamforming at the transmitter and receiver, which provides an array gain to mitigate the effect of path loss. Sectored directional antenna model is used to find the effective antenna gain similar to [9], [13], [32]. First, perfect beam alignment is assumed between the MU and the serving BS. Then, the effect of beamsteering errors is investigated. Another distinct feature of mmWave communication is that a BS can be in the LOS or in the NLOS of MU and different path loss laws are applied for LOS and NLOS links. Here, we adopt the equivalent LOS ball model in [9] to determine whether a BS is LOS or NLOS.

2.2 System Model

In this section, we introduce our system model for the downlink mmWave cellular network consisting of BSs distributed according to some homogeneous PPP Ψ of density λ in the Euclidean plane. Without loss of generality, we consider that a typical MU is located at the origin. A shortest distance cell criterion is assumed, i.e., MU is served by the nearest BS which is denoted by BS_0. The distance from the ith BS to the MU is denoted by r_i for $i \in \Psi$. Thus, the distance between the MU and serving BS (BS_0) is r_0 which is a random variable (RV) with PDF $f_{r_0}(\xi) = 2\pi\lambda\xi \exp\{-\pi\lambda\xi^2\}$ [33]. The set of interfering BSs $i \in \Psi - \text{BS}_0$ is still a homogeneous PPP, denoted by $\Psi^{(\setminus 0)}$, according to the Slivnyak-Mecke's Theorem [29]. We assume that all the interfering BSs are transmitting in the same frequency band as the serving BS (full frequency reuse), therefore $\Psi^{(\setminus 0)}$ has density λ as well.

We have the following two assumptions in the construction of the system model.

Assumption 2.1 *Antenna arrays at both the BSs and MU are used to perform directional beamforming such that the main lobe is directed towards the dominant propaga-*

tion path while smaller sidelobes direct energy in other directions. For tractability in the analysis, antenna arrays are approximated by a sectored antenna model, in which the array gains are assumed to be equal to a constant M *for all angles in the main lobe and another smaller constant* m *in the side lobe [34]. The MU and serving BS,* BS_0*, are assumed to have perfect beam alignment and therefore have an antenna gain of* MM*. Also, the beam direction of the MU and each interfering BS can be modeled as a uniform random variable on* $[0, 2\pi]$*. Therefore, the effective antenna gain is a discrete RV described by*

$$G_i = \begin{cases} MM & \textit{with prob. } p_{MM} = (\frac{\theta}{2\pi})^2 \\ Mm & \textit{with prob. } p_{Mm} = 2\frac{\theta}{2\pi}\frac{2\pi-\theta}{2\pi} \\ mm & \textit{with prob. } p_{mm} = (\frac{2\pi-\theta}{2\pi})^2 \end{cases}, \tag{2.1}$$

where θ *is the beam width of the main lobe.*

Assumption 2.2 *A BS can be either LOS or NLOS BS to the MU according to the LOS probability function* $p(r)$ *which is the probability that a link of length* r *is LOS. Using field measurements and stochastic blockage models,* $p(r)$ *can be formulated as* $e^{-\beta d}$ *where decay rate* β *depends on the building parameter and density [35]. LOS probability function* $p(r)$ *can be approximated by a step function in order to simplify the analysis. In this approach, the irregular geometry of the LOS region is replaced with its equivalent LOS ball model with radius* R_B *[9]. A BS is a LOS BS to the MU if it is inside the ball, otherwise it is a NLOS BS. Different path loss laws are applied to LOS and NLOS links. Thus, the path-loss exponent on each interfering link can be expressed as follows:*

$$\alpha_i = \begin{cases} \alpha_L & \textit{if}\, r \le R_B \\ \alpha_N & \textit{if}\, r > R_B \end{cases}, \tag{2.2}$$

where α_L *and* α_N *are the LOS and NLOS path-loss exponents, respectively.*

By combining these two assumptions with the described network model above, the received signal at the MU can be written as,

$$y = \underbrace{\sqrt{G_0 E_0} r_0^{-\alpha_L} h_0 s_0}_{x} + \underbrace{\sum_{i \in \Psi^{(\backslash 0)}} \sqrt{G_i E_0} r_i^{-\alpha_i} h_i s_i}_{I_{\text{agg}}} + n. \tag{2.3}$$

where x is the signal arriving from the serving BS to MU, I_{agg} is the aggregate network interference, and n is the Gaussian distributed noise component with zero mean and variance N_0. Moreover, G_0 is the effective antenna gain of the BS$_0$-MU link and it is assumed to be equal to MM, E_0 is the BSs' transmit-energy per transmission, α_L is the LOS path-loss exponent of the BS$_0$-MU link, $s_0 = a_0 \exp\{j\theta_0\}$ is the information symbol transmitted by BS$_0$ with amplitude a_0 and phase θ_0, $h_0 = |h_0| \exp\{j\phi_0\}$ is the fading coefficient in the BS$_0$-MU link where $|h_0|^2$ is an exponential RV with parameter $\sigma_0 = \mathbb{E}|h_0|^2 = 1$ and the phase ϕ_0 is a uniformly distributed RV in the range $[0, 2\pi)$. A similar notation is used for I_{agg}, but note that the effective antenna gain G_i and path loss exponent α_i are different for different interfering links as described in (2.1) and (2.2), respectively. Also, considering phase modulation, we assume that $a_0 = a_i = 1$ for $i \in \Psi^{(\backslash 0)}$.

At the MU, an interference-unaware maximum-likelihood (ML) demodulator is used as in [31], which can be formulated as [36]

$$\hat{s}_0 = \arg\min_{\tilde{s}_0} \{D(\tilde{s}_0) = |y - \sqrt{G_0 E_0} r_0^{-\alpha_L} h_0 \tilde{s}_0|^2\}. \tag{2.4}$$

Inserting (2.3) into (2.4) and neglecting some irrelevant constants after algebraic manipulations, we can express the decision metric as

$$D(\tilde{s}_0) \propto r_0^{-2\alpha_L} G_0 E_0 |\Delta_{s,\tilde{s}}|^2 |h_0|^2 + 2 r_0^{-\alpha_L} \sqrt{G_0 E_0} \text{Re}\{(I_{\text{agg}} + n)|h_0| \exp\{-j\phi_0\} \Delta^*_{s,\tilde{s}}\}, \tag{2.5}$$

where $\Delta_{s,\tilde{s}} = s_0 - \tilde{s}_0$, $I_{\text{agg}} = \sum_{i\in\Psi(\backslash 0)} \sqrt{G_i E_0} r_i^{-\alpha_i} h_i s_i$ and $n \sim \mathcal{CN}(0, N_0)$. Since the effective antenna gain between the MU and each interfering BS is modeled as an independent RV, we can employ the thinning property of PPP to split the aggregate network interference I_{agg} into 6 independent PPPs as follows [32]:

$$\begin{aligned} I_{\text{agg}} &= (I^{MM}_{\Psi_{\text{LOS}}} + I^{MM}_{\Psi_{\text{NLOS}}}) + (I^{Mm}_{\Psi_{\text{LOS}}} + I^{Mm}_{\Psi_{\text{NLOS}}}) + (I^{mm}_{\Psi_{\text{LOS}}} + I^{mm}_{\Psi_{\text{NLOS}}}) \\ &= \sum_{G\in\{MM,Mm,mm\}} (I^{G}_{\Psi_{\text{LOS}}} + I^{G}_{\Psi_{\text{NLOS}}}), \end{aligned} \tag{2.6}$$

where each interfering BS is either a LOS or NLOS BS and the superscripts represent the discrete random antenna gain defined in (2.1). According to the thinning theorem, each independent PPP has a density of λp_G where p_G is given in (2.1) for each antenna gain $G \in \{MM, Mm, mm\}$.

2.3 Average Error Probability Analysis

In this section, we investigate the error performance of a downlink mmWave cellular network. The first step in obtaining an approximation of the average error probability is to compute the pairwise error probability (PEP) associated with the transmitted symbols. Hence, initially we derive an expression for PEP, conditioned on fading gain ($|h_0|$) and random shortest distance of the MU-serving BS link (r_0), in terms of the characteristic function (CF) of the aggregate network interference and the noise. A closed-form expression is determined for the CF of the aggregate network interference for PPP distributed BSs. Then, APEP is computed by averaging the conditional PEP over fading and the position of the serving BS. Finally, ASEP is approximated from APEP using the NN approximation.

2.3.1 Derivation of Pairwise Error Probability

The PEP is defined as the probability of deciding in favor of $\hat{s}_0$ when actually s_0 is transmitted. It is assumed that these two symbols are the only two symbols in the signal-constellation, and therefore decision is made strictly between these two symbols. Using the decision metric in (2.5), PEP conditioned on $|h_0|$ and r_0 can be computed as

$$P\{s_0 \to \hat{s}_0 | |h_0|, r_0\} = P\{D(\tilde{s}_0 = \hat{s}_0) < D(\tilde{s}_0 = s_0)\}. \tag{2.7}$$

When $\tilde{s}_0 = s_0$, $\Delta_{s,\tilde{s}} = s_0 - \tilde{s}_0$ becomes zero by definition. As a result, $D(\tilde{s}_0 = s_0)$ is zero. Let $U = I_{\text{agg}} + n$. Note that U is a circularly symmetric RV. Thus, $U \exp\{j\phi_0\} \arg\{\Delta^*_{s,\hat{s}}\} \overset{d}{=} U$ [37]. Thus, PEP can be computed as follows:

$$\begin{aligned} P\{s_0 \to \hat{s}_0 | |h_0|, r_0\} &= P\{D(\tilde{s}_0 = \hat{s}_0) < 0\} \\ &= P\left\{\text{Re}\{U|h_0| \exp\{j\phi_0\}\Delta^*_{s,\hat{s}}\} < -\frac{\sqrt{G_0 E_0}}{2r_0^{\alpha_L}} |\Delta_{s,\hat{s}}|^2 |h_0|^2\right\} \\ &= P\left\{\text{Re}\{U\} < -\frac{\sqrt{G_0 E_0}}{2r_0^{\alpha_L}} |\Delta_{s,\hat{s}}||h_0|\right\} \\ &= F_{U_{\text{Re}}}\left(-\frac{\sqrt{G_0 E_0}}{2r_0^{\alpha_L}} |\Delta_{s,\hat{s}}||h_0|\right) \end{aligned} \tag{2.8}$$

where $F_{U_{\text{Re}}}$ denotes the CDF of the RV $U_{\text{Re}} = \text{Re}\{U\}$.

Gil-Pelaez inversion theorem can be employed to compute the CDF $F_{U_{\text{Re}}}$ by using the CF of U_{Re}, $\Phi_{U_{\text{Re}}}(w)$, as follows [38]:

$$\begin{aligned} F_{U_{\text{Re}}}(u) &= \frac{1}{2} - \frac{1}{\pi}\int_0^\infty \frac{\text{Im}\{\mathrm{e}^{-jwu}\Phi_{U_{\text{Re}}}(w)\}}{w} dw \\ &= \frac{1}{2} - \frac{1}{\pi}\int_0^\infty \frac{\text{Im}\{(\cos(wu) - j\sin(wu))(\text{Re}\{\Phi_{U_{\text{Re}}}(w)\} + j\text{Im}\{\Phi_{U_{\text{Re}}}(w)\})\}}{w} dw \\ &= \frac{1}{2} + \frac{1}{\pi}\int_0^\infty \frac{\sin(wu)\Phi_U(w)}{w} dw, \end{aligned} \tag{2.9}$$

where the last equation follows from the fact that the CF $\Phi_{U_{\text{Re}}}(w)$ is a real function, i.e., $\mathrm{Im}\{\Phi_{U_{\mathrm{Re}}}(w)\} = 0$ and $\mathrm{Re}\{\Phi_{U_{\mathrm{Re}}}(w)\} = \Phi_{U_{\mathrm{Re}}}(w)$, and $U(.)$ is a circularly symmetric RV, i.e., $\Phi_{U_{\mathrm{Re}}}(w) = \Phi_U(w)$.

By inserting (2.9) into (2.8), PEP can be written as

$$P\{s_0 \to \hat{s}_0 | |h_0|, r_0\} = \frac{1}{2} - \frac{1}{\pi}\int_0^{\infty} \sin\left(\frac{\sqrt{G_0 E_0}}{2 r_0^{\alpha_L}} |\Delta_{s,\hat{s}}| |h_0| w\right) w^{-1} \Phi_U(w) dw. \tag{2.10}$$

In (2.10), PEP is computed using the CF of the RV U. Since U is the summation of two independent RVs, I_{agg} and n, $\Phi_U(w)$ is equal to the product of the CFs of these two RVs, i.e., $\Phi_U(w) = \Phi_{I_{\mathrm{agg}}}(w)\Phi_n(w)$. $\Phi_n(w) = \exp\{-w^2(N_0/4)\}$ is the CF of a Gaussian RV [39] and $\Phi_{I_{\mathrm{agg}}}(w)$ is calculated in the next subsection.

2.3.2 Characteristic Function of the Aggregate Interference I_{agg}

Since I_{agg} is the sum of six independent PPPs as seen in (2.6), using stochastic geometry, its CF can be written as

$$\Phi_{I_{\mathrm{agg}}}(w) = \prod_{G \in \{MM, Mm, mm\}} \Phi_{I^G_{\Psi_{\mathrm{LOS}}}}(w) \Phi_{I^G_{\Psi_{\mathrm{NLOS}}}}(w), \tag{2.11}$$

where $\Phi_{I^G_{\Psi_{\mathrm{LOS}}}}(w)$ and $\Phi_{I^G_{\Psi_{\mathrm{LOS}}}}(w)$ are the CFs of LOS and NLOS components with antenna gain G.

Let $z_i = s_i h_i = |h_i| \exp\{j(\theta_i + \phi_i)\}$. The interference due to a LOS component with a generic antenna gain G can be written as $I^G_{\Psi_{\mathrm{LOS}}} = \sum_{i \in \Psi_{\mathrm{LOS}}} \sqrt{G E_0} r_i^{-\alpha_L} z_i$. Then, its CF $\Phi_{I^G_{\Psi_{\mathrm{LOS}}}}(w) = \mathbb{E}\{\exp\{jw I^G_{\Psi_{\mathrm{LOS}}}\}\}$ can be obtained using the same steps as those in [40] and can be expressed as

$$\begin{aligned}
&\Phi_{I^G_{\Psi_{\mathrm{LOS}}}}(w) \\
&= \sum_{k=0}^{\infty} \frac{\exp\{-\lambda p_G \pi (R_B^2 - r_0^2)\}[\lambda p_G \pi (R_B^2 - r_0^2)]^k}{k!} \big(\mathbb{E}_{z_i, r_i}\{\exp\{jw\sqrt{GE_0} r_i^{-\alpha_L} z_i\}\}\big)^k.
\end{aligned} \tag{2.12}$$

By using the Taylor series expansion for the exponential function, one can rewrite the equation in (2.12) and further express it using similar steps as in [30] as follows:

$$\begin{aligned}
\Phi_{I^G_{\Psi_{\mathrm{LOS}}}}(w) &= \exp\{\lambda p_G \pi (R_B^2 - r_0^2)[-1 + \mathbb{E}_{z_i, r_i}\{\exp\{jw\sqrt{GE_0} r_i^{-\alpha_L} z_i\}\}]\} \\
&\overset{(a)}{=} \exp\left\{2\lambda p_G \pi \mathbb{E}_{z_i}\{\int_{r_0}^{R_B} (\exp\{jw\sqrt{GE_0} r_i^{-\alpha_L} z_i\} - 1)\} r_i dr_i\right\} \\
&\overset{(b)}{=} \exp\left\{2\lambda p_G \pi \int_{r_0}^{R_B} (\Phi_{\mathbf{z}}(\sqrt{GE_0} w r_i^{-\alpha_L}) - 1) r_i dr_i\right\} \\
&\overset{(c)}{=} \exp\left\{2\lambda p_G \pi \int_{r_0}^{R_B} (\Phi_0(\sqrt{GE_0}|w| r_i^{-\alpha_L}) - 1) r_i dr_i\right\} \\
&\overset{(d)}{=} \exp\left\{-2\lambda p_G \pi \frac{(\sqrt{GE_0}|w|)^{2/\alpha_L}}{\alpha_L} \int_{\sqrt{GE_0}|w| R_B^{-\alpha_L}}^{\sqrt{GE_0}|w| r_0^{-\alpha_L}} \frac{1 - \Phi_0(t)}{t^{2/\alpha_L + 1}} dt\right\},
\end{aligned} \tag{2.13}$$

where (a) follows from r_i having a PDF of $2r_i/(R_B^2 - r_0^2)$ if $r_0 \leq r_i \leq R_B$ and zero otherwise, (b) originates from the definition of the CF, (c) follows from the fact that $\mathbf{z}$ has a spherically symmetric (SS) PDF and its CF is also SS, i.e., $\Phi_{\mathbf{z}}(w) = \Phi_0(w)$ for some $\Phi_0(.)$, (d) is obtained by applying a change of variables with $t = \sqrt{GE_0}|w| r_i^{-\alpha_L}$.

$\Phi_0(t)$ can be found using the properties of an SS distribution:

$$\begin{aligned}
\Phi_0(t) = \Phi_{z_i}(t) &= \mathbb{E}\{\mathrm{e}^{jtz_i}\} \\
&= \mathbb{E}_{x_i}\{\cos(tx_i)\} + j \underbrace{\mathbb{E}_{y_i}\{\sin(ty_i)\}}_{0} \\
&= \mathbb{E}_{x_i}\{\cos(tx_i)\}
\end{aligned} \tag{2.14}$$

where $x_i = \mathrm{Re}\{z_i\}$, $y_i = \mathrm{Im}\{z_i\}$ and the second term is zero because sin is an odd-symmetric function.

By inserting the result in (2.14) into (2.13) and taking the expectation operator $\mathbb{E}_{x_i}\{.\}$ outside, the integral inside the exponential function can be calculated using the result from [41, Eq. (3.771.4)] as

$$\begin{aligned}
T_i &= \int_0^{\sqrt{GE_0}|w|r_0^{-\alpha_L}} \frac{1-\cos(tx_i)}{t^{2/\alpha_L+1}} - \int_0^{\sqrt{GE_0}|w|R_B^{-\alpha_L}} \frac{1-\cos(tx_i)}{t^{2/\alpha_L+1}} \\
&= \frac{\alpha_L}{2}\left(\sqrt{GE_0}|w|\right)^{-2/\alpha L}\Bigg[R_B^2 - r_0^2 + {}_1F_2\left(-\frac{1}{\alpha_L}; \frac{1}{2}, 1-\frac{1}{\alpha_L}; -\frac{GE_0|w|^2}{4r_0^{2\alpha_L}}x_i^2\right) \\
&- {}_1F_2\left(-\frac{1}{\alpha_L}; \frac{1}{2}, 1-\frac{1}{\alpha_L}; -\frac{GE_0|w|^2}{4R_B^{2\alpha_L}}x_i^2\right)\Bigg],
\end{aligned} \tag{2.15}$$

where ${}_pF_q$ is the generalized hypergeometric function. Then, by inserting the result of the integral in (2.15) into (2.13) and applying similar steps as in [31], we obtain the closed-form expression for $\Phi_{I^G_{\Psi_{\mathrm{LOS}}}}(w)$ as follows:

$$\begin{aligned}
\Phi_{I^G_{\Psi_{\mathrm{LOS}}}}(w) &= \exp\{\lambda p_G \pi (r_0^2 - R_B^2)\} \\
&\times \exp\Bigg\{ -\lambda p_G \pi r_0^2 {}_2F_2\left(-\frac{1}{2}, -\frac{1}{\alpha_L}; \frac{1}{2}, 1-\frac{1}{\alpha_L}; -\frac{GE_0|w|^2\sigma_0}{4r_0^{2\alpha_L}}\right) \\
&+ \lambda p_{\mathrm{G}} \pi R_B^2 {}_2F_2\left(-\frac{1}{2}, -\frac{1}{\alpha_L}; \frac{1}{2}, 1-\frac{1}{\alpha_L}; -\frac{GE_0|w|^2\sigma_0}{4R_B^{2\alpha_L}}\right)\Bigg\}.
\end{aligned} \tag{2.16}$$

Similarly, a closed-form expression for the CF of the interference due to NLOS BSs, $\Phi_{I^G_{\Psi_{\mathrm{LOS}}}}(w)$, can be obtained by changing the boundaries of the integral and replacing α_L with α_N in (2.13). More specifically, since NLOS BSs lie outside of the ball, integral is evaluated from R_B to infinity and the expression for $\Phi_{I^G_{\Psi_{\mathrm{LOS}}}}(w)$ is found as

$$\begin{aligned}&\Phi_{I^{G}_{\Psi_{\text{NLOS}}}}(w)\\&=\exp\{\lambda p_G\pi R_B^2\}\exp\left\{-\lambda p_G\pi R_B^2{}_2F_2\left(-\frac{1}{2},-\frac{1}{\alpha_N};\frac{1}{2},1-\frac{1}{\alpha_N};-\frac{GE_0|w|^2\sigma_0}{4R_B^{2\alpha_N}}\right)\right\}.\end{aligned}\tag{2.17}$$

Finally, a closed-form expression for the CF of the aggregate network interference, $\Phi_{I_{\text{agg}}}(w)$, can be obtained by inserting equations (2.16) and (2.17) into (2.11).

2.3.3 Average Pairwise Error Probability

In this section, APEP is computed by averaging PEP. Averaging can be performed by taking the integral of the conditional PEP over $|h_0|$ and r_0 as follows:

$$\begin{aligned}P_{\text{avg}}\{s_0\to\hat{s}_0\}&=\mathbb{E}_{|h_0|,r_0}\{P\{s_0\to\hat{s}_0||h_0|,r_0\}\}\\&=\mathbb{E}_{|h_0|,r_0}\left\{\frac{1}{2}-\frac{1}{\pi}\int_0^{\infty}\sin\left(\frac{\sqrt{G_0E_0}}{2r_0^{\alpha_L}}|\Delta_{s,\hat{s}}||h_0|w\right)w^{-1}\Phi_U(w)dw\right\}\\&\overset{(a)}{=}\frac{1}{2}-\frac{1}{\pi}\int_0^{\infty}\mathbb{E}_{r_0}\left\{\mathbb{E}_{|h_0|}\left\{\sin\left(\frac{\sqrt{G_0E_0}}{2r_0^{\alpha_L}}|\Delta_{s,\hat{s}}||h_0|w\right)\right\}\Phi_U(w)\right\}w^{-1}dw,\end{aligned}\tag{2.18}$$

where (a) follows from the fact that $\Phi_U(w)$ depends only on r_0 not $|h_0|$. Hence, the expectation over $|h_0|$ can be computed in closed-form by employing the PDF of Rayleigh distribution and calculating the resulting integral as [41]

$$\begin{aligned}\mathbb{E}_{|h_0|}\left\{\sin\left(\frac{\sqrt{\mathrm{G}_0E_0}}{2r_0^{\alpha_L}}|\Delta_{s,\hat{s}}||h_0|w\right)\right\}&=\int_0^{\infty}\sin\left(\frac{\sqrt{G_0E_0}}{2r_0^{\alpha_L}}|\Delta_{s,\hat{s}}||h_0|w\right)\frac{2\nu}{\sigma_0}\exp\{-\frac{\nu^2}{\sigma_0}\}d\nu\\&=\sqrt{\pi}\frac{\sqrt{G_0E_0\sigma_0}}{4r_0^{\alpha_L}}|\Delta_{s,\hat{s}}|w\exp\left\{-\frac{G_0E_0\sigma_0}{16r_0^{2\alpha_L}}|\Delta_{s,\hat{s}}|^2w^2\right\}.\end{aligned}\tag{2.19}$$

By substituting (2.19) and the PDF of r_0 (i.e., $f_{r_0}(\xi)$) into (2.18), APEP can be expressed as follows:

$$\begin{aligned} P_{\text{avg}}\{s_0 \to \hat{s}_0\} = \frac{1}{2} - \frac{1}{\pi} \int_0^\infty \int_0^\infty \sqrt{\pi} \frac{\sqrt{G_0 E_0 \sigma_0}}{4\xi^{\alpha_L}} |\Delta_{s,\hat{s}}| w \exp\left\{ - \frac{G_0 E_0 \sigma_0}{16 \xi^{2\alpha_L}} |\Delta_{s,\hat{s}}|^2 w^2 \right\} \\ 2\pi\lambda\xi \exp\{-\pi\lambda\xi^2\} \Phi_U(w) w^{-1} d\xi dw. \end{aligned} \tag{2.20}$$

Finally, substituting $\Phi_U(w)$ into (2.20) and after some algebraic manipulations, APEP can be rewritten as

$$\begin{aligned} & P_{\text{avg}}\{s_0 \to \hat{s}_0\} = \\ & \frac{1}{2} - \sqrt{\pi}\lambda \frac{\sqrt{G_0 \text{SNR}}}{2} |\Delta_{s,\hat{s}}| \int_0^\infty \int_0^\infty \exp\left\{ - \frac{\text{SNR}}{4\xi^{2\alpha_L}} |\Delta_{s,\hat{s}}|^2 w^2 \right\} \exp\{-\pi\lambda\xi^2\} \\ & \times \exp\{-w^2 N_0/4\} \prod_{G \in \{MM, Mm, mm\}} \big[\exp\left\{\lambda p_G \pi \xi^2\right\} \exp\big\{ - \lambda p_G \pi \xi^2 {}_2F_2(\xi, \alpha_L) + \\ & \lambda p_G \pi R_B^2 \left[{}_2F_2(R_B, \alpha_L) - {}_2F_2(R_B, \alpha_N) \right] \big\} \big]^{p_G} d\xi dw, \end{aligned} \tag{2.21}$$

where we define $\text{SNR} = E_0 \sigma_0 / 4$ and

$${}_2F_2(x, y) = {}_2F_2\left(\frac{1}{2}, -\frac{1}{y}; \frac{1}{2}, 1 - \frac{1}{y}; -\frac{G \text{SNR} |w|^2}{x^{2y}} \right). \tag{2.22}$$

2.3.4 Average Symbol Error Probability

In this section, we approximate ASEP from APEP in (2.21) by using NN approximation. The advantage of the NN approximation is that it only depends on the minimum distance in the constellation and the number of nearest neighbors [42]. In Section II, $|\Delta_{s,\hat{s}}|$ is defined as the distance between the constellation points s_0 and $\hat{s}_0$. Hence, we define Δ_{min} as the distance of s_0 to its nearest neighbors, i.e., $\Delta_{min} = \min_{\hat{s}_0 \neq s_0} |\Delta_{s_0, \hat{s}_0}|$. Also, let $k_{d_{\min}}$ denote the number of nearest neighbors of s_0 having distance Δ_{min}. Now, ASEP can be approximated as

$$\text{ASEP} \approx k_{d_{\min}} P_{\text{avg}}\{\Delta_{min}\}, \tag{2.23}$$

where $k_{d_{\min}} = 2$ when modulation order (γ) is greater than 2, and $\Delta_{min} = 2\sin(\pi/\gamma)$ assuming multilevel phase shift keying (MPSK) modulation.

2.4 ASEP in the Presence of Beamsteering Errors

In Section 2.3, MU and the serving BS are assumed to be aligned perfectly and ASEP is calculated in the absence of beamsteering errors. However, in practice, it may not be easy to have perfect alignment. Therefore, in this section, we investigate the effect of beamforming alignment errors on ASEP. We employ an error model similar to that in [43]. Let $|\epsilon|$ be the random absolute beamsteering error of the MU's beam toward the serving BS with zero-mean and bounded absolute error $\epsilon_{\max} \leq \pi$. It is appropriate to consider the absolute beamsteering error due to symmetry in the gain G. The PDF of the effective antenna gain G with alignment error can be explicitly written as [13]

$$\begin{aligned} f_G(\mathrm{g}) = {} & F_{|\epsilon|}\left(\frac{\theta}{2}\right)^2 \delta(\mathrm{g} - MM) + 2F_{|\epsilon|}\left(\frac{\theta}{2}\right)\left(1 - F_{|\epsilon|}\left(\frac{\theta}{2}\right)\right) \delta(\mathrm{g} - Mm) \\ & + \left(1 - F_{|\epsilon|}\left(\frac{\theta}{2}\right)\right)^2 \delta(\mathrm{g} - mm), \end{aligned} \tag{2.24}$$

where $\delta(\cdot)$ is the Kronecker's delta function, $F_{|\epsilon|}(x)$ is the CDF of the misalignment error and (2.24) follows from the definition of CDF, i.e., $F_{|\epsilon|}(x) = P\{|\epsilon| \leq x\}$. Assume that the error is distributed according to a Gaussian distribution, so absolute error $|\epsilon|$ follows a half normal distribution and $F_{|\epsilon|}(x) = \mathrm{erf}(x/(\sqrt{2}\sigma_{\mathrm{BE}}))$, where $\mathrm{erf}(\cdot)$ denotes the error function.

From (2.21), it is clear that PEP depends on the effective antenna gain between the MU and the serving BS, and so does the ASEP. Thus, PEP can be calculated by averaging over the distribution of G, $f_G(\mathrm{g})$, as follows:

$$\begin{aligned} P_{\mathrm{avg}}\{s_0 \to \hat{s}_0\} &= \mathbb{E}_G\{P_{\mathrm{avg}}\{s_0 \to \hat{s}_0; G\}\} \\ &= \int_0^\infty P_{\mathrm{avg}}\{s_0 \to \hat{s}_0; \mathrm{g}\} f_G(\mathrm{g}) d\mathrm{g} \\ &= (F_{|\epsilon|}(\theta/2))^2 P_{\mathrm{avg}}\{s_0 \to \hat{s}_0; MM\} \\ &+ 2(F_{|\epsilon|}(\theta/2))\bar{F}_{|\epsilon|}(\theta/2) P_{\mathrm{avg}}\{s_0 \to \hat{s}_0; Mm\} \\ &+ \bar{F}_{|\epsilon|}(\theta/2)^2 P_{\mathrm{avg}}\{s_0 \to \hat{s}_0; mm\}, \end{aligned} \tag{2.25}$$

where we define $\bar{F}_{|\epsilon|}(\theta/2) = 1 - F_{|\epsilon|}(\theta/2)$.

2.5 Numerical Results

In this section, we provide numerical results to evaluate the error performance of a downlink mmWave cellular network. In all figures, LOS and NLOS path loss exponents are $\alpha_L = 2.1$ and $\alpha_N = 4$, respectively. In the non-mmW case, all BSs are assumed to be LOS and the path loss component is equal to 2.1. Also, the radius of the LOS ball R_B is assumed to be equal to 141 meters similarly as in [9].

First, we compare the performance of the mmWave network with that of the non-mmWave network (antennas are omnidirectional, and all BSs are LOS). In Fig. 2.1, ASEP versus SNR is plotted for different BS densities with BPSK modulation. As shown in Fig. 2.1, we have better error performance in the mmWave scenario than in the non-mmWave one. Also, with the increasing BS density, ASEP is decreasing.

Next, we plot the ASEP with different antenna main lobe gains and different BS densities. The numerical results in Fig. 2.2 show that with increasing main lobe gain M, ASEP decreases significantly. Also, note that different combinations of main lobe gain and BS density, e.g. ($M = 20dB$, $\lambda = 10^{-5}$) and ($M = 10dB$, $\lambda = 10^{-4}$) lead to the same error performance. Hence, the same error performance can be achieved by

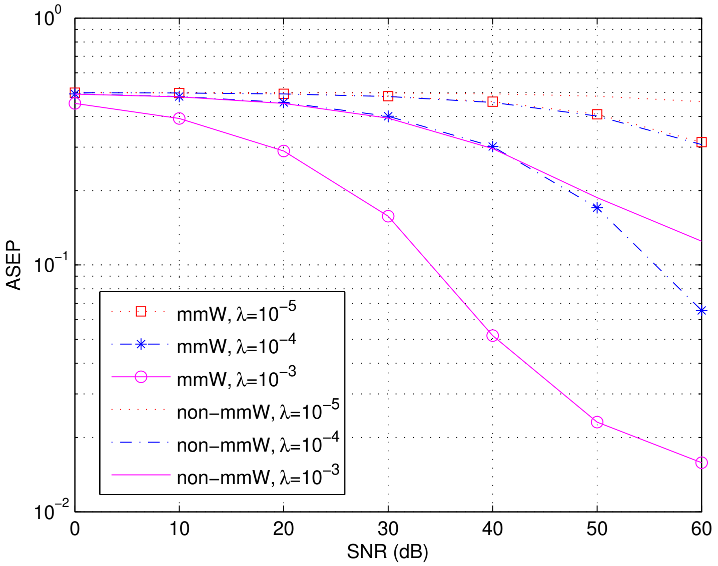

Figure 2.1: ASEP as a function of the SNR $= E_0\sigma_0/4$ for different BS densities λ ($\alpha_L = 2.1$, $\alpha_N = 4$, $M = 10$ dB, $m = -10$ dB, $\theta = 15$, BPSK)

either decreasing BS density while increasing the main lobe gain, or vice versa.

In Fig. 2.3, we also compare ASEP for different modulation orders assuming MPSK modulation. As the modulation order increases, the minimum distance between the nearest neighbors decreases. Thus, as expected, error performance of the network gets worse with the increase in modulation size.

Finally, the effect of beamsteering errors on the error performance is analyzed in Fig. 2.4. ASEP versus SNR is plotted for different standard deviations of the alignment error. As can be seen, ASEP is getting worse with the degradation in the alignment angle. $\sigma_{\mathrm{BE}} = 0$ corresponds to the case with no alignment error and it has the best error performance as expected. Since $\sigma_{\mathrm{BE}} = 2$ has the same ASEP with $\sigma_{\mathrm{BE}} = 0$, we can infer that the alignment error until $\sigma_{\mathrm{BE}} = 2$ can be tolerated and ASEP increases significantly for $\sigma_{\mathrm{BE}} > 2$.

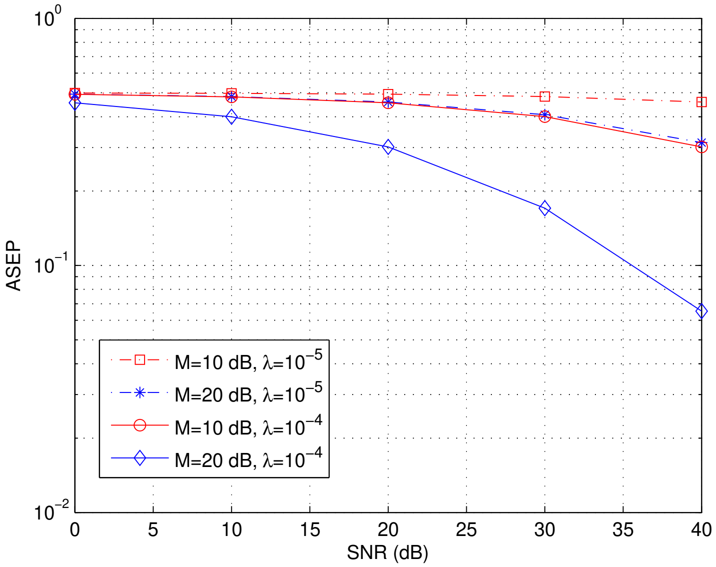

Figure 2.2: ASEP as a function of the SNR $= E_0\sigma_0/4$ for different antenna main lobe gains M and BS densities λ ($\alpha_L = 2.1$, $\alpha_N = 4$, $m = -10$ dB, $\theta = 15$, BPSK)

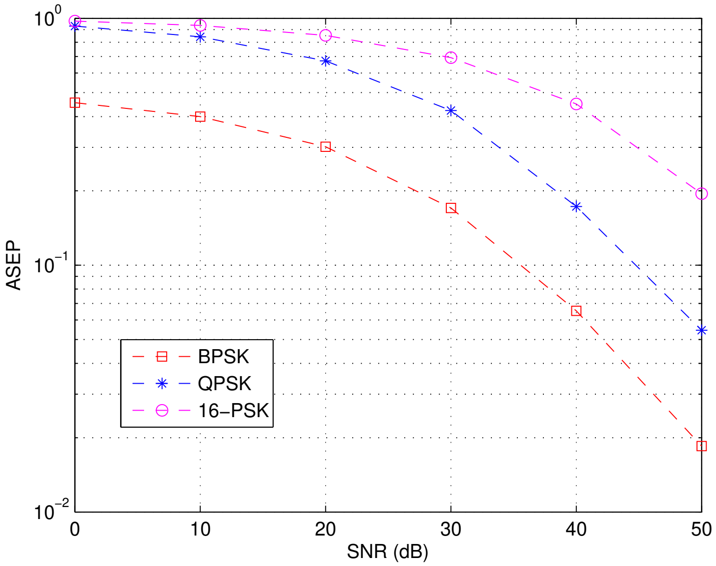

Figure 2.3: ASEP as a function of the SNR $= E_0\sigma_0/4$ for different modulation orders Mo ($\alpha_L = 2.1$, $\alpha_N = 4$, $M = 20$, dB $m = -10$ dB, $\theta = 15$, $\lambda = 10^{-4}$)

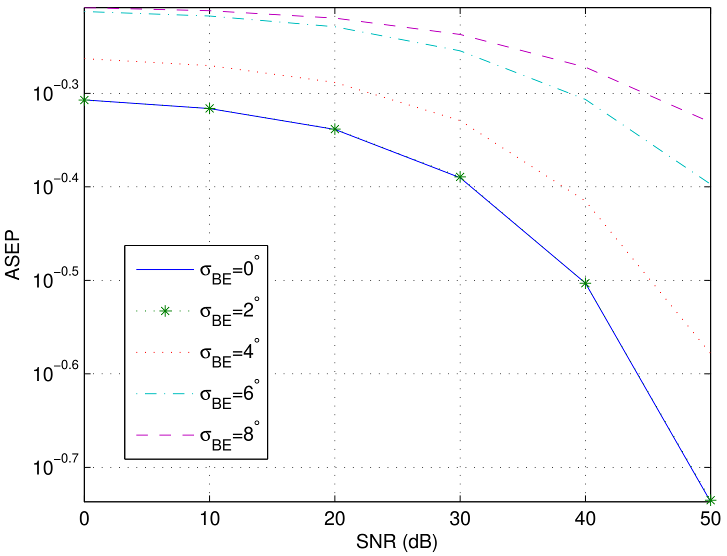

Figure 2.4: ASEP as a function of the SNR $= E_0\sigma_0/4$ in the presence of beamsteering error for different standard deviations of alignment error ($\alpha_L = 2.1$, $\alpha_N = 4$, $M = 20$, dB $m = -10$ dB, $\theta = 15$, $\lambda = 10^{-5}$, BPSK)

2.6 Conclusion

In this chapter, we have analyzed the average error performance of downlink mmWave cellular networks, incorporating the distinguishing features of mmWave communication into the average error probability analysis. Sectored antenna and simplified ball-LOS models have been considered to simplify the analysis. Numerical results show that employing directional antennas improves the error performance. Also, we show that better ASEP values can be obtained by increasing BS density and main lobe gain.

Chapter 3

Energy Efficiency in Relay-Assisted Millimeter Wave Cellular Networks

In this chapter, energy efficiency of relay-assisted mmWave cellular networks with PPP distributed BSs and relay stations (RSs) is analyzed using tools from stochastic geometry. The distinguishing features of mmWave communications such as directional beamforming and having different path loss laws for LOS and NLOS links are incorporated into the energy efficiency analysis. Following the description of the system model for mmWave cellular networks, coverage probabilities are computed for each link. Subsequently, average power consumption of BSs and RSs are modeled and energy efficiency is determined in terms of system parameters. Energy efficiency in the presence of beamforming alignment errors is also investigated to get insight on the performance in practical scenarios. Finally, the impact of BS and RS densities, antenna gains, main lobe beam widths, LOS interference range, and alignment errors on the energy efficiency is analyzed via numerical results.

3.1 Introduction

As we discussed in Section 1, it has been shown that mmWave networks can achieve comparable coverage area and much higher data rates than μWave networks when the BS density is sufficiently high and highly directional antennas are used [9]. With increase in the number of BSs in mmWave networks, however, energy efficiency is becoming an important consideration as well.

Energy efficiency of cellular networks has been extensively studied recently. Use of RS has been considered an effective way to have energy efficient and flexible networks while maintaining the coverage area and date rates. Unlike the BSs, RSs are not connected to the core network with wired backhaul, and therefore this provides a significant reduction in energy consumption. In [44], energy efficiency of relay-assisted networks are investigated using stochastic geometry. Authors of [45] analyzed the effect of station density on the energy efficiency of relay-assisted cellular networks. However, these studies cannot be directly applied to mmWave cellular networks since unique features of mmWave communication have not been considered. Energy efficiency of millimeter wave cellular networks is studied in [46] and [47]. In [46], the impact of mmWave cellular channels on data rates and power consumption is analyzed using consumption factor framework. In [47], employment of RSs are combined with mmWave channel model. However, these two papers have not taken into account, in their energy efficiency analysis, the network model based on stochastic geometry. Therefore, we employ stochastic geometry to analyze the energy efficiency of relay-assisted downlink mmWave cellular networks.

3.2 System Model

In this section, we introduce our system model for the relay-assisted downlink mmWave cellular network. The locations of BSs and RSs are modeled according to two independent homogeneous PPPs Φ_B and Φ_R of densities λ_B and λ_R, respectively, on the Euclidean plane. Mobile users (MUs) are distributed according to some independent stationary point process. Two different types of MUs are considered: non-cooperative MU (MU_{nc}) and cooperative MU (MU_c). MU_{nc}s directly communicate with the serving BS which we denote by BS_0, while MU_cs communicate with the serving BS via the help of the RSs. It assumed that the MUs are served by the closest nodes in the network. Let BS_0 and RS_0 be the closest base station and the closest relay, respectively, to a typical MU. MU is classified as MU_{nc} if its distance to BS_0 is less than that to RS_0. Similarly, it is designated as a MU_c if RS_0 is closer to this MU than BS_0. Also, RSs are associated with the closest BS, denoted by BS_0^R.

As shown in Fig. 1, BS_0-MU_{nc} and BS_0-RS_0-MU_c links work in non-overlapping frequency bands with bandwidths B_{nc} and B_c, respectively. A two-slot synchronous communication protocol is assumed in each cell for the BS_0-RS_0-MU_c link. In the first time slot, BSs transmit signals to RSs, while in the second time slot, RSs forward the data (decoded from the received signal in the first time slot) to the MU_cs. The time duration of both time slots are assumed to be equal. Since separate frequency bands are assumed, the other-cell interference at MU_{nc} is due to the BSs that use the same resource block with BS_0. Similarly, the other-cell interference at RSs is from the BSs operating at the same frequency with BS_0^R, and interference at MU_c is due to the RSs using the same frequency with RS_0.

In this setting, we have the following three assumptions regarding the system model of the downlink mmWave cellular network:

Assumption 3.1 *Antenna arrays at the BSs, RSs and MUs are assumed to perform directional beamforming where the main lobe is directed towards the dominant propagation path while smaller sidelobes direct energy in other directions. For tractability in the analysis, antenna arrays are approximated by a sectored antenna model, in which the array gains are assumed to be constant M for all angles in the main lobe and*

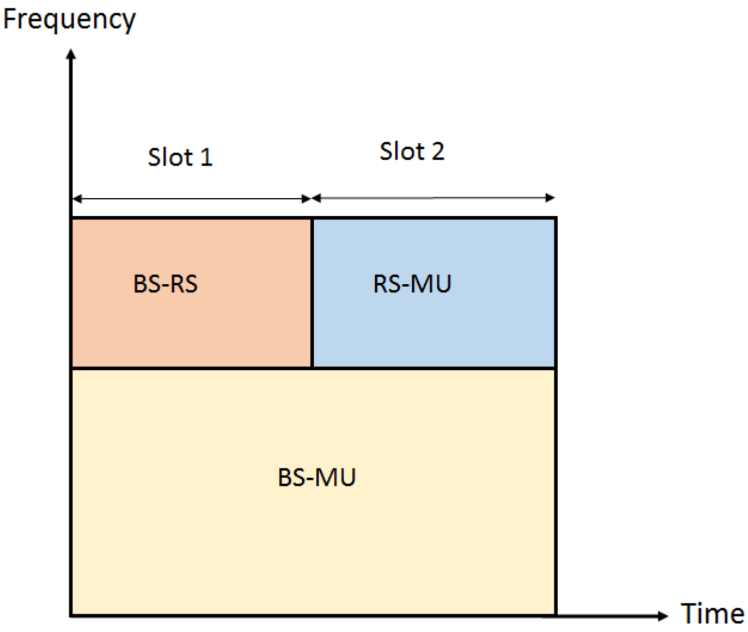

Figure 3.1: Relay-assisted mmWave Cellular Network Frame Structure

another smaller constant m in the side lobe [34]. Initially, perfect beam alignment is assumed in the BS_0-MU_{nc}, BS_0^R-RS_0 and RS_0-MU_c links[1]*, leading to an overall antenna gain of MM. Also, beam direction of the interfering nodes is modeled as a uniform random variable on $[0, 2\pi]$. Therefore, the effective antenna gain is a discrete random variable (RV) described by*

$$G = \begin{cases} MM & \text{with prob. } p_{MM} = (\frac{\theta}{2\pi})^2 \\ Mm & \text{with prob. } p_{Mm} = 2\frac{\theta}{2\pi}\frac{2\pi-\theta}{2\pi} \\ mm & \text{with prob. } p_{mm} = (\frac{2\pi-\theta}{2\pi})^2, \end{cases} \tag{3.1}$$

where θ is the beam width of the main lobe, and p_G is the probability of having an antenna gain of G.

Assumption 3.2 *A BS or RS can either have a LOS or NLOS link to the MU according to the LOS probability function $p(r)$ which is the probability that a link of length r is LOS. Using field measurements and stochastic blockage models, $p(r)$ can*

---

[1] Subsequently, beamsteering errors are also addressed.

be modeled as $e^{-\beta r}$ *where decay rate* β *depends on the building parameter and density [35]. For simplicity, LOS probability function* $p(r)$ *can be approximated by a step function. In this approach, the irregular geometry of the LOS region is replaced with its equivalent LOS ball model with radius* R_B *[9]. A BS or RS is a LOS node to the MU if it is inside the ball, otherwise it is a NLOS node. Different path loss laws are applied to LOS and NLOS links. Thus, the path-loss exponent on each interfering link can be expressed as follows:*

$$\alpha_i = \begin{cases} \alpha_L & if\, r \leq R_B \\ \alpha_N & if\, r > R_B, \end{cases} \tag{3.2}$$

where α_L *and* α_N *are the LOS and NLOS path-loss exponents, respectively.*

Assumption 3.3 *Serving nodes (BS or RS) are assumed to be LOS to the corresponding receiving nodes (RS or MU), and therefore the path loss exponent in the serving link is always equal to* α_L*.*

3.3 Coverage Probability

In this section, we first express the SINRs at the RSs and MUs by combining the above three assumptions with the described network model. Then, we derive the coverage probabilities for each link.

3.3.1 Signal-to-Interference-plus-Noise Ratio (SINR)

1)BS$_0$*-MU*$_{nc}$ *link:* The SINR in the downlink from the the BS$_0$ to the MU$_{nc}$ can be written as:

$$\mathrm{SINR}_{BU} = \frac{P_{BU} G_0 h_0 x_0^{-\alpha_L}}{\sigma^2 + \underbrace{\sum_{i \in \Phi_B^{\setminus \mathrm{BS}_0}} P_{BU} G_i h_i x_i^{-\alpha_i}}_{I_{BU}}}, \tag{3.3}$$

where P_{BU} is the transmit power of BS$_0$, G_0 is the effective antenna gain of the link which is assumed to be equal to MM, h_0 is the small-scale fading gain, α_L is the LOS path-loss exponent of the link, x_0 is the transmission distance, σ^2 is the variance of the additive white Gaussian noise component, and I_{BU} is the aggregate other-cell interference at MU$_{nc}$. A similar notation is used for I_{BU}, but note that the effective antenna gain G_i and path loss exponent α_i are different for different interfering links as described in (3.1) and (3.2), respectively.

2)BS$_0^R$-RS$_0$ and RS$_0$-MU$_c$ links: The SINRs in the downlink from the the BS$_0^R$ to the RS$_0$, and from the RS$_0$ to the MU$_c$ can be written, respectively, as follows:

$$\mathrm{SINR}_{BR} = \frac{P_{BR} G_0 g_0 y_0^{-\alpha_L}}{\sigma^2 + \underbrace{\sum_{i \in \Phi_B^{\backslash \mathrm{BS}_0^R}} P_{BR} G_i g_i y_i^{-\alpha_i}}_{I_{BR}}}, \tag{3.4}$$

$$\mathrm{SINR}_{RU} = \frac{P_{RU} G_0 \tilde{g}_0 \tilde{y}_0^{-\alpha_L}}{\sigma^2 + \underbrace{\sum_{i \in \Phi_R^{\backslash \mathrm{RS}_0}} P_{RU} G_i \tilde{g}_i \tilde{y}_i^{-\alpha_i}}_{I_{RU}}}, \tag{3.5}$$

where a notation similarly as described in (3.3) is used with similar parameter definitions.

All links are assumed to be subject to independent Nakagami fading (i.e., small-scale fading gains have a gamma distribution). Parameters of Nakagami fading are N_L and N_N for LOS and NLOS links, respectively, and they are assumed to be positive integers for simplicity.

3.3.2 SINR Coverage Probability

The SINR coverage probability $\mathrm{P_C}$ is defined as the probability that the received SINR is larger than a certain threshold $T > 0$, i.e., $\mathrm{P_C} = \mathbb{P}(\mathrm{SINR} > T)$. The coverage probability in the single-hop transmission and dual-hop relayed transmission can be formulated as follows:

$$\mathrm{P_C} = \begin{cases} \mathbb{P}(\mathrm{SINR}_{BU} > T) & \text{for } \mathrm{MU}_{nc} \\ \mathbb{P}(\mathrm{SINR}_{BR} > T)\mathbb{P}(\mathrm{SINR}_{RU} > T) & \text{for } \mathrm{MU}_{c}. \end{cases} \tag{3.6}$$

Since decode-and-forward relaying strategy is employed by the RSs, a MU_c is served if the SINRs of both links are larger than the threshold T. In other words, BS_0-RS_0-MU_c link works if both RS and MU_c can decode the received signal successfully.

Now, the coverage probability for the BS_0-MU_{nc} link can be calculated as

$$\begin{aligned} \mathrm{P_C^{BU}} &= \mathbb{P}(\mathrm{SINR}_{BU} > T) \\ &= \int_{x_0>0} \mathbb{P}\left(h_0 \geq \frac{T x_0^{\alpha_L}(\sigma^2 + I_{BU})}{P_{BU} G_0} \mid x_0 \right) f_{x_0}(x_0) dx_0 \\ &= \int_0^{R_B} \sum_{n=1}^{N_L} (-1)^{n+1} \binom{N_L}{n} e^{-\frac{n\eta_L T x_0^{\alpha_L} \sigma^2}{P_{BU} G_0}} \mathcal{L}_{I_{BU}}\left(\frac{n\eta_L T x_0^{\alpha_L} I_{BU}}{P_{BU} G_0} \right) f_{x_0}(x_0) dx_0, \end{aligned} \tag{3.7}$$

where $f_{x_0}(x_0) = 2\pi\lambda x_0 \exp\{-\pi\lambda x_0^2\}$ is the probability density function of the distance between an MU and its nearest LOS BS [33], $\eta_L = N_L(N_L!)^{-\frac{1}{N_L}}$, $\mathcal{L}_{I_{BU}}(s)$ is the Laplace transform of I_{BU} evaluated at s, and (3.7) is derived noting that $|h_0|^2$ is a normalized gamma random variable with parameter N_L and using the similar steps in [9]. Since *LOS probability function* $p(\cdot)$ is equal to one inside the ball of radius R_B and zero otherwise, integral in (3.7) is from 0 to R_B. We can employ the thinning property of PPP to split the I_{BU} into 6 independent PPPs as follows [32]:

$$\begin{aligned} I_{BU} &= I_{BU,L} + I_{BU,N} \\ &= I_{BU,L}^{MM} + I_{BU,L}^{Mm} + I_{BU,L}^{mm} + I_{BU,N}^{MM} + I_{BU,N}^{Mm} + I_{BU,N}^{mm} \\ &= \sum_{G \in \{MM,Mm,mm\}} (I_{BU,L}^{G} + I_{BU,N}^{G}), \end{aligned} \tag{3.8}$$

where $I_{BU,L}$ is the aggregate LOS interference arising from the BSs inside the LOS ball, $I_{BU,N}$ is the aggregate NLOS interference from outside the LOS ball, and $I^{G}_{BU,L}$ and $I^{G}_{BU,N}$ denote the LOS and NLOS interferences, respectively, with random antenna gain G defined in (3.1). According to the thinning theorem, each independent PPP has a density of $\lambda_B p_G$ where p_G is given in (3.1) for each antenna gain $G \in \{MM, Mm, mm\}$.

Inserting (3.8) into the Laplace transform expression and using the definition of Laplace transform yield

$$\begin{aligned}
\mathcal{L}_{I_{BU}}(s) &= \mathbb{E}_{I_{BU}}[e^{-sI_{BU}}] = \mathbb{E}_{I_{BU}}[e^{-s(I_{BU,L}+I_{BU,N})}] \\
&\overset{(a)}{=} \mathbb{E}_{I_{BU,L}}\left[e^{-s(I^{MM}_{BU,L}+I^{Mm}_{BU,L}+I^{mm}_{BU,L})}\right]\mathbb{E}_{I_{BU,N}}\left[e^{-s(I^{MM}_{BU,N}+I^{Mm}_{BU,N}+I^{mm}_{BU,N})}\right] \\
&= \prod_{G}\prod_{j}\mathbb{E}_{I^{G}_{BU,j}}[e^{-sI^{G}_{BU,j}}],
\end{aligned} \tag{3.9}$$

where $G \in \{MM, Mm, mm\}$, $j \in \{L, N\}$, $s = \frac{n\eta_L T x_0^{\alpha_L}}{P_{BU}G_0}$, and (a) follows from the fact that $I_{BU,L}$ and $I_{BU,N}$ are interferences generated from two independent thinned PPPs $\Phi_{B,L}$ and $\Phi_{B,N}$, respectively. Now, we can compute the Laplace transform for the LOS interfering links with a generic antenna gain G using stochastic geometry as follows:

$$\begin{aligned}
\mathbb{E}_{I^{G}_{BU,L}}[e^{-sI^{G}_{BU,L}}] &= e^{-2\pi\lambda_B p_G\int_{x_0}^{R_B}(1-\mathbb{E}_h[e^{-sP_{BU}Ght^{-\alpha_L}}])p(t)tdt} \\
&\overset{(a)}{=} e^{-2\pi\lambda_B p_G\int_{x_0}^{R_B}(1-1/(1+sP_{BU}Gt^{-\alpha_L}/N_L)^{N_L})tdt},
\end{aligned} \tag{3.10}$$

where $p(\cdot)$ is again the *LOS probability function*, which is equal to 1 inside the ball and (a) is obtained by computing the moment generating function (MGF) of the gamma random variable h. Similarly, Laplace transform for the NLOS interfering links with a generic antenna gain G can be calculated as

$$\begin{aligned}\mathbb{E}_{I_{BU,N}^{G}}[e^{-sI_{BU,N}^{G}}] &= e^{-2\pi\lambda_B p_G \int_{R_B}^{\infty}(1-\mathbb{E}_h[e^{-sP_{BU}Ght^{-\alpha_N}}])(1-p(t))tdt} \\ &= e^{-2\pi\lambda_B p_G \int_{R_B}^{\infty}(1-1/(1+sP_{BU}Gt^{-\alpha_N}/N_N)^{N_N})tdt}. \end{aligned} \tag{3.11}$$

By inserting (3.10) and (3.11) into (3.9), Laplace transform of I_{BU} can be obtained. Finally, SINR coverage probability for the BS$_0$-MU$_{nc}$ link is given by

$$\begin{aligned}\mathrm{P}_{\mathrm{C}}^{BU} &= \int_0^{R_B}\sum_{n=1}^{N_L}(-1)^{n+1}\binom{N_L}{n}e^{-\frac{n\eta_L T x_0^{\alpha_L}\sigma^2}{P_{BU}G_0}} \\ &\times e^{-2\pi\lambda_B(\sum_{i=1}^{3}p_{G_i}\int_{x_0}^{R_B}(1-1/(1+sP_{BU}Gt^{-\alpha_L}/N_L)^{N_L})tdt+\sum_{i=1}^{3}p_{G_i}\int_{R_B}^{\infty}(1-1/(1+sP_{BU}Gt^{-\alpha_N}/N_N)^{N_N})tdt)} \\ &\times e^{-\pi\lambda_B x_0^2}2\pi\lambda_B x_0 dx_0. \end{aligned} \tag{3.12}$$

SINR coverage probability for the BS$_0^R$-RS$_0$ link can be computed by following similar steps, and it is given by

$$\begin{aligned}\mathrm{P}_{\mathrm{C}}^{BR} &= \int_0^{R_B}\sum_{n=1}^{N_L}(-1)^{n+1}\binom{N_L}{n}e^{-\frac{n\eta_L T y_0^{\alpha_L}\sigma^2}{P_{BR}G_0}} \\ &\times e^{-2\pi\lambda_{min}(\sum_{i=1}^{3}p_{G_i}\int_{y_0}^{R_B}(1-1/(1+sP_{BR}Gt^{-\alpha_L}/N_L)^{N_L})tdt+\sum_{i=1}^{3}p_{G_i}\int_{R_B}^{\infty}(1-1/(1+sP_{BR}Gt^{-\alpha_N}/N_N)^{N_N})tdt)} \\ &\times e^{-\pi\lambda_B y_0^2}2\pi\lambda_B y_0 dy_0. \end{aligned} \tag{3.13}$$

where $s = \frac{n\eta_L T y_0^{\alpha_L}}{P_{BR}G_0}$, $\lambda_{min} = \min\{\lambda_B, \lambda_R\}$. The only difference is that in the derivation of the Laplace transform λ_{min} is used instead of λ_B because at any time only at most λ_{min} BSs per square meter are transmitting signals to RSs.

For the RS$_0$ $-$ MU$_c$ link, SINR coverage probability can be computed similarly as for the other links, but the distance between RS and MU follows a different distribution. Since the RSs are distributed according to a PPP and MUs follows some independent stationary point process in the given circular region around the RS, the distance between the MU and its corresponding RS follows a distribution with pdf $f_R(r) = 2r/a^2$ for $0 \leq r \leq a$ [44]. Also, since only the RSs with received SINR larger than a certain threshold can decode and forward the signal to the MU_cs, the density used in SINR coverage calculation for this link is $\lambda' = \lambda_{min}\mathrm{P}_{\mathrm{C}}^{BR}$. Finally, coverage probability for the $\mathrm{RS}_0 - \mathrm{MU}_c$ link is given by

$$\mathrm{P}_{\mathrm{C}}^{RU} = \int_0^a \sum_{n=1}^{N_L} (-1)^{n+1} \binom{N_L}{n} e^{-\frac{n\eta_L T \tilde{y}_0^{\alpha_L} \sigma^2}{P_{RU} G_0}}$$
$$\times\, e^{-2\pi\lambda' (\sum_{i=1}^{3} p_{G_i} \int_{\tilde{y}_0}^{R_B} (1-1/(1+sP_{RU}Gt^{-\alpha_L}/N_L)^{N_L}) t dt + \sum_{i=1}^{3} p_{G_i} \int_{R_B}^{\infty} (1-1/(1+sP_{RU}Gt^{-\alpha_N}/N_N)^{N_N}) t dt)}$$
$$\times\, \frac{2\tilde{y}_0}{a^2} d\tilde{y}_0. \tag{3.14}$$

where $s = \frac{n\eta_L T \tilde{y}_0^{\alpha_L}}{P_{RU} G_0}$.

3.4 Energy Efficiency Analysis

3.4.1 Power Model

The total power consumption per BS or RS can be modeled as $P_{tot} = P_0 + \beta P_T$, where $1/\beta$ is the efficiency of the power amplifier, and P_0 is the static power consumption due to signal processing, battery backup, site cooling etc., and P_T corresponds to the transmit power [48]. Using this power formulation, the average power consumption of BSs (per unit area) in the cellular network can be expressed as

$$P_{B_{avg}} = \lambda_B P_{B_0} + \beta_B(\lambda_B P_{BU} + \lambda_{min} P_{BR}/2),, \tag{3.15}$$

where P_{B_0} is the static power consumption of a BS, $1/\beta_B$ is the efficiency of power amplifiers at the BSs, and $1/2$ factor is due to the fact that RSs are active only in one of the two time slots as depicted in Fig. 3.1. The first term is the average static power consumed regardless of whether the BSs are active or inactive, and the second term is the average transmit power consumed at BSs transmitting to MU_{nc}s and RSs. Note that at most only $\lambda_{min} = \min\{\lambda_B, \lambda_R\}$ BSs per square meter are transmitting signals to RSs.

Similarly, the average power consumption of the RSs (per unit area) in the cellular network is given by

$$P_{R_{avg}} = (\lambda_R - \lambda')P_{R_0} + \lambda'(\beta_R P_{RU}/2 + P_{R_0}), \tag{3.16}$$

where P_{R_0} is the static power consumption of an RS, $1/\beta_R$ is the efficiency of power amplifiers at the RSs, and 1/2 factor is due to the fact that RSs are active only in the second time slot. In this scenario, only the RSs which can decode the signals from BSs can successfully forward them to MU_cs, and therefore the density of the active RSs is $\lambda' = \lambda_{min}\mathrm{P}_{\mathrm{C}}^{BR}$. As a result, $(\lambda_R - \lambda')$ RSs per square meter are inactive and they consume only static power. Thus, the second term is the sum of average transmit power and average static power consumed at active RSs.

3.4.2 Energy Efficiency Metric

Energy efficiency can be measured and quantified as the ratio of the area spectral efficiency to the average network power consumption:

$$\mathrm{EE} = \frac{\tau_{nc} + \tau_c}{P_{B_{avg}} + P_{R_{avg}}}(bps/Hz/W) \tag{3.17}$$

where τ_{nc} and τ_c are the area spectral efficiencies taken over all the BS-MU and BS-RS-MU links, respectively. The area spectral efficiency (i.e., network throughput) can be defined as the product of the throughput at a given link and density of transmitters (BSs or RSs), and can be formulated as follows [44]:

$$\tau_{nc} = \frac{B_{nc}}{B_{nc} + B_c}\lambda_B \mathrm{P}_{\mathrm{C}}^{BU} \log_2(1 + T) \tag{3.18}$$

$$\tau_c = \frac{1}{2}\frac{B_c}{B_{nc} + B_c}\lambda_{min}\mathrm{P}_{\mathrm{C}}^{BR}\mathrm{P}_{\mathrm{C}}^{RU} \log_2(1 + T), \tag{3.19}$$

where 1/2 factor is due to half-duplex operation of the RSs.

3.4.3 Coverage and Energy Efficiency In the Presence of Beamsteering Errors

In Section 3.4.2 and the preceding analysis, antenna arrays at the serving nodes (BS or RS) and receiving nodes (RS or MU) are assumed to be aligned perfectly and energy efficiency is calculated in the absence of beamsteering errors. However, in practice, it may not be easy to have perfect alignment. Therefore, in this section, we investigate the effect of beamforming alignment errors on the energy efficiency of the network. We employ an error model similar to that in [43]. Let $|\epsilon|$ be the random absolute beamsteering error of the transmitting node toward the receiving node with zero-mean and bounded absolute error $|\epsilon|_{\max} \leq \pi$. Due to symmetry in the gain G_0, it is appropriate to consider the absolute beamsteering error. The PDF of the effective antenna gain G_0 with alignment error can be explicitly written as [13]

$$\begin{aligned} f_{G_0}(\mathrm{g}) = {} & F_{|\epsilon|}\left(\frac{\theta}{2}\right)^2 \delta(\mathrm{g} - MM) + 2F_{|\epsilon|}\left(\frac{\theta}{2}\right)\left(1 - F_{|\epsilon|}\left(\frac{\theta}{2}\right)\right) \delta(\mathrm{g} - Mm) \\ & + \left(1 - F_{|\epsilon|}\left(\frac{\theta}{2}\right)\right)^2 \delta(\mathrm{g} - mm), \end{aligned} \tag{3.20}$$

where $\delta(\cdot)$ is the Kronecker's delta function, $F_{|\epsilon|}(x)$ is the CDF of the misalignment error and (3.20) follows from the definition of CDF, i.e., $F_{|\epsilon|}(x) = \mathbb{P}\{|\epsilon| \leq x\}$. Assume that the error ϵ is Gaussian distributed, and therefore the absolute error $|\epsilon|$ follows a half normal distribution with $F_{|\epsilon|}(x) = \mathrm{erf}(x/(\sqrt{2}\sigma_{\mathrm{BE}}))$, where $\mathrm{erf}(\cdot)$ denotes the error function and σ_{BE} is the standard deviation of the Gaussian error ϵ.

It is clear that all SINR coverage probability expressions in Section 3.3.2 depend on the effective antenna gain G_0 between the serving and the receiving nodes, and so does the energy efficiency. Thus, SINR coverage probability $\mathrm{P_C}$ for a generic link can

Table 3.1: System Parameters

Parameters	Values
α_L, α_N	2, 4
N_L, N_N	3, 2
M, m	20dB, -10dB
λ_R	$10^{-4}/m^2$
R_B, a	100m, 30m
T, σ^2	30dB, -70dBm
B_{nc}, B_c	1GHz, 100MHz
P_{BU}, P_{BR}, P_{RU}	50dBm, 50dBm, 30dBm
P_{B_0}, P_{R_0}	100W, 5W
β_B, β_R	5, 4

be calculated by averaging over the distribution of G_0, $f_{G_0}(\mathrm{g})$, as follows:

$$\begin{aligned}\mathrm{P_C} &= \int_0^\infty \mathrm{P_C}(g) f_{G_0}(\mathrm{g}) d\mathrm{g} \\ &= (F_{|\epsilon|}(\theta/2))^2 \mathrm{P_C}(MM) + 2(F_{|\epsilon|}(\theta/2))\bar{F}_{|\epsilon|}(\theta/2)\mathrm{P_C}(Mm) \\ &+ \bar{F}_{|\epsilon|}(\theta/2)^2 \mathrm{P_C}(mm), \end{aligned} \tag{3.21}$$

where we define $\bar{F}_{|\epsilon|}(\theta/2) = 1 - F_{|\epsilon|}(\theta/2)$.

Applying this averaging to coverage probability expressions in all links, and inserting them to the area spectral efficiency and the average network power consumption formulas, we can obtain the modified energy efficiency expressions in the presence of beamsteering errors.

3.5 Numerical Results

In this section, numerical results are provided to analyze the impact of key system parameters on the energy efficiency of a downlink mmWave cellular network. We employ the parameter values listed in Table 3.1 unless stated otherwise.

First, we display the energy efficiency for different antenna patterns. We investigate the effect of the main lobe gain and the main lobe beam width in Fig. 3.2. It

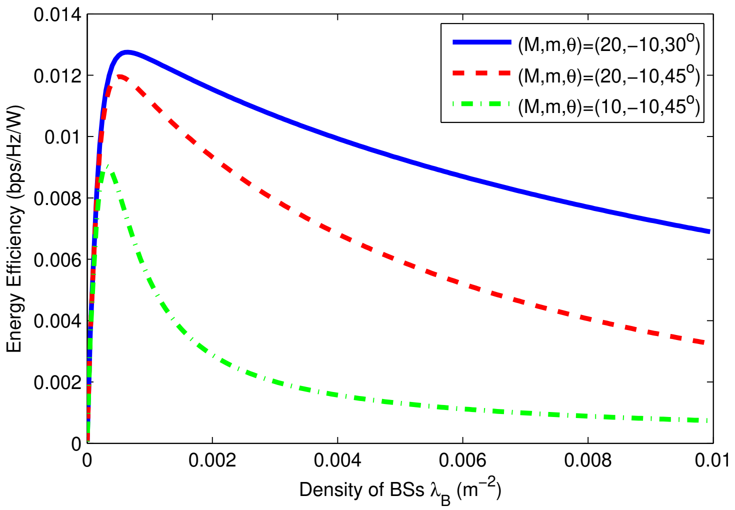

Figure 3.2: EE as a function of the BS density λ_B for different antenna patterns (M,m,θ).

can be seen that for fixed θ, energy efficiency improves with increasing main lobe gain M. Similarly, for fixed M decreasing θ improves energy efficiency because narrower main lobe beam width means that receiving nodes (RS or MU) are less likely to be interfered by the main lobe of other transmitting nodes (BS or RS). Also note that optimal BS density, denoted by λ_B^*, with which the energy efficiency is maximized, decreases slightly with increasing beam width and decreasing gain due to growing impact of interference.

Next, we plot the energy efficiency for different values of the LOS ball radius R_B and LOS path loss exponent α_L in Fig. 3.3 in order to investigate the effect of LOS interference range. We notice that optimal BS density λ_B^* decreases with increasing ball radius, because the number of interfering LOS BSs increases with increasing ball radius, and we have assumed that serving nodes are always LOS to the receiving nodes. As a result, the maximum energy efficiency is achieved with smaller BS density for higher ball radiuses. Also, energy efficiency improves with increasing LOS path loss exponent for fixed R_B, while λ_B^* remains almost same for the same R_B. Therefore, optimal BS density is generally insensitive to the path loss exponent.

In Fig. 3.4, we plot the energy efficiency (EE), area spectral efficiency (ASE)

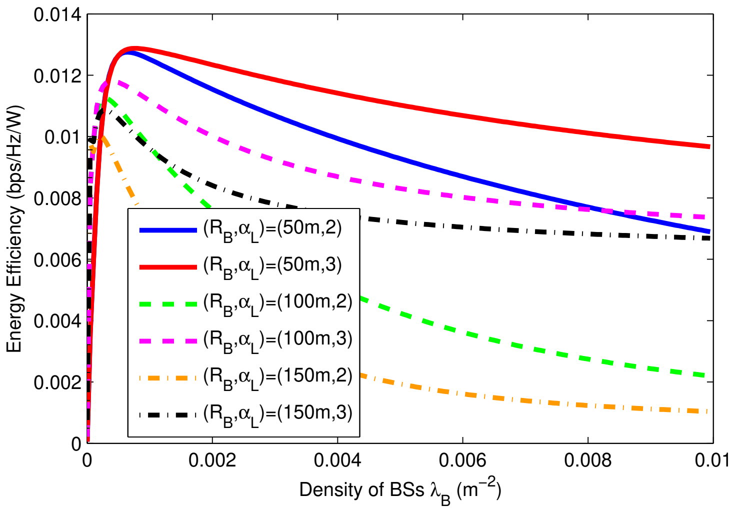

Figure 3.3: EE as a function of the BS density λ_B for different LOS ball radiuses R_B and LOS path-loss exponents α_L.

and average network power consumption (ANPC) as a function of the BS density λ_B for different values of RS density λ_R, and investigate the effect of RS density on energy efficiency. As shown in the middle sub-figure, area spectral efficiency of the network increases only very slightly (which is difficult to notice in the figure but can be seen with higher resolution) with the increasing RS density because of the increase in SINR coverage probabilities. At the same time, however, having higher number of RSs means more power consumption. Consequently, average power consumption of the network also increases as shown in the bottom sub-figure. Since increase in area spectral efficiency cannot compensate for the increase in average network power consumption, energy efficiency degrades with increasing RS density as shown in the top sub-figure. This behavior indicates a tradeoff between area spectral efficiency and energy efficiency depending on the RS density.

Finally, we investigate the effect of beam steering errors between the serving and receiving nodes on the energy efficiency in Fig. 3.5. As shown in the figure, energy efficiency diminishes with increasing alignment error. Although the interference from interfering nodes remains unchanged, its effect grows with the increase in alignment

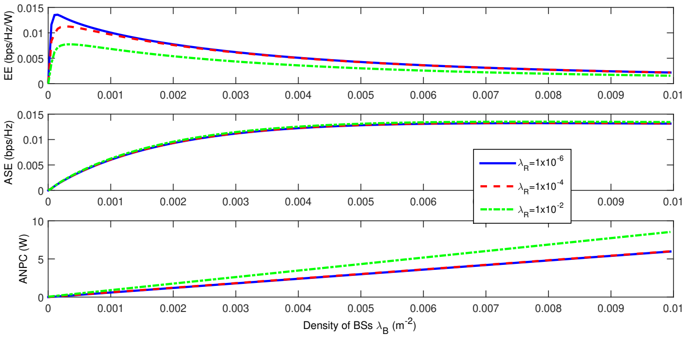

Figure 3.4: EE, ASE and ANPC as a function of the BS density λ_B for different RS densities λ_R.

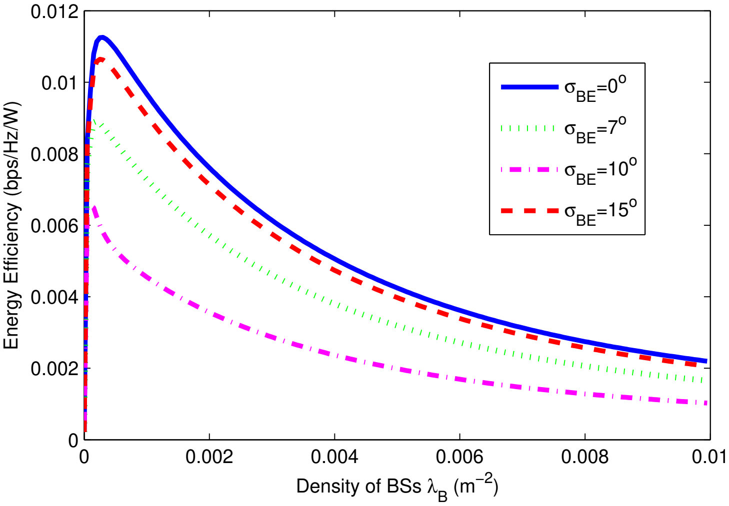

Figure 3.5: EE as a function of the BS density λ_B for different alignment errors σ_{BE}.

error on the main link. Also, due to this increase in the relative impact of interference, less number of BSs is preferred with increasing alignment error to achieve the maximum energy efficiency.

3.6 Conclusion

In this chapter, we have analyzed the energy efficiency of relay-assisted downlink mmWave cellular networks by incorporating the distinguishing features of mmWave communication into the energy efficiency analysis. Directional beamforming with sectored antenna model and simplified ball-LOS models have been considered in the analysis. BSs and RSs are assumed to be distributed according to independent PPPs, and SINR coverage probabilities are derived using tools from stochastic geometry to characterize the energy efficiency. Numerical results demonstrate that employing directional antennas makes the mmWave cellular networks more energy efficient. In other words, increasing the main lobe gain and decreasing the main lobe beam width results in improved energy efficiency. We have also shown that BS density should be lowered to achieve the maximum energy efficiency when the LOS ball radius is larger. Moreover, we have observed that there is a tradeoff between the area spectral efficiency and energy efficiency depending on the RS density. Finally, the effect of alignment error on energy efficiency is quantified.

Chapter 4

Coverage in Heterogeneous Downlink Millimeter Wave Cellular Networks

In this chapter, we provide an analytical framework to analyze heterogeneous downlink mmWave cellular networks consisting of K tiers of randomly located BSs where each tier operates in a mmWave frequency band. Signal-to-interference-plus-noise ratio (SINR) coverage probability is derived for the entire network using tools from stochastic geometry. The distinguishing features of mmWave communications such as directional beamforming and having different path loss laws for LOS and NLOS links are incorporated into the coverage analysis by assuming averaged biased-received power association and Nakagami fading. By using the noise-limited assumption for mmWave networks, a simpler expression requiring the computation of only one numerical integral for coverage probability is obtained. Also, effect of beamforming alignment errors on the coverage probability analysis is investigated to get insight on the performance in practical scenarios. Downlink rate coverage probability is derived as well to get more insights on the performance of the network. Moreover, effect of deploying low-power smaller cells and the impact of biasing factor on energy efficiency is analyzed. Finally, a hybrid cellular network operating in both mmWave and μWave frequency bands is addressed.

4.1 Introduction

A key feature of mmWave cellular networks is expected to be heterogeneity to have higher data rates and expanded coverage [6]. A general model for heterogeneous cellular networks is described as a combination of K spatially and spectrally coexisting tiers which are distinguished by their transmit powers, spatial densities, blockage models [49], [50]. For example, high-power and low-density large-cell BSs may coexist with denser but lower power small-cell BSs. Small cell BSs can help the congested large-cell BSs by offloading some percentage of their user equipments (UEs), which results in a better quality of service per UE [14]. Moreover, to provide more relief to the large-cell network, cell range expansion technique which is enabled through cell biasing for load balancing was considered e.g., in [50], [51], [52].

Several recent studies have also addressed heterogeneous mmWave cellular networks. In [53], authors consider two different types of heterogeneity in mmWave cellular networks: spectrum heterogeneity and deployment heterogeneity. In spectrum heterogeneity, mmWave UEs may use higher frequencies for data communication while the lower frequencies are exploited for control message exchange. Regarding deployment heterogeneity, two deployment scenarios are introduced. In the standalone scenario, all tiers will be operating in mmWave frequency bands, while in the integrated scenario, μWave network coexists with mmWave networks. A similar hybrid cellular network scenario is considered in [10] for characterizing uplink-downlink coverage and rate distribution of self-backhauled mmWave cellular networks, and in [54] for the analysis of downlink-uplink decoupling. In both papers, mmWave small cells are opportunistically used and UEs are offloaded to the μWave network when it is not possible to establish a mmWave connection. In [55], a hybrid spectrum access scheme (where exclusive access is used at frequencies in the 20/30 GHz range while spectrum sharing is used at frequencies around 70 GHz) is considered to harvest the maximum benefit from emerging mmWave technologies. A more general mathematical framework to analyze the multi-tier mmWave cellular networks is provided in [13]. In [56], benefits of BS cooperation in the downlink of a heterogeneous mmWave cellular system are analyzed. Contrary to the hybrid scenario, each tier is assumed to operate in a mmWave frequency band in both [13] and [56]. Similarly, in this chapter we consider a cellular network operating exclusively with mmWave cells, while, as we demonstrate in Section 4.4.3, an extension to a hybrid scenario can be addressed and a similar analytical framework can be employed by eliminating the unique properties of mmWave transmissions in the analysis of the μWave tier.

Stochastic geometry has been identified as a powerful mathematical tool to analyze the system performance of mmWave cellular networks due to its tractability and accuracy. Therefore, in most of the recent studies on heterogeneous and/or mmWave cellular networks, spatial distribution of the BSs is assumed to follow a point process and the most commonly used distribution is the PPP due to its tractability and accuracy in approximating the actual cellular network topology [14], [15]. In [15], authors provide a comprehensive tutorial on stochastic geometry based analysis for cellular networks. Additionally, a detailed overview of mathematical models and analytical techniques for mmWave cellular systems are provided in [16]. Since the path loss and blockage models for mmWave communications are significantly different from μWave communications, three different states, namely LOS, NLOS and outage states, are considered for mmWave frequencies [12], [13]. For analytical tractability, equivalent LOS ball model was proposed in [9]. In [10], authors considered probabilistic LOS ball model, which is more flexible than the LOS ball model to capture the effect of different realistic settings. In [13], probabilistic LOS ball model is generalized to a two-ball model, which is based on path loss intensity matching algorithm. Path loss intensity matching approach to estimate the parameters of the path loss distribution is also employed in [13], [57], [58].

4.1.1 Main Contributions

Employing the tools from stochastic geometry and incorporating the distinguishing features of mmWave communications, we study heterogeneous donwlink mmWave cellular networks. Our main contributions can be summarized as follows:

- A general expression of SINR coverage probability is derived for K-tier heterogeneous mmWave cellular networks by considering different Nakagami fading parameters for LOS and NLOS components, and employing the D-ball approximation for blockage modeling. Key differences from the previous work on mmWave heterogeneous cellular networks (e.g., [13]) are the following: We incorporate small-scale fading in the analysis and also use the more general D-ball model (rather than the two-ball model) for blockage modeling. Also, different from [13] which considers the noise-limited approximation at the beginning of the analysis, we first provide a detailed and general analysis including interference calculation for both LOS and NLOS components, characterize the SINR coverage probability, and then identify under which conditions the noise-limited approximation is valid/accurate via numerical results. Moreover, we investigate the effect of biasing on mmWave heterogeneous cellular networks.

- A simple expression for coverage probability for noise-limited case is obtained, and also a closed-form expression for some special values of LOS and NLOS path loss exponents is provided.

- Energy efficiency analysis is conducted for K-tier heterogeneous mmWave cellular networks. Different from previous works, effect of biasing factor on energy efficiency is investigated for the first time in the literature.

- Moreover, we describe how the analysis can be adapted to determine the coverage in hybrid cellular network scenarios, involving a μWave large cell and mmWave smaller cells. We provide interesting observations and comparisons between the performances in the all-mmWave and hybrid scenarios. In particular, we highlight the impact of increased interference in the hybrid cellular network.

4.2 System Model

A K-tier heterogeneous downlink mmWave cellular network is modeled where the BSs in the k^{th} tier are distributed according to a homogeneous PPP Φ_k of density λ_k on the Euclidean plane for $k = 1, 2, \ldots, K$. BSs in all tiers are assumed to be transmitting in a mmWave frequency band, and the BSs in the k^{th} tier are distinguished by their transmit power P_k, biasing factor B_k, and blockage model parameters. The UEs are also spatially distributed according to an independent homogeneous PPP Φ_u of density λ_u. Without loss of generality, a typical UE is assumed to be located at the origin according to Slivnyak's theorem [29], and it is associated with the tier providing the maximum average biased-received power.

In this setting, we have the following assumptions regarding the system model of the K-tier heterogeneous downlink mmWave cellular network:

Assumption 4.1 *(Directional beamforming) Antenna arrays at the BSs of all tiers and UEs are assumed to perform directional beamforming where the main lobe is directed towards the dominant propagation path while smaller sidelobes direct energy in other directions. For tractability in the analysis and similar to [9], [10], [13], [32], [43], [59] antenna arrays are approximated by a sectored antenna model, in which* *the array gains are assumed to be constant M for all angles in the main lobe and another smaller constant m in the side lobes [34]. Initially, perfect beam alignment is assumed in between UE and its serving BS*[1]*, leading to an overall antenna gain of MM. In other words, maximum directivity gain can be achieved for the intended link by assuming that the serving BS and UE can adjust their antenna steering orientation using the estimated angles of arrivals. Also, beam direction of the interfering links is modeled as a uniform random variable on $[0, 2\pi]$. Therefore, the effective antenna gain between an interfering BS and UE is a discrete random variable (RV) described by*

$$G = \begin{cases} MM & \text{with prob. } p_{MM} = \left(\frac{\theta}{2\pi}\right)^2 \\ Mm & \text{with prob. } p_{Mm} = 2\frac{\theta}{2\pi}\frac{2\pi-\theta}{2\pi} \\ mm & \text{with prob. } p_{mm} = \left(\frac{2\pi-\theta}{2\pi}\right)^2, \end{cases} \tag{4.1}$$

where θ is the beam width of the main lobe, and p_G is the probability of having an antenna gain of $G \in \{MM, Mm, mm\}$.

Assumption 4.2 *(Path loss model and blockage modeling) Link between a BS and a typical UE can be either a LOS or NLOS link. However, according to recent results on mmWave channel modeling, an additional outage state can also be included to represent link conditions. Therefore, a link can be in a LOS, NLOS or in an outage state [12]. In a LOS state, BS should be visible to UE, i.e., there is no blockage in the link. On the other hand, in a NLOS state, blockage occurs in the link, and if this blockage causes a very high path loss, an outage state occurs, i.e, no link is established between the BS and the UE.*

Consider an arbitrary link of length r, and define the LOS probability function $p(r)$ as the probability that the link is LOS. Using field measurements and stochastic blockage models, $p(r)$ can be modeled as $e^{-\gamma r}$ where decay rate γ depends on the building parameter and density [35]. For analytical tractability, LOS probability function

---

[1] Subsequently, beamsteering errors are also addressed.

$p(r)$ can be approximated by step functions. In this approach, the irregular geometry of the LOS region is replaced with its equivalent LOS ball model. Approximation by step functions provides tractable but also accurate results [58], [60]. Authors in both [58] and [60] employ piece-wise LOS probability functions and multi-ball ball models. Furthermore, in [58], comparisons of the intensity measures of empirical models (in London and Manchester) and 3GPP-based models with their 3-ball counterpart approximation models have been provided and good matching accuracy has been observed.

In this study, we adopt a D-ball approximation model similar to the piece-wise LOS probability function approach proposed in [58]. As shown in Fig. 4.1, a link is in LOS state with probability $p(r) = \beta_1$ inside the first ball with radius R_1, while NLOS state occurs with probability $1 - \beta_1$. Similarly, LOS probability is equal to $p(r) = \beta_d$ for r between R_{d-1} and R_d for $d = 2, \ldots, D$, and all links with distances greater than R_D are assumed to be in outage state.

Different path loss laws are applied to LOS and NLOS links. Thus, the path loss on each link in the kth tier can be expressed as follows:

$$L_k(r) = \begin{cases} \begin{cases} \kappa_1^L r^{\alpha_1^{k,L}} \textit{ with prob. } \beta_{k1} \\ \kappa_1^N r^{\alpha_1^{k,N}} \textit{ with prob. } (1-\beta_{k1}) \end{cases} & \textit{if } r \in [0, R_{k1}) \\ \begin{cases} \kappa_2^L r^{\alpha_2^{k,L}} \textit{ with prob. } \beta_{k2} \\ \kappa_2^N r^{\alpha_2^{k,N}} \textit{ with prob. } (1-\beta_{k2}) \end{cases} & \textit{if } r \in [R_{k1}, R_{k2}) \\ \vdots & \\ \begin{cases} \kappa_D^L r^{\alpha_D^{k,L}} \textit{ with prob. } \beta_{kD} \\ \kappa_D^N r^{\alpha_D^{k,N}} \textit{ with prob. } (1-\beta_{kD}) \end{cases} & \textit{if } r \in [R_{k(D-1)}, R_{kD}) \\ \textit{outage} & \textit{if } r \geq R_{kD}, \end{cases} \tag{4.2}$$

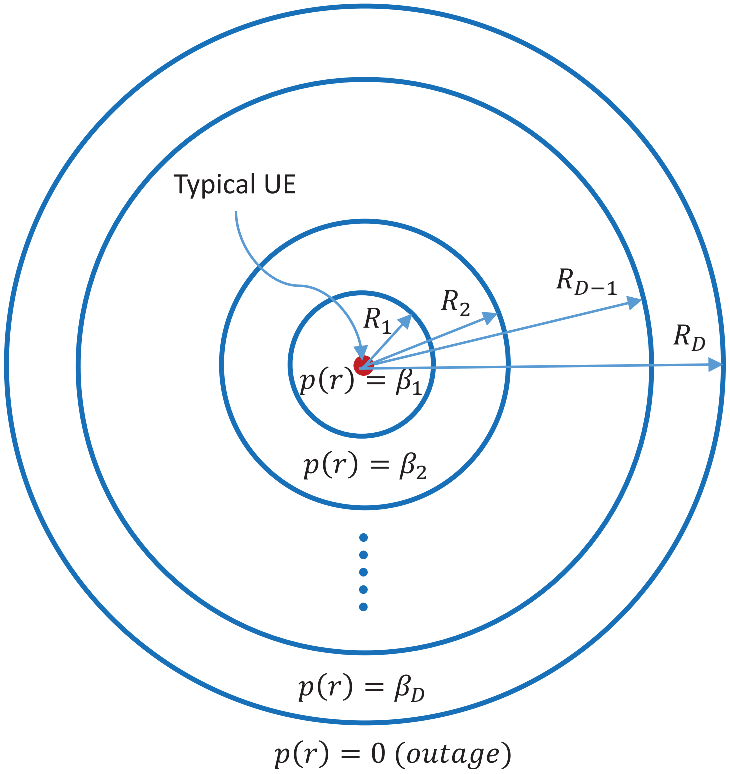

Figure 4.1: LOS ball model

where $\alpha_d^{k,L}$, *and* $\alpha_d^{k,N}$ *are the LOS and NLOS path loss exponents for the dth ball of the kth tier, respectively,* κ_d^L *and* κ_d^N *are the path loss of LOS and NLOS links at a distance of 1 meter for the dth ball, respectively and* R_{kd} *is the radius of the dth ball of the kth tier, for* $d = 1, \ldots, D$.

4.2.1 Statistical Characterization of the Path Loss

Let $\mathcal{N}_k = \{L_k(r)\}_{r \in \phi_k}$ denote the point process of the path loss between the typical UE and BSs in the kth tier. The characteristics of the typical UE which depend on the path loss can be determined by the distribution of $\mathcal{N}_k$ [61]. Therefore, in Lemma 4.1 and Lemma 4.2 below, characterization of the complementary cumulative distribution function (CCDF) and the probability density function (PDF) of the path loss are provided.

Lemma 4.1 *The CCDF of the path loss from a typical UE to the BS in the kth tier can be formulated as*

$$\bar{F}_{L_k}(x) = \mathbb{P}(L_k(r) > x) = \exp(-\Lambda_k([0,x))) \text{ for } k = 1, 2, \ldots, K \tag{4.3}$$

by applying the void probability theorem of PPPs [61] with $\Lambda_k([0,x))$ defined as

$$\begin{aligned}\Lambda_k([0,x)) = \pi\lambda_k \sum_{d=1}^{D} \Bigg(&\beta_{kd}\Bigg(\left(R_{kd}^2 - R_{k(d-1)}^2\right) \mathbb{1}\left(x > \kappa_d^L R_{kd}^{\alpha_d^{k,L}}\right) \\ &+ \left(\left(x/\kappa_d^L\right)^{\frac{2}{\alpha_d^{k,L}}} - R_{k(d-1)}^2\right) \mathbb{1}\left(\kappa_d^L R_{k(d-1)}^{\alpha_d^{k,L}} < x < \kappa_d^L R_{kd}^{\alpha_d^{k,L}}\right)\Bigg) \\ &+ (1-\beta_{kd})\Bigg(\left(R_{kd}^2 - R_{k(d-1)}^2\right) \mathbb{1}\left(x > \kappa_d^N R_{kd}^{\alpha_d^{k,N}}\right) \\ &+ \left(\left(x/\kappa_d^N\right)^{\frac{2}{\alpha_d^{k,N}}} - R_{k(d-1)}^2\right) \mathbb{1}\left(\kappa_d^N R_{k(d-1)}^{\alpha_d^{k,N}} < x < \kappa_d^N R_{kd}^{\alpha_d^{k,N}}\right)\Bigg)\Bigg),\end{aligned} \tag{4.4}$$

where $\mathbb{1}(\cdot)$ is the indicator function and also note that $R_{k0} = 0$.

Proof: See Appendix A.

Lemma 4.2 *The CCDF of the path loss from the typical UE to the LOS/NLOS BS in the kth tier can be formulated as*

$$\bar{F}_{L_{k,s}}(x) = \mathbb{P}(L_{k,s}(r) > x) = \exp(-\Lambda_{k,s}([0,x))), \tag{4.5}$$

for $k = 1, 2, \ldots, K$, where $s \in \{LOS, NLOS\}$ and $\Lambda_{k,s}([0,x))$ is defined for LOS and NLOS, respectively, as follows:

$$\begin{aligned}\Lambda_{k,LOS}([0,x)) = \pi\lambda_k \sum_{d=1}^{D} \Bigg(&\beta_{kd}\Bigg(\left(R_{kd}^2 - R_{k(d-1)}^2\right) \mathbb{1}\left(x > \kappa_d^L R_{kd}^{\alpha_d^{k,L}}\right) \\ &+ \left(\left(x/\kappa_d^L\right)^{\frac{2}{\alpha_d^{k,L}}} - R_{k(d-1)}^2\right) \mathbb{1}\left(\kappa_d^L R_{k(d-1)}^{\alpha_d^{k,L}} < x < \kappa_d^L R_{kd}^{\alpha_d^{k,L}}\right)\Bigg)\Bigg).\end{aligned} \tag{4.6}$$

$$\Lambda_{k,NLOS}([0,x)) = \pi\lambda_k \sum_{d=1}^{D} \Bigg((1-\beta_{kd}) \Bigg(\left(R_{kd}^2 - R_{k(d-1)}^2\right) \mathbb{1}\left(x > \kappa_d^N R_{kd}^{\alpha_d^{k,N}}\right) \\ + \left(\left(x/\kappa_d^N\right)^{\frac{2}{\alpha_d^{k,N}}} - R_{k(d-1)}^2 \right) \mathbb{1}\left(\kappa_d^N R_{k(d-1)}^{\alpha_d^{k,N}} < x < \kappa_d^N R_{kd}^{\alpha_d^{k,N}}\right) \Bigg) \Bigg). \tag{4.7}$$

Proof: We can compute the intensities, $\Lambda_{k,\mathrm{LOS}}(\cdot)$ and $\Lambda_{k,\mathrm{NLOS}}(\cdot)$ of $\Phi_{k,\mathrm{LOS}}$ and $\Phi_{k,\mathrm{NLOS}}$, respectively, by following similar steps as in the proof of Lemma 4.1. $\square$

Also, the PDF of $L_{k,s}(r)$, denoted by $f_{k,s}$, which will be used in the following section is given by

$$f_{L_{k,s}} = -\frac{d\bar{F}_{L_{k,s}}(x)}{dx} = \Lambda'_{k,s}([0,x)) \exp(-\Lambda_{k,s}([0,x))), \tag{4.8}$$

where $\Lambda'_{k,s}([0,x))$ is given as

$$\Lambda'_{k,s}([0,x)) = \\ \begin{cases} 2\pi\lambda_k \sum_{d=1}^{D} \frac{\left(x/\kappa_d^L\right)^{2/\alpha_d^{k,L}-1}}{\alpha_d^{k,L}} \left(\beta_{kd}\mathbb{1}\left(\kappa_d^L R_{k(d-1)}^{\alpha_d^{k,L}} < x < \kappa_d^L R_{kd}^{\alpha_d^{k,L}}\right)\right) & \text{for } s = \text{LOS} \\ 2\pi\lambda_k \sum_{d=1}^{D} \frac{\left(x/\kappa_d^N\right)^{2/\alpha_d^{k,N}-1}}{\alpha_d^{k,N}} \left((1-\beta_{kd})\mathbb{1}\left(\kappa_d^N R_{k(d-1)}^{\alpha_d^{k,N}} < x < \kappa_d^N R_{kd}^{\alpha_d^{k,N}}\right)\right) & \text{for } s = \text{NLOS} \end{cases}. \tag{4.9}$$

The results of Lemma 4.1 and Lemma 4.2 are used in the calculation of association probabilities and SINR coverage probabilities in the following sections.

4.2.2 Cell Association

In this work, a flexible cell association scheme similarly as in [33] is considered. In this scheme, UEs are assumed to be associated with the BS offering the strongest long-term averaged biased-received power. In other words, a typical UE is associated with a BS in tier-k for $k = 1, 2, \ldots, K$ if

$$P_k G_k B_k L_k(r)^{-1} \geq P_j G_j B_j L_{min,j}(r)^{-1} \quad \forall j \neq k, \tag{4.10}$$

where P, G and B denote the transmission power, effective antenna gain of the intended link and biasing factor, respectively, in the corresponding tier (indicated by the index in the subscript), $L_k(r)$ is the path loss in the k^{th} tier as formulated in (4.2), and $L_{min,j}(r)$ is the minimum path loss of the typical UE from a BS in the jth tier. Antenna gain of the intended network G is assumed to equal to MM in all tiers for all-mmWave network, and it is equal to $M_\mu M$ for hybrid network where M_μ is defined as the antenna gain of the tier operating in μWave frequency band. Although the analysis is done according to averaged biased-received power association, other association schemes like smallest path loss and highest average received power can be considered as well because they are special cases of biased association. When $B_k = 1/(P_k G_k)$ for $k = 1, 2, \ldots, K$, biased association becomes the same as the smallest path loss association while $B_k = 1$ for $k = 1, 2, \ldots, K$ corresponds to highest average received power association. In the following lemma, we provide the association probabilities with a BS in the kth tier using the result of Lemma 4.1.

Lemma 4.3 *The probability that a typical UE is associated with a LOS/NLOS BS in tier-k for $k = 1, 2, \ldots, K$ is*

$$\mathcal{A}_{k,s} = \int_0^\infty \Lambda'_{k,s}([0, l_k)) e^{-\sum_{j=1}^{K} \Lambda_j \left([0, \frac{P_j G_j B_j}{P_k G_k B_k} l_k)\right)} dl_k, \tag{4.11}$$

with $s \in \{LOS\ , NLOS\}$, where $\Lambda_j([0, x))$, and $\Lambda'_{k,s}([0, x))$ are given in (4.4) and (4.9), respectively.

Proof: See Appendix B.

In the corollary below, we derive a closed-form expression for the association probability for a special case in order to provide several insights on the effects of different parameters on association probability.

Corollary 4.1 *Consider a* 2*-tier network with* 1*-ball model for which the LOS probability is* $\beta_{k1} = 1$ *and ball radius is* R_{k1} *for tiers* $k = 1, 2$*. Further assume that* $\alpha_1^{k,L} = 2$ *for* $k = 1, 2$*. Following several algebraic operations on (4.11), closed-form expressions for the probability that a typical UE is associated with a LOS BS in tier-*k *for* $k = 1, 2$*, respectively, can be expressed as*

$$\mathcal{A}_{1,L} = \begin{cases} \frac{\lambda_1 P_1 G_1 B_1}{\sum_{j=1}^{2} \lambda_j P_j G_j B_j} \left(1 - e^{-\frac{\pi R_{11}^2}{P_1 G_1 B_1}\left(\sum_{j=1}^{2} \lambda_j P_j G_j B_j\right)}\right), & \text{if } \frac{P_1 G_1 B_1}{P_2 G_2 B_2} R_{21}^2 > R_{11}^2 \\ \frac{\lambda_1 P_1 G_1 B_1}{\sum_{j=1}^{2} \lambda_j P_j G_j B_j} \left(1 - e^{-\frac{\pi R_{21}^2}{P_2 G_2 B_2}\left(\sum_{j=1}^{2} \lambda_j P_j G_j B_j\right)}\right) & \\ + e^{-\frac{\pi R_{21}^2}{P_2 G_2 B_2} \sum_{j=1}^{2} \lambda_j P_j G_j B_j} - e^{-\pi \sum_{j=1}^{2} (\lambda_j R_{j1}^2)}, & \text{otherwise} \end{cases} \tag{4.12}$$

$$\mathcal{A}_{2,L} = \begin{cases} \frac{\lambda_2 P_2 G_2 B_2}{\sum_{j=1}^{2} \lambda_j P_j G_j B_j} \left(1 - e^{-\frac{\pi R_{21}^2}{P_2 G_2 B_2}\left(\sum_{j=1}^{2} \lambda_j P_j G_j B_j\right)}\right), & \text{if } \frac{P_2 G_2 B_2}{P_1 G_1 B_1} R_{11}^2 > R_{21}^2 \\ \frac{\lambda_2 P_2 G_2 B_2}{\sum_{j=1}^{2} \lambda_j P_j G_j B_j} \left(1 - e^{-\frac{\pi R_{11}^2}{P_1 G_1 B_1}\left(\sum_{j=1}^{2} \lambda_j P_j G_j B_j\right)}\right) & \\ + e^{-\frac{\pi R_{11}^2}{P_1 G_1 B_1} \sum_{j=1}^{2} \lambda_j P_j G_j B_j} - e^{-\pi \sum_{j=1}^{2} (\lambda_j R_{j1}^2)}, & \text{otherwise.} \end{cases} \tag{4.13}$$

For sufficiently large values of R_{11} and R_{21}, the terms involving the exponential functions in the above expressions decay to zero. Therefore, we can simplify (4.12) and (4.13) further and association probabilities can be approximated with the following expression (which also confirms the result in [33]):

$$\mathcal{A}_{k,L} \approx \frac{\lambda_k P_k G_k B_k}{\sum_{j=1}^{K} \lambda_j P_j G_j B_j}. \tag{4.14}$$

Above in (4.14), since the term $\sum_{j=1}^{K} \lambda_j P_j G_j B_j$ is a sum over all tiers and does not depend on k, a typical UE obviously prefers to connect to a tier with higher BS density, transmit power, effective antenna gain and biasing factor.

4.3 SINR Coverage Analysis

In this section, we develop a theoretical framework to analyze the downlink SINR coverage probability for a typical UE using stochastic geometry. Although an averaged biased-received power association scheme is considered for tier selection, the developed framework can also be applied to different tier association schemes.

4.3.1 Signal-to-Interference-plus-Noise Ratio (SINR)

The SINR experienced at a typical UE at a random distance r from its associated BS in the kth tier can be written as

$$\mathrm{SINR}_k = \frac{P_k G_0 h_{k,0} L_k^{-1}(r)}{\sigma_k^2 + \sum_{j=1}^{K} \sum_{i \in \Phi_j \setminus B_{k,0}} P_j G_{j,i} h_{j,i} L_{j,i}^{-1}(r)}, \tag{4.15}$$

where G_0 is the effective antenna gain of the link between the serving BS and UE which is assumed to be equal to MM, $h_{k,0}$ is the small-scale fading gain from the serving BS, σ_k^2 is the variance of the additive white Gaussian noise component. Interference has two components: intracell and intercell interference, where the first one is from the active BSs operating in the same cell with the serving BS, and the second one is from the BSs in other cells. A similar notation is used for interfering links, but note that the effective antenna gains $G_{j,i}$ are different for different interfering links as described in (4.1). Since the small-scale fading in mmWave links is less severe than the conventional systems due to deployment of directional antennas, all links are assumed to be subject to independent Nakagami fading (i.e., small-scale fading gains have a gamma distribution). Parameters of Nakagami fading are N_{LOS} and

N_{NLOS} for LOS and NLOS links, respectively, and they are assumed to be positive integers for simplicity. When $N_{\text{LOS}} = N_{\text{NLOS}} = 1$, the Nakagami fading specializes to Rayleigh fading.

4.3.2 SINR Coverage Probability

The SINR coverage probability $\text{P}_{\text{C}}^{k}(\Gamma_k)$ is defined as the probability that the received SINR is larger than a certain threshold $\Gamma_k > 0$ when the typical UE is associated with a BS from the kth tier, i.e., $\text{P}_{\text{C}}^{k}(\Gamma_k) = \mathbb{P}(\text{SINR}_k > \Gamma_k; t = k)$ where t indicates the associated tier. Moreover, homogeneous PPP describing the spatial distribution of the BSs in each tier can be decomposed into two independent non-homogeneous PPPs: the LOS BS process $\Phi_{k,\text{LOS}}$ and NLOS BS process $\Phi_{k,\text{NLOS}}$. Therefore, the total SINR coverage probability P_{C} of the network can be computed using the law of total probability as follows:

$$\text{P}_{\text{C}} = \sum_{k=1}^{K} \left[\text{P}_{\text{C}}^{k,\text{LOS}}(\Gamma_k)\mathcal{A}_{k,\text{LOS}} + \text{P}_{\text{C}}^{k,\text{NLOS}}(\Gamma_k)\mathcal{A}_{k,\text{NLOS}} \right], \tag{4.16}$$

where $s \in \{\text{LOS}, \text{NLOS}\}$, $\text{P}_{\text{C}}^{k,s}$ is the conditional coverage probability given that the UE is associated with a BS in $\Phi_{k,s}$, and $\mathcal{A}_{k,s}$ is the association probability with a BS in $\Phi_{k,s}$, which is given in Lemma 4.3. In the next theorem, we provide the main result for the total network coverage.

Theorem 4.1 *: The total SINR coverage probability of the K-tier heterogeneous mmWave cellular network under Nakagami fading with parameter N_s is*

$$\begin{aligned} P_C \approx & \sum_{k=1}^{K} \sum_{s\in\{LOS,NLOS\}} \int_0^\infty \sum_{n=1}^{N_s} (-1)^{n+1} \binom{N_s}{n} e^{-\frac{n\eta_s\Gamma_k l_{k,s}\sigma_k^2}{P_k G_0}} \\ & e^{-\sum_{j=1}^{K}\left(A+B+\Lambda_j\left(\left[0,\frac{P_jG_jB_j}{P_kG_kB_k}l_{k,s}\right)\right)\right)} \Lambda'_{k,s}([0,l_{k,s}))dl_{k,s}, \end{aligned} \tag{4.17}$$

where

$$A = \sum_{G \in \{MM, Mm, mm\}} p_G \int_{\frac{P_j B_j}{P_k B_k} l_{k,s}}^{\infty} \Psi\left(N_{LOS}, \frac{n \eta_{LOS} \Gamma_k P_j G l_{k,s}}{P_k G_0 t N_L}\right) \Lambda_{j,LOS}(dt) \tag{4.18}$$

and

$$B = \sum_{G \in \{MM, Mm, mm\}} p_G \int_{\frac{P_j B_j}{P_k B_k} l_{k,s}}^{\infty} \Psi\left(N_{NLOS}, \frac{n \eta_{NLOS} \Gamma_k P_j G l_{k,s}}{P_k G_0 t N_N}\right) \Lambda_{j,NLOS}(dt) \tag{4.19}$$

and $\Psi(N, x) = 1 - 1/(1 + x)^N$, $\eta_s = N_s (N_s!)^{-\frac{1}{N_s}}$, p_G *is the probability of having antenna gain* G *and is given in (4.1).*

Proof: See Appendix C.

General sketch of the proof is as follows: First, SINR coverage probability is computed given that a UE is associated with a LOS/NLOS BS in the kth tier. Subsequently, each of the conditional probabilities are summed up to obtain the total coverage probability of the network. In determining the coverage probability given that a UE is associated with a LOS/NLOS BS in the kth tier, Laplace transforms of LOS/NLOS interferences from the kth tier are obtained using the thinning theorem and the moment generating function (MGF) of the gamma variable.

We also note that the result of Theorem 4.1 is an approximation due to the tail probability of a gamma random variable. Although the characterization in Theorem 4.1 involves multiple integrals, computation can be carried out relatively easily by using numerical integration tools. Additionally, we can simplify the result further for the noise-limited case as demonstrated in the following corollaries, where computation of only a single integral is required in Corollary 4.2, and the result of Corollary 4.3 is in closed-form requiring only the computation of the erf function.

4.3.3 Special Case: Noise-limited Network

In the previous section, we analyzed the coverage probability for the general case in which both noise and interference are present. However, recent studies show that mmWave networks tend to be noise-limited rather than being interference-limited [5], [10], [11], [12], [13]. Hence, in the following corollary coverage probability expression is provided assuming a noise-limited cellular network.

Corollary 4.2 *When there is no interference, coverage probability of the network is given by*

$$P_C \approx \sum_{k=1}^{K} \sum_{s\in\{LOS,NLOS\}} \int_0^\infty \sum_{n=1}^{N_s} (-1)^{n+1} \binom{N_s}{n} e^{-\frac{n\eta_s \Gamma_k l_{k,s} \sigma_k^2}{P_k G_0}} e^{-\sum_{j=1}^{K}\left(\Lambda_j\left(\left[0,\frac{P_j G_j B_j}{P_k G_k B_k} l_{k,s}\right)\right)\right)} \\ \times \Lambda'_{k,s}([0, l_{k,s}))dl_{k,s}. \tag{4.20}$$

We obtain (4.20) directly from (4.17) by making the terms A and B, which arise from interference, equal to zero. Note that computation of (4.20) requires only a single integral.

Corollary 4.3 *When* $\alpha_d^{k,L} = 2, \alpha_d^{k,N} = 4\ \forall k$ *and* $\forall d$*, the SNR coverage probability of the network reduces to*

$$\begin{aligned} P_C &\approx \sum_{k=1}^{K} \left[P_C^{k,LOS}(\Gamma_k)\mathcal{A}_{k,LOS} + P_C^{k,NLOS}(\Gamma_k)\mathcal{A}_{k,NLOS}\right] \\ &= \sum_{k=1}^{K} \sum_{n=1}^{N_{LOS}} (-1)^{n+1} \binom{N_{LOS}}{n} 2\pi\lambda_k \left[\sum_{n=1}^{N} \beta_{kn} \int_{\sqrt{\kappa_n^L} R_{k(n-1)}}^{\sqrt{\kappa_n^L} R_{kn}} x e^{-(a_L x^2 + b_L x^2 + c_L x + d_L)} dx\right] \\ &+ \sum_{k=1}^{K} \sum_{n=1}^{N_{NLOS}} (-1)^{n+1} \binom{N_{NLOS}}{n} \pi\lambda_k \left[\sum_{n=1}^{N} (1-\beta_{kn}) \int_{\sqrt{\kappa_n^N} R_{k(n-1)}^2}^{\sqrt{\kappa_n^N} R_{kn}^2} e^{-(a_N x^2 + b_N x^2 + c_N x + d_N)} dx\right], \end{aligned} \tag{4.21}$$

where we define

$$
\begin{aligned}
a_L &= \frac{n\eta_{LOS}\Gamma_k\sigma_k^2}{P_kG_0}, \quad a_N = \frac{n\eta_{NLOS}\Gamma_k\sigma_k^2}{P_kG_0} \\
b_L = b_N &= \sum_{j=1}^{K}\pi\lambda_j\sum_{d=1}^{D}\beta_{jd}\mathbb{1}\left(\zeta_d^L R_{j(d-1)} < x < \zeta_d^L R_{jd}\right) \\
c_L = c_N &= \sum_{j=1}^{K}\pi\lambda_j\sum_{d=1}^{D}\left(1-\beta_{jd}\right)\mathbb{1}\left(\zeta_d^N R_{j(d-1)}^2 < x < \zeta_d^N R_{jd}^2\right) \\
d_L = d_N &= \sum_{j=1}^{K}\pi\lambda_j\sum_{d=1}^{D}\left(R_{jd}^2 - R_{j(d-1)}^2\right)\left(\beta_{jd}\mathbb{1}\left(x > \zeta_d^L R_{jd}\right)\right. \\
&\left. + \left(1-\beta_{jd}\right)\mathbb{1}\left(x > \zeta_d^N R_{jd}^2\right)\right) - R_{j(d-1)}^2\Bigg(\beta_{jd}\mathbb{1}\left(\zeta_d^L R_{j(d-1)} < x < \zeta_d^L R_{jd}\right) \\
&+ \left(1-\beta_{jd}\right)\mathbb{1}\left(\zeta_d^N R_{j(d-1)}^2 < x < \zeta_d^N R_{jd}^2\right)\Bigg),
\end{aligned}
\tag{4.22}
$$

where $\zeta_d^L = \sqrt{\kappa_d^L\frac{P_kG_kB_k}{P_jG_jB_j}}$ *and* $\zeta_d^N = \sqrt{\kappa_d^N\frac{P_kB_k}{P_jB_j}}$*, and the indefinite integrals can computed as follows:*

$$
\int xe^{-(ax^2+bx^2+cx+d)}dx = -\frac{e^{-x((a+b)x+c)-d}}{4(a+b)^{3/2}}\sqrt{\pi}ce^{\frac{(2(a+b)x+c)^2}{4(a+b)}}\,erf\left(\frac{2x(a+b)+c}{2\sqrt{a+b}} + 2\sqrt{a+b}\right)
\tag{4.23}
$$

$$
\int e^{-(ax^2+bx^2+cx+d)}dx = -\frac{\sqrt{\pi}e^{\frac{c^2}{4(a+b)}-d}}{2\sqrt{a+b}}\,erf\left(\frac{2x(a+b)+c}{2\sqrt{a+b}}\right).
\tag{4.24}
$$

We obtain the coverage probability expression in (4.21) by inserting $\alpha_d^{k,L} = 2, \alpha_d^{k,N} = 4\ \forall k$ and $\forall d$ into (4.20) and applying a change of variables with $l_{k,\text{LOS}} = l_{k,\text{NLOS}} = x^2$. Above, erf denotes the error function. Depending on the values of $\sqrt{\kappa_d^L}R_{k(d-1)}$, $\sqrt{\kappa_d^L}R_{kd}$, $\sqrt{\kappa_d^N}R_{k(d-1)}^2$ and $\sqrt{\kappa_d^N}R_{kd}^2$ for $k = 1, \ldots, K$ and $d = 1, \ldots, D$, values of b_L, c_L, d_L, b_N, c_N, and d_N become either zero or some constant in the intervals of each integral. Hence, the given expression is practically in closed-form which requires only the computation of the error function $\text{erf}(\cdot)$.

4.3.4 SINR Coverage Probability Analysis In the Presence of Beamsteering Errors

In Section 4.3.2 and the preceding analysis, antenna arrays at the serving BS and the typical UE are assumed to be aligned perfectly and downlink SINR coverage probability is calculated in the absence of beamsteering errors. However, in practice, it may not be easy to have perfect alignment. Therefore, in this section, we investigate the effect of beamforming alignment errors on the coverage probability analysis. We employ an error model similar to that in [43]. Let $|\epsilon|$ be the random absolute beamsteering error of the transmitting node toward the receiving node with zero-mean and bounded absolute error $|\epsilon|_{\max} \leq \pi$. Due to symmetry in the gain G_0, it is appropriate to consider the absolute beamsteering error. The PDF of the effective antenna gain G_0 with alignment error can be explicitly written as [13]

$$\begin{aligned} f_{G_0}(\mathrm{g}) = F_{|\epsilon|}\left(\frac{\theta}{2}\right)^2 \delta(\mathrm{g} - MM) + 2F_{|\epsilon|}\left(\frac{\theta}{2}\right)\left(1 - F_{|\epsilon|}\left(\frac{\theta}{2}\right)\right) \delta(\mathrm{g} - Mm) \\ + \left(1 - F_{|\epsilon|}\left(\frac{\theta}{2}\right)\right)^2 \delta(\mathrm{g} - mm), \end{aligned} \tag{4.25}$$

where $\delta(\cdot)$ is the Kronecker's delta function, $F_{|\epsilon|}(x)$ is the CDF of the misalignment error and (4.25) follows from the definition of CDF, i.e., $F_{|\epsilon|}(x) = \mathbb{P}\{|\epsilon| \leq x\}$. Assume that the error ϵ is Gaussian distributed, and therefore the absolute error $|\epsilon|$ follows a half normal distribution with $F_{|\epsilon|}(x) = \mathrm{erf}(x/(\sqrt{2}\sigma_{\mathrm{BE}}))$, where $\mathrm{erf}(\cdot)$ again denotes the error function and σ_{BE} is the standard deviation of the Gaussian error ϵ.

It is clear that total SINR coverage probability expression in (4.17) depends on the effective antenna gain G_0 between the typical UE and the serving BS in each tier. Thus, total SINR coverage probability $\mathrm{P_C}$ can be calculated by averaging over the distribution of G_0, $f_{G_0}(\mathrm{g})$, as follows:

$$\begin{aligned}\mathrm{P_C} &= \int_0^\infty \mathrm{P_C}(g) f_{G_0}(\mathrm{g}) d\mathrm{g} \\ &= F_{|\epsilon|}(\theta/2)^2 \mathrm{P_C}(MM) + 2F_{|\epsilon|}(\theta/2)\bar{F}_{|\epsilon|}(\theta/2)\mathrm{P_C}(Mm) + \bar{F}_{|\epsilon|}(\theta/2)^2 \mathrm{P_C}(mm),\end{aligned} \tag{4.26}$$

where we define $\bar{F}_{|\epsilon|}(\theta/2) = 1 - F_{|\epsilon|}(\theta/2)$.

4.4 Extensions to Other Performance Metrics and Hybrid Scenario

In this section, we provide extensions of our main analysis, and formulate other performance metrics using the SINR coverage probability expression obtained in the previous section to get more insights on the performance of the network. First, downlink rate coverage probability expression for a typical UE is obtained. Then, we formulate the energy efficiency metric. Finally, we address the hybrid scenario involving both μWave and mmWave frequency bands.

4.4.1 Rate Coverage Probability

In this subsection, we derive the downlink rate coverage probability for a typical UE. Since rate characterizes the data bits received per second per UE, it is also an important performance metric like SINR as an indicator of the serving link quality, and it is one of the main reasons motivating the move to mmWave frequency bands [62]. Similar to SINR coverage probability, the rate coverage probability $\mathrm{R}_\mathrm{C}^k(\rho_k)$ is defined as the probability that the rate is larger than a certain threshold $\rho_k > 0$ when the typical UE is associated with a BS from the kth tier. Therefore, the total rate coverage $\mathrm{R_C}$ of the network can be computed as follows:

$$\mathrm{R_C} = \sum_{k=1}^{K} \mathrm{R}_{\mathrm{C}}^{k}(\rho_k)\mathcal{A}_k, \tag{4.27}$$

where $\mathcal{A}_k = \mathcal{A}_{k,L} + \mathcal{A}_{k,N}$ is the association probability with a BS in Φ_k. Conditional rate coverage probability can be calculated in terms of SINR coverage probability as follows:

$$\begin{aligned} \mathrm{R}_{\mathrm{C}}^{k}(\rho_k) = \mathbb{P}(\mathrm{Rate}_k > \rho_k) &= \mathbb{P}\left(\frac{W}{N_k}\log(1+\mathrm{SINR}_k) > \rho_k\right) \\ &= \mathbb{P}\left(\mathrm{SINR}_k > 2^{\frac{\rho_k N_k}{W}} - 1\right) \\ &= \mathrm{P}_{\mathrm{C}}^{k}(2^{\frac{\rho_k N_k}{W}} - 1), \end{aligned} \tag{4.28}$$

where $\mathrm{P}_{\mathrm{C}}^{k}(\cdot)$ is the SINR coverage probability of the kth tier (analyzed in Section 4.3.2), the instantaneous rate of the typical UE is defined as $\mathrm{Rate}_k = \frac{W}{N_k}\log(1 + \mathrm{SINR}_k)$, and N_k, also referred to as load, denotes the total number of UEs served by the serving BS. Note that the total available resource W at the BS is assumed to be shared equally among all UEs connected to that BS. Round-robin scheduling is the well known example of the schedulers resulting in such a fair partition of resources to each UE. The load N_k can be found using the mean load approximation as follows [63]

$$N_k = 1 + \frac{1.28\lambda_u \mathcal{A}_k}{\lambda_k}. \tag{4.29}$$

4.4.2 Energy Efficiency Analysis

The deployment of heterogeneous mmWave cellular networks consisting of multiple tiers with different sizes will provide an opportunity to avoid coverage holes and improve the throughput. Additionally, dense deployment of low-power small cells can also improve the energy efficiency of the network by providing higher throughput and consuming less power. Moreover, load biasing can increase the energy efficiency further by providing more relief to the large-cell BSs. With these motivations, we investigate the energy efficiency of the proposed heterogeneous network with K tiers. First, we describe the power consumption model and area spectral efficiency for each tier, and then formulate the energy efficiency metric, using the SINR coverage probability expression derived in the previous section.

Power Consumption Model

Largest portion of the energy in cellular networks are consumed by BSs [64]. In practice, total BS power consumption has two components: the transmit power and static power consumption. Therefore, we can model the total power consumption per BS using linear approximation model as $P_{tot} = P_0 + \Delta P$, where $1/\Delta$ is the efficiency of the power amplifier, and P_0 is the static power consumption due to signal processing, battery backup, site cooling etc., and P corresponds to the transmit power [48]. Using this model, average power consumption (per unit area) of BSs in the kth tier can be expressed as

$$P_{avg,k} = \lambda_k (P_{0,k} + \Delta_k P_k). \tag{4.30}$$

Area Spectral Efficiency

The area spectral efficiency (i.e., network throughput) can be defined as the product of the throughput at a given link and density of BSs, and for the kth tier it can be formulated as follows:

$$\tau_k = \lambda_k \mathrm{P}_{\mathrm{C}}^{k}(\Gamma_k) \log_2(1 + \Gamma_k), \tag{4.31}$$

where $\mathrm{P}_{\mathrm{C}}^{k}(\Gamma_k)$ is the SINR coverage probability when the typical UE is associated with a BS from the kth tier. Also, note that we assume universal frequency reuse among all BSs from the each tier, meaning that BSs share the same bandwidth.

Energy Efficiency Metric

We can formulate the energy efficiency metric as the ratio of the total area spectral efficiency to the average network power consumption as follows:

$$\mathrm{EE} = \frac{\sum_{k=1}^{K} \tau_k}{\sum_{k=1}^{K} P_{avg,k}} = \frac{\sum_{k=1}^{K} \lambda_k \mathrm{P}_{\mathrm{C}}^{k}(\Gamma_k) \log_2(1+\Gamma_k)}{\sum_{k=1}^{K} \lambda_k (P_{0,k} + \Delta_k P_k)} \quad \text{bps/Hz/W} \tag{4.32}$$

where $P_{avg,k}$ and τ_k are given in (4.30) and (4.31), respectively. Given the characterizations of the coverage probabilities in Section 4.3.2, energy efficiency can be computed easily as demonstrated with the numerical results in Section 4.5.

4.4.3 Analysis of Hybrid Cellular Network Scenario

Although in the preceding analysis we consider a cellular network operating exclusively with mmWave cells, proposed analytical framework can also be employed in the analysis of a hybrid cellular network in which the large cell is operating in the lower μWave frequency band, and smaller cells are operating in the mmWave frequency band. The reason for considering a hybrid scenario is that coexistence of mmWave cells with a traditional μWave cellular network is a likely deployment scenario in the transition process to the cellular network operating exclusively with mmWave cells. This is especially so in the case of sparse deployment of cellular networks [10]. Considering this hybrid scenario, we have different antenna and path loss models in the large μWave cell. Particulary, large-cell BSs employ also directional antennas also but with a smaller main lobe gain and larger beam width of the main lobe, i.e., we set $M_\mu = 3$dB and $\theta = 120°$. Regarding the path loss model, all the links from the large-cell BSs to the UEs are assumed to be LOS links, i.e., there are no blockages between BSs and UEs. With these assumptions, the SINR coverage probability of the hybrid network is now given by

$$\begin{aligned}
\mathrm{P_C} \approx & \sum_{s\in\{\mathrm{LOS}\}} \int_0^\infty \sum_{n=1}^{N_s} (-1)^{n+1} \binom{N_s}{n} e^{-\frac{n\eta_s \Gamma_1 l_{1,s}\sigma_1^2}{P_1 G_0}} e^{-(A(j=1)+B(j=1))} \\
& \times e^{-\sum_{j=1}^{K}\left(\Lambda_j\left(\left[0,\frac{P_j G_j B_j}{P_1 G_1 B_1} l_{1,s}\right)\right)\right)} \Lambda'_{1,s}([0,l_{1,s}))dl_{1,s} \\
+ & \sum_{k=2}^{K} \sum_{s\in\{\mathrm{LOS,NLOS}\}} \int_0^\infty \sum_{n=1}^{N_s} (-1)^{n+1} \binom{N_s}{n} e^{-\frac{n\eta_s \Gamma_k l_{k,s}\sigma_k^2}{P_k G_0}} e^{-\sum_{j=2}^{K}(A+B)} \\
& \times e^{-\sum_{j=1}^{K}\left(\Lambda_j\left(\left[0,\frac{P_j G_j B_j}{P_k G_k B_k} l_{k,s}\right)\right)\right)} \Lambda'_{k,s}([0,l_{k,s}))dl_{k,s}, \qquad (4.33)
\end{aligned}$$

where the first term is the coverage probability of the large cell operating in μWave frequency bands, the second term is the total coverage probability of smaller cells operating in mmWave frequency bands, and A and B are given in (4.18) and (4.19), respectively. Note that since large cell and smaller cells are operating in different frequency bands, interference experienced in the large cell is only from other large-cell BSs in the same tier, and similarly interference in smaller cells is from only the BSs in the smaller cells.

4.5 Simulation and Numerical Results

In this section, we evaluate the theoretical expressions numerically. Simulation results are also provided to validate the the accuracy of the proposed model for the heterogeneous downlink mmWave cellular network as well as the accuracy of the analytical characterizations. In the numerical evaluations and simulations, unless otherwise stated, a 3-tier heterogeneous network is considered and the parameter values are listed in Table 4.1. For this 3-tier scenario, $k = 1$, $k = 2$ and $k = 3$ correspond to the microcell, picocell, and femtocell, respectively. In other words, a relatively high-power microcell network coexists with denser but lower-power picocells and femtocells. For the microcell network, D-ball approximation is used with $D = 2$ and the ball param-

Table 4.1: System Parameters

Parameters	**Values**
$\alpha_d^{k,L}$, $\alpha_d^{k,N}$ $\forall k$, $\forall d$	2, 4
N_{LOS}, N_{NLOS}	3, 2
M, m, θ	10dB, -10dB, 30°
λ_1, λ_2, λ_3, λ_u	10^{-5}, 10^{-4}, 5×10^{-4}, 10^{-3} $(1/m^2)$
P_1, P_2, P_3	53dBm, 33dBm, 23dBm
$P_{0,1}$, $P_{0,2}$, $P_{0,3}$	130W, 10W, 5W
Δ_1, Δ_2, Δ_3	4, 6, 8
B_1, B_2, B_3	1, 1, 1
$[R_{11}R_{12}]$, $[\beta_{11}\beta_{12}]$	[50 200], [0.8 0.2]
$[R_{21}R_{22}]$, $[\beta_{21}\beta_{22}]$	[40 60], [1 0]
$[R_{31}R_{32}]$, $[\beta_{31}\beta_{32}]$	[20 40], [1 0]
Γ_k $\forall k$	0dB
Carrier frequency(F_c)	28 GHz
Bandwidth(W)	1GHz
$\kappa_d^L = \kappa_d^N$ $\forall d$	$(F_c/4\pi)^2$
σ_k^2 $\forall k$	-174 dBm/Hz +10log10(W) + 10 dB

eters are rounded from the values presented in [13] for 28 GHz. For smaller cells, we also employ the two-ball approximation in which the inner ball only consists of LOS BSs, and in the outer ball, only NLOS BSs are present.

First, we investigate the noise-limited assumption of the mmWave cellular networks. In Fig. 4.2, we plot the SINR and SNR coverage probabilities for three different number of tiers. When only microcell exists, since the interference is only from the same tier (i.e., microcell BSs), SINR and SNR coverage probabilities match with each other almost perfectly. As the number of tiers increases, the difference between SINR and SNR coverage probabilities become noticeable for higher values of the threshold because in a multi-tier scenario, interference is arising from BSs from different type of cells in different tiers as well. However, this performance gap is generally small and heterogeneous mmWave cellular networks can be assumed to be noise-limited (unless potentially the number of tiers is high). Also, note that as more tiers are added to the network, coverage probability increases significantly. Specifically, multi-tier network outperforms that with a single tier especially for small to

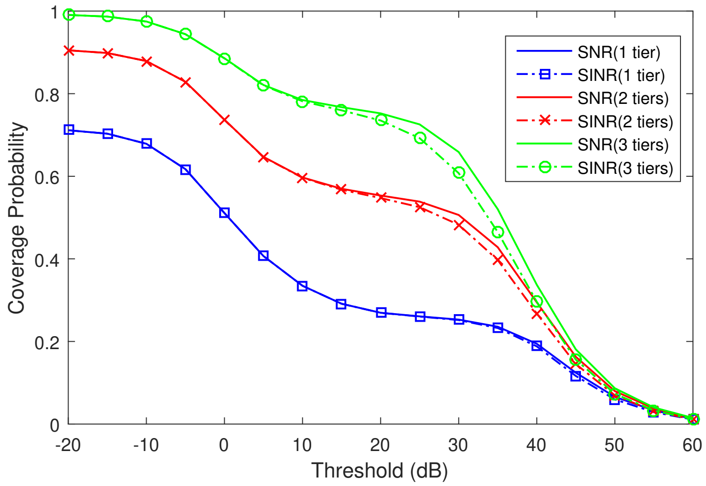

Figure 4.2: Coverage Probability as a function of the threshold in dB comparison between SINR and SNR.

medium values of the threshold.

Since in Fig. 4.2 we show that the difference between SINR and SNR coverage probabilities are negligible even in multi-tier network scenarios, we henceforth consider the SNR coverage probabilities in the remaining simulation and numerical results. Next, we compare the SNR coverage probabilities for different values of the antenna main lobe gain M. As expected, better SNR coverage is achieved with increasing main lobe gain as shown in Fig. 4.3. In Fig. 4.4, SNR coverage probability is plotted for different parameters of the D-ball model. Solid line corresponds to the coverage probability with the default parameters, i.e. 2-ball model with ball radii $(R_{11}, R_{12}), (R_{21}, R_{22}), (R_{31}, R_{32})$ in three tiers, respectively, and the corresponding β parameters given as listed in Table 4.1 (and also provided in the legend of Fig. 4.4). Dashed line and dot-dashed lines are the coverage probabilities for the 3-ball model with ball radii $(R_{11} = 50m, R_{12} = 150m, R_{13} = 200m), (R_{21} = 40m, R_{22} = 50m, R_{23} = 60m), (R_{31} = 20m, R_{32} = 30m, R_{33} = 40m)$ for the three tiers, respectively, but with different LOS probabilities (denoted by β) as listed in the legend of Fig. 4.4. Note that the LOS probabilities are higher for the case described by the dashed line (which implies that the signals are less likely to be blocked, for instance,

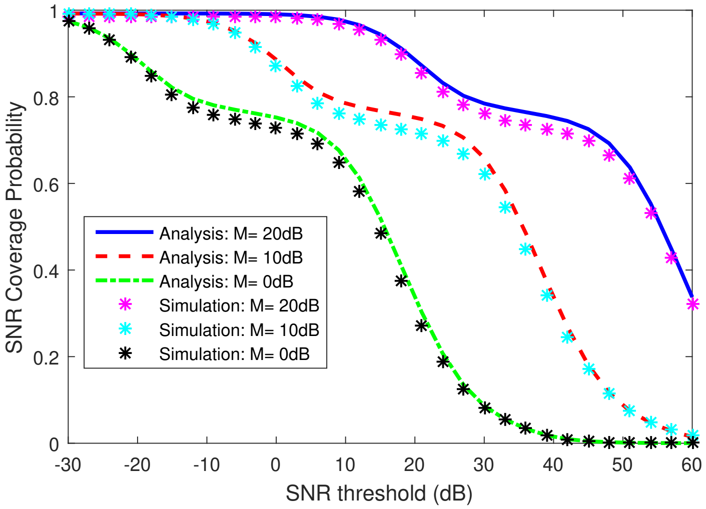

Figure 4.3: SNR Coverage Probability as a function of the threshold in dB for different values of antenna main lobe gain M.

as in a scenario with a less crowded environment and less buildings/blockages). Correspondingly, this high-LOS-probability 3-tier 3-ball model results in higher coverage probabilities. In the case of the dot-dashed curve, LOS probabilities are even smaller than those in the 2-ball model, resulting in degradation in the coverage probability. These numerical (and the accompanying simulation) results demonstrate that system parameters such as ball number and radii, and LOS probabilities have impact on the performance. Hence, appropriate modeling of the physical environment is critical in predicting the performance levels. Also note that, in Figs. 4.2, 4.3 and 4.4, there are break points at certain points of the curves after which coverage probability degrades faster. In Fig. 4.3, for example, break points occur at approximately 70% of the SNR coverage probability. These break points are occurring due to the assumption of the D-ball model. Finally, we also observe that simulation results very closely match the analytical results.

In Fig. 4.5, we analyze the effect of biasing factor on the SNR coverage performance. We use the same biasing factor for picocells and femtocells, and no biasing for microcells. As the biasing factor increases, number of UEs associated with smaller

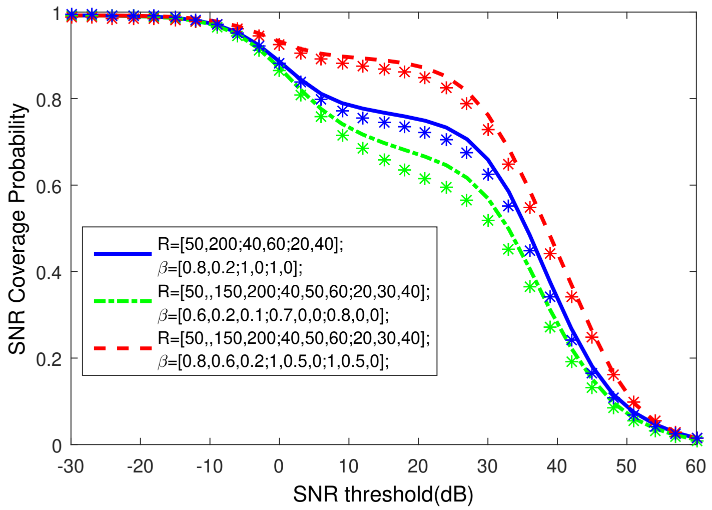

Figure 4.4: Coverage Probability as a function of the threshold in dB for different values of D-ball model parameters R and β.

cells increases resulting in an increase in coverage probabilities for picocells and femtocells while causing a degradation in the coverage performance of the microcell. This result is quite intuitive because with positive biasing, more UEs are encouraged to connect with the smaller cells. On the other hand, with biasing, UEs are associated with the BS not offering the strongest average received power, and thus the overall network coverage probability slightly decreases with the increasing biasing factor.

In Fig. 4.6, we show the effect of beam steering errors between the serving BS and the typical UE on the SNR coverage probability. As shown in the figure, coverage probability diminishes with the increase in alignment error standard deviation, and this deterioration becomes evident after $\sigma_{BE} = 7°$.

Fig. 4.7 shows the rate coverage probability as a function of the rate threshold. Rate coverage probability decreases with increasing rate threshold. Although there is a decrease in rate coverage probability, approximately %50 percent coverage is provided for a rate of 9 Gbps, and 9.5 Gbps rate can be achieved with around %25 percent coverage probability. Also, there are two transition lines in the overall network's rate coverage probability curve between 8.7-9.3 Gbps and 9.5-9.7 Gbps,

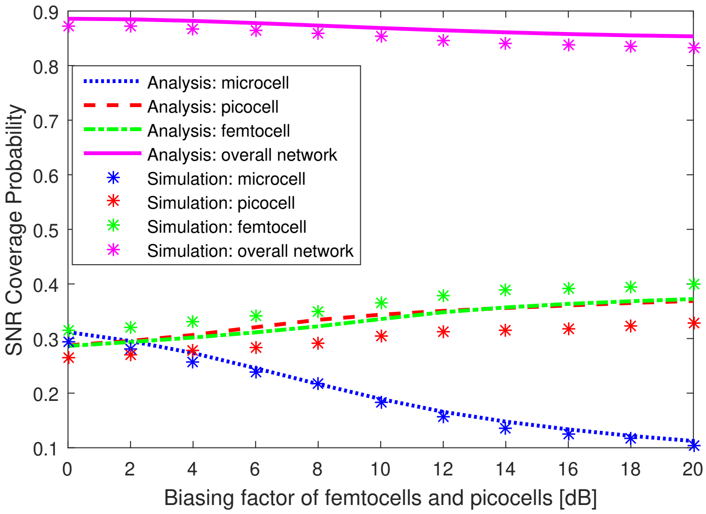

Figure 4.5: SNR Coverage Probability as a function of the biasing factor of picocells and femtocells in dB ($B_1 = 0dB$).

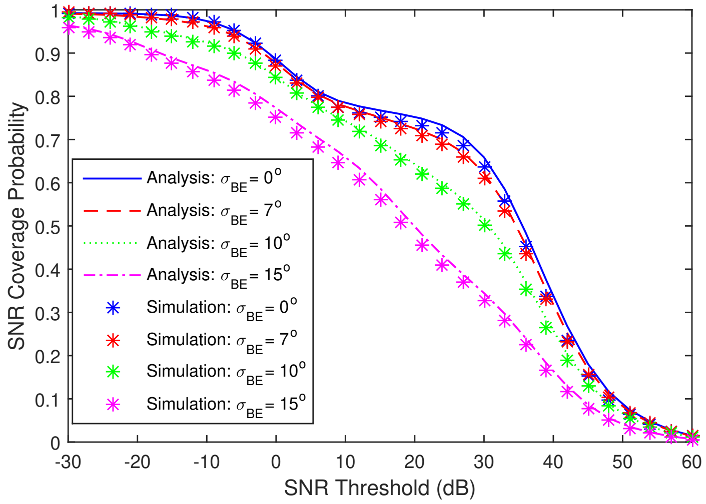

Figure 4.6: SNR Coverage Probability as a function of the threshold in dB for different alignment errors σ_{BE}.

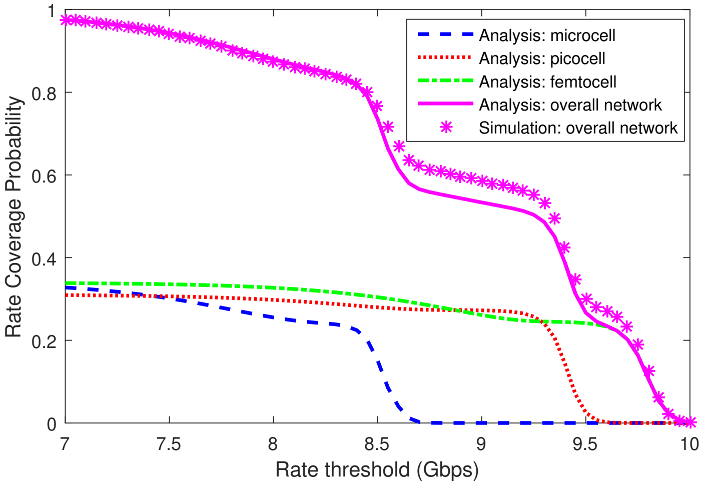

Figure 4.7: Rate Coverage Probability as a function of the threshold in Gbps.

respectively. The transition regions mainly distinguish the different tiers from each other. In other words, in the first transition region, microcell could not provide any rate coverage, and similarly picocells drop in the second region. Therefore, only femtocells can provide a rate greater than 9.5 Gbps.

In Fig. 4.8, energy efficiency of a 3-tier heterogeneous downlink mmWave cellular network is plotted as a function of the biasing factor of femtocells for different values of the microcell and femtocell BS densities. As biasing factor increases, energy efficiency first increases and reaches its maximum point, and then it starts decreasing. Since biasing provides more relief to the high-power microcell and picocell BSs, energy efficiency initially improves with the increasing biasing factor due to the reduction in the total power consumption. However, further increase in the biasing factor causes a degradation in energy efficiency because the reduction in the total power consumption cannot compensate the decrease in the total coverage probability. Solid line corresponds to the energy efficiency curve for the default values of microcell and femtocell BS densities (given in Table 4.1). When we increase the microcell BS density, energy efficiency degrades. On the other hand, when femtocell BS density is increased, energy efficiency improves. The reason is that introducing more low-power

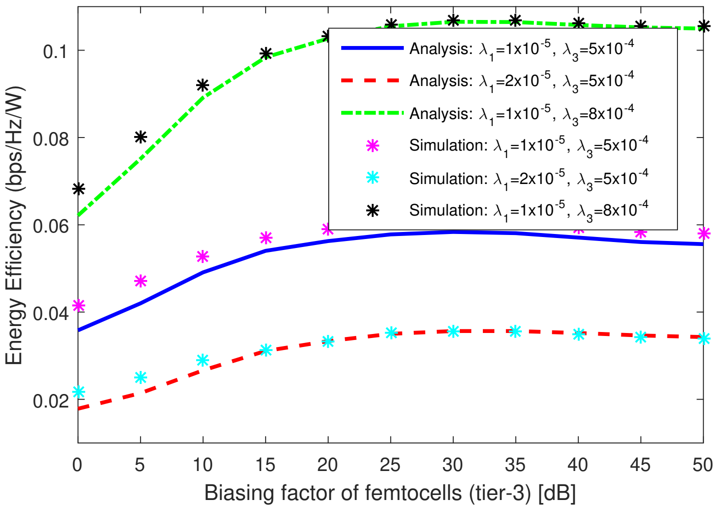

Figure 4.8: Energy Efficiency as a function of the biasing factor of femtocells in dB ($B_1 = B_2 = 0dB$).

femto BSs is more energy efficient than the addition of more high-power micro BSs.

We plot the cell association probability for all-mmWave and hybrid network scenarios as a function of the biasing factor of picocells and femtocells in Fig. 4.9 and Fig. 4.10, respectively. In the hybrid network setup, we use the same parameters given in Table 4.1 with some differences for the microcell network operating at lower μWave frequencies. More specifically, different from the previous figures, microcell BSs employ directional antennas with smaller main lobe gain, i.e., $M_\mu = 3$dB and larger beam width $\theta = 120°$, and the links from these BSs to the UEs are assumed to be LOS links with $R_{11} = 1500m$. Also, carrier frequency of the microcell network is $F_c = 2$GHz and noise power is equal to $\sigma_1^2 = -174$ dBm/Hz $+ 10 \log_{10} W +$ 10dB where $W = 20$MHz. Cell association probability of both all-mmWave and hybrid networks exhibit similar trends with the increase in biasing factor. However, association probability with microcell BSs (using μWave frequencies) in the hybrid network is greater than that in the all-mmWave network despite the smaller antenna main lobe gain. Since average received power cell association criteria is employed for cell selection and microcell μWave BSs have a larger LOS ball radius than smaller cells in

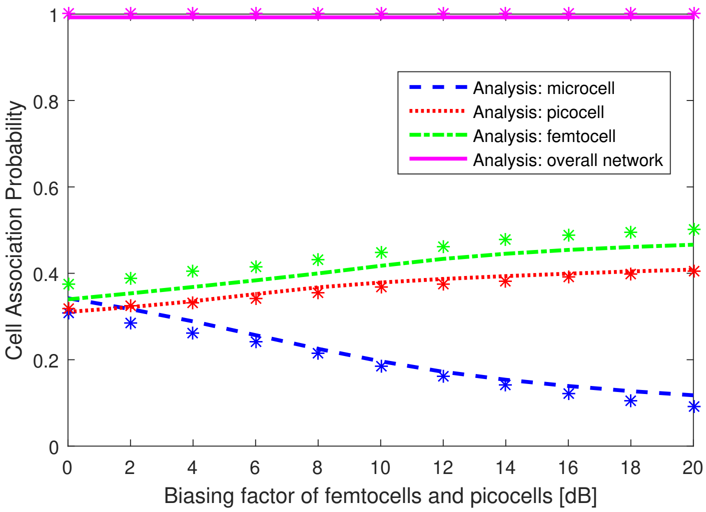

Figure 4.9: Cell Association Probability for all-mmWave network as a function of the biasing factor of picocells and femtocells in dB ($B_1 = 0$dB).

the hybrid network, UEs tend to connect to μWave BSs rather than mmWave BSs.

In Fig. 4.11, we plot the SINR coverage probability for hybrid network scenario as a function of the SINR threshold for different biasing factors of smaller cells. Although μWave BSs provide higher average received power, overall SINR coverage probability becomes less when compared with the all-mmWave network scenario (as noticed when the coverage curves in Fig. 4.11 are compared with previous numerical results) because of the following reasons. Essentially, interference becomes an important concern with more impact in μWave frequency bands, limiting the coverage performance. For instance, employment of omnidirectional antennas in microcell BSs is a critical factor (leading to increased interference and causing a poor coverage performance), along with having potentially more interfering μWave microcell BSs due to longer possible link distances with LOS. Therefore, as noted before, overall SINR coverage probability is less than that in the all-mmWave network scenario. Also, as seen in the figure, SINR coverage probability increases as the biasing factor for the picocells and femtocells are increased (contrary to the previous observations in the all-mmWave network scenario where an increase in the biasing factor of the picocells

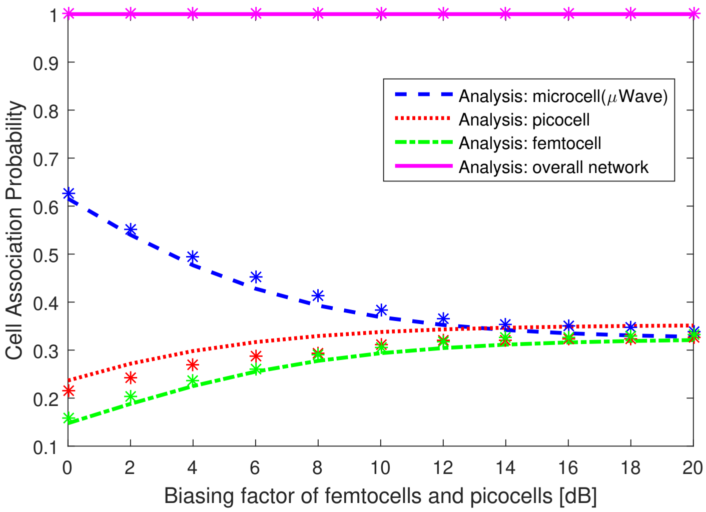

Figure 4.10: Cell Association Probability for hybrid network as a function of the biasing factor of picocells and femtocells in dB ($B_1 = 0$dB).

and femtocells has slightly reduced the overall network coverage probability as seen in Fig. 4.5). This again verifies the reasoning provided above. Specifically, with larger biasing factors, more UEs connect to the picocells and femtocells operating in the mmWave bands, and experience improved coverage due to employment of directional antennas and noise-limited nature of mmWave cells.

Fig. 4.12 shows the effect of microcell BS density on the SINR coverage performance again for the hybrid scenario. Same parameter values are used as in Fig. 4.11 but with no biasing. We notice in this figure that coverage probability increases with decreasing microcell BS density due to the fact that when there is a smaller number of microcell BSs, interference from other BSs transmitting at the μWave frequency band decreases.

4.6 Conclusion

In this chapter, we have provided a general analytical framework to compute the SINR and rate coverage probabilities in heterogeneous downlink mmWave cellular networks composed of K tiers. Moreover, we have studied the energy efficiency met-

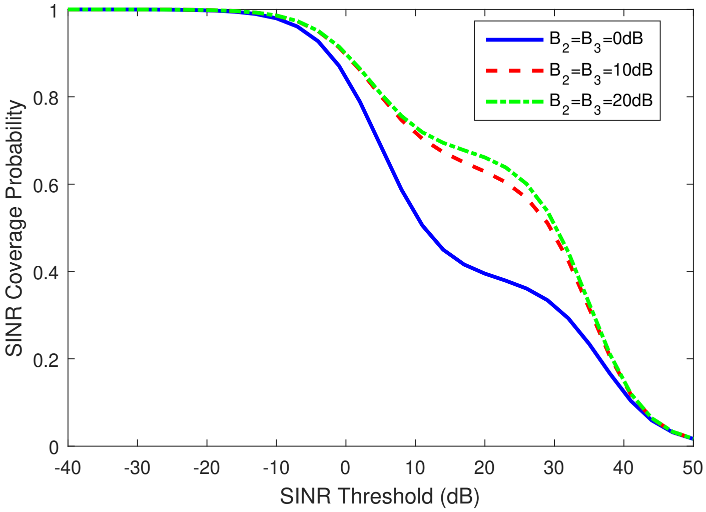

Figure 4.11: SINR Coverage Probability as a function of the threshold in dB for hybrid network for different biasing factor of picocells and femtocells in dB ($B_1 = 0dB$).

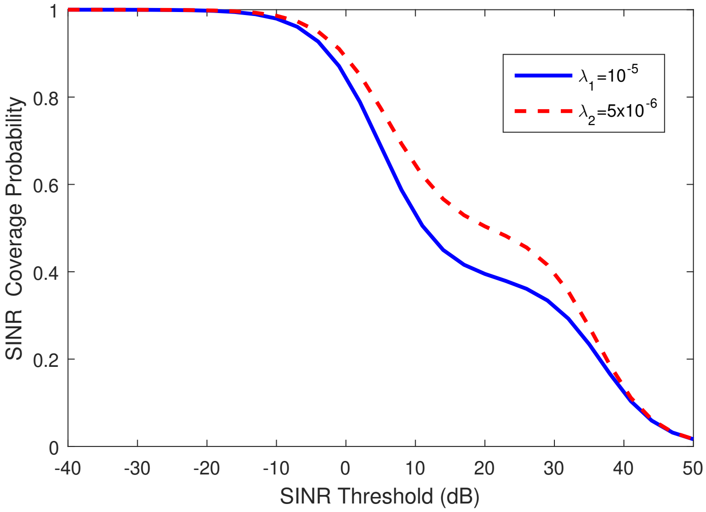

Figure 4.12: SINR Coverage Probability as a function of the threshold in dB for hybrid network for different density of microcells λ_1.

ric and analyzed the effect of biasing on energy efficiency. Directional beamforming with sectored antenna model and D-ball approximation for blockage model have been considered in the analysis. BSs of each tier and UEs are assumed to be distributed according to independent PPPs, and UEs are assumed to be connected to the tier providing the maximum average biased-received power. Numerical results show that mmWave cellular networks can be approximated to be noise-limited rather than being interference-limited especially if the number of tiers is small. We have also shown that increasing main lobe gain results in higher SNR coverage. Moreover, we have observed the effect of biasing. Increase in the biasing factor of smaller cells has led to better coverage probability of smaller cells because of the higher number of UEs connected to them, while the overall network coverage probability has slightly diminished due to association with the BS not offering the strongest average received power. Furthermore, we have shown that smaller cells provide higher rate than larger cells. Additionally, it is verified that there is an optimal biasing factor to achieve the maximum energy efficiency. The effect of alignment error on coverage probability is also quantified. Finally, we have demonstrated that the proposed analytical framework is also applicable to μWave-mmWave hybrid networks, and gleaned interesting insight on the impact of interference when operating in μWave frequency bands.

Chapter 5

Uplink Performance Analysis in D2D-Enabled Millimeter Wave Cellular Networks

In this chapter, we provide an analytical framework to analyze the uplink performance of device-to-device (D2D)-enabled mmWave cellular networks. Signal-to-interference-plus-noise ratio (SINR) outage probabilities are derived for both cellular and D2D links using tools from stochastic geometry. The distinguishing features of mmWave communications such as directional beamforming and having different path loss laws for LOS and NLOS links are incorporated into the outage analysis by employing a flexible mode selection scheme and Nakagami fading.

5.1 Introduction

With the employment of highly directional antennas, high propagation loss in the side lobes can be taken advantage of to support simultaneous communication with very limited or almost no interference to achieve lower link outage probabilities, much higher data rates and network capacity than those in μWave networks. A promising solution to improve the network capacity is to enable D2D communication in cellular networks. D2D communication allows proximity user equipments (UEs) to establish a direct communication link with each other by bypassing the BS. In other words, conventional two-hop cellular link is replaced by a direct D2D link to enhance the network capacity. Network performance of D2D communication in cellular networks has recently been extensively studied as an important component of fourth generation (4G) cellular networks by using stochastic geometry, but it has been gaining even more importance in 5G networks and it is expected to be an essential part of mmWave 5G cellular networks.

Several recent studies have also addressed the mmWave D2D communication. In [65], authors considered two types of D2D communication schemes in mmWave 5G cellular networks: local D2D and global D2D communications. Local D2D communication is performed by offloading the traffic from the BSs, while global D2D communication is established with multihop wireless transmissions via BSs between two wireless devices associated with different cells. The authors in [65] also proposed a resource sharing scheme to share network resources among local D2D and global D2D communications by considering the unique features of mmWave transmissions. In [66], authors proposed a resource allocation scheme in mmWave frequency bands, which enables underlay D2D communications to improve the system throughput and the spectral efficiency. mmWave D2D multi-hop routing for multimedia applications was studied in [68] to maximize the sum video quality by taking into account the unique characteristics of the mmWave propagation.

5.1.1 Main Contributions

Our main contributions can be summarized as follows:

- We provide an analytical framework to analyze the uplink performance of D2D-enabled mmWave cellular networks by using tools from stochastic geometry.

- We derive SINR outage probability expressions for both cellular and D2D links, considering different Nakagami fading parameters for LOS and NLOS components, employing the modified LOS ball model for blockage modeling, and considering a flexible mode selection scheme.
- We investigate the effect of spectrum sharing type in SINR outage probability.

5.2 System Model

In this section, the system model for D2D communication enabled mmWave cellular networks is presented. We consider a single-tier uplink network. BSs and UEs are spatially distributed according to two independent homogeneous PPPs Φ_B and Φ_U with densities λ_B and λ_U, respectively, on the Euclidean plane. UEs are categorized as cellular UEs and potential D2D UEs with probabilities q and $(1-q)$, respectively, where q is the probability of being a cellular UE. A cellular UE is assumed to be associated with its closest BS. Potential D2D UEs have the capability of establishing a direct D2D link and can operate in one of the two modes according to the mode selection scheme: cellular and D2D mode. When operating in D2D mode, a UE can bypass the BS and communicate directly with its intended receiver. The density of UEs which communicate in D2D mode is $\lambda_d = (1-q)\lambda_U P_{D2D}$, and the density of UEs which communicate in cellular mode is equal to $\lambda_c = q\lambda_U + (1-q)\lambda_U(1-P_{D2D})$, where P_{D2D} is the probability of potential D2D UE selecting the D2D mode, and it will be described and characterized in detail later in the chapter.

In this setting, we have the following assumptions regarding the system model of the D2D-enabled mmWave cellular network:

Assumption 5.1 *(Directional beamforming) Antenna arrays at the BSs and UEs are assumed to perform directional beamforming with the main lobe being directed towards the dominant propagation path while smaller side lobes direct energy in other* *directions. For tractability in the analysis, antenna arrays are approximated by a sectored antenna model, in which the array gains are assumed to be constant* M *for all angles in the main lobe and another smaller constant* m *in the side lobe [34]. Perfect beam alignment is assumed in between the transmitting nodes (e.g., cellular or potential D2D UEs) and receiving nodes (e.g., BSs or receiving D2D UEs), leading to an overall antenna gain of* MM*. Also, the beam direction of the interfering nodes is modeled as a uniform random variable on* $[0, 2\pi)$*. Therefore, the effective antenna gain is a discrete random variable (RV) described by*

$$G = \begin{cases} MM & \textit{with prob. } p_{MM} = \left(\frac{\theta}{2\pi}\right)^2 \\ Mm & \textit{with prob. } p_{Mm} = 2\left(\frac{\theta}{2\pi}\right)\left(\frac{2\pi-\theta}{2\pi}\right) \\ mm & \textit{with prob. } p_{mm} = \left(\frac{2\pi-\theta}{2\pi}\right)^2, \end{cases} \tag{5.1}$$

where θ *is the beam width of the main lobe, and* p_G *is the probability of having an antenna gain of* G*.*

Assumption 5.2 *(Path-loss exponents and link distance modeling) A transmitting UE can either have a LOS or NLOS link to the BS or the receiving UE. In a LOS state, UE should be visible to the receiving nodes, indicating that there is no blockage in the link. On the other hand, in a NLOS state, blockage occurs in the link. Consider an arbitrary link of length* r*, and define the LOS probability function* $p(r)$ *as the probability that the link is LOS. Using field measurements and stochastic blockage models,* $p(r)$ *can be modeled as* $e^{-\zeta r}$ *where decay rate* ζ *depends on the building parameter and density [35]. For simplicity, LOS probability function* $p(r)$ *can be approximated by a step function. In this approach, the irregular geometry of the LOS region is replaced with its equivalent LOS ball model. Modified LOS ball model is adopted similarly as in [10]. According to this model, the LOS probability function of a link* $p_L(r)$ *is equal to some constant* p_L *if the link distance* r *is less than ball radius* R_B *and zero otherwise. The parameters* p_L *and* R_B *depend on geographical regions.*

$(p_{L,c}, R_{B,c})$ and $(p_{L,d}, R_{B,d})$ are the LOS ball model parameters for cellular and D2D links, respectively[1]*. Therefore, LOS and NLOS probability function for each link can be expressed as follows:*

$$\begin{aligned} p_{L,\kappa}(r) &= p_{L,\kappa}\mathbb{1}(r \leq R_{B,\kappa}) \\ p_{N,\kappa}(r) &= (1 - p_{L,\kappa})\mathbb{1}(r \leq R_{B,\kappa}) + \mathbb{1}(r > R_{B,\kappa}), \end{aligned} \tag{5.2}$$

for $\kappa \in \{c, d\}$ where $\mathbb{1}(\cdot)$ is the indicator function. Different path loss laws are applied to LOS and NLOS links, thus $\alpha_{L,\kappa}$ and $\alpha_{N,\kappa}$ are the LOS and NLOS path-loss exponents for $\kappa \in \{c, d\}$, respectively.

Since the link distance between D2D UEs is generally relatively small, we assume that the transmitting UEs are always LOS to the receiving UE, i.e., inside the LOS ball we have $p_{L,d} = 1$, and therefore the path loss exponent for the D2D link is always equal to $\alpha_{L,d}$. For the sake of simplicity, we also assume that each potential D2D UE has its own receiving UE uniformly distributed within the LOS ball with radius $R_{B,d}$. Therefore, the probability density function (pdf) of the D2D link distance r_d is given by $f_{r_d}(r_d) = 2r_d/R_{B,d}^2$, $0 \leq r_d \leq R_{B,d}$. Pdf of the cellular link distance r_c to the nearest LOS/NLOS BS is given by [9]

$$f_s(r_c) = 2\pi\lambda_B r_c p_{s,c}(r_c) e^{-2\pi\lambda_B \psi_s(r_c)}/\mathcal{B}_{s,c} \quad \text{for } s \in \{L, N\}, \tag{5.3}$$

where $\psi_s(r_c) = \int_0^{r_c} x p_s(x) dx$, $\mathcal{B}_{s,c} = 1 - e^{-2\pi\lambda_B \int_0^\infty x p_s(x) dx}$ is the probability that a UE has at least one LOS/NLOS BS, and $p_s(x)$ is given in (5.2) for $s \in \{L, N\}$.

---

[1] Throughout the chapter, subscripts c and d denote associations with cellular and D2D links, respectively.

5.2.1 Spectrum Sharing

Cellular spectrum can be shared between cellular and D2D UEs in two different ways: underlay and overlay. In the underlay type of sharing, D2D UEs can opportunistically access the channel occupied by the cellular UEs. While for the overlay type of sharing, the uplink spectrum is divided into two orthogonal portions, i.e., a fraction δ of the cellular spectrum is assigned to D2D mode and the remaining part $(1-\delta)$ is used for cellular communication, where δ is the spectrum partition factor [67]. Also, β is defined as the spectrum sharing indicator which is equal to one for underlay and zero for overlay type of sharing.

5.2.2 Interference Modeling

Each cellular UE is assigned a unique and orthogonal channel by its associated BS which means that there is no intra-cell interference between cellular UEs in the same cell. However, we assume universal frequency reuse across the entire cellular network causing inter-cell interference from the other cells' cellular UEs. In the underlay case, we focus on one uplink channel which is shared by the cellular and D2D UEs. Since the D2D UEs coexist with the cellular UEs in an uplink channel, they cause both intra-cell and inter-cell interference at the BSs and other D2D UEs. On the other hand, in the overlay case, since the uplink spectrum is divided into two orthogonal portions, there is no cross-mode interference, i.e., no interference from the cellular (D2D) UEs to the D2D (cellular) UEs. Moreover, we consider a congested network scenario in which density of cellular UEs is much higher than the density of BSs. Since $\lambda_U \gg \lambda_B$, each BS will always have at least one cellular UE to serve in the uplink channel. Therefore, the interfering cellular UEs in different cells is modeled as another PPP Φ_c with density λ_B.

5.2.3 Mode Selection

In this work, a flexible mode selection scheme similarly as in [69] is considered. In this scheme, a potential D2D UE chooses the D2D mode if the biased D2D link quality is at least as good as the cellular uplink quality. In other words, a potential D2D UE will operate in D2D mode if $T_d r_d^{-\alpha_{L,d}} \geq r_c^{-\alpha_{s,c}}$, where $T_d \in [0, \infty)$ is the biasing factor, and r_c and r_d are the cellular and D2D link distances, respectively. Since we assume potential D2D UEs are always LOS to the receiving UEs, LOS path loss exponent $\alpha_{L,d}$ is used for the D2D links. Biasing factor T_d has two extremes, $T_d = 0$ and $T_d \to \infty$. In the first extreme case, D2D communication is disabled, while in the second case, each potential D2D UE is forced to select the D2D mode. The probability of selecting D2D mode, P_{D2D}, can be found as follows:

$$
\begin{aligned}
P_{D2D} &= 1 - P_{cellular} \\
&= 1 - \mathbb{P}\left(T_d r_d^{-\alpha_{L,d}} \leq r_c^{-\alpha_{s,c}}\right) \mathcal{B}_{s,c} \\
&= 1 - \mathbb{P}\left(r_c \leq r_d^{\alpha_{L,d}/\alpha_{s,c}} T_d^{-1/\alpha_{s,c}}\right) \mathcal{B}_{s,c} \\
&= 1 - \sum_{s \in \{L,N\}} \int_0^{R_{B,d}} F_s\left(\frac{r_d^{a_s}}{T_d^{1/\alpha_{s,c}}}\right) f_{r_d}(r_d) \mathcal{B}_{s,c} dr_d \\
&\overset{(a)}{=} 1 - \sum_{s \in \{L,N\}} \int_0^{R_{B,d}} \left(1 - e^{-\pi\lambda_B \psi_s\left(\frac{r_d^{a_s}}{T_d^{1/\alpha_{s,c}}}\right)}\right) \frac{2r_d}{R_{B,d}^2} dr_d, \qquad (5.4)
\end{aligned}
$$

where $a_s = \alpha_{L,d}/\alpha_{s,c}$, $F_s(r_c) = \left(1 - e^{-2\pi\lambda_B \psi_s(r_c)}\right) / \mathcal{B}_{s,c}$ is the cumulative distribution function (cdf) of the cellular link distance r_c to the nearest LOS/NLOS BS, and (a) follows from the substitution of the cdf of r_c and pdf of r_d into the expression.

5.3 Analysis of Uplink SINR Outage Probability

In this section, we first develop a theoretical framework to analyze the uplink SINR outage probability for a generic UE using stochastic geometry. Although a biasing-based mode selection scheme is considered for selecting between D2D and cellular modes, the developed framework can also be applied for different mode selection schemes.

5.3.1 SINR Analysis

Without loss of generality, we consider a typical receiving node (BS or UE) located at the origin according to Slivyank's theorem for PPP. The SINR experienced at a typical receiving node can be written as

$$SINR^{\kappa} = \frac{P_{\kappa} G_0 h_0 r_0^{-\alpha_{\kappa}(r_0)}}{\sigma^2 + \underbrace{\sum_{i \in \Phi_c} P_c G_i h_i r_i^{-\alpha_{\kappa}(r_i)}}_{I_{c\kappa}} + \underbrace{\sum_{j \in \Phi_d} P_d G_j h_j r_j^{-\alpha_{\kappa}(r_j)}}_{I_{d\kappa}}}, \tag{5.5}$$

where P_{κ} is the transmit power of the UE operating in mode $\kappa \in \{c, d\}$, G_0 is the effective antenna gain of the link which is assumed to be equal to MM, h_0 is the small-scale fading gain, $\alpha_{\kappa}(r_0)$ is the path-loss exponent of the link which is determined according to the LOS probability function, r_0 is the transmission distance, σ^2 is the variance of the additive white Gaussian noise component, $I_{c\kappa}$ is the aggregate interference at the receiving node from cellular UEs using the same uplink channel in different cells which constitute a PPP Φ_c, and $I_{d\kappa}$ is the aggregate interference at the receiving node from D2D UEs located anywhere (hence including both inter-cell and intra-cell D2D UEs), which constitute another PPP Φ_d. Actually, neither Φ_c nor Φ_d is a PPP due to the interaction between the point processes of BSs and UEs, and the mode selection scheme. Also, they are not independent. However, for analytical tractability based on the assumptions in [69], we assume interfering UEs operating in cellular mode and D2D mode constitute independent PPPs Φ_c and Φ_d with densities λ_B and λ_d, respectively. A similar notation is used for $I_{c\kappa}$ and $I_{d\kappa}$, but note that the effective antenna gains G_i and G_j, and path loss exponents $\alpha_\kappa(r_i)$ and $\alpha_\kappa(r_j)$ are different for different interfering links as described in (5.1) and (5.2), respectively. All links are assumed to be subject to independent Nakagami fading (i.e., small-scale fading gains have a gamma distribution). Parameters of Nakagami fading are N_L and N_N for LOS and NLOS links, respectively, and they are assumed to be positive integers for simplicity. When $N_L = N_N = 1$, Nakagami fading specializes to Rayleigh fading.

The above description implicitly assumes underlay spectrum sharing between cellular and D2D UEs. Note that since there is no cross-mode interference in the overlay case, the SINR expression in this case reduces to $SINR^\kappa = \frac{P_\kappa G_0 h_0 r_0^{-\alpha_\kappa(r_0)}}{\sigma^2 + I_{\kappa\kappa}}$.

The uplink SINR outage probability $\mathrm{P_{out}}$ is defined as the probability that the received SINR is less than a certain threshold $\Gamma > 0$, i.e., $\mathrm{P_{out}} = \mathbb{P}(\mathrm{SINR} < \Gamma)$. The outage probability for a typical UE in cellular mode is given in the following theorem.

Theorem 5.1 *In a single-tier D2D communication enabled mmWave cellular network, the outage probability for a typical cellular UE can be expressed as*

$$\begin{aligned} P^c_{out}(\Gamma) = \sum_{s\in\{L,N\}} \int_0^\infty \sum_{n=1}^{N_s} (-1)^n \binom{N_s}{n} e^{-\frac{n\eta_s \Gamma r_0^{\alpha_{s,c}} \sigma^2}{P_c G_0}} \times \\ \mathcal{L}_{I_{cc}}\left(\frac{n\eta_s \Gamma r_0^{\alpha_{s,c}}}{P_c G_0}\right) \mathcal{L}_{I_{dc}}\left(\frac{\beta n\eta_s \Gamma r_0^{\alpha_{s,c}}}{P_c G_0}\right) f_s(r_0) \mathcal{B}_{s,c} dr_0, \end{aligned} \tag{5.6}$$

where

$$\mathcal{L}_{I_{cc}}\left(\frac{n\eta_s\Gamma r_0^{\alpha_{s,c}}}{P_cG_0}\right) = \exp\Bigg(-2\pi\lambda_B\Bigg(\sum_{j\in\{L,N\}}\sum_{i=1}^{3}p_{G_i}\times \\ \Bigg(\int_0^\infty\Bigg(1-1/\Bigg(1+\frac{n\eta_s\Gamma r_0^{\alpha_{s,c}}G_i}{G_0N_jt^{\alpha_{j,c}}}\Bigg)^{N_j}\Bigg)p_{j,c}(t)tdt\Bigg)\Bigg)\Bigg), \tag{5.7}$$

and

$$\mathcal{L}_{I_{dc}}\left(\frac{\beta n\eta_s\Gamma r_0^{\alpha_{s,c}}}{P_cG_0}\right) = \exp\Bigg(-2\pi\lambda_d\Bigg(\sum_{j\in\{L,N\}}\sum_{i=1}^{3}p_{G_i}\times \\ \Bigg(\int_0^\infty\Bigg(1-1/\Bigg(1+\frac{\beta n\eta_s\Gamma r_0^{\alpha_{s,c}}P_dG_i}{P_cG_0N_jt^{\alpha_{j,c}}}\Bigg)^{N_j}\Bigg)p_{j,c}(t)tdt\Bigg)\Bigg)\Bigg), \tag{5.8}$$

are the Laplace transforms $\mathcal{L}_{I_{cc}}(v)$ *and* $\mathcal{L}_{I_{dc}}(\beta v)$ *of* I_{cc} *and* I_{dc} *evaluated at* $v = \frac{n\eta_s\Gamma r_0^{\alpha_{s,c}}}{P_cG_0}$*, respectively,* $f_s(r_0)$ *is the pdf of the cellular link distance given in (5.3),* $\eta_s = N_s(N_s!)^{-\frac{1}{N_s}}$*, and* $p_{j,c}(\cdot)$ *is given in (5.2).*

Proof: The outage probability for a typical UE in cellular mode can be calculated as follows

$$\begin{aligned}
\mathrm{P}^c_{\mathrm{out}}(\Gamma) &= \mathrm{P}^c_{\mathrm{out},L}(\Gamma)\mathcal{B}_{L,c} + \mathrm{P}^c_{\mathrm{out},N}(\Gamma)\mathcal{B}_{N,c} \\
\mathrm{P}^c_{\mathrm{out}}(\Gamma) &= \sum_{s\in\{L,N\}}\mathbb{P}\left(\frac{P_cG_0h_0r_0^{-\alpha_{s,c}}}{\sigma^2+I_{cc}+I_{dc}}\leq\Gamma\right)\mathcal{B}_{s,c} \\
&= \sum_{s\in\{L,N\}}\int_0^\infty\mathbb{P}\left(h_0\leq\frac{\Gamma r_0^{\alpha_{s,c}}}{P_cG_0}\left(\sigma^2+I_{cc}+I_{dc}\right)|r_0\right)f_s(r_0)\mathcal{B}_{s,c}dr_0 \\
&= \sum_{s\in\{L,N\}}\int_0^\infty\sum_{n=1}^{N_s}(-1)^n\binom{N_s}{n}e^{-v\sigma^2}\mathcal{L}_{I_{cc}}(v)\mathcal{L}_{I_{dc}}(\beta v)f_s(r_0)\mathcal{B}_{s,c}dr_0,
\end{aligned} \tag{5.9}$$

where $v = \frac{n\eta_s\Gamma r_0^{\alpha_{s,c}}}{P_cG_0}$, and (5.9) is derived noting that h_0 is a normalized gamma random variable with parameter N_s, and using similar steps as in [9].

We can apply concepts from stochastic geometry to compute the Laplace transform of I_{cc} and I_{dc}. The thinning property of PPP can be employed to split the $I_{\kappa c}$ into 8 independent PPPs as follows [32]:

$$
\begin{aligned}
I_{\kappa c} &= I_{\kappa c,L} + I_{\kappa c,N} \\
&= \sum_{G \in \{MM, Mm, mm\}} \sum_{j \in \{L,N\}} I^{G}_{\kappa c,s},
\end{aligned}
\tag{5.10}
$$

where $I_{\kappa c,L}$ and $I_{\kappa c,N}$ are the aggregate LOS and NLOS interferences arising from the cellular UEs using the same uplink channel in different cells for $\kappa = c$ and D2D UEs in the same cell and out-of-cell for $\kappa = d$, and $I^{G}_{\kappa c,j}$ denotes the interference for $j \in \{L, N\}$ with random antenna gain G defined in (5.1). According to the thinning theorem, each independent PPP has a density of $\lambda_B p_G$ for $\kappa = c$ and $\lambda_d p_G$ for $\kappa = d$ where p_G is given in (5.1) for each antenna gain G.

Inserting (5.10) into the Laplace transform expression and using the definition of the Laplace transform yield

$$
\begin{aligned}
\mathcal{L}_{I_{\kappa c}}(v) &= \mathbb{E}_{I_{\kappa c}}\left[e^{-vI_{\kappa c}}\right] = \mathbb{E}_{I_{\kappa c}}\left[e^{-v\left(I_{\kappa c,L}+I_{\kappa c,N}\right)}\right] \\
&\overset{(a)}{=} \mathbb{E}_{I_{\kappa c,L}}\left[e^{-v\sum_G I^{G}_{\kappa c,L}}\right]\mathbb{E}_{I_{\kappa c,N}}\left[e^{-v\sum_G I^{G}_{\kappa c,N}}\right] \\
&= \prod_{G}\prod_{j}\mathbb{E}_{I^{G}_{\kappa c,j}}\left[e^{-vI^{G}_{\kappa c,j}}\right],
\end{aligned}
\tag{5.11}
$$

where $G \in \{MM, Mm, mm\}$, $j \in \{L, N\}$, $v = \frac{n\eta_s \Gamma r_0^{\alpha_{s,c}}}{P_c G_0}$, and (a) follows from the fact that $I_{\kappa c,L}$ and $I_{\kappa c,N}$ are interferences generated from two independent thinned PPPs. Now, we can compute the Laplace transform for $I^{G}_{\kappa c,j}$ using stochastic geometry as follows:

$$
\begin{aligned}
\mathbb{E}_{I^{G}_{\kappa c,j}}\left[e^{-vI^{G}_{\kappa c,j}}\right] &= e^{-2\pi\lambda_\kappa p_G \int_0^\infty \left(1-\mathbb{E}_h\left[e^{-vP_\kappa G h t^{-\alpha_{j,c}}}\right]\right)p_{j,c}(t)tdt} \\
&\overset{(a)}{=} e^{-2\pi\lambda_\kappa p_G \int_0^\infty \left(1-1/\left(1+vP_\kappa G t^{-\alpha_{j,c}}/N_j\right)^{N_j}\right)p_{j,c}(t)tdt},
\end{aligned}
\tag{5.12}
$$

where $p_{j,c}(\cdot)$ is given in (5.2), $\lambda_\kappa = \lambda_B$ for cellular interfering links and $\lambda_\kappa = \lambda_d$ for D2D interfering links. (a) is obtained by computing the moment generating function (MGF) of the gamma random variable h. By inserting (5.12) into (5.11), Laplace transform of $I_{\kappa c}$ can be obtained for $\kappa \in \{c, d\}$.

Theorem 5.2 *In a single-tier D2D communication enabled mmWave cellular network, the outage probability for a typical D2D UE can be expressed as*

$$P^d_{out}(\Gamma) = \int_0^\infty \sum_{n=1}^{N_L} (-1)^n \binom{N_L}{n} e^{-\frac{n\eta_L \Gamma r_0^{\alpha_{L,d}} \sigma^2}{P_d G_0}} \times \\ \mathcal{L}_{I_{dd}}\left(\frac{n\eta_L \Gamma r_0^{\alpha_{L,d}}}{P_d G_0}\right) \mathcal{L}_{I_{cd}}\left(\frac{\beta n\eta_L \Gamma r_0^{\alpha_{L,d}}}{P_d G_0}\right) f_{r_d}(r_0) dr_0, \tag{5.13}$$

where

$$\mathcal{L}_{I_{dd}}\left(\frac{n\eta_L \Gamma r_0^{\alpha_{L,d}}}{P_d G_0}\right) = \exp\Bigg(-2\pi\lambda_d \Bigg(\sum_{j\in\{L,N\}} \sum_{i=1}^{3} p_{G_i} \times \\ \Bigg(\int_0^\infty \Bigg(1 - 1/\Bigg(1 + \frac{n\eta_s \Gamma r_0^{\alpha_{s,d}} G_i}{G_0 N_j t^{\alpha_{j,d}}}\Bigg)^{N_j}\Bigg) p_{j,d}(t) t dt \Bigg)\Bigg)\Bigg), \tag{5.14}$$

and

$$\mathcal{L}_{I_{cd}}\left(\frac{\beta n\eta_L \Gamma r_0^{\alpha_{L,d}}}{P_d G_0}\right) = \exp\Bigg(-2\pi\lambda_B \Bigg(\sum_{j\in\{L,N\}} \sum_{i=1}^{3} p_{G_i} \times \\ \Bigg(\int_0^\infty \Bigg(1 - 1/\Bigg(1 + \frac{\beta n\eta_s \Gamma r_0^{\alpha_{s,d}} P_d G_i}{P_d G_0 N_j t^{\alpha_{j,d}}}\Bigg)^{N_j}\Bigg) p_{j,d}(t) t dt \Bigg)\Bigg)\Bigg), \tag{5.15}$$

are the Laplace transforms $\mathcal{L}_{I_{dd}}(v)$ *and* $\mathcal{L}_{I_{cd}}(\beta v)$ *of* I_{dd} *and* I_{cd} *evaluated at* $v = \frac{n\eta_L \Gamma r_0^{\alpha_{L,d}}}{P_d G_0}$*, respectively,* $f_{r_d}(r_0)$ *is the pdf of the D2D link distance given by* $2r_d/R^2_{B,d}$ *for* $0 \le r_d \le R_{B,d}$*, and* $p_{j,d}(\cdot)$ *is given in (5.2).*

Proof: Proof follows similar steps as in the proof of Theorem 5.1, and the details are omitted for the sake of brevity.

Table 5.1: System Parameters

Parameters	**Values**
$\alpha_{L,c}$, $\alpha_{N,c}$; $\alpha_{L,d}$, $\alpha_{N,d}$	2, 4; 2, 4
N_L, N_N	3, 2
M, m, θ	20dB, -10dB, 30^o
λ_B, λ_U,	10^{-5}, 10^{-3} $(1/m^2)$
$(p_{L,c}, R_{B,c})$, $(p_{L,d}, R_{B,d})$	(1, 100), (1, 50)
q, β, δ, T_d	0.2, 1, 0.2, 1
Γ, σ^2	0dB, -74dBm
P_c, P_d	200mW, 200mW

5.4 Simulation and Numerical Results

In this section, theoretical expressions are evaluated numerically. We also provide simulation results to validate the the accuracy of the proposed model for the D2D-enabled uplink mmWave cellular network as well as to confirm the accuracy of the analytical characterizations. In the numerical evaluations and simulations, unless otherwise stated, the parameter values listed in Table 5.1 are used.

First, we investigate the effect of D2D biasing factor T_d on the probability of selecting D2D mode for different values of LOS ball model parameter $p_{L,c}$ for the cellular link in Fig. 5.1. As the D2D biasing factor increases, probability of selecting D2D mode expectedly increases. Also, since the number of LOS BSs increases with the increase in $p_{L,c}$, probability of selecting D2D mode decreases with increasing $p_{L,c}$.

Next, we compare the SINR outage probabilities for different values of the antenna main lobe gain M and beam width of the main lobe θ in Fig. 5.2. Outage probability improves with the increase in the main lobe gain M for the same value of θ. Since we assume perfect beam alignment for serving links, outage probability increases with the increase in the beam width of the main lobe due to growing impact of the interference.

In Fig. 5.3, the effect of spectrum sharing type is investigated. As described in Section 5.2, β indicates the type of spectrum sharing; i.e., it is equal to one for

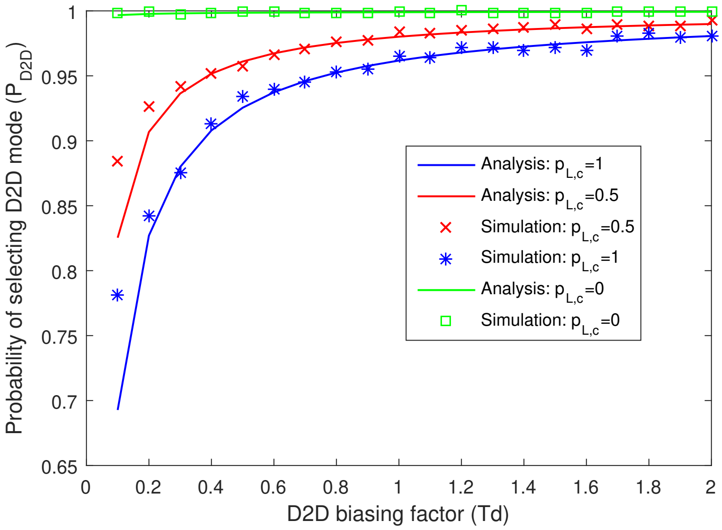

Figure 5.1: Probability of selecting D2D mode as a function of the D2D biasing factor T_d.

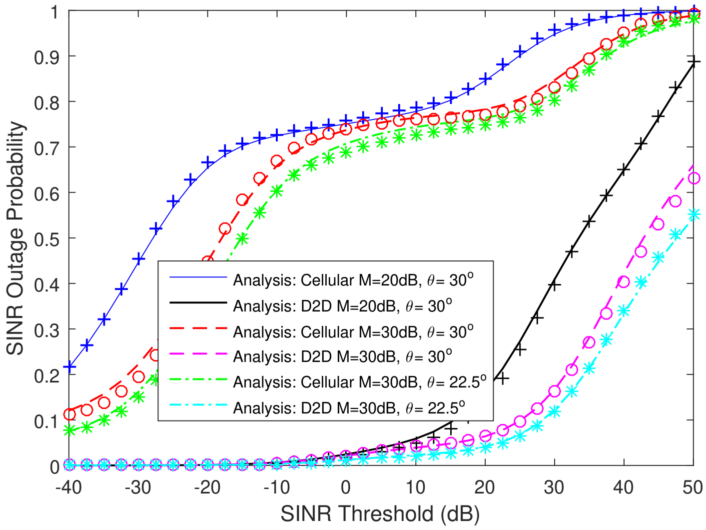

Figure 5.2: SINR outage probability as a function of the threshold in dB for different antenna parameters. Simulation results are also plotted with markers.

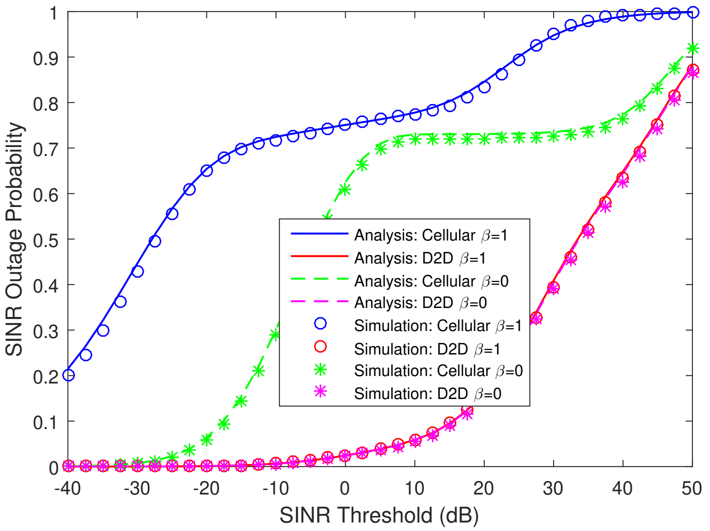

Figure 5.3: SINR outage probability as a function of the threshold in dB for different β values.

underlay and zero for overlay scheme. For cellular UEs, outage probability is smaller in the overlay scheme compared to underlay since cross-mode interference from D2D UEs becomes zero in the case of overlay spectrum sharing. On the other hand, outage probability of D2D UEs remains same with both overlay and underlay sharing, showing that the effect of cross-mode interference from cellular UEs is negligible even under the congested network scenario assumption.

5.5 Conclusion

In this chapter, we have provided an analytical framework to compute SINR outage probabilities for both cellular and D2D links in a D2D-enabled mmWave cellular network. Directional beamforming with sectored antenna model and modified LOS ball model for blockage modeling have been considered in the analysis. BSs and UEs are assumed to be distributed according to independent PPPs, and potential D2D UEs are allowed to choose cellular or D2D mode according to a flexible mode selection scheme. Numerical results show that probability of selecting D2D mode increases with increasing biasing factor T_d and decreasing $p_{L,c}$. We have also shown that increasing the main lobe gain and decreasing the beam width of the main lobe result in lower SINR outage. Moreover, we have observed that the type of spectrum sharing plays a crucial role in SINR outage performance of cellular UEs.

Chapter 6

Uplink Performance Analysis in D2D-Enabled Millimeter Wave Cellular Networks with Clustered Users

In this chapter, an analytical framework is provided to analyze the uplink performance of device-to-device (D2D)-enabled millimeter wave (mmWave) cellular networks with clustered D2D user equipments (UEs). Locations of cellular UEs are modeled as a Poison Point Process (PPP), while locations of potential D2D UEs are modeled as a Poisson Cluster Process (PCP). Signal-to-interference-plus-noise ratio (SINR) outage probabilities are derived for both cellular and D2D links using tools from stochastic geometry. The distinguishing features of mmWave communications such as directional beamforming and having different path loss laws for line-of-sight (LOS) and non-line-of-sight (NLOS) links are incorporated into the outage analysis by employing a flexible mode selection scheme and Nakagami fading. Also, the effect of beamforming alignment errors on the outage probability is investigated to get insight on the performance in practical scenarios. Moreover, area spectral efficiency (ASE) of the cellular and D2D networks are determined for both underlay and overlay types of sharing. Optimal spectrum partition factor is determined for overlay sharing by considering the optimal weighted proportional fair spectrum partition.

6.1 Introduction

As discussed in Chapter 5, a promising solution to improve the network capacity is to enable D2D communication in cellular networks. Network performance of D2D communication in cellular networks has recently been extensively studied as an important component of fourth generation (4G) cellular networks by using stochastic geometry. In [67] and [69], outage and spectrum efficiency of D2D-enabled uplink cellular networks were studied by considering mode selection schemes along with truncated channel inversion power control. In [67], a distance-based mode selection scheme was employed while [69] considered a flexible mode selection scheme. Also, effect of spectrum sharing type on the performance was investigated in [67]. In these works, locations of the transmitting potential D2D UEs were modeled using Poisson Point Processes (PPPs) while the receiving D2D UEs were assumed to be distributed within a circle around the transmitting D2D UE. However, in D2D networks, UEs are very likely to form clusters rather than being distributed uniformly in the network. Therefore, a more realistic spatial model has been considered in several recent studies by modeling the locations of the D2D UEs as Poisson Cluster Process (PCP) distributed [70], [71], [72]. In [70], authors obtained expressions for the coverage probability and area spectral efficiency of an out-of-band D2D network. Performance of cluster-centric content placement in a cache-enabled D2D network was studied in [71], where the authors have considered a cluster-centric approach which optimizes the performance of the entire cluster rather than the individual D2D UEs. In-band D2D communication where the cellular and D2D networks coexist in the same frequency band was considered in [72] by combining PCP with a Poisson Hole Process (PHP). In particular, D2D UE locations are modeled by a Hole Cluster Process (HCP). However, neither of these works on D2D communication has addressed transmission in mmWave frequency bands. Network performance of D2D communication in cellular networks has been gaining even more importance in 5G networks and it is expected to be an essential part of mmWave 5G cellular networks.

In Chapter 5, we have studied the uplink performance of D2D-enabled mmWave cellular networks where the locations of both cellular and potential D2D UEs are modeled as a PPP. In other words, correlation among the locations of potential D2D UEs was not taken into account (and also beamsteering errors and area spectral efficient were not addressed in Chapter 5). In this chapter, we consider a single-tier uplink network in which the BSs and cellular UEs coexist with the potential D2D UEs. We model the locations of BSs and cellular UEs as independent homogeneous PPPs. Unlike previous works on mmWave D2D communication systems where the D2D UEs are assumed to be uniformly distributed in the network, we model the locations of potential D2D UEs as a PCP to provide a more appropriate and realistic model. Moreover, potential D2D UEs in the clusters can choose to operate in cellular and D2D mode according to a mode selection scheme. Although there is a higher possibility of operating in D2D mode due to closer distances between the UEs in the clusters, this mode selection strategy provides flexibility and generality in our analysis. Additionally, different from the previous studies on D2D communications, most of which consider only underlay or overlay types of sharing, we take into account both types of sharing strategies to show their impact on the performance of the mmWave D2D networks.

6.1.1 Main Contributions

Our main contributions can be summarized as follows:

- We provide an analytical framework to analyze the uplink performance of D2D-enabled mmWave cellular networks with clustered UEs by using tools from stochastic geometry. In particular, cellular and potential D2D UEs can coexist in the same band, and the cellular UEs are distributed uniformly and potential D2D UEs form clusters in the network.

- An expression for the probability of selecting the D2D mode for a potential D2D UE located in a cluster is derived by considering a flexible mode selection scheme. Laplace transform expressions for both cellular and D2D interference links are obtained. Using these characterizations, we derive SINR outage probability expressions for both cellular and D2D links employing the modified LOS ball model for blockage modeling, and considering Nakagami fading.

- We investigate the effect of spectrum sharing type on SINR outage probability. The effect of LOS ball model parameters is also identified. Additionally, the impact of alignment errors on the SINR outage probability is investigated to get insight on the performance in practical scenarios.

- Area spectral efficiency (ASE) of the cellular and D2D networks are determined for both underlay and overlay types of sharing. We have shown that an optimal value for the average number of simultaneously active D2D links, maximizing the ASE of D2D network, exists and this optimal value is independent of the cluster center density. Moreover, optimal spectrum partition factor is found for overlay sharing by considering the optimal weighted proportional fair spectrum partition.

6.2 System Model

In this section, the system model for D2D-communication-enabled mmWave cellular networks with clustered UEs is presented. We consider a single-tier uplink network, where BSs are spatially distributed according to an independent homogeneous PPP Φ_B with density λ_B on the Euclidean plane. UEs are categorized as cellular UEs and potential D2D UEs. Cellular UEs are distributed according to an independent homogeneous PPP Φ_{CU} with density λ_{CU}, while potential D2D UEs are clustered around the cluster centers in which the cluster centers are also distributed according to an independent homogeneous PPP Φ_C with density λ_C. For instance, cellular UEs can be regarded as pedestrians or UEs in transit which are more likely to be uniformly distributed in the network, and therefore homogeneous PPP is a better choice for the modeling of such UEs. On the other hand, potential D2D UEs are located in high UE density areas, i.e. hotspots, and are expected to be closer to each other forming clusters, and thus PCP is a more appropriate and accurate model than a homogeneous PPP. The proposed network model is shown in Fig. 6.1.

Cluster members, i.e. potential D2D UEs, are assumed to be symmetrically independently and identically distributed (i.i.d.) around the cluster center. The union of cluster members' locations form a PCP, denoted by Φ_D. In this chapter, we model Φ_D as a Thomas cluster process, where the UEs are scattered around the cluster center $x \in \Phi_C$ according to a Gaussian distribution with variance σ_d^2 and the probability density function (pdf) of a potential D2D UE's location is given by [40]

$$f_Y(y) = \frac{1}{2\pi\sigma_d^2} \exp\left(-\frac{\|y\|^2}{2\sigma_d^2}\right), \quad y \in \mathbb{R}^2. \tag{6.1}$$

where y is the UE's location relative to the cluster center and $\|\cdot\|$ is the Euclidean norm. Each potential D2D UE (i.e., each cluster member) in a cluster $x \in \Phi_C$ has the capability of establishing a direct D2D link with the cluster members in the same

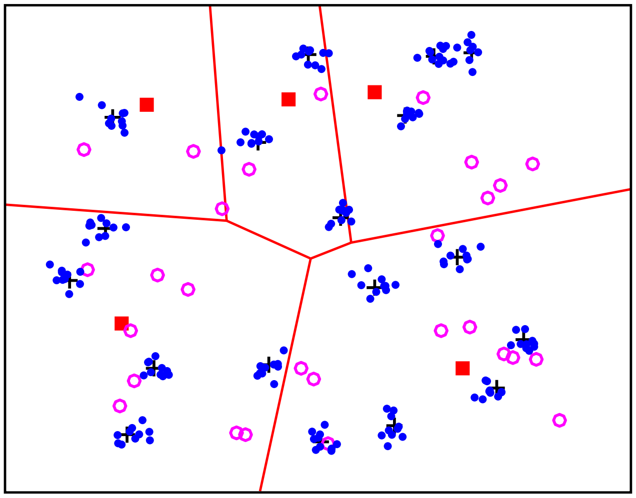

Figure 6.1: BSs (red squares) and cellular UEs (pink circles) are distributed as independent PPPs, potential D2D UEs (blue dots) are normally distributed around PPP distributed cluster centers (black plus signs). The average number of potential D2D UEs per cluster is set to 10.

cluster or they can communicate with a BS in Φ_B. Hence, potential D2D UEs can operate in one of the two modes according to the mode selection scheme: cellular and D2D mode. When operating in D2D mode, a potential D2D UE in the cluster bypasses the BS and communicates directly with its intended receiver in the same cluster. Let $\mathcal{N}^x$ denote the set of all potential D2D UEs in a cluster $x \in \Phi_C$. $\mathcal{N}^x$ can be divided into two subsets: set of possible transmitting potential D2D UEs ($\mathcal{N}_t^x$), and set of possible receiving D2D UEs ($\mathcal{N}_r^x$). The set of all simultaneously transmitting potential D2D UEs is denoted by $\mathcal{A}^x \subset \mathcal{N}_t^x$ where $|\mathcal{A}^x|$ is modeled as a Poisson distributed random variable with mean $\bar{n}$. $\mathcal{A}^x$ can also be divided into two subsets: set of simultaneously transmitting potential D2D UEs in D2D mode ($\mathcal{A}_d^x$) and set of simultaneously transmitting potential D2D UEs in cellular mode ($\mathcal{A}_c^x$) which are modeled as Poisson distributed random variables with means $\bar{n}P_{D2D}$ and $\bar{n}(1 - P_{D2D})$, respectively. [1] P_{D2D} above is the probability of potential D2D UE

---

[1] Note that there are two kinds of cellular UEs in the network: uniformly distributed cellular UEs and clustered potential D2D UEs operating in cellular mode. Locations of uniformly distributed

selecting the D2D mode, and this probability will be described and characterized in detail later in this chapter.

Without loss of generality, a typical receiving node (BS) is assumed to be located at the origin according to Slivnyak's theorem for cellular UEs and potential D2D UEs transmitting in cellular mode, and these UEs are assumed to be associated with their closest BS. The link between the BSs and cellular UEs/potential D2D UEs transmitting in cellular mode is called the cellular link, and the link between the transmitting and receiving D2D UEs in the same cluster is called the D2D link in the rest of the chapter. For the D2D link, we conduct an analysis for a typical D2D UE located at the origin, which is randomly chosen in a randomly chosen cluster. This cluster is referred to as the representative cluster centered at $x_0 \in \Phi_C$ throughout this chapter.

6.3 Transmission Strategies and Interference Characterizations

In this section, we provide characterizations for the transmission strategies and interference models. In particular, we describe two types of spectrum sharing policies between the cellular and D2D UEs, identify the interference experienced in cellular uplink and D2D links, and characterize the distributions of the link distances. Furthermore, we discuss the mode selection strategy and specify the beamforming assumptions.

---

cellular UEs follow a PPP distribution, while potential D2D UEs operating in cellular mode are clustered around the cluster centers. When we say that the set of simultaneously transmitting potential D2D UEs in cellular mode are modeled as a Poisson distributed random variable, we refer to the distribution of the *number* of simultaneously transmitting potential D2D UEs in cellular mode rather than the distribution of their *locations*.

6.3.1 Spectrum Sharing

Cellular spectrum can be shared between the cellular and D2D UEs in two different ways: underlay and overlay. In the underlay type of sharing, D2D UEs can access the channel occupied by the cellular UEs. While for the overlay type of sharing, the uplink spectrum is divided into two orthogonal portions, i.e., a fraction δ of the cellular spectrum is assigned to D2D mode and the remaining $(1 - \delta)$ fraction is used for cellular communication, where δ is the spectrum partition factor [67]. Also, parameter β is defined as the spectrum sharing indicator which is equal to one for underlay and zero for overlay type of sharing.

6.3.2 Interference Modeling

Interference in cellular uplink

The total interference in a cellular uplink experienced by a typical receiving node, i.e. the BS located at the origin, emerges from two sources: 1) interference from other cellular UEs/potential D2D UEs transmitting in cellular mode and 2) interference from other potential UEs transmitting in D2D mode (if underlay type of spectrum sharing is employed). Each cellular UE/potential D2D UE transmitting in cellular mode is assigned a unique and orthogonal channel by its associated BS which means that there is no intra-cell interference between UEs transmitting in cellular mode in the same cell. However, we assume universal frequency reuse across the entire cellular network causing inter-cell interference from the other cells' cellular UEs. Moreover, we consider a congested network scenario in which the total density of cellular UEs and potential D2D UEs in cellular mode is much higher than the density of BSs. In other words, each BS will always have at least one cellular UE to serve in the uplink channel. Different from the downlink communication, in which we can model the interfering cellular UEs and potential D2D UEs in cellular mode in different cells as a PPP with density λ_B, modeling of the cellular interference in uplink is more complicated [49]. For example, an interfering UE in uplink can be arbitrarily close to the BS, i.e., it can be closer than the UE being served. Therefore, one commonly used approach is to model the other-cell interferers in uplink as a non-homogeneous PPP Φ_c with a radially symmetric distance dependent density function given by

$$\lambda_u(t) = \lambda_{u,L}(t) + \lambda_{u,N}(t) = \sum_{j\in\{L,N\}} \lambda_B p_{j,c}(t) Q\left(t^{\alpha_{j,c}}\right) \tag{6.2}$$

where $p_{j,c}(t)$ is the LOS/NLOS probability function for the cellular link given in (6.4), and

$$Q(y) = 1 - \exp\left(- 2\pi\lambda_B \left(\int_0^{y^{1/\alpha_{L,c}}} x p_{L,c}(x)dx + \int_0^{y^{1/\alpha_{N,c}}} x p_{N,c}(x)dx \right)\right) \tag{6.3}$$

is the probability that the path loss of a cellular UE to its serving BS is smaller than y^{-1} [16]. In the underlay case, we focus on one uplink channel which is shared by the cellular and D2D UEs. Since the potential D2D UEs operating in D2D mode coexist with the cellular UEs in an uplink channel, they cause both intra-cell and inter-cell interference at the BSs. On the other hand, in the overlay case, since the uplink spectrum is divided into two orthogonal portions, there is no cross-mode interference, i.e., no interference from the D2D UEs to the cellular UEs and vice versa.

Interference in D2D link

The total interference experienced by a typical D2D UE $\in \mathcal{N}_r^{x_0}$ in the representative cluster originates from three different sources: 1) cross-mode interference caused by the other cellular UEs/potential D2D UEs transmitting in cellular mode (if underlay sharing is adopted); 2) intra-cluster interference caused by the simultaneously transmitting D2D UEs in D2D mode inside the representative cluster; and 3) inter-cluster interference caused by the simultaneously transmitting D2D UEs in D2D mode outside the representative cluster. In the overlay case, there is no cross-mode interference, i.e., no interference from the cellular UEs/potential D2D UEs transmitting in cellular mode to the D2D UEs.

6.3.3 Path-loss exponents and link distance modeling

A transmitting UE can either have a line-of-sight (LOS) or non-line-of-sight (NLOS) link to the BS or the receiving UE. In a LOS state, UE should be visible to the receiving nodes, indicating that there is no blockage in the link. On the other hand, in a NLOS state, blockage occurs in the link. Consider an arbitrary link of length r, and define the LOS probability function $p(r)$ as the probability that the link is LOS. Using field measurements and stochastic blockage models, $p(r)$ can be modeled as $e^{-\zeta r}$ where decay rate ζ depends on the building parameter and density [35]. For analytical tractability, LOS probability function $p(r)$ can be approximated by a step function. In this approach, the irregular geometry of the LOS region is replaced with its equivalent LOS ball model. In this chapter, modified LOS ball model is adopted similarly as in [16]. According to this model, the LOS probability function of a link $p_L(r)$ is equal to some constant p_L if the link distance r is less than ball radius R_B and zero otherwise. The parameters p_L and R_B depend on geographical regions. $(p_{L,c}, R_{B,c})$ and $(p_{L,d}, R_{B,d})$ are the LOS ball model parameters for cellular and D2D links, respectively[2]. Therefore, LOS and NLOS probability function for each link can be expressed as follows:

$$\begin{aligned} p_{L,\kappa}(r) &= p_{L,\kappa}\mathbf{1}(r \le R_{B,\kappa}) \\ p_{N,\kappa}(r) &= (1 - p_{L,\kappa})\mathbf{1}(r \le R_{B,\kappa}) + \mathbf{1}(r > R_{B,\kappa}) \end{aligned} \tag{6.4}$$

---

[2] Throughout the chapter, subscripts c and d denote associations with cellular and D2D links, respectively.

for $\kappa \in \{c, d\}$, where $\mathbf{1}(\cdot)$ is the indicator function. Different path loss laws are applied to LOS and NLOS links, and thus $\alpha_{L,\kappa}$ and $\alpha_{N,\kappa}$ are the LOS and NLOS path-loss exponents for $\kappa \in \{c, d\}$, respectively.

D2D communication

Regarding the distance modeling for potential D2D UEs which are assumed to be located inside the clusters, there are three types of distances: 1) D2D link distance, i.e., serving distance, 2) intra-cluster interferer distances and 3) inter-cluster interferer distances. Without loss of generality, a typical receiving D2D UE $\in \mathcal{N}_r^{x_0}$ is assumed to be located at the origin, and is associated with another D2D UE $\in \mathcal{A}_d^{x_0}$ located at y_0 chosen uniformly at random within the same cluster. It is assumed that the content of interest for this typical receiving D2D UE is available at the associated transmitting D2D UE. Note that the cluster center location is x_0 with respect to the origin (where the typical receiving D2D UE is), and transmitting D2D UE location is y_0 with respect to the cluster center. Fig. 6.2 illustrates the considered setting where the relative locations are denoted by vectors. Also, let $r_{d0} = \|x_0 + y_0\|$ denote the distance between the transmitting and typical receiving D2D UEs. Similarly, let $\{r_{d1} = \|x_0 + y\|, \forall y \in \mathcal{A}_d^{x_0} \setminus y_0\}$ denote the set of the distances from simultaneously transmitting D2D UEs in D2D mode inside the representative cluster to a typical receiving D2D UE $\in \mathcal{N}_r^{x_0}$. Distances r_{d0} and r_{d1} are also illustrated in Fig. 6.2. Note that, r_{d0} is the serving distance, and $\{r_{d1}\}$ is the set of distances from intra-cluster interfering D2D UEs. Actually, these distances are correlated due to the common factor x_0. By conditioning on $\omega_0 = \|x_0\|$ and using the fact that y_0 and $\{y\}$ are i.i.d. zero-mean Gaussian random variables with variance σ_d^2 in $\mathbb{R}^2$, the serving distance $r_{d0} = \|x_0 + y_0\|$ and the the set of distances from intra-cluster interfering D2D UEs $\{r_{d1} = \|x_0+y\|, \forall y \in \mathcal{A}_d^{x_0} \setminus y_0\}$ are conditionally i.i.d. It is shown that conditioning on ω_0 instead of x_0 is sufficient [70]. Therefore, the pdf of each distance is characterized

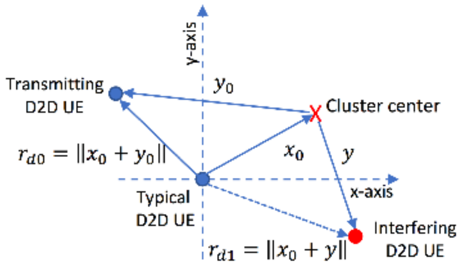

Figure 6.2: Illustration of the distances r_{d0} and r_{d1} in the representative cluster. The typical D2D UE is assumed to be located at the origin. Cluster center is located at x_0 with respect to (w.r.t.) the origin. Transmitting D2D UE is located at y_0 w.r.t. the cluster center. Intra-cluster interfering D2D UEs are located at $\{y\}$ w.r.t. the cluster center (Only one of them is shown in the figure). Arrows represent the coordinate vectors (and do not indicate the direction of communication).

by a Rician distribution [70]:

$$f_{R_{d0}}(r_{d0}|\omega_0) = \text{Ricepdf}(r_{d0}, \omega_0; \sigma_d^2) \tag{6.5}$$

$$f_{R_{d1}}(r_{d1}|\omega_0) = \text{Ricepdf}(r_{d1}, \omega_0; \sigma_d^2) \tag{6.6}$$

where $\text{Ricepdf}(a, b; \sigma_d^2) = \frac{a}{\sigma_d^2}\exp(-\frac{a^2+b^2}{2\sigma_d^2})I_0(\frac{ab}{\sigma_d^2})$ and $I_0(\cdot)$ is the modified Bessel function of the first kind with order zero. Similarly, let $\{r_{d2} = \|x + y\|, \forall y \in \mathcal{A}_d^x\}$ denote the set of the distances from simultaneously transmitting D2D UEs in D2D mode in the other clusters to a typical D2D UE $\in \mathcal{N}_r^{x_0}$, i.e., $\{r_{d2}\}$ is the set of distances from inter-cluster interfering D2D UEs. By conditioning on $\omega = \|x\|$, the pdf of each distance is given by $f_{R_{d2}}(r_{d2}|\omega) = \text{Ricepdf}(r_{d2}, \omega; \sigma_d^2)$.

Cellular communication

Recall that cellular UEs and potential D2D UEs transmitting in cellular mode are assumed to be associated with their closest BS, and therefore, given the typical cellular UE observes at least one LOS/NLOS BS, the pdf of the cellular link distance r_c to the nearest LOS/NLOS BS is given by [9]

$$f_s(r_c) = 2\pi\lambda_B r_c p_{s,c}(r_c) e^{-2\pi\lambda_B \psi_s(r_c)} / \mathcal{B}_{s,c} \tag{6.7}$$

for $s \in \{L, N\}$, where $\psi_s(r_c) = \int_0^{r_c} x p_{s,c}(x) dx$, $\mathcal{B}_{s,c} = 1 - e^{-2\pi\lambda_B \int_0^\infty x p_{s,c}(x) dx}$ is the probability that a UE has at least one LOS/NLOS BS, and $p_{s,c}(x)$ is given in (6.4) for $s \in \{L, N\}$. The pdf given in (6.7) is a modified Rayleigh pdf by considering LOS/NLOS transmissions and it is the pdf of the distance between two PPP distributed nodes. Since both BSs and cellular UEs are distributed according to independent PPPs, we employ this pdf distribution in our calculations. Recall that cellular uplink analysis is performed for a typical BS which is assumed to be located at the origin. However, there is no guarantee that there exists a BS at the origin due to the randomness of PPP distribution. Moreover, locations of cellular UEs and BSs are correlated due to the structure of Poisson-Voronoi tessellation, i.e., a cellular UE should lie in the same cell with its serving BS [73], [74]. Therefore, pdf given in (6.7) is just an approximation for the uplink. Indeed, pdf given in (6.7) is also an approximation for modeling the distance between the potential D2D UEs transmitting in cellular mode to the closest BS. Potential D2D UEs are distributed according to a PCP around the cluster centers in which the cluster centers are PPP distributed. However, a very good match between analytical results and simulation results, in which do not assume any distributions for the distances, verifies that this assumption is quite reasonable for both cellular UEs and potential D2D UEs in cellular mode especially for small values of the scattering variance σ_d^2.

Let $\{r_{y_x} = \|x+y\|, \forall x \in \Phi_C, \forall y \in \mathcal{A}_d^x\}$ be the set of distances from the cross-mode interferers, i.e. D2D UEs, to a typical BS at the origin. Then, the pdf of each distance is given by $f_{R_{y_x}}(r_{y_x}|\omega) = \text{Ricepdf}(r_{y_x}, \omega; \sigma_d^2)$ where $\omega = \|x\|$.

6.3.4 Mode Selection

In this work, a flexible mode selection scheme similarly as in [69] is considered. In this scheme, a potential D2D UE chooses the D2D mode if the biased D2D link quality is at least as good as the cellular uplink quality. In other words, a potential D2D UE will operate in D2D mode if $T_d r_d^{-\alpha_{s,d}} \geq r_c^{-\alpha_{s,c}}$, where $T_d \in [0, \infty)$ is the biasing factor, and r_c and r_d are the cellular and D2D link distances, respectively. Biasing factor T_d has two extremes, $T_d = 0$ and $T_d \rightarrow \infty$. In the first extreme case, D2D communication is disabled, while in the second case, each potential D2D UE is forced to select the D2D mode. Let P_{D2D} denote the probability of selecting the D2D mode. Therefore, the uplink transmission with probability $(1 - P_{D2D})$ means that a potential D2D has a better link quality towards the serving BS. For example, a BS can be closer to the potential D2D UE than another receiving D2D UE or it can be LOS while the receiving D2D UE is NLOS.

In the calculation of the probability of selecting D2D mode, analysis is conducted for a potential D2D UE located in a cluster $x \in \Phi_C$ and this potential D2D UE is assumed to be located at the origin. This potential D2D UE can be associated with another D2D UE located at y with respect to the cluster center within the same cluster, or it can be associated with its closest BS at a distance r_c. Since the cellular link distance is the distance from a potential D2D UE located at the origin to its closest BS, the pdf of the cellular link distance r_c is given by (6.7). Regarding the D2D link distance, since the other D2D UE is located at y with respect to the cluster center and potential D2D UE is at the origin, D2D link distance is given by $r_d = \|x + y\|$. By conditioning on $\omega = \|x\|$ and using the fact that y is a zero-mean Gaussian random variable with variance σ_d^2 in $\mathbb{R}^2$ whose pdf is given by (6.1), the pdf of the D2D link distance is characterized by a Rician distribution $f_{R_d}(r_d|\omega) = \text{Ricepdf}(r_d, \omega; \sigma_d^2)$. As discussed in [70], conditioning on w instead of x is sufficient, and the pdf of w is given by Rayleigh pdf $f_\Omega(\omega) = \frac{\omega}{\sigma_d^2} \exp(-\frac{\omega^2}{2\sigma_d^2})$. The probability of selecting D2D mode,

P_{D2D}, is provided in the following Lemma.

Lemma 6.1 *Probability of selecting D2D mode for a potential D2D UE located in a cluster* $x \in \Phi_C$ *is*

$$P_{D2D} = \sum_{s\in\{L,N\}} \sum_{s'\in\{L,N\}} \int_0^\infty \int_0^\infty e^{-2\pi\lambda_B \psi_s\left(r_d^{\alpha_{s',d}/\alpha_{s,c}} / T_d^{1/\alpha_{s,c}}\right)} f_{R_d}(r_d|\omega) f_\Omega(\omega) p_{s',d}(r_d) dr_d d\omega \tag{6.8}$$

where $\psi_s(a) = \int_0^a x p_{s,c}(x)dx$, $p_{s,c}(x)$ *and* $p_{s',d}(r_d)$ *are given in (6.4),* $f_{R_d}(r_d|\omega) = \mathit{Ricepdf}(r_d, \omega; \sigma_d^2)$, *and* $f_\Omega(\omega) = \frac{\omega}{\sigma_d^2}\exp(-\frac{\omega^2}{2\sigma_d^2})$.

Proof: See Appendix D.

6.3.5 Directional beamforming

Antenna arrays at the BSs and UEs are assumed to perform directional beamforming where the main lobe being directed towards the dominant propagation path while smaller side lobes direct energy in other directions. For tractability in the analysis and similar to [9], [32], [43], [13], antenna arrays are approximated by a sectored antenna model [34]. The array gains are assumed to be constant M_ν for all angles in the main lobe and another smaller constant m_ν in the side lobe for $\nu \in \{\mathrm{BS}_0, \mathrm{UE}\}$. Initially, perfect beam alignment [3] is assumed in between the transmitting nodes (e.g., cellular or potential D2D UEs) and receiving nodes (e.g., BSs or receiving D2D UEs), leading to an overall antenna gain of $M_{\mathrm{BS}_0}M_{\mathrm{UE}}$ for cellular link and $M_{\mathrm{UE}}M_{\mathrm{UE}}$ for D2D link. In other words, maximum directivity gain can be achieved for the intended link by assuming that the transmitting node and receiving node can adjust their antenna steering orientation using the estimated angles of arrivals. Also, the beam direction of the interfering nodes is modeled as a uniform random variable on $[0, 2\pi)$. Therefore, the effective antenna gain is a discrete random variable (RV) described by

---

[3] Subsequently, beamsteering errors are also addressed.

$$G = \begin{cases} M_l M_{\mathrm{UE}} & \text{w. p. } p_{M_l M_{\mathrm{UE}}} = \frac{\theta_l}{2\pi}\frac{\theta_{\mathrm{UE}}}{2\pi} \\ M_l m_{\mathrm{UE}} & \text{w. p. } p_{M_l m_{\mathrm{UE}}} = \frac{\theta_l}{2\pi}\frac{2\pi-\theta_{\mathrm{UE}}}{2\pi} \\ m_l M_{\mathrm{UE}} & \text{w. p. } p_{m_l M_{\mathrm{UE}}} = \frac{2\pi-\theta_l}{2\pi}\frac{\theta_{\mathrm{UE}}}{2\pi} \\ m_l m_{\mathrm{UE}} & \text{w. p. } p_{m_l m_{\mathrm{UE}}} = \frac{2\pi-\theta_l}{2\pi}\frac{2\pi-\theta_{\mathrm{UE}}}{2\pi} \end{cases} \tag{6.9}$$

for $l \in \{\mathrm{BS}_0, \mathrm{UE}\}$, where θ_ν is the beam width of the main lobe for $\nu \in \{\mathrm{BS}_0, \mathrm{UE}\}$, and p_G is the probability of having an antenna gain of G.

6.4 Analysis of Uplink SINR Outage Probability

In this section, we first develop a theoretical framework to analyze the uplink SINR outage probability for a generic UE operating in cellular mode or D2D mode using stochastic geometry. Although a biasing-based mode selection scheme is considered for selecting between D2D and cellular modes, the developed framework can also be applied to different mode selection schemes.

6.4.1 Signal-to-Interference-plus-Noise Ratio (SINR)

Recall that, without loss of generality, we consider a typical receiving node (BS or D2D UE $\in \mathcal{N}_r^{x_0}$ in the representative cluster) located at the origin. Therefore, the SINR experienced at a typical receiving node in cellular and D2D modes, respectively, for underlay spectrum sharing can be written as

$$SINR^c = \frac{P_c G_0 h_0 r_c^{-\alpha_c(r_c)}}{\sigma_N^2 + \underbrace{\sum_{i \in \Phi_c} P_c G_i h_i r_i^{-\alpha_c(r_i)}}_{I_{cc}} + \underbrace{\sum_{x \in \Phi_C} \sum_{y \in \mathcal{A}_d^x} P_d G_{y_x} h_{y_x} r_{y_x}^{-\alpha_d(r_{y_x})}}_{I_{dc}}} \tag{6.10}$$

$$SINR^d =$$

$$\frac{P_d G_0 h_0 r_{d0}^{-\alpha_d(r_{d0})}}{\sigma_N^2 + \underbrace{\sum_{i\in\Phi_c} P_c G_i h_i r_i^{-\alpha_c(r_i)}}_{I_{cd}} + \underbrace{\sum_{y\in\mathcal{A}_d^{x_0}\backslash y_0} P_d G_{y_{x_0}} h_{y_{x_0}} r_{d1}^{-\alpha_d(r_{d1})}}_{I_{dd_{\text{intra}}}} + \underbrace{\sum_{x\in\Phi_C\backslash x_0}\sum_{y\in\mathcal{A}_d^x} P_d G_{y_x} h_{y_x} r_{d2}^{-\alpha_d(r_{d2})}}_{I_{dd_{\text{inter}}}}} \tag{6.11}$$

where P_κ is the transmit power of the UE operating in mode $\kappa \in \{c, d\}$, G_0 is the effective antenna gain of the link which is assumed to be equal to $M_{\text{BS}_0} M_{\text{UE}}$ for cellular link and $M_{\text{UE}} M_{\text{UE}}$ for D2D link, h_0 is the small-scale fading gain, $\alpha_\kappa(\cdot)$ is the path-loss exponent of the link, which depends on whether the link is LOS on NLOS, r_c and r_{d0} are the cellular and D2D link distances, respectively, σ_N^2 is the variance of the additive white Gaussian noise component, $I_{c\kappa}$ is the aggregate interference at the receiving node from cellular UEs using the same uplink channel in different cells, which constitute a non-homogeneous PPP Φ_c with density function given in (6.2), and $I_{d\kappa}$ is the aggregate interference at the receiving node from D2D UEs located inside the clusters (hence including both inter-cell and intra-cell D2D UEs). For the D2D link, I_{dd} has two components: intra-cluster interference $I_{dd_{\text{intra}}}$ and inter-cluster interference $I_{dd_{\text{inter}}}$. A similar notation is used for I_{cc}, I_{cd}, I_{dc}, $I_{dd_{\text{intra}}}$ and $I_{dd_{\text{inter}}}$, but note that the effective antenna gains G_i, G_{y_x} and $G_{y_{x_0}}$, and path loss exponents $\alpha_\kappa(\cdot)$ are different for different interfering links as described in Section 6.3.5 and Section 6.3.3, respectively. While small-scale fading has a relatively minor impact in mmWave cellular networks according to the recent channel measurements [3], independent Nakagami fading is commonly used in the analysis of mmWave cellular networks [16]. Therefore, we assume that all links are subject to independent Nakagami fading, i.e., small-scale fading gains denoted by h have a gamma distribution. Parameters of Nakagami fading are N_L and N_N for LOS and NLOS links, respectively, and they are assumed to be positive integers for simplicity. When $N_L = N_N = 1$, the Nakagami fading specializes to Rayleigh fading.

The above description implicitly assumes underlay spectrum sharing between cellular and D2D UEs. Note that since there is no cross-mode interference in the overlay case, the SINR expression in this case reduces to $SINR^c = \frac{P_c G_0 h_0 r_c^{-\alpha_c(r_c)}}{\sigma_N^2 + I_{cc}}$, and $SINR^d = \frac{P_d G_0 h_0 r_{d0}^{-\alpha_d(r_{d0})}}{\sigma_N^2 + I_{dd_{\text{intra}}} + I_{dd_{\text{inter}}}}$, for mode $\kappa \in \{c, d\}$.

6.4.2 Laplace Transform of Interferences

Before conducting the outage probability analysis, we first provide the Laplace transform expressions for each interference component. The thinning property of Poisson processes can be employed to split the interference component I_χ for $\chi \in \{cc, dc, cd, dd_{\text{intra}}, dd_{\text{inter}}\}$ into 8 independent PPPs or PCPs as follows:

$$\begin{aligned} I_\chi &= I_{\chi,L} + I_{\chi,N} \\ &= \sum_{G \in \left\{ \substack{M_l M_{\text{UE}}, M_l m_{\text{UE}}, \\ m_l M_{\text{UE}}, m_l m_{\text{UE}}} \right\}} \sum_{j \in \{L,N\}} I^G_{\chi,j}, \end{aligned} \tag{6.12}$$

for $l \in \{\text{BS}_0, \text{UE}\}$, where $I_{\chi,L}$ and $I_{\chi,N}$ are the aggregate LOS and NLOS interferences, and $I^G_{\chi,j}$ denotes the interference for $j \in \{L, N\}$ with random antenna gain G defined in (6.9). According to the thinning theorem, each independent nonhomogeneous PPP has a density of $\lambda_B p_{j,c}(t) Q(t^{\alpha_{j,c}}) p_G$ for $\chi = \{cc, cd\}$ where $Q(y)$ is given in (6.3) and p_G is given in (6.9) for each antenna gain G. Thinning theorem can also be applied for clustered potential D2D UEs. To thin the interferences $I^G_{\chi,j}$ for $\chi = \{dc, dd_{\text{inter}}\}$, where the interference is from the potential D2D UEs in D2D mode, number of interfering D2D UEs is thinned by multiplying p_G with $\bar{n}P_{D2D}$ where $\bar{n}P_{D2D}$ is the mean number of simultaneously transmitting potential D2D UEs in D2D mode. Similarly, for intra-cluster interference on D2D link, i.e. $I_{dd_{\text{intra}}}$, number of interfering D2D UEs is thinned by multiplying p_G with $\bar{n}P_{D2D}-1$. Note that, for interfering cellular UEs and potential D2D UEs in cellular mode, i.e., interference component forming PPP, p_G is obtained for $l = \mathrm{BS}_0$, while for interfering potential D2D UEs in D2D mode, i.e., interference components forming PCP, p_G is obtained for $l = \mathrm{UE}$.

Inserting (6.12) into the Laplace transform expression and using the definition of the Laplace transform yield

$$\begin{aligned}\mathcal{L}_{I_\chi}(v) &= \mathbb{E}_{I_\chi}[e^{-vI_\chi}] = \mathbb{E}_{I_\chi}[e^{-v(I_{\chi,L}+I_{\chi,N})}] \\ &\overset{(a)}{=} \mathbb{E}_{I_{\chi,L}}\left[e^{-v\sum_G I^G_{\chi,L}}\right]\mathbb{E}_{I_{\chi,N}}\left[e^{-v\sum_G I^G_{\chi,N}}\right] \\ &= \prod_G\prod_j \mathbb{E}_{I^G_{\chi,j}}\left[e^{-vI^G_{\chi,j}}\right] \\ &= \prod_G\prod_j \mathcal{L}_{I^G_{\chi,j}}(v), \end{aligned} \tag{6.13}$$

where $G \in \{M_lM_{\mathrm{UE}}, M_lm_{\mathrm{UE}}, m_lM_{\mathrm{UE}}, m_lm_{\mathrm{UE}}\}$ for $l \in \{\mathrm{BS}_0, \mathrm{UE}\}$, $j \in \{L, N\}$, and (a) follows from the fact that $I_{\chi,L}$ and $I_{\chi,N}$ are interferences generated from two independent thinned PPPs or PCPs.

Laplace transform expressions for each interference component are provided in the following Lemmas.

Lemma 6.2 *Laplace transform of the aggregate interference at the BS from cellular UEs using the same uplink channel in different cells is given by*

$$\mathcal{L}_{I_{cc}}(v) = \exp\left(-2\pi\lambda_B \sum_{j\in\{L,N\}}\sum_{i=1}^{4} p_{G_i}\int_0^\infty \Psi\left(N_j, \frac{vP_cG_it^{-\alpha_{j,c}}}{N_j}\right) Q\left(t^{\alpha_{j,c}}\right) p_{j,c}(t)tdt\right) \tag{6.14}$$

where $\Psi(N,x) = 1-1/(1+x)^N$, $v = \frac{n\eta_s\Gamma r_c^{\alpha_{s,c}}}{P_cG_0}$. $\eta_s = N_s(N_s!)^{-\frac{1}{N_s}}$, N_s *are the parameters of the Nakagami small scale fading for* $s \in \{L,N\}$, $Q(y)$ *is given in (6.3) and* $p_{j,c}(t)$ *is the LOS/NLOS probability function for the cellular link given in (6.4).*

Proof: See Appendix E.

Lemma 6.3 *Laplace transform of the aggregate interference at the BS from both intra-cell and inter-cell D2D UEs operating in D2D mode is given by*

$$\mathcal{L}_{I_{dc}}(v) = \exp\Bigg(- 2\pi\lambda_C \sum_{j\in\{L,N\}} \int_0^\infty \Bigg(1 - \exp\Bigg(- \bar{n}P_{D2D} \sum_{i=1}^{4} p_{G_i} \int_0^\infty \Psi\left(N_j, \frac{vP_dG_iu^{-\alpha_{j,d}}}{N_j}\right) f_U(u|w)p_{j,d}(u)du\Bigg)\Bigg)wdw\Bigg) \tag{6.15}$$

which can be lower bounded by

$$\mathcal{L}_{I_{dc}}(v) \geq \exp\Bigg(- 2\pi\lambda_C\bar{n}P_{D2D} \sum_{j\in\{L,N\}} \sum_{i=1}^{4} p_{G_i} \int_0^\infty \Psi\left(N_j, \frac{vP_dG_iu^{-\alpha_{j,d}}}{N_j}\right) p_{j,d}(u)udu\Bigg) \tag{6.16}$$

where $\Psi(N,x) = 1 - 1/(1+x)^N$, $v = \frac{n\eta_s\Gamma r_c^{\alpha_{s,c}}}{P_cG_0}$, $\eta_s = N_s(N_s!)^{-\frac{1}{N_s}}$, $p_{j,d}(u)$ *is the LOS/NLOS probability function for the D2D link given in (6.4).*

Proof: See Appendix F.

Lemma 6.4 *Laplace transform of the aggregate interference at the typical D2D UE from cellular UEs using the same uplink channel in different cells is given by*

$$\mathcal{L}_{I_{cd}}(v) = \exp\Bigg(- 2\pi\lambda_B \sum_{j\in\{L,N\}} \sum_{i=1}^{4} p_{G_i} \int_0^\infty \Psi\left(N_j, \frac{vP_cG_it^{-\alpha_{j,c}}}{N_j}\right) Q\left(t^{\alpha_{j,c}}\right) p_{j,c}(t)tdt\Bigg) \tag{6.17}$$

where $\Psi(N,x) = 1 - 1/(1+x)^N$, $v = \frac{n\eta_s\Gamma r_{d0}^{\alpha_{s,d}}}{P_dG_0}$, $\eta_s = N_s(N_s!)^{-\frac{1}{N_s}}$, $Q(y)$ *is given in (6.3) and* $p_{j,c}(t)$ *is the LOS/NLOS probability function for the cellular link given in (6.4).*

Proof: Proof follows similar steps as in the proof of Lemma 6.2.

Lemma 6.5 *Laplace transform of the intra-cluster interference at the typical D2D*

UE $\in \mathcal{N}_r^{x_0}$ *in the representative cluster is given by*

$$\mathcal{L}_{I_{dd_{intra}}}(v|w_0) = \exp\Bigg(- (\bar{n}P_{D2D} - 1) \sum_{j\in\{L,N\}} \sum_{i=1}^{4} p_{G_i} \times \int_0^\infty \Psi\left(N_j, \frac{vP_dG_iu^{-\alpha_{j,d}}}{N_j}\right) f_U(u|w_0)p_{j,d}(u)du\Bigg) \tag{6.18}$$

where $\Psi(N,x) = 1 - 1/(1+x)^N$, $v = \frac{n\eta_s\Gamma r_{d0}^{\alpha_{s,d}}}{P_dG_0}$, $\eta_s = N_s(N_s!)^{-\frac{1}{N_s}}$, *and* $p_{j,d}(u)$ *is the LOS/NLOS probability function for the D2D link given in (6.4).*

Proof: See Appendix G.

Lemma 6.6 *Laplace transform of the inter-cluster interference at the typical UE* $\in \mathcal{N}_r^{x_0}$ *in the representative cluster is given by*

$$\mathcal{L}_{I_{dd_{inter}}}(v) = \exp\Bigg(- 2\pi\lambda_C \sum_{j\in\{L,N\}} \int_0^\infty \Bigg(1 - \exp\Bigg(- \bar{n}P_{D2D} \times \sum_{i=1}^{4} p_{G_i} \int_0^\infty \Psi\left(N_j, \frac{vP_dG_iu^{-\alpha_{j,d}}}{N_j}\right) f_U(u|w)p_{j,d}(u)du\Bigg)\Bigg)wdw\Bigg) \tag{6.19}$$

which can be lower bounded by

$$\mathcal{L}_{I_{dd_{inter}}}(v) \geq \exp\Bigg(- 2\pi\lambda_C\bar{n}P_{D2D} \sum_{j\in\{L,N\}} \sum_{i=1}^{4} p_{G_i} \int_0^\infty \Psi\left(N_j, \frac{vP_dG_iu^{-\alpha_{j,d}}}{N_j}\right) p_{j,d}(u)udu\Bigg) \tag{6.20}$$

where $\Psi(N,x) = 1 - 1/(1+x)^N$, $v = \frac{n\eta_s\Gamma r_{d0}^{\alpha_{s,d}}}{P_dG_0}$, $\eta_s = N_s(N_s!)^{-\frac{1}{N_s}}$, *and* $p_{j,d}(u)$ *is the LOS/NLOS probability function for the D2D link given in (6.4).*

Proof: Proof follows similar steps as in the proof of 6.3.

6.4.3 Uplink SINR Outage Probability

The uplink SINR outage probability $\mathrm{P}_{\mathrm{out}}$ is defined as the probability that the received SINR is less than a certain threshold $\Gamma > 0$, i.e., $\mathrm{P}_{\mathrm{out}} = \mathbb{P}(\mathrm{SINR} < \Gamma)$. The outage probability for a typical UE in cellular mode is given in the following theorem.

Theorem 6.1 *: In a single-tier D2D-communication-enabled mmWave cellular network, the outage probability for a typical cellular UE can be expressed as*

$$P^{c}_{out}(\Gamma) \approx \sum_{s\in\{L,N\}} \int_0^\infty \sum_{n=0}^{N_s} (-1)^n \binom{N_s}{n} e^{-\frac{n\eta_s\Gamma r_c^{\alpha_{s,c}}\sigma_N^2}{P_c G_0}} \mathcal{L}_{I_{cc}}\left(\frac{n\eta_s\Gamma r_c^{\alpha_{s,c}}}{P_c G_0}\right) \\ \times \mathcal{L}_{I_{dc}}\left(\frac{\beta n\eta_s\Gamma r_c^{\alpha_{s,c}}}{P_c G_0}\right) f_s(r_c)\mathcal{B}_{s,c} dr_c \tag{6.21}$$

where the Laplace transforms $\mathcal{L}_{I_{cc}}(v)$ and $\mathcal{L}_{I_{dc}}(\beta v)$ are given in Lemma 6.2 and Lemma 6.3, respectively, $\eta_s = N_s(N_s!)^{-\frac{1}{N_s}}$ and $f_s(r_c)$ is the pdf of the cellular link distance given in (6.7).

Proof: See Appendix H.

Theorem 6.2 *: In a single-tier D2D-communication-enabled mmWave cellular network, the outage probability for a typical D2D UE can be expressed as*

$$P^{d}_{out}(\Gamma) \approx \sum_{s\in\{L,N\}} \int_0^\infty \sum_{n=0}^{N_s} (-1)^n \binom{N_s}{n} e^{-\frac{n\eta_s\Gamma r_{d0}^{\alpha_{s,d}}\sigma_N^2}{P_d G_0}} \mathcal{L}_{I_{dd_{intra}}}\left(\frac{n\eta_s\Gamma r_{d0}^{\alpha_{s,d}}}{P_d G_0}|w_0\right) \\ \times \mathcal{L}_{I_{dd_{inter}}}\left(\frac{n\eta_s\Gamma r_{d0}^{\alpha_{s,d}}}{P_d G_0}\right) \mathcal{L}_{I_{cd}}\left(\frac{\beta n\eta_s\Gamma r_{d0}^{\alpha_{s,d}}}{P_d G_0}\right) p_{s,d}(r_{d0}) f_{R_{d0}}(r_{d0}|w_0) f_{\Omega_0}(w_0) dr_{d0} dw_0 \tag{6.22}$$

where the Laplace transforms $\mathcal{L}_{I_{dd_{intra}}}(v|w_0)$, $\mathcal{L}_{I_{dd_{inter}}}(v)$ and $\mathcal{L}_{I_{cd}}(\beta v)$ are given in Lemma 6.4, Lemma 6.5 and Lemma 6.6, respectively, $\eta_s = N_s(N_s!)^{-\frac{1}{N_s}}$, $p_{s,d}(r_{d0})$ is the LOS/NLOS probability function for D2D link given in (6.4), $f_{R_{d0}}(r_{d0}|w_0)$ is the pdf of the D2D link distance given in (6.5), and $f_{\Omega_0}(\omega_0) = \frac{\omega_0}{\sigma_d^2}\exp(-\frac{\omega_0^2}{2\sigma_d^2})$.

Proof: Proof follows similar steps as in the proof of Theorem 6.1, and the details are omitted for the sake of brevity.

We also note that the result of Theorem 6.1 and Theorem 6.2 are approximations due to the tail probability of a gamma random variable.

6.4.4 Uplink SINR Outage Probability Analysis with Power Control

According to the recent studies, the uplink transmit power in mmWave networks is expected to be even smaller than that of the networks transmitting in sub-6GHz frequency bands [16]. In these cases, power control may not be employed. Hence, considering such scenarios, in the preceding analysis UEs are assumed to be transmitting with constant power in uplink. At the same time, as the reviewer has suggested, outage probability analysis presented in Section 6.4.3 can be extended to incorporate power control for this uplink mmWave network. In this section, we describe how we can obtain the outage probabilities with power control.

We assume that both cellular UEs and potential D2D UEs employ a distance-based fractional power control of the form $P_\kappa r^{\alpha_\kappa(r)\tau}$, where $\tau \in [0,1]$ is the power control factor, P_κ and $\alpha_\kappa(r)$ are the transmit power and the path loss exponent of the UE operating in mode $\kappa \in \{c,d\}$, respectively. With the power control, the SINR experienced at a typical receiving node in cellular and D2D modes, respectively, for underlay spectrum sharing can be rewritten as

$$SINR^c = \frac{P_c G_0 h_0 r_c^{\alpha_c(r_c)(\tau-1)}}{\sigma_N^2 + \underbrace{\sum_{i\in\Phi_c} P_c G_i h_i d_i^{\tau\alpha_c(d_i)} r_i^{-\alpha_c(r_i)}}_{I_{cc}} + \underbrace{\sum_{x\in\Phi_C}\sum_{y\in\mathcal{A}_d^x} P_d G_{y_x} h_{y_x} d_{y_x}^{\tau\alpha_d(d_{y_x})} r_{y_x}^{-\alpha_d(r_{y_x})}}_{I_{dc}}} \tag{6.23}$$

$$SINR^d = \frac{P_d G_0 h_0 r_{d0}^{-\alpha_d(r_{d0})(\tau-1)}}{\sigma_N^2 + \underbrace{\sum_{i\in\Phi_c} P_c G_i h_i d_i^{\tau\alpha_c(d_i)} r_i^{-\alpha_c(r_i)}}_{I_{cd}} + \underbrace{\sum_{y\in\mathcal{A}_d^{x0}\setminus y_0} P_d G_{y_{x_0}} h_{y_{x_0}} d_{d1}^{\tau\alpha_d(d_{d1})} r_{d1}^{-\alpha_d(r_{d1})}}_{I_{dd_{\text{intra}}}} + \underbrace{\sum_{x\in\Phi_C\setminus x_0}\sum_{y\in\mathcal{A}_d^x} P_d G_{y_x} h_{y_x} d_{d2}^{\tau\alpha_d(d_{d2})} r_{d2}^{-\alpha_d(r_{d2})}}_{I_{dd_{\text{inter}}}}} \tag{6.24}$$

where r_i and d_i denote the distance between the typical BS and the interfering UE in cellular mode and the distance of an interfering UE in cellular mode to its own serving BS, respectively, r_{y_x} and d_{y_x} denote the distance between the typical BS and the interfering UE in D2D mode and the distance of an interfering UE in D2D mode to its own receiving D2D UE in the same cluster, respectively. Similar notation is used for the distances in the SINR received at the typical D2D UE. All of these distances are random, hence, we need to average over these distances in the calculation of Laplace transforms. The pdf of the distances can be easily modeled similar to the other pdfs. Finally, similar steps in Section 6.4.3 can be followed to obtain the uplink SINR outage probabilities.

6.4.5 Uplink SINR Outage Probability Analysis In the Presence of Beamsteering Errors

In Section 6.4.3 and the preceding analysis, antenna arrays at the transmitting nodes (cellular or potential D2D UEs) and receiving nodes (BSs or UEs) are assumed to be aligned perfectly and uplink SINR outage probabilities are calculated in the absence of beamsteering errors. However, in practice, it may not be easy to have perfect alignment. Therefore, in this section, we investigate the effect of beamforming alignment errors on the outage probability analysis. We employ an error model similar to that in [43]. Let $|\epsilon|$ be the random absolute beamsteering error of the transmitting node toward the receiving node with zero-mean and bounded absolute error $|\epsilon|_{\max} \leq \pi$. Due to the symmetry in the gain G_0, it is appropriate to consider the absolute beamsteering error. The pdf of the effective antenna gain G_0 with alignment error can be explicitly written as [13]

$$\begin{aligned} f_{G_0}(\mathrm{g}) &= F_{|\epsilon|}\left(\frac{\theta_l}{2}\right) F_{|\epsilon|}\left(\frac{\theta_{\mathrm{UE}}}{2}\right) \delta(\mathrm{g} - M_l M_{\mathrm{UE}}) \\ &+ F_{|\epsilon|}\left(\frac{\theta_l}{2}\right)\left(1 - F_{|\epsilon|}\left(\frac{\theta_{\mathrm{UE}}}{2}\right)\right) \delta(\mathrm{g} - M_l m_{\mathrm{UE}}) \\ &+ \left(1 - F_{|\epsilon|}\left(\frac{\theta_l}{2}\right)\right) F_{|\epsilon|}\left(\frac{\theta_{\mathrm{UE}}}{2}\right) \delta(\mathrm{g} - m_l M_{\mathrm{UE}}) \\ &+ \left(1 - F_{|\epsilon|}\left(\frac{\theta_l}{2}\right)\right)\left(1 - F_{|\epsilon|}\left(\frac{\theta_{\mathrm{UE}}}{2}\right)\right) \delta(\mathrm{g} - m_l m_{\mathrm{UE}}), \end{aligned} \tag{6.25}$$

for $l \in \{\mathrm{BS}_0, \mathrm{UE}\}$ where $\delta(\cdot)$ is the Kronecker's delta function, $F_{|\epsilon|}(x)$ is the CDF of the misalignment error and (6.25) follows from the definition of CDF, i.e., $F_{|\epsilon|}(x) = \mathbb{P}\{|\epsilon| \leq x\}$. Assume that the error ϵ is Gaussian distributed, and therefore the absolute error $|\epsilon|$ follows a half normal distribution with $F_{|\epsilon|}(x) = \mathrm{erf}(x/(\sqrt{2}\sigma_{\mathrm{BE}}))$, where $\mathrm{erf}(\cdot)$ denotes the error function and σ_{BE} is the standard deviation of the Gaussian error ϵ.

It is clear that the uplink SINR outage probability expressions in Section 6.4.3 depend on the effective antenna gain G_0 between the transmitting and the receiving nodes. Thus, uplink SINR outage probability $\mathrm{P}^{\kappa}_{\mathrm{out}}(\Gamma)$ for a typical UE in mode $\kappa \in \{c, d\}$ can be calculated by averaging over the distribution of G_0, $f_{G_0}(\mathrm{g})$, as follows:

$$\begin{aligned} \mathrm{P}^{\kappa}_{\mathrm{out}}(\Gamma) &= \int_0^{\infty} \mathrm{P}^{\kappa}_{\mathrm{out}}(\Gamma; g) f_{G_0}(\mathrm{g}) d\mathrm{g} \\ &= F_{|\epsilon|}(\theta_l/2) F_{|\epsilon|}(\theta_{\mathrm{UE}}/2) \mathrm{P}^{\kappa}_{\mathrm{out}}(\Gamma; M_l M_{\mathrm{UE}}) \\ &+ F_{|\epsilon|}(\theta_l/2) \bar{F}_{|\epsilon|}(\theta_{\mathrm{UE}}/2) \mathrm{P}^{\kappa}_{\mathrm{out}}(\Gamma; M_l m_{\mathrm{UE}}) \\ &+ \bar{F}_{|\epsilon|}(\theta_l/2) F_{|\epsilon|}(\theta_{\mathrm{UE}}/2) \mathrm{P}^{\kappa}_{\mathrm{out}}(\Gamma; m_l M_{\mathrm{UE}}) \\ &+ \bar{F}_{|\epsilon|}(\theta_l/2) \bar{F}_{|\epsilon|}(\theta_{\mathrm{UE}}/2) \mathrm{P}^{\kappa}_{\mathrm{out}}(\Gamma; m_l m_{\mathrm{UE}}), \end{aligned} \tag{6.26}$$

for $l \in \{\mathrm{BS}_0, \mathrm{UE}\}$ where we define $\bar{F}_{|\epsilon|}(\theta/2) = 1 - F_{|\epsilon|}(\theta/2)$.

6.5 Analysis of Area Spectral Efficiency

In Section 6.4, we have analyzed the uplink outage probability and obtained outage probability expressions for a typical cellular and D2D link. In this section, we consider another performance metric, namely area spectral efficiency (ASE), to measure the network capacity. ASE is defined as the average number of bits transmitted per unit time per unit bandwidth per unit area. ASE for both cellular and D2D networks can be mathematically defined as follows:

$$\mathrm{ASE}_c = \lambda_B(1 - \mathrm{P}^c_{\mathrm{out}}(\Gamma)) \log_2(1 + \Gamma) \tag{6.27}$$

$$\mathrm{ASE}_d = \bar{n} P_{D2D} \lambda_C (1 - \mathrm{P}^d_{\mathrm{out}}(\Gamma)) \log_2(1 + \Gamma) \tag{6.28}$$

where $\mathrm{P}^c_{\mathrm{out}}(\Gamma)$ and $\mathrm{P}^d_{\mathrm{out}}(\Gamma)$ are given with $\beta = 1$ in (6.21) and (6.22), respectively, $\bar{n} P_{D2D} \lambda_C$ and λ_B are the average number of simultaneously active D2D links and cellular links per unit area, respectively. Note that ASE for cellular network defined in (6.27) is valid for a saturated network scenario, i.e., each BS has at least one cellular UE to serve in the uplink channel. If the network is not saturated, the presence of inactive BSs will lead to increased SINR for both cellular and D2D links (due to lower interference), and outage probability will decrease. However, ASE may be lower as a result of fewer number of active cellular links per unit area. The ASE expressions in (6.27) and (6.28) are given for underlay type of spectrum sharing. For overlay type of sharing, the uplink spectrum is divided into two orthogonal portions. Therefore, ASE for both cellular and D2D networks can be redefined as follows:

$$\begin{aligned}\mathrm{ASE}_c &= (1-\delta)\lambda_B(1-\mathrm{P}^c_{\mathrm{out}}(\Gamma))\log_2(1+\Gamma)\\ \mathrm{ASE}_d &= \delta\bar{n}P_{D2D}\lambda_C(1-\mathrm{P}^d_{\mathrm{out}}(\Gamma))\log_2(1+\Gamma)\end{aligned} \tag{6.29}$$

where δ is the spectrum partition factor, $\mathrm{P}^c_{\mathrm{out}}(\Gamma)$ and $\mathrm{P}^d_{\mathrm{out}}(\Gamma)$ are given with $\beta = 0$ in (6.21) and (6.22), respectively. In the case of overlay spectrum sharing, the following optimization problem can be formulated in order to determine the optimal value of δ:

$$\delta^* = \arg\max_{\delta\in[0,1]} \mathrm{ASE}_c + \mathrm{ASE}_d \tag{6.30}$$

The solution of this optimization problem is given as follows: if $\lambda_B(1-\mathrm{P}^c_{\mathrm{out}}(\Gamma)) > \bar{n}P_{D2D}\lambda_C(1-\mathrm{P}^d_{\mathrm{out}}(\Gamma))$, $\delta^* = 0$; otherwise, $\delta^* = 1$. In other words, all bandwidth is assigned to the cellular or D2D network depending on which one is performing better. Therefore, this is a greedy approach that does not address any fairness considerations. In numerical results, we have shown that if cellular communication is disabled, i.e. $\delta = 1$, ASE for D2D network is maximized. To overcome this unfairness in the spectrum allocation between D2D and cellular communication, we consider the optimal weighted proportional fair spectrum partition which is formulated as follows:

$$\delta^* = \arg\max_{\delta\in[0,1]} w_c\log(\mathrm{ASE}_c) + w_d\log(\mathrm{ASE}_d) \tag{6.31}$$

where w_c and w_d are the introduced weights. If we take the derivative of the objective function in (6.31) with respect to δ and make it equal to zero, the optimal spectrum partition factor is obtained as $\delta^* = \frac{w_d}{w_c+w_d} = w_d$ which is simply equal to the weight we assign to the potential D2D UEs. In other words, w_d portion of the spectrum should be assigned to D2D communication to achieve proportional fairness.

Table 6.1: System Parameters

Parameters	**Values**
$\alpha_{L,c}$, $\alpha_{N,c}$; $\alpha_{L,d}$, $\alpha_{N,d}$	2, 4; 2, 4
N_L, N_N	3, 2
M_ν, m_ν, θ_ν for $\nu \in \{\text{BS}_0, \text{UE}\}$	20dB, -10dB, 30^o
λ_B, λ_C	10^{-5}, 10^{-4} $(1/m^2)$
$\bar{n}$	3
$(p_{L,c}, R_{B,c})$, $(p_{L,d}, R_{B,d})$	(1, 100), (1, 50)
β, δ, T_d	1, 0.2, 1
Γ, σ_N^2, σ_d^2	0dB, -74dBm, 25
P_c, P_d	200mW, 200mW

6.6 Simulation and Numerical Results

In this section, theoretical expressions are evaluated numerically. We also provide simulation results to validate the accuracy of the proposed model for the D2D-enabled uplink mmWave cellular network with clustered UEs as well as to confirm the accuracy of the analytical characterizations. In the numerical evaluations and simulations, unless stated otherwise, the parameter values listed in Table 6.1 are used.

First, we investigate the effect of UE distribution's standard deviation σ_d on the probability of selecting D2D mode for different values of the LOS probability function $p_{L,c}$ for cellular link and $p_{L,d}$ for D2D link in Fig. 6.3. As the standard deviation increases, the distance between the transmitting and receiving potential D2D UEs also increases. As a result, probability of selecting the D2D mode decreases. Also, since the number of LOS BSs increases with the increase in $p_{L,c}$, probability of selecting D2D mode decreases with increasing $p_{L,c}$. On the other hand, probability of selecting D2D mode increases when we increase $p_{L,d}$ as a result of increasing number of LOS potential D2D UEs in the cluster. As we have discussed in Section 6.3.3, although the cluster centers are distributed according to a PPP, modeling the pdf of the distance between the nearest LOS/NLOS BS and potential D2D UE using Eq. (6.7) is only an approximation because the potential D2D UEs are distributed according to a PCP around the cluster centers. However, as shown in Fig. 6.3, this pdf assumption agrees

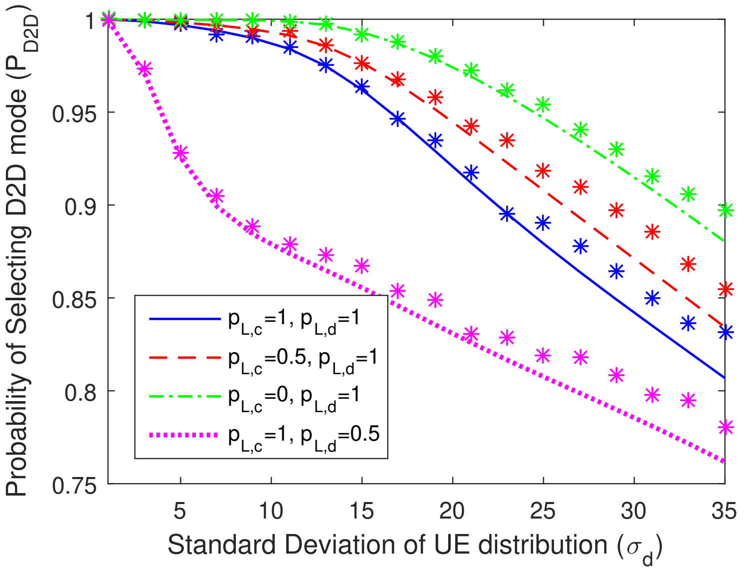

Figure 6.3: Probability of selecting D2D mode as a function of UE distribution's standard deviation σ_d for different values of $p_{L,c}$ and $p_{L,d}$. Simulation results are also plotted with markers.

well with the simulation results especially for small values of σ_d. On the other hand, there is a minor deviation between the analysis and simulation results for larger values of σ_d. This is because potential D2D UEs are located farther from the cluster center for larger σ_d.

In Fig. 6.4, we plot the SINR outage probability of cellular and D2D links as a function of average number of simultaneously transmitting potential D2D UEs $\bar{n}$ in each cluster for different values of cluster center density λ_C. Moreover, the effect of spectrum sharing type is investigated. As described in Section 6.2, β indicates the type of spectrum sharing; i.e., it is equal to one for underlay and zero for the overlay scheme. For the underlay type of spectrum sharing, when the average number of simultaneously transmitting potential D2D UEs gets higher, both intra-cluster and inter-cluster interferences increase and as a result SINR outage probabilities for both cellular and D2D links increase. Similarly, inter-cluster interference increases with the increase in cluster center density. Therefore, outage probabilities for both cellular and D2D links increase. For the overlay type of spectrum sharing, outage probability

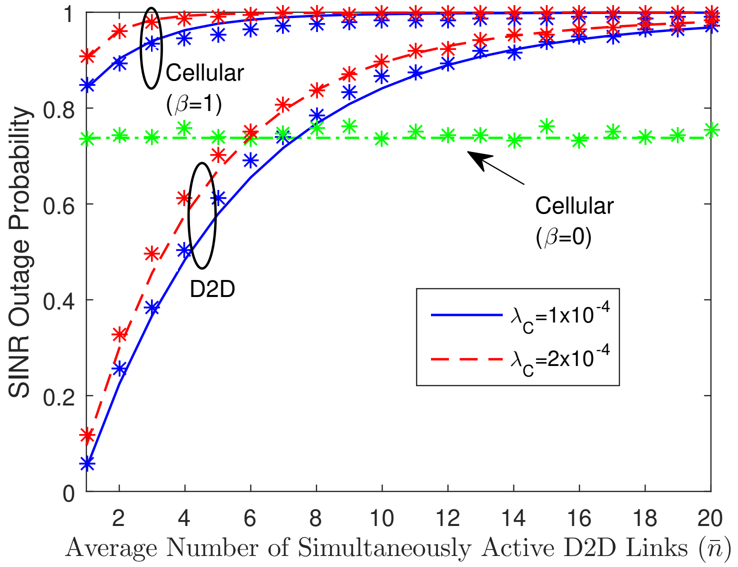

Figure 6.4: SINR outage probability as a function of average number of simultaneously active D2D links $\bar{n}$ for different values of cluster center density λ_C ($\Gamma = 40dB$). Simulation results are also plotted with markers.

is smaller for cellular UEs compared to underlay and it is independent of $\bar{n}$ since cross-mode interference from D2D UEs becomes zero in the case of overlay spectrum sharing. On the other hand, outage probability of D2D UEs remains the same with both overlay and underlay sharing, showing that the effect of cross-mode interference from cellular UEs is negligible even under the congested network scenario assumption.

In Fig. 6.5, we investigate the effect of UE distribution's standard deviation σ_d on SINR outage probability of D2D links for different values of LOS ball radius $R_{B,d}$. We have two different observations depending on the value of σ_d. For small values of σ_d, i.e. when the potential D2D UEs in the cluster are distributed closer to each other, outage probability is less for small LOS ball radius $R_{B,d}$. On the other hand, outage probability with smaller LOS ball radius $R_{B,d}$ becomes greater for bigger values of σ_d. For small σ_d, main link is more likely be a LOS link and effect of interference is small if the LOS ball radius is small, hence outage probability is low. However, the main link becomes more likely to be a NLOS link and the effect of interference becomes relatively more dominant with the increasing σ_d.

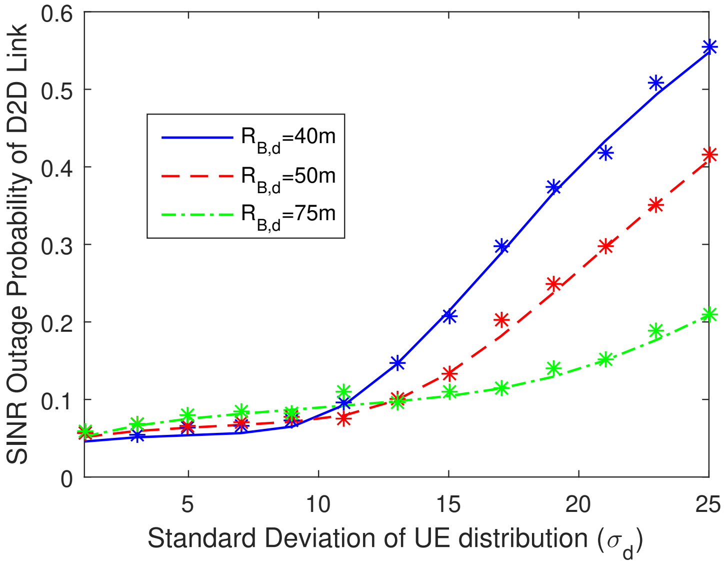

Figure 6.5: SINR outage probability as a function of UE distribution's standard deviation σ_d for different values of LOS ball radius $R_{B,d}$ ($\Gamma = 20dB$). Simulation results are also plotted with markers.

Next, we compare the SINR outage probabilities for different values of the antenna main lobe gain M_ν and beam width of the main lobe θ_ν for $\nu \in \{\text{BS}_0, \text{UE}\}$ in Fig. 6.6. Outage probability improves with the increase in the main lobe gain M_ν for the same value of θ_ν for $\nu \in \{\text{BS}_0, \text{UE}\}$. On the other hand, since we assume perfect beam alignment for serving links, outage probability increases with the increase in the beam width of the main lobe due to the growing impact of the interference. Finally, we notice that for given SINR threshold, the outage probabilities for D2D links are smaller than those for cellular links, owing to generally smaller communication distances in D2D links.

Effect of beam steering errors between the transmitting nodes (cellular or potential D2D UEs) and receiving nodes (BSs or UEs) on the SINR outage probability of cellular and D2D links is shown in Fig. 6.7. As shown in the figure, outage probability becomes worse for both cellular and D2D links with the increase in the standard deviation of the alignment error. Although the interference from interfering nodes remains unchanged, its effect grows with the increase in alignment error on the

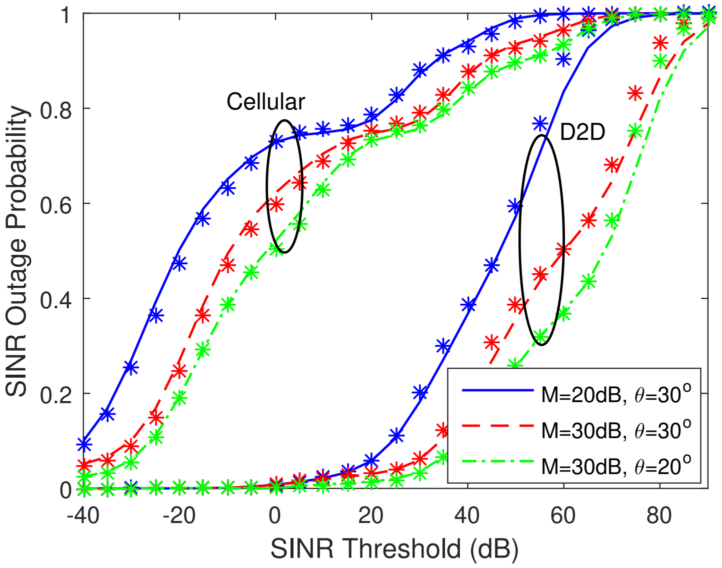

Figure 6.6: SINR outage probability as a function of the threshold in dB for different antenna parameters. Simulation results are also plotted with markers.

main link. This proves the importance of having perfect beam alignment to achieve improved performance.

In the numerical analysis, we also investigate the ASE of both cellular and D2D networks for underlay type of sharing. In Fig. 6.8, we plot the ASE of cellular and D2D networks as a function of the average number of simultaneously active D2D links $\bar{n}$ in each cluster for different values of the cluster center density λ_C. Increase in both the number of simultaneously active D2D links $\bar{n}$ and the cluster center density λ_C result in a decrease in ASE for cellular network due to the growing impact of interference from the D2D UEs. On the other hand, ASE for D2D network first increases and then decreases with the increase in the average number of simultaneously active D2D links. Therefore, an optimal value that maximizes ASE for D2D network exists. Below this optimal value, increasing the average number of simultaneously active D2D links helps in improving the spatial frequency reuse. Once the optimal value is exceeded, however, the effect of intra-cluster interference offsets the benefit of having larger average number of simultaneously active D2D links. Moreover,

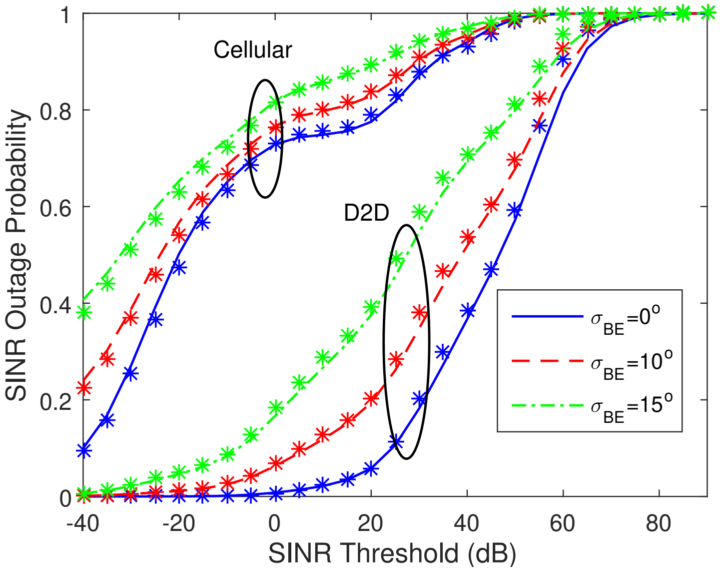

Figure 6.7: SINR outage probability as a function of the threshold in dB for different alignment errors σ_{BE}. Simulation results are also plotted with markers.

increasing the cluster center density for the same average number of simultaneously active D2D links in each cluster improves the ASE in the D2D network. We note that as the cluster center density grows, the inter-cluster interference increases while the spatial frequency reuse improves, i.e. $\bar{n}\lambda_C$ increases. Since the inter-cluster interference does not have a dominant impact on outage probability and intra-cluster interference remains the same, ASE for D2D network increases for the same average number of simultaneously active D2D links. Interestingly, the optimal number of simultaneously active D2D links is independent of the cluster center density because intra-cluster interference is more dominant than inter-cluster interference.

Finally, ASE of both cellular and D2D networks are investigated for overlay type of spectrum sharing. In Fig. 6.9, ASE of cellular and D2D networks are plotted as a function of the average number of simultaneously active D2D links in each cluster $\bar{n}$ for different values of spectrum partition factor δ. As expected, ASE for cellular network is independent of $\bar{n}$ due to the overlay type of sharing (no interference from D2D UEs). Also, with the decrease in the spectrum partition factor δ, i.e. assignment

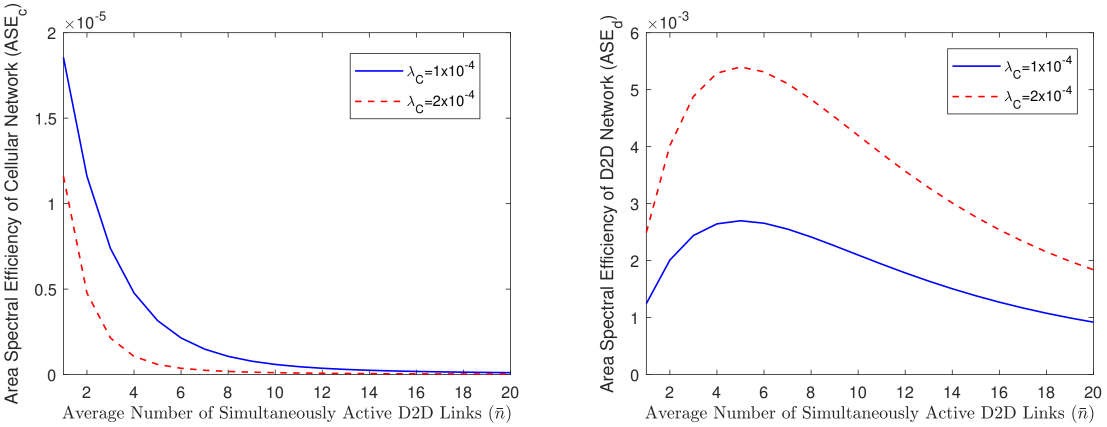

Figure 6.8: Area Spectral Efficiency (ASE) for underlay type of sharing for (a) cellular network, (b) D2D network as a function of average number of simultaneously active D2D links $\bar{n}$ for different values of cluster center density λ_C ($\Gamma = 40dB$).

of more bandwidth to cellular links, ASE for cellular network increases. Since intra-cluster and inter-cluster interferences from D2D links are present in both underlay and overlay cases for D2D network, ASE of D2D network for overlay case exhibits similar trends with the underlay case. Moreover, as mentioned in Section 6.5, ASE for D2D network is maximized if all bandwidth is assigned to D2D links, i.e. $\delta = 1$. We also consider the optimal weighted proportional fair spectrum partition in Section 6.5, and plot the objective function in (6.31) as a function of δ. As shown in Fig. 6.10, optimal spectrum partition factor is equal to $\delta^* = 0.4 = w_d$ which validates our result in Section 6.5.

6.7 Conclusion

In this chapter, we have provided an analytical framework to compute the SINR outage probabilities for both cellular and D2D links in a D2D-enabled mmWave cellular network with clustered UEs. Distinguishing features of mmWave communications, such as directional beamforming with sectored antenna model, modified LOS ball model for blockage modeling and Nakagami fading, have been considered in the analysis. BSs and cellular UEs are assumed to be distributed according to independent

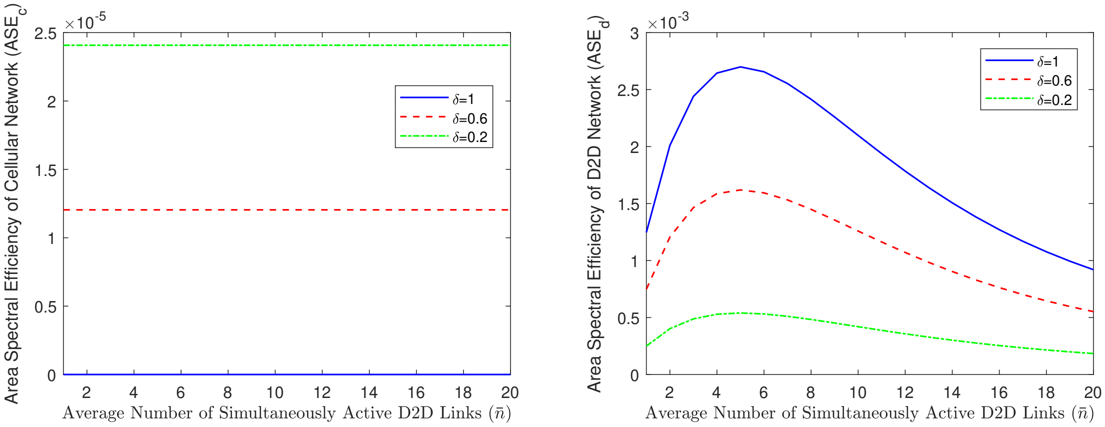

Figure 6.9: Area Spectral Efficiency (ASE) for overlay type of sharing for (a) cellular network, (b) D2D network as a function of average number of simultaneously active D2D links $\bar{n}$ for different values of spectrum partition factor δ ($\Gamma = 40dB$).

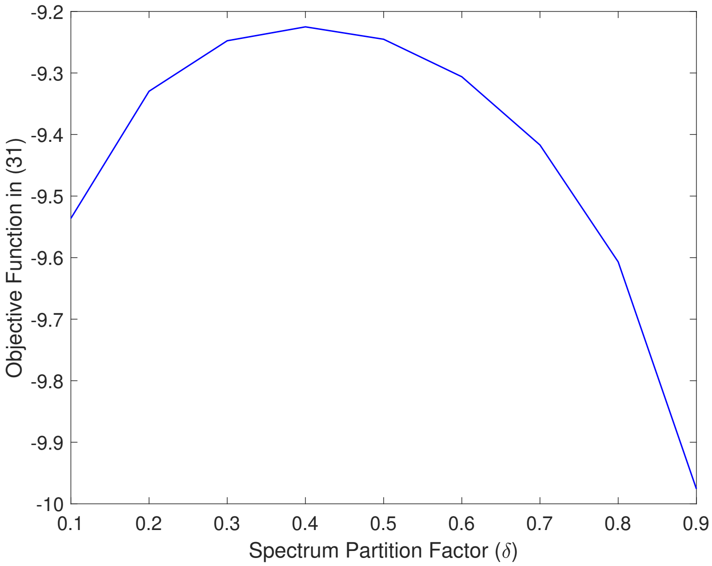

Figure 6.10: Objective function in (6.31) as a function of spectrum partition factor δ ($\Gamma = 40dB$).

PPPs, while potential D2D UEs locations' are modeled as a PCP. Potential D2D UEs in the clusters are allowed to choose cellular or D2D mode according to a flexible mode selection scheme. Under these assumptions, we have analyzed the interference experienced in cellular uplink and D2D links, and characterized the SINR outage probabilities.

Numerical results show that probability of selecting D2D mode decreases with increasing UE distribution's standard deviation σ_d and increasing $p_{L,c}$, while increase in $p_{L,d}$ leads to higher D2D mode selection probability. We have also shown that more simultaneously transmitting potential D2D UEs and/or higher cluster center density result in higher outage probabilities for both cellular and D2D links due to the growing impact of interference. Moreover, the type of spectrum sharing plays a crucial role in the SINR outage performance of cellular UEs. Another interesting observation is that smaller LOS ball radius is preferred for small values of σ_d while the opposite is advantageous for large values of σ_d. Moreover, increasing the main lobe gain and decreasing the beam width of the main lobe result in lower SINR outage. Effect of alignment error on outage probability is also quantified and importance of beam alignment in improving the performance is noted. Finally, ASE of the cellular and D2D networks are analyzed for both underlay and overlay types of sharing. We have shown that there is an optimal number of simultaneously active D2D links, maximizing the ASE in the D2D network. This optimal number is independent of the cluster center density and spectrum partition factor. For overlay sharing, there exists an optimal spectrum partition factor if the optimal weighted proportional fair spectrum partition is considered.

Chapter 7

Downlink Analysis in Unmanned Aerial Vehicle (UAV) Assisted Cellular Networks with Clustered Users

The use of unmanned aerial vehicles (UAVs) operating as aerial base stations (BSs) has emerged as a promising solution especially in scenarios requiring rapid deployments (e.g., in the cases of crowded hotspots, sporting events, emergencies, natural disasters) in order to assist the ground BSs. In this chapter, an analytical framework is provided to analyze the signal-to-interference-plus-noise ratio (SINR) coverage probability of unmanned aerial vehicle (UAV) assisted cellular networks with clustered user equipments (UEs). Locations of UAVs and ground BSs are modeled as Poison point processes (PPPs), and UEs are assumed to be distributed according to a Poisson cluster process (PCP) around the projections of UAVs on the ground. Initially, the complementary cumulative distribution function (CCDF) and probability density function (PDF) of path losses for both UAV and ground BS tiers are derived.

Subsequently, association probabilities with each tier are obtained. SINR coverage probability is derived for the entire network using tools from stochastic geometry. Finally, area spectral efficiency (ASE) of the entire network is determined, and SINR coverage probability expression for a more general model is presented by considering that UAVs are located at different heights. Via numerical results, we have shown that UAV height and path-loss exponents play important roles on the coverage performance. Moreover, coverage probability can be improved with smaller number of UAVs, while better area spectral efficiency is achieved by employing more UAVs and having UEs more compactly clustered around the UAVs.

7.1 Introduction

Mobile data demand has been growing exponentially in recent years due to, e.g., ever increasing use of smart phones, portable devices, and data-hungry multimedia applications. In order to meet this increasing data demand, new technologies and designs have been under consideration for 5G cellular networks. One of them is expected to be the deployment of dense low-power small-cell BSs to assist the congested lower-density high-power large-cell BSs by offloading some percentage of their UEs, resulting in a better quality of service per UE [5], [14]. Additionally, in the case of unexpected scenarios such as disasters, accidents, and other emergencies or temporary events requiring the excessive need for network resources such as concerts and sporting events, it is important to provide wireless connectivity rapidly [18], [19]. In such scenarios, the deployment of UAV BSs, also known as drone BSs, has attracted considerable attention recently as a possible solution.

In [75], optimal altitude of low-altitude aerial platforms (LAPs) providing maximum coverage is studied. Coverage probability expression is obtained for a UAV network as a function of network and environmental parameters, and their effect on the performance is investigated in [76]. In [77], authors derived the coverage probability expression for a finite network of UAVs by modeling the locations of UAVs as a uniform binomial point process (BPP). Aggregate interference from neighboring UAVs and the link coverage probability are derived in [78] to obtain the optimum antenna beamwidth, density and altitude. In [79], authors studied spectrum sharing in the deployment of aerial BSs within cellular networks and obtained the optimal drone small-cell (DSC) BS density to maximize the downlink throughput in different scenarios. An efficient 3-D placement algorithm for drone-cells in cellular networks is proposed in [80]. In [81], optimal 3D deployment of multiple UAVs is also investigated to maximize the downlink coverage performance using circle packing theory. Mathematical tools of optimal transport theory is used to determine the optimal deployment and cell association of UAVs in [82], and the delay-optimal cell association considering both terrestrial BSs and UAVs in [83]. Same authors have analyzed the coverage and rate performance of a network consisting of a single UAV and underlaid device-to-device (D2D) users in [84]. In [85], performance of inter-cell interference coordination (ICIC) and cell range expansion (CRE) methods are studied for a public safety communications (PSC) heterogeneous network consisting of UAVs. Employment of emergency flexible aerial nodes is studied for the communication recovery in situations such as natural disasters in [86]. Uplink performance of a two-cell cellular network with a terrestrial BS and an aerial BS is studied in [87] to provide better coverage probability in temporary events.

Stochastic geometry is a powerful mathematical tool to analyze the system performance of cellular networks. Hence, in most recent studies on 2D cellular networks, BS locations are assumed to follow a point process and the most commonly used distribution is the Poisson point process (PPP) due to its tractability and accuracy in approximating the actual cellular network topology [14], [15]. A similar stochastic geometry analysis can be conducted for a network of UAVs by considering UAVs distributed randomly in 3D space. Moreover, locations of the user equipments (UEs) are modeled by a Poisson cluster process (PCP) in recent studies. In [88], authors analyzed the large random wireless networks by considering the locations of the nodes distributed according to a PCP on the plane. Performance of a device-to-device (D2D) network in which the device locations are modeled as a PCP is studied in [70] for two realistic content availability setups. In [25], the uplink performance of D2D-enabled millimeter wave (mmWave) cellular networks with clustered D2D UEs are studied. The cumulative density function (CDF) of the nearest neighbor and contact distance distributions are derived for the Thomas cluster process (TCP) in [89] and for the Matérn cluster process (MCP) in [90] which are the special cases of PCP. In addition to modeling locations of UEs as a PCP, small-cell BS clustering is considered in [91] to capture the correlation between the large-cell and small-cell BS locations. In [92], authors develop a unified heterogeneous network model in which a fraction of UEs and arbitrary number of BS tiers are modeled as PCPs to reduce the gap between the 3GPP simulation models and the popular PPP-based analytic models for heterogeneous networks. A K-tier heterogeneous network model in which the locations of UEs are modeled by a PCP with one small-cell BS located at the center of each cluster process is studied in [93] for two different types of PCPs. In [94], a similar heterogeneous network model with user-centric small cell deployments is developed by considering the distinguishing features of mmWave communication.

7.1.1 Main Contributions

In this chapter, we consider a two-tier downlink network in which a network of UAVs operating at a certain altitude above ground coexisting with a network of ground BSs. Our main contributions can be summarized as follows:

- We provide an analytical framework to analyze the downlink coverage performance of UAV assisted cellular networks with clustered UEs by using tools from stochastic geometry. UAVs are considered to coexist with the ground BSs in the network, and locations of both UAVs and BSs are modeled as independent homogeneous PPPs. Since UAVs are planned to be deployed in overloaded scenarios, the UEs are expected to form clusters around the UAVs. Therefore, unlike previous works where the user equipment (UE) and UAV locations are assumed to be uncorrelated, we model the locations of UEs as a PCP to provide a more appropriate and realistic model.

- CCDFs and PDFs of the path losses for each tier are derived. Then, association probabilities are obtained by considering averaged biased received power cell association criterion. Different from [22] and [94], UAV height is taken into account in the derivation of CCDF and PDF of path losses for UAVs.

- Laplace transforms of interferences from each tier are obtained using tools from stochastic geometry to calculate the total SINR coverage probability of the network.

- Area spectral efficiency (ASE) of the entire network is determined. We have provided the design insights in Numerical Results section to improve network performance. In particular, we have shown that an optimal value for UAV density, maximizing the ASE, exists and this optimal value increases when UEs are located more compactly in the clusters.

- An extension is provided to the baseline model by considering that UAVs are located at different heights. SINR coverage probability expression for this more general and practical model is presented.

7.2 System Model

In this section, the system model for UAV assisted cellular networks with clustered UEs is presented. We consider a two-tier downlink network, where the UAVs and ground BSs are spatially distributed according to two independent homogeneous PPPs Φ_U and Φ_B with densities λ_U and λ_B, respectively, on the Euclidean plane. UAVs are placed at a height of H above the ground, and H is assumed to be constant[1]. UAVs are deployed to provide relief to the ground cellular BSs by offloading traffic from them around hotspots or large gatherings such as sporting events or concerts. They can also be deployed during emergencies or other instances during which ground BS resources are strained [85]. UEs are clustered around the projections of UAVs on the ground, and the union of cluster members' locations form a PCP, denoted by Φ_C. Since UEs are located in high UE density areas, they are expected to be closer to each other forming clusters. Therefore, PCP is a more appropriate and accurate model than a homogeneous PPP. In this chapter, we model Φ_C as a Thomas cluster process, where the UEs are symmetrically independently and identically distributed (i.i.d.) around the cluster centers, (which are projections of UAVs on the ground), according to a Gaussian distribution with zero mean and variance σ_c^2, and the probability density function (PDF) and complementary cumulative distribution function (CCDF) of a UE's location are given, respectively, by [95]

$$f_D(d) = \frac{d}{\sigma_c^2} \exp\left(-\frac{d^2}{2\sigma_c^2}\right), \quad d \in \mathbb{R}^2, \tag{7.1}$$

$$\bar{F}_D(d) = \exp\left(-\frac{d^2}{2\sigma_c^2}\right), \quad d \in \mathbb{R}^2. \tag{7.2}$$

Without loss of generality, a typical UE is assumed to be located at the origin according to Slivnyak's theorem [29], and it is associated with the tier providing the maximum average biased-received power. Also, we consider an additional tier, named

---

[1] Subsequently, extension to considering multiple height values is also addressed.

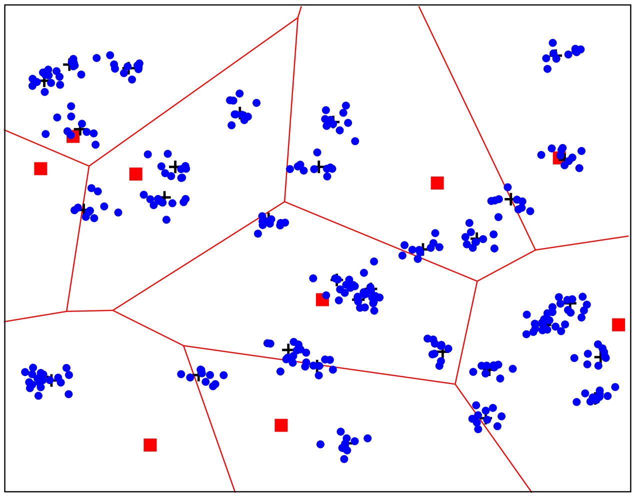

Figure 7.1: UAVs (black plus signs) and BSs (red squares) are distributed as independent PPPs, UEs (blue dots) are normally distributed around projections of UAVs on the ground.

as 0^{th} tier that only includes the UAV at the cluster center of the typical UE similarly as in [93] and [94]. Thus, our model consists of three tiers; a 0^{th} tier cluster-center UAV, 1^{st} tier UAVs, and 2^{nd} tier ground BSs. The proposed network model is shown in Fig. 7.1.

Link between a UAV and the typical UE can be either a line-of-sight (LOS) or non-line-of-sight (NLOS) link. Path-loss in NLOS links is generally higher than the path-loss in LOS links due to the reflection and scattering of signals. Therefore, an additional path-loss is experienced in NLOS links. Specifically, the path-loss of LOS and NLOS links in tier k for $k = 0, 1$ can be modelled as follows [75], [96]:

$$\begin{aligned} L_{k,\text{LOS}}(r) &= \eta_{\text{LOS}}(r^2 + H^2)^{\alpha_{\text{LOS}}/2} \\ L_{k,\text{NLOS}}(r) &= \eta_{\text{NLOS}}(r^2 + H^2)^{\alpha_{\text{NLOS}}/2} \end{aligned} \tag{7.3}$$

where r is the distance between the typical UE and the cluster center of the UAVs on the 2-D plane, i.e., projections of UAVs on the ground, H is the UAV height,

α_{LOS} and α_{NLOS} are the path-loss exponents, η_{LOS} and η_{NLOS} are the additional path losses in LOS and NLOS links, respectively. Path-loss for the 2nd tier ground BSs can be modeled by $L_2(r) = \eta_B r^{\alpha_B}$ where η_B is the additional path-loss over the free space path-loss and α_B is the path-loss exponent. Similar to the UAV-to-typical UE link, the link between a BS and the typical UE can have two states, namely LOS and NLOS, with a LOS probability function which depends on the size and the density of the blockages in the environment. When communication occurs in mmWave frequency bands, the effect of blockages plays an important role and cause a significant difference between the LOS and NLOS path losses in the BS-to-typical UE link. Although the analysis of two-state path-loss model would be very similar to that of the UAV-to-typical UE link, in this chapter, we consider the transmission in lower frequencies in which the difference between the LOS and NLOS path losses is not very large, and we model the path-loss in the link between the BS and the typical UE using a single state. Regarding the probability of LOS in UAV links, different models have been proposed in the literature. In this chapter, we adopt the model proposed in [75]:

$$\mathcal{P}_{\text{LOS}}(r) = \frac{1}{1 + b\exp\left(-c\left(\frac{180}{\pi}\tan^{-1}\left(\frac{H}{r}\right) - b\right)\right)} \tag{7.4}$$

where b and c are constants which depend on the environment. As can be seen in (7.4), probability of having a LOS connection increases as the height of the UAVs increases.

7.2.1 Statistical Characterization of the Path Loss

We first characterize the complementary cumulative distribution function (CCDF) and the probability density function (PDF) of the path-loss in the following lemmas and corollaries.

Lemma 7.1 *The CCDF of the path-loss from the typical UE to a* 0^{th} *tier UAV can be formulated as*

$$\begin{aligned}\bar{F}_{L_0}(x) &= \sum_{s\in\{LOS,NLOS\}} \bar{F}_{L_{0,s}}(x) \\ &= \sum_{s\in\{LOS,NLOS\}} \int_{\sqrt{\left(\frac{x}{\eta_s}\right)^{2/\alpha_s}-H^2}}^{\infty} \mathcal{P}_s\left(\sqrt{d^2+H^2}\right) f_D(d)\mathrm{d}d \qquad (7.5)\end{aligned}$$

where $f_D(d)$ *and* $\mathcal{P}_{LOS}(r)$ *are given in (7.1) and (7.4), respectively, and* $\mathcal{P}_{NLOS}(r) = 1 - \mathcal{P}_{LOS}(r)$.

Proof: See Appendix I.

Lemma 7.2 *CCDF of the path-loss from the typical UE to a* 1^{st} *tier UAV is given by*

$$\bar{F}_{L_1}(x) = \exp(-\Lambda_1([0,x))) \qquad (7.6)$$

where $\Lambda_1([0,x))$ *is defined as follows:*

$$\begin{aligned}\Lambda_1([0,x)) &= \Lambda_{1,LOS}([0,x)) + \Lambda_{1,NLOS}([0,x)) \\ &= \sum_{s\in\{LOS,NLOS\}} 2\pi\lambda_U \int_0^{\sqrt{(x/\eta_s)^{2/\alpha_s}-H^2}} \mathcal{P}_s(r) r dr. \qquad (7.7)\end{aligned}$$

Similarly, the CCDF of the path-loss from the typical UE to a 2^{nd} *tier BS is given by*

$$\bar{F}_{L_2}(x) = \exp(-\Lambda_2([0,x))) \qquad (7.8)$$

where $\Lambda_2([0,x)) = \pi\lambda_B(x/\eta_B)^{2/\alpha_B}$.

Proof: See Appendix J.

Corollary 7.1 *The PDF of the path-loss from the typical UE to a LOS/NLOS* 0^{th} *tier UAV can be computed as*

$$\begin{aligned} f_{L_{0,s}}(x) &= -\frac{dF_{L_{0,s}}(x)}{dx} \\ &= \frac{1}{\sigma_c^2}\frac{x^{2/\alpha_s-1}}{\alpha_s\eta_s^{2/\alpha_s}}\mathcal{P}_s\left(\sqrt{\left(\frac{x}{\eta_s}\right)^{2/\alpha_s}-H^2}\right)\exp\left(-\frac{1}{2\sigma_c^2}\left(\left(\frac{x}{\eta_s}\right)^{2/\alpha_s}-H^2\right)\right). \end{aligned} \tag{7.9}$$

Corollary 7.2 *The PDF of the path-loss from the typical UE to a LOS/NLOS* 1^{st} *tier UAV can be computed as*

$$f_{L_{1,s}}(x) = -\frac{d\bar{F}_{L_{1,s}}(x)}{dx} = \Lambda'_{1,s}([0,x))\exp(-\Lambda_{1,s}([0,x))) \tag{7.10}$$

where $\Lambda'_{1,s}([0,x))$ *is obtained as follows using the Leibniz integral rule:*

$$\Lambda'_{1,s}([0,x)) = 2\pi\lambda_U\frac{x^{2/\alpha_s-1}}{\alpha_s\eta_s^{2/\alpha_s}}\mathcal{P}_s\left(\sqrt{\left(\frac{x}{\eta_s}\right)^{2/\alpha_s}-H^2}\right). \tag{7.11}$$

Similarly, the PDF of the path-loss from the typical UE to a 2^{nd} *tier BS is given by*

$$f_{L_2}(x) = -\frac{d\bar{F}_{L_2}(x)}{dx} = \Lambda'_2([0,x))\exp(-\Lambda_2([0,x))) \tag{7.12}$$

where $\Lambda'_2([0,x)) = 2\pi\lambda_B\frac{x^{2/\alpha_B-1}}{\alpha_B\eta_B^{2/\alpha_B}}$.

7.2.2 Cell Association

In this work, we consider a flexible cell association scheme similarly as in [22], [50]. In this scheme, UEs are assumed to be associated with a UAV or a BS offering the strongest long-term averaged biased-received power (ABRP). In other words, the typical UE is associated with a UAV or a BS in tier-k for $k = 0, 1, 2$ if

$$P_k B_k L_k(r)^{-1} \geq P_j B_j L_{min,j}(r)^{-1}, \text{for all } j = 0, 1, 2, j \neq k \tag{7.13}$$

where P and B denote the transmit power, and biasing factor, respectively, in the corresponding tier (indicated by the index in the subscript), $L_k(r)$ is the path-loss in the k^{th} tier as formulated in (7.3), and $L_{min,j}(r)$ is the minimum path-loss of the typical UE from a UAV or BS in the j^{th} tier. In the following lemmas, we provide the association probabilities with a UAV/BS in the k^{th} tier using the result of Lemma 1 and Corollary 1.

Lemma 7.3 *The probability that the typical UE is associated with a 0^{th} tier LOS/NLOS UAV is*

$$\mathcal{A}_{0,s} = \int_{\eta_s H^{\alpha_s}}^{\infty} f_{L_{0,s}}(l_{0,s}) e^{-\sum_{j=1}^{2} \Lambda_j \left(\left[0, \frac{P_j B_j}{P_0 B_0} l_{0,s}\right)\right)} dl_{0,s} \tag{7.14}$$

for $s \in \{LOS\ , NLOS\}$ where $\Lambda_1([0,x))$, $\Lambda_2([0,x))$, and $f_{L_{0,s}}(l_0)$ are given in (7.7), (7.8), and (7.9), respectively. The probability that the typical UE is associated with a 1^{st} tier LOS/NLOS UAV is

$$\mathcal{A}_{1,s} = \int_{\eta_s H^{\alpha_s}}^{\infty} \Lambda'_{1,s}([0, l_{1,s})) \bar{F}_{L_0}\left(\frac{P_0 B_0}{P_1 B_1} l_{1,s}\right) e^{-\sum_{j=1}^{2} \Lambda_j \left(\left[0, \frac{P_j B_j}{P_1 B_1} l_{1,s}\right)\right)} dl_{1,s} \tag{7.15}$$

for $s \in \{LOS\ , NLOS\}$ where $\bar{F}_{L_0}(x)$, and $\Lambda'_{1,s}([0,x))$ are given in (7.5) and (7.11), respectively.

The probability that the typical UE is associated with a 2^{nd} tier BS is

$$\mathcal{A}_2 = \int_{0}^{\infty} \Lambda'_2([0, l_2)) \bar{F}_{L_0}\left(\frac{P_0 B_0}{P_2 B_2} l_2\right) e^{-\sum_{j=1}^{2} \Lambda_j \left(\left[0, \frac{P_j B_j}{P_2 B_2} l_2\right)\right)} dl_2 \tag{7.16}$$

where $\Lambda'_2([0,x))$ is given in (7.12).

Proof: See Appendix K.

7.3 SINR Coverage Analysis

In this section, we develop a theoretical framework to analyze the downlink SINR coverage probability for the typical UE clustered around the 0^{th} tier UAV using stochastic geometry.

7.3.1 Signal-to-Interference-plus-Noise Ratio (SINR)

The SINR experienced at the typical UE at a random distance r from its associated UAV/BS in the k^{th} tier can be written as

$$\text{SINR}_k = \frac{P_k h_{k,0} L_k^{-1}(r)}{\sigma_k^2 + \sum_j I_{j,k}} \tag{7.17}$$

where

$$I_{j,k} = \sum_{i \in \Phi_j \setminus \mathcal{E}_{k,0}} P_j h_{j,i} L_{j,i}^{-1}(r) \tag{7.18}$$

represents the sum of the interferences from the UAVs/BSs in the j^{th} tier, $h_{k,0}$ is the small-scale fading gain from the serving BS, and σ_k^2 is the variance of the additive white Gaussian noise component. Small-scale fading gains denoted by h are assumed to have an independent exponential distribution in all links. According to the cell association policy, the typical UE is associated with a BS/UAV whose path-loss is $L_k(r)$, and therefore there exists no BS/UAV within a disc of radius $\frac{P_j B_j}{P_k B_k} L_k(r)$ centered at the origin. This region is referred to as the exclusion disc and is denoted by $\mathcal{E}_{k,0}$. [2]

---

[2] In this chapter, UAVs, BSs and UEs are assumed to have omnidirectional antennas, i.e. antennas with unit gain. However, the analysis can be extended to the case of directional antennas without much difficulty. For instance, in this case, one needs to multiply the transmit powers of the serving and interfering UAVs/BSs with the antenna gain, and update the exclusion discs for each tier by considering antenna beamwidth.

7.3.2 SINR Coverage Probability

The SINR coverage probability $\mathrm{P}_k^{\mathrm{C}}(\Gamma_k)$ is defined as the probability that the received SINR is larger than a certain threshold $\Gamma_k > 0$ when the typical UE is associated with a BS/UAV from the k^{th} tier, i.e., $\mathrm{P}_k^{\mathrm{C}}(\Gamma_k) = \mathbb{P}(\mathrm{SINR}_k > \Gamma_k | t = k)$ where t indicates the associated tier. The total SINR coverage probability P^{C} of the network can be computed as follows:

$$\mathrm{P}^{\mathrm{C}} = \sum_{k=0}^{1} \sum_{s \in \{\mathrm{LOS},\mathrm{NLOS}\}} \left[\mathrm{P}_{k,s}^{\mathrm{C}}(\Gamma_k)\mathcal{A}_{k,s}\right] + \mathrm{P}_2^{\mathrm{C}}(\Gamma_2)\mathcal{A}_2, \tag{7.19}$$

where $\mathrm{P}_{k,s}^{\mathrm{C}}(\Gamma_k)$ is the conditional coverage probability given that the UE is associated with a k^{th} tier LOS/NLOS UAV, $\mathcal{A}_{k,s}$ is the association probability with the k^{th} tier for $k \in \{0, 1\}$, and $\mathrm{P}_2^{\mathrm{C}}(\Gamma_2)$ is the conditional coverage probability given that the UE is associated with a BS in the 2^{nd} tier and $\mathcal{A}_2$ is the association probability with the 2^{nd} tier. In the following theorem, we provide the main result for the total network coverage.

Theorem 7.1 : *The total SINR coverage probability of the UAV assisted cellular networks with clustered UEs is given as*

$$\begin{aligned}
&P^C = \\
&\sum_{s\in\{LOS,NLOS\}} \int_{\eta_s H^{\alpha_s}}^{\infty} e^{-\frac{\Gamma_0 l_{0,s} \sigma_0^2}{P_0}} \left(\prod_{j=1}^{2} \mathcal{L}_{I_{j,0}}\left(\frac{\Gamma_0 l_{0,s}}{P_0}\right)\right) f_{L_{0,s}}(l_{0,s}) e^{-\sum_{j=1}^{2}\Lambda_j\left(\left[0,\frac{P_j B_j}{P_0 B_0} l_{0,s}\right)\right)} dl_{0,s} \\
&+ \sum_{s\in\{LOS,NLOS\}} \int_{\eta_s H^{\alpha_s}}^{\infty} e^{-\frac{\Gamma_1 l_{1,s} \sigma_1^2}{P_1}} \left(\prod_{j=0}^{2} \mathcal{L}_{I_{j,1}}\left(\frac{\Gamma_1 l_{1,s}}{P_1}\right)\right) \Lambda'_{1,s}([0, l_{1,s})) \bar{F}_{L_0}\left(\frac{P_0 B_0}{P_1 B_1} l_{1,s}\right) \\
&\qquad\qquad \times e^{-\sum_{j=1}^{2}\Lambda_j\left(\left[0,\frac{P_j B_j}{P_1 B_1} l_{1,s}\right)\right)} dl_{1,s} \\
&+ \int_{0}^{\infty} e^{-\frac{\Gamma_2 l_2 \sigma_2^2}{P_2}} \left(\prod_{j=0}^{2} \mathcal{L}_{I_{j,2}}\left(\frac{\Gamma_2 l_2}{P_2}\right)\right) \Lambda'_2([0, l_2)) \bar{F}_{L_0}\left(\frac{P_0 B_0}{P_2 B_2} l_2\right) e^{-\sum_{j=1}^{2}\Lambda_j\left(\left[0,\frac{P_j B_j}{P_2 B_2} l_2\right)\right)} dl_2
\end{aligned} \tag{7.20}$$

where

$$\mathcal{L}_{I_{0,k}}(u) = \sum_{s' \in \{LOS, NLOS\}} \int_{\mathcal{E}_{0,0}}^{\infty} \frac{1}{1+uP_0x^{-1}} f_{L_{0,s'}}(x)dx \tag{7.21}$$

$$\mathcal{L}_{I_{1,k}}(u) = \prod_{s' \in \{LOS, NLOS\}} \exp\left(-\int_{\mathcal{E}_{1,0}}^{\infty} \frac{uP_1x^{-1}}{1+uP_1x^{-1}} \Lambda'_{1,s'}(dx)\right) \tag{7.22}$$

$$\mathcal{L}_{I_{2,k}}(u) = \exp\left(-\int_{\mathcal{E}_{2,0}}^{\infty} \frac{uP_2x^{-1}}{1+uP_2x^{-1}} \Lambda'_{2}(dx)\right). \tag{7.23}$$

Proof: See Appendix L.

General sketch of the proof is as follows: First, SINR coverage probability is computed given that the typical UE is associated with a k^{th} tier LOS/NLOS UAV or a 2^{nd} tier BS. Subsequently, each of the conditional probabilities are multiplied with their corresponding association probabilities, and then they are summed up to obtain the total coverage probability of the network. In order to determine the conditional coverage probabilities, Laplace transforms of interferences from each tier are obtained using tools from stochastic geometry. We also note that although the characterization in Theorem 7.1 involves multiple integrals, the computation can be performed relatively easily by using numerical integration tools.

7.4 Area Spectral Efficiency

In Section 7.3, we have analyzed the SINR coverage probability performance of a UAV assisted cellular network with clustered UEs. In this section, we consider another crucial performance metric, namely area spectral efficiency (ASE), to measure the network capacity. ASE is defined as the average number of bits transmitted per unit time per unit bandwidth per unit area. It can be mathematically defined as follows:

$$\mathrm{ASE} = \Bigg(\lambda_U \Bigg(\sum_{k=0}^{1} \sum_{s\in\{\mathrm{LOS},\mathrm{NLOS}\}} \left[\mathrm{P}^{\mathrm{C}}_{k,s}(\Gamma_k)\mathcal{A}_{k,s}\right]\Bigg) + \lambda_B \mathrm{P}^{\mathrm{C}}_{2}(\Gamma_2)\mathcal{A}_2\Bigg)\log_2(1+\Gamma) \quad (7.24)$$

where $\mathrm{P}^{\mathrm{C}}_{k,s}(\Gamma_k)$ is the conditional coverage probability given that the UE is associated with a k^{th} tier LOS/NLOS UAV for $k \in \{0,1\}$, and $\mathrm{P}^{\mathrm{C}}_{2}(\Gamma_2)$ is the conditional coverage probability given that the UE is associated with a BS in the 2^{nd} tier, λ_U and λ_B are the average densities of simultaneously active UAV and BS links per unit area, respectively. Note that ASE defined in (7.24) is valid for a saturated network scenario, i.e., each UAV and BS has at least one cellular UE to serve in the downlink. If the network is not saturated, the presence of inactive UAVs and BSs will lead to increased SINR (due to lower interference), and coverage probability will increase. However, ASE may be lower as a result of fewer number of active links per unit area.

7.5 Extension to a Model with UAVs at Different Heights

In the preceding analysis, we consider that UAVs are located at a height of H above the ground, and H is assumed to be the same for all UAVs. However, the proposed analytical framework can also be employed to analyze the coverage probability when UAV height is not fixed, i.e., UAVs are assumed to be located at different heights. In this setup, we assume that there are M groups of UAVs such that the m^{th} UAV group is located at the height level H_m for $m = 1, 2, \dots, M$ and UAVs at each height level can be considered as a UAV-tier distributed according to an independent homogeneous PPP with density of $\lambda_{U,m}$ and the total density is equal to $\sum_{m=1}^{M} \lambda_{U,m} = \lambda_U$. Different from the preceding analysis in which we have considered a single typical UE located at the origin and named its cluster center UAV as 0^{th} tier UAV, a separate typical

UE for each UAV tier needs to be considered in the coverage probability analysis for this model with UAVs at different heights. For example, when we are analyzing the coverage probability of the network for a UE clustered around an m^{th} tier UAV, we assume that the typical UE is located at the origin and its cluster center UAV is considered as the 0^{th} tier UAV similar to the previous model. Therefore, SINR coverage probability of the network given that the typical UE is clustered around an m^{th} tier UAV for $m = 1, 2, \ldots, M$ can be computed as follows:

$$\mathrm{P}_m^{\mathrm{C}} = \sum_{k=0}^{M} \sum_{\substack{s \in \{\text{LOS}, \\ \text{NLOS}\}}} \left[\mathrm{P}_{m,k,s}^{\mathrm{C}}(\Gamma_k) \mathcal{A}_{m,k,s} \right] + \mathrm{P}_{m,M+1}^{\mathrm{C}}(\Gamma_{M+1}) \mathcal{A}_{m,M+1}, \tag{7.25}$$

where $\mathrm{P}_{m,k,s}^{\mathrm{C}}(\Gamma_k)$ is the conditional coverage probability given that the typical UE is clustered around an m^{th} tier UAV and it is associated with a k^{th} tier LOS/NLOS UAV, $\mathcal{A}_{m,k,s}$ is the association probability with a k^{th} tier LOS/NLOS UAV, $\mathrm{P}_{m,M+1}^{\mathrm{C}}(\Gamma_{M+1})$ is the conditional coverage probability given that the typical UE is clustered around an m^{th} tier and it is associated with a BS in the $(M+1)^{\text{st}}$ tier, and $\mathcal{A}_{m,M+1}$ is the association probability with the $(M+1)^{\text{st}}$ tier.

Theorem 7.2 *SINR coverage probability of the network given that the typical UE is* *clustered around an m^{th} tier UAV is given as*

$$
\begin{aligned}
&P_m^C = \\
&\sum_{s\in\{LOS,NLOS\}} \int_{\eta_s H_m^{\alpha_s}}^{\infty} e^{-\frac{\Gamma_0 l_{0,s}\sigma_0^2}{P_0}} \left(\prod_{j=1}^{M+1} \mathcal{L}_{I_{j,0}}\left(\frac{\Gamma_0 l_{0,s}}{P_0}\right)\right) f_{L_{0,s}}(l_{0,s}) e^{-\sum_{j=1}^{M+1}\Lambda_j\left(\left[0,\frac{P_j B_j}{P_0 B_0} l_{0,s}\right)\right)} dl_{0,s} \\
&+\sum_{k=1}^{M} \sum_{s\in\{LOS,NLOS\}} \int_{\eta_s H_k^{\alpha_s}}^{\infty} e^{-\frac{\Gamma_k l_{k,s}\sigma_k^2}{P_k}} \left(\prod_{j=0}^{M+1} \mathcal{L}_{I_{j,k}}\left(\frac{\Gamma_k l_{k,s}}{P_k}\right)\right) \Lambda'_{k,s}([0,l_{k,s}))\bar{F}_{L_0}\left(\frac{P_0 B_0}{P_k B_k} l_{k,s}\right) \\
&\times e^{-\sum_{j=1}^{M+1}\Lambda_j\left(\left[0,\frac{P_j B_j}{P_k B_k} l_{k,s}\right)\right)} dl_{k,s} \\
&+\int_0^{\infty} e^{-\frac{\Gamma_{M+1} l_{M+1}\sigma_{M+1}^2}{P_{M+1}}} \left(\prod_{j=0}^{M+1} \mathcal{L}_{I_{j,M+1}}\left(\frac{\Gamma_{M+1} l_{M+1}}{P_{M+1}}\right)\right) \Lambda'_2([0,l_{M+1}))\bar{F}_{L_0}\left(\frac{P_0 B_0}{P_{M+1} B_{M+1}} l_{M+1}\right) \\
&\times e^{-\sum_{j=1}^{M+1}\Lambda_j\left(\left[0,\frac{P_j B_j}{P_{M+1} B_{M+1}} l_{M+1}\right)\right)} dl_{M+1} \qquad (7.26)
\end{aligned}
$$

Proof: Derivation of $\mathrm{P}_m^{\mathrm{C}}$ follows similar steps as that of P^{C} in (7.20). In particular, Laplace transforms $\mathcal{L}_{I_{0,k}}$ and $\mathcal{L}_{I_{j,k}}$ for $j = 1, 2, \ldots, M$ are computed using the Laplace transform equations given in (7.21) and (7.22), respectively, by updating UAV height as H_j and UAV density as λ_j for $j = 0, 1, \ldots, M$. Similarly, $\mathcal{L}_{I_{M+1,k}}$ is computed using the Laplace transform expression given in (7.23). $\Lambda_j([0, x))$ for $j = 1, 2, \ldots, M$ and $\Lambda'_{k,s}([0, x))$ for $k = 1, 2, \ldots, M$ are computed using the equations $\Lambda_1([0, x))$ and $\Lambda'_{1,s}([0, x))$ given in (7.7) and (7.11), respectively, by inserting the UAV height and UAV density for each tier. Similarly, $\Lambda_{M+1}([0, x))$ and $\Lambda'_{M+1}([0, x))$ are obtained using the equations for the 2nd tier BSs, $\Lambda_2([0, x))$ and $\Lambda'_2([0, x))$, respectively. Furthermore, $\bar{F}_{L_0}(x)$ and $f_{L_{0,s}}(x)$ are computed using (7.5) and (7.9), respectively, by denoting the UAV height as H_m.

Table 7.1: System Parameters

Description	**Parameter**	**Value**
Path-loss exponents	α_{LOS}, α_{NLOS}, α_B	3, 3.5, 3.5
Average additional path-loss for LOS and NLOS	η_{LOS}, η_{NLOS}, η_B	1, 10, 1
Environment dependent constants	b, c	11.95, 0.136
Height of UAVs	H	10m
Transmit power	P_0, P_1, P_2	37dBm, 37dBm, 40dBm
UAV and BS densities	λ_U, λ_B	10^{-4}, 10^{-5} $(1/m^2)$
Biasing factor, SINR threshold, noise variance	B_k, Γ_k, σ_k^2 $\forall k$	1, 0dB, -90dBm
UEs distribution's variance	σ_c^2	25

7.6 Simulation and Numerical Results

In this section, theoretical expressions are evaluated numerically. We also provide simulation results to validate the accuracy of the proposed model for the UAV-assisted downlink cellular network with clustered UEs as well as to confirm of the analytical characterizations. In the numerical evaluations and simulations, unless stated otherwise, the parameter values listed in Table 7.1 are used.

First, we investigate the effect of UE distribution's standard deviation σ_c on the association probability for different values of the UAV height H in Fig. 7.2. As the standard deviation increases, the UEs have a wider spread and the distances between the 0^{th} tier UAV and UEs also increase. As a result, association probability with the 0^{th} tier UAV decreases, while association probability with 1^{st} tier UAVs and 2^{nd} tier ground BSs increases. Similarly, 0^{th} tier association probability decreases also with the increase in the heights of the UAVs due to increase in the relative distances between the 0^{th} tier UAV and UEs. Association probability with 2^{nd} tier BSs increases, while association probability with 1^{st} tier UAVs remains almost unchanged. The intuitive reason behind this behavior is that when all UAVs are at a higher height, UEs are still more likely to be associated with the 0^{th} tier UAV, which is at the center of cluster,

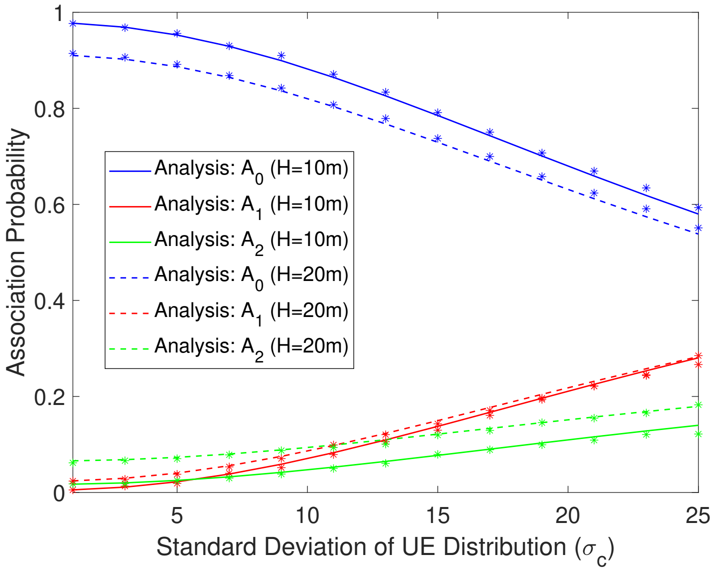

Figure 7.2: Association probability as a function of UE distribution's standard deviation σ_c for different values of UAV height H. Simulation results are also plotted with markers.

rather than 1st tier UAVs. Therefore, more UEs get connected to the ground BSs if the UAV height increases. Finally, we note that simulation results are also plotted in the figure with markers and there is a very good match between simulation and analytical results, further confirming our analysis.

Next, in Fig. 7.3 we plot the SINR coverage probabilities of different tiers (i.e., P_0^C, P_1^C and P_2^C) and also the total SINR coverage probability P^C as a function of the SINR threshold for different values of UAV height H. As seen in Fig. 7.2, UEs are more likely to be associated with the 0th tier UAV, which is the UAV at their cluster center, and therefore we observe in Fig. 7.3 that the coverage probability of 0th tier UAV is much higher than that of 1st tier UAVs and 2nd tier BSs. Fig. 7.3 also demonstrates that the total coverage probability gets worse with the increasing UAV height as a result of the increase in the distances between the 0th tier UAV and UEs. As also noted in Fig. 7.3, this increase in the distances causes coverage probability of ground BSs to increase. Also similarly as before, since the association probability with the 1st tier UAVs remains almost unchanged with the increasing UAV height,

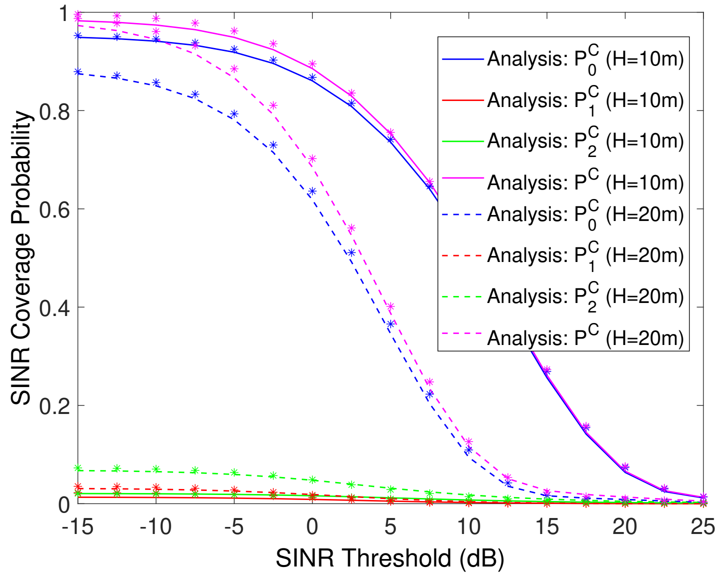

Figure 7.3: SINR Coverage probability as a function of the threshold in dB for different values of UAV height H. Simulation results are also plotted with markers.

their coverage probability also remains same.

In Fig. 7.4, the effect of path-loss exponents on the coverage probability is investigated at different values of the UAV height by assuming $\alpha_{\text{LOS}} = \alpha_{\text{NLOS}} = \alpha_B$ (additional path-loss for NLOS UAV links, η_{NLOS}, is still present.). Coverage probability initially improves when the path-loss exponents increase, but then it starts diminishing. As path-loss exponents increase, received power from the serving UAV or BS decreases, but the received power from interfering nodes also diminishes resulting in an increase in the coverage performance. However, further increasing the path-loss exponents deteriorates the coverage performance. Therefore, there exists an optimal value for path-loss exponents in which the coverage probability is maximized and this optimal value changes for different values of UAV height. For instance, we notice in the figure that the optimal value decreases when the UAV height increases. Increasing the height reduces the received power from the serving UAV, and hence lower path-loss exponent is preferred to optimize the performance. Another observation from Fig. 7.4 is that coverage probability performance is not affected significantly

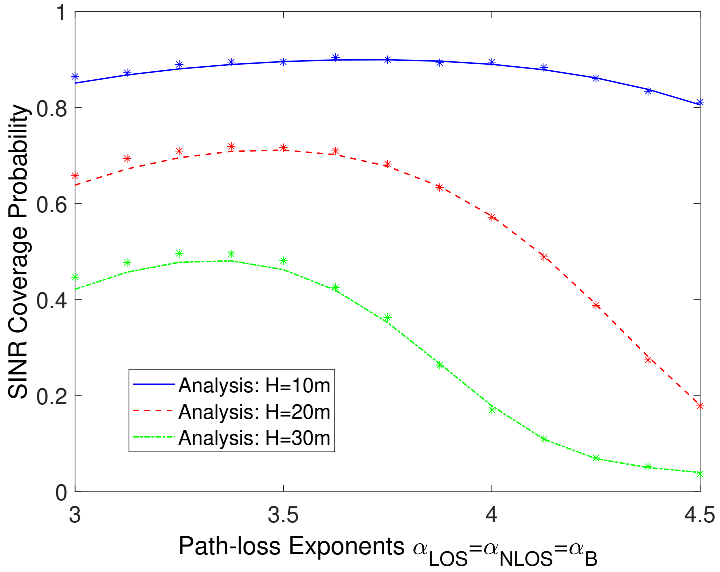

Figure 7.4: SINR coverage probability as a function of the path-loss exponents $\alpha_{\text{LOS}} = \alpha_{\text{NLOS}} = \alpha_B$ for different values of UAV height H. Simulation results are also plotted with markers.

from varying the path-loss exponent if the UAV height is small.

Next, SINR coverage probability is plotted as a function of the SINR threshold for different values of UAV density λ_U in Fig. 7.5. As shown in the figure, increase in the UAV density results in a degradation in the coverage probability. Since UEs are clustered around the projections of UAVs on the ground, they are more likely to be associated with the 0^{th} tier UAV, i.e., the UAV at their cluster center. Therefore, increasing UAV density results in higher interference levels from other UAVs and consequently lower coverage probabilities. However, as we have shown in Fig. 7.6 increase in UAV density leads to higher area spectral efficiency (ASE) because more UEs are covered in the network.

Specifically, in Fig. 7.6, we plot ASE as a function of the UAV density λ_U for different values of standard deviation σ_c of the UE distribution. As the UAV density λ_U increases, ASE first increases and then starts decreasing. This shows that there exists an optimal value for λ_U maximizing the ASE. Below this optimal value, increasing UAV density λ_U helps improving the spatial frequency reuse. However, after

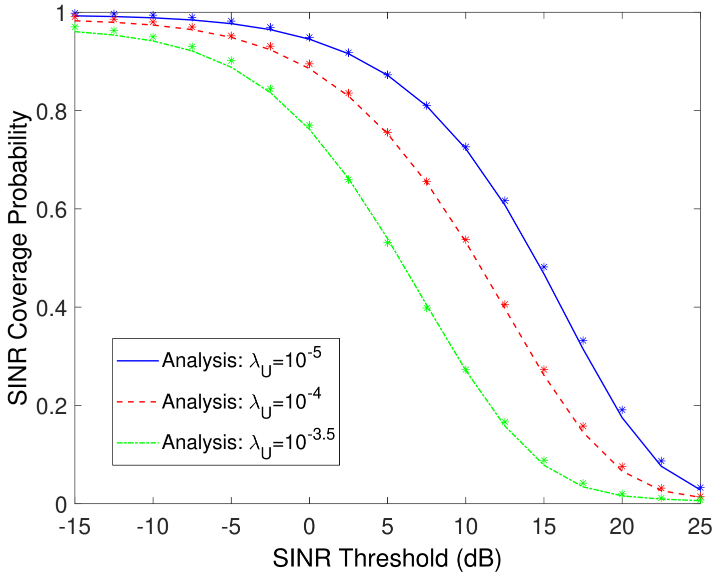

Figure 7.5: SINR coverage probability as a function of the threshold in dB for different values of UAV density λ_U. Simulation results are also plotted with markers.

this optimal value, the effect of the increased received power from interfering UAVs offsets the benefit of covering more UEs due to having more UAVs. Furthermore, decrease in the UE distribution's standard deviation σ_c results in a higher ASE for the same value of λ_U. Smaller σ_c means that UEs are, on average, more compactly packed around the cluster center, and hence the distance between the UAV at the cluster center is shorter. Therefore, coverage probability is improved for smaller σ_c. Also, optimal value for λ_U increases with decreasing σ_c indicating that more UAVs can be deployed to support more UEs if UEs are located compactly in each cluster.

Finally, in Fig. 7.7, we plot the SINR coverage probability as a function of the SINR threshold for two different values of the UE distribution's standard deviation σ_c when UAVs are assumed to be located at different heights. In this setup, we use the same parameters given in Table 7.1 with some differences for UAV height and UAV density. More specifically, we consider $M = 2$ groups of UAVs located at altitudes $H_1 = 10$m and $H_2 = 20$m with densities $\lambda_{U,1} = \lambda_{U,2} = \lambda_U/2$ and transmit powers $P_1 = P_2 = 37$dBm. Therefore, transmit power of the 0^{th} UAV is also equal

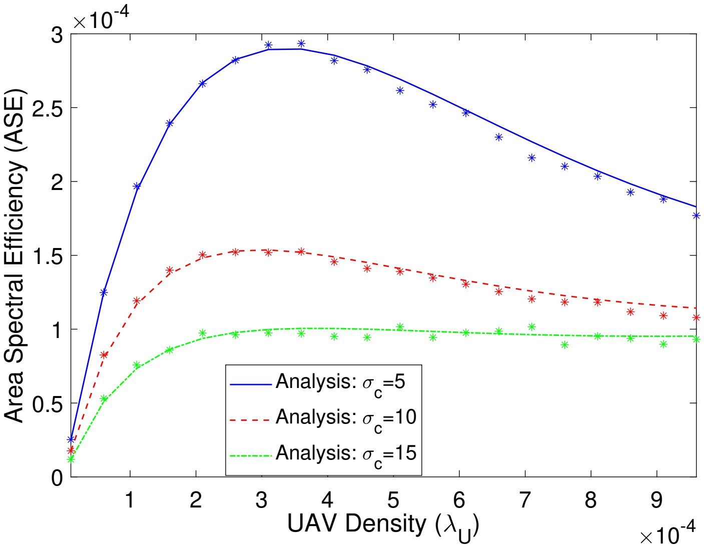

Figure 7.6: Area spectral efficiency (ASE) as a function of UAV density λ_U for different values of UE distribution's standard deviation σ_c. Simulation results are also plotted with markers.

to $P_0 = 37$dBm. Moreover, transmit power of the 3rd tier ground BSs is equal to $P_3 = 40$dBm. In Fig. 7.7, solid lines plot the coverage probabilities when the height is the same for all UAVs. Dashed lines display the coverage probabilities when half of the UAVs are located at height H_1 and the other half are located at height H_2, and the typical UE is clustered around a UAV at either height H_1 or H_2. As shown in the figure, for $\sigma_c = 5$ when the typical UE is clustered around a UAV at height $H_1 = 10$m in the model with two different UAV heights, it experiences almost the same coverage performance with the typical UE when all UAVs are at the same height of $H_1 = 10$m. The same observation can be made for the case of $H_2 = 20$m. On the other hand, when σ_c gets larger (and hence the UEs are more widely spread around the cluster-center UAV), coverage performance in the model with UAVs at two different height levels becomes worse than that of the case in which all UAVs are at the same height. Moreover, coverage performances for the typical UEs clustered around UAVs at heights $H_1 = 10$m and $H_2 = 20$m approach each other. There are mainly three reasons behind these results: 1) association probability with the other

UAVs and BSs rather than the cluster-center 0^{th} tier UAV increases for larger values of σ_c (e.g., see Fig. 7.2); 2) when the typical UAV is clustered around a UAV at height $H_1 = 10$m, interference from half of the UAVs located at height $H_2 = 20$m is smaller than that if all UAVs were at the same height of $H_1 = 10$m, but at the same time if the UE is associated not with its cluster center UAV but with a UAV at height $H_2 = 20$m, link distance will be larger, adversely affecting the coverage probability; 3) when the typical UE is clustered around a UAV at height $H_2 = 20$m, interference from half of the UAVs located at the lower height of $H_1 = 10$m is greater but if the UE is associated with a non-cluster-center UAV at height $H_1 = 10$m then the link quality can be better due to shorter distance. Hence, there are several interesting competing factors and tradeoffs. As a result, we observe in the case of large σ_c that due to either increased interference or higher likelihood of being associated with a UAV at a larger height, coverage performances in the model with different UAV heights get degraded compared to the scenario in which all UAVs are at the same height.

7.7 Conclusion

In this chapter, we have provided an analytical framework to compute the SINR coverage probability of UAV assisted cellular networks with clustered UEs. Moreover, we have formulated the ASE, and investigated the effect of UAV density and standard deviation of the UE distribution on the ASE. Furthermore, we have presented SINR coverage probability expression for a more general model by considering that UAVs are located at different heights. UAVs and ground BSs are assumed to be distributed according to independent PPPs, while locations of UEs are modeled as a PCP around the projections of UAVs on the ground and UEs are assumed to be connected to the tier providing the maximum average biased-received power.

Using numerical results, we have shown that standard deviation of UE distribu-

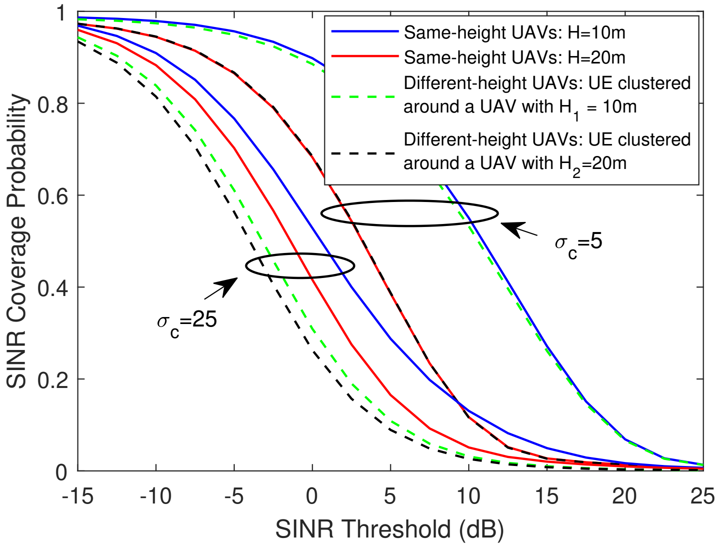

Figure 7.7: SINR coverage probability as a function of the threshold in dB for two different values of the UE distribution's standard deviation σ_c. Solid lines show the coverage probabilities when half of the UAVs are located at height $H_1 = 10$m and the other half are located at height $H_2 = 20$m, and the typical UE is clustered around a UAV at either height H_1 or H_2.

tion σ_c and UAV height H have significant impact on association probabilities. For instance, less compactly located UEs and higher UAV height lead to a decrease in the association with the cluster center UAV. We have also shown that total coverage probability can be improved by reducing the UAV height as a result of the decrease in the distances between cluster center UAV and UEs. Moreover, path-loss exponents play a crucial role in the coverage performance if the UAV height is high, and there exists an optimal value for path-loss exponents in which the coverage probability is maximized. Another important observation is that smaller number of UAVs results in a better coverage performance, while deployment of more UAVs lead to a higher ASE. Furthermore, a higher ASE can be achieved if the UES are located more compactly in each cluster.

Chapter 8

Energy Harvesting in Unmanned Aerial Vehicle Networks with 3D Antenna Radiation Patterns

In this chapter, an analytical framework is provided to analyze the energy coverage performance of unmanned aerial vehicle (UAV) energy harvesting networks with clustered user equipments (UEs). Locations of UAVs are modeled as a Poison Point Process (PPP), while locations of UEs are modeled as a Poisson Cluster Process (PCP). Two different models are considered for the line-of-sight (LOS) probability function to compare their effect on the network performance. Moreover, ultra-wideband (UWB) antennas with doughnut-shaped radiation patterns are employed in both UAVs and UEs, and the impact of practical 3D antenna radiation patterns on the network performance is also investigated. Initially, the complementary cumulative distribution function (CCDF) and probability density function (PDF) of path losses for each tier are derived. Subsequently, association probabilities with each tier are obtained. Energy coverage probability is derived for the entire network using tools from stochastic geometry. Via numerical results, we have shown that cluster size and UAV height play crucial roles on the energy coverage performance. Furthermore, energy coverage probability is significantly affected by the antenna orientation and number of UAVs in the network.

8.1 Introduction

In order to meet the growing data demand due to increasing use of smart phones, portable devices, and data-hungry multimedia applications, new technologies and designs have been under consideration for 5G cellular networks. As we discussed in Chapter 7, one of them is expected to be the deployment UAV BSs. UAVs have been primarily considered as high-altitude platforms at altitudes of kilometers to provide coverage in rural areas. On the other hand, use of low-altitude UAVs has also become popular recently due to the advantage of having better link quality in shorter-distance line-of-sight (LOS) channels with the ground users. Moreover, owing to the relative flexibility in UAV deployments, UAV BSs can be employed in a variety of scenarios including public safety communications and data collection in Internet of Things (IoT) applications. Other scenarios include disasters, accidents, and other emergencies and also temporary events requiring substantial network resources in the short-term such as in concerts and sporting events, in order to provide wireless connectivity rapidly [17]–[19].

In addition to growing data traffic, increasing number of devices results in a significant growth in energy demand. RF (radio frequency) energy harvesting where a harvesting device may extract energy from the incident RF signals has emerged as a promising solution to power up low-power consuming devices [97], [98]. Therefore, the advances in energy harvesting technologies have motivated research in the study of different wireless energy harvesting networks. For example, wireless energy and/or information transfer in large-scale millimeter-wave and microwave networks has been studied in [99]–[102]. In these works, energy is harvested wirelessly from energy transmitters which are generally deployed at fixed locations. However, low-power consuming devices can potentially be distributed in a large area, and in such cases the performance of energy harvesting will be limited by the low end-to-end power transmission efficiency due to the loss of RF signals over long distances [103].

In order to improve the efficiency, instead of fixed energy transmitters such as ground base stations (BSs), the deployment of mobile energy transmitters is proposed recently. In particular, UAV-assisted energy harvesting has become attractive due to the flexibility and relative ease in deploying UAV BSs. In [104], mobility of the UAV with a directional antenna is exploited by jointly optimizing the altitude, trajectory, and transmit beamwidth of the UAV in order to maximize the energy transferred to two energy receivers over a finite charging period. In [103], authors consider a more general scenario with more than two energy receivers where the amount of received energy by all energy receivers is maximized via trajectory control. In [105], a UAV-enabled wireless power transfer network is studied as well. Minimum received energy among all ground nodes is maximized by optimizing the UAV's one-dimensional trajectory. Both downlink wireless power transfer and uplink information transfer is considered in [106] with one UAV and a set of ground users in which the UAV charges the users in downlink and users use the harvested energy to send the information to the UAV in the uplink. Similarly, a wireless-powered communication network with a mobile hybrid access point UAV is considered in [107] where the UAV performs weighted energy transfer and receives information from the far-apart nodes based on the weighted harvest-then-transmit protocol.

In a separate line of research in the literature, the performance of UAV-assisted wireless networks is extensively studied recently. Similar to 2D networks, stochastic geometry has been employed in the network level analysis of UAV networks by considering UAVs distributed randomly in 3D space. Effect of different network parameters on the coverage probability is explored in several recent works such as [27], [76], [77]. Spectrum sharing in UAV networks is analyzed in [79], [84], [108]. Additionally, optimal deployment of UAVs is investigated in [80]–[83].

It is important to note that the antenna number, type, and orientation are critical factors that affect the performance in UAV-assisted networks. Indeed, several recent studies, e.g., [109] and [110], have addressed scenarios in which antenna arrays are deployed in UAV-assisted cellular networks. Regarding the antenna type, omnidirectional antennas can be used especially considering the mobility of UAVs [111]. At the same time, since even the UAV's own body can shadow the antenna and result in a poor link quality, the orientation of the antennas plays an important role on the performance [112]. There has been limited analytical and experimental works studying the effect of three dimensional (3D) antenna radiation patterns on the link quality between the UAV and ground users. In [112], impact of antenna orientation is investigated by placing two antennas on a fixed wing UAV flying on a linear path with 802.11a interface. Similarly, path loss and small-scale fading characteristics of UAV-to-ground user links are analyzed with a simple antenna extension to 802.11 devices in [113]. In [114], ultra-wideband (UWB) antennas with doughnut-shaped radiation patterns are employed at both UAVs and ground users to analyze the link quality at different link distances, UAV heights, and antenna orientations. Authors develop a simple analytical model to approximate the impact of the 3D antenna radiation pattern on the received signal. However, none of these works study the effect of UAV antenna orientation on the network performance.

Similar to Chapter 7, in this chapter we also consider a UAV network consisting of UAVs operating at a certain altitude above ground. While we model the locations of UAVs as Poisson Point Process (PPP) distributed, locations of UEs are modeled as a Poisson cluster process (PCP). Since UAVs are deployed in overloaded scenarios, locations of UAVs and UEs are expected to be correlated and UEs are more likely to form clusters. Hence, modeling the UE locations by PCP is more appropriate and realistic. Moreover, we consider that UWB antennas with doughnut-shaped radiation patterns are employed at both UAVs and UEs, and we study the effect of practical 3D antenna radiation patterns on the network performance.

More specifically, our main contributions can be summarized as follows:

- An analytical framework is provided to analyze energy coverage performance of a UAV network with clustered UEs by employing tools from stochastic geometry. Locations of UEs are modeled as PCP distributed to capture the correlations between the UAV and UE locations.
- We divide the network into two tiers: 0^{th} tier UAV and 1^{st} tier UAVs. 0^{th} tier UAV is the cluster center UAV around which the typical UE is located, while other UAVs constitute the 1^{st} tier.
- Two different LOS probability functions, i.e., a high-altitude model and a low-altitude model, are considered in order to investigate and compare their impact on the network performance.
- Different from the previous studies, more practical antennas with doughnut-shaped radiation patterns are employed at both UAVs and UEs to provide a more realistic performance evaluation for the network.
- We first derive the CCDFs and the PDFs of the path losses for each tier, then obtain the association probabilities by using the averaged received power UAV association rule.
- Total energy coverage probability is determined by deriving the Laplace transforms of the interferences from each tier using tools from stochastic geometry.

8.2 System Model

In this section, the system model for a UAV network with clustered UEs is presented. We consider a downlink network, where the UAVs are spatially distributed according to an independent homogeneous PPP Φ_U with density λ_U on the Euclidean plane. UAVs are placed at a height of H above the ground. UAVs are deployed to provide relief to the ground cellular BSs by offloading traffic from them around hotspots or large gatherings such as sporting events or concerts. In energy harvesting applications, UAVs can be used to transfer energy to e.g., ground sensors, to energize them. They can also be deployed during emergencies or other instances during which ground BS resources are strained [85]. UEs are clustered around the projections of UAVs on the ground, and the union of cluster members' locations form a PCP, denoted by Φ_C. Since UEs are located in high UE density areas, they are expected to be closer to each other, forming clusters. Therefore, PCP is a more appropriate and accurate model than a homogeneous PPP.

In this chapter, we model Φ_C as a Thomas cluster process, where the UEs are symmetrically independently and identically distributed (i.i.d.) around the cluster centers (which are projections of UAVs on the ground), according to a Gaussian distribution with zero mean and variance σ_c^2. The probability density function (PDF) and complementary cumulative distribution function (CCDF) of a UE's location are given, respectively, by [40]

$$f_D(d) = \frac{d}{\sigma_c^2} \exp\left(-\frac{d^2}{2\sigma_c^2}\right), \quad d \in \mathbb{R}^2, \tag{8.1}$$

$$\bar{F}_D(d) = \exp\left(-\frac{d^2}{2\sigma_c^2}\right), \quad d \in \mathbb{R}^2. \tag{8.2}$$

where d is the 2D distance of a UE with respect to the cluster center on the ground. Without loss of generality, a typical UE is assumed to be located at the origin according to Slivnyak's theorem, and it is associated with the UAV providing the maximum

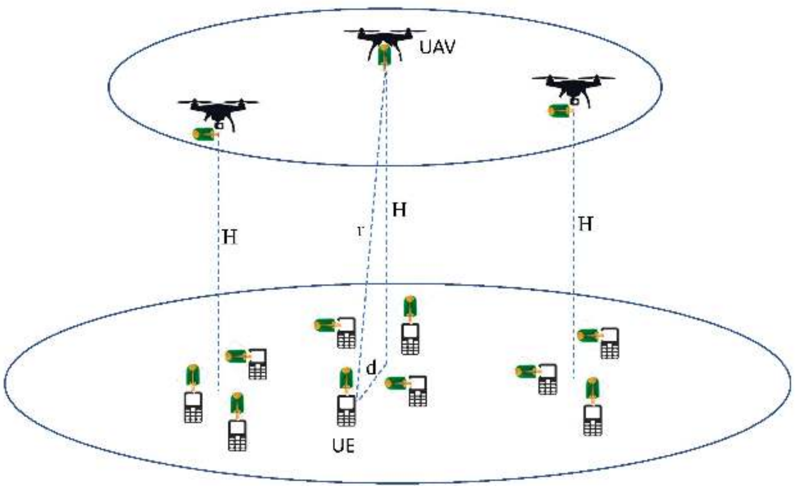

Figure 8.1: Network model for a UAV energy harvesting network. BSs are distributed as a PPP, while UEs are normally distributed around the cluster centers (projections of UAVs on the ground). Both BS and UEs are equipped with UWB antennas with different antenna orientations.

average received power. Although we have only one tier network composed of UAVs, we also consider an additional tier, named as 0^{th} tier that only includes the cluster center of the typical UE similarly as in [27] and [93]. Thus, our network model can be considered as a two-tier network consisting of a 0^{th} tier cluster-center UAV and 1^{st} tier UAVs. The proposed network model is shown in Fig. 8.1.

8.2.1 Path Loss and Blockage Modeling

A transmitting UAV can either have a line-of-sight (LOS) or non-line-of-sight (NLOS) link to the typical UE. Consider an arbitrary link of length r between a UE and a UAV, and define the LOS probability function as the probability that the link is LOS. Different LOS probability functions have been proposed in the literature. In this chapter, we adopt the two models proposed in [75] and [115], which are high-altitude and low-altitude models, respectively.

High-altitude model is widely used especially in satellite communications where the altitude is around thousands of meters. It has also been widely employed in UAV-assisted networks recently. LOS probability function for the high-altitude model is given as follows:

$$\mathcal{P}_{\text{LOS}}^{\text{high}}(r) = \left(\frac{1}{1 + b \exp\left(-c\left(\frac{180}{\pi}\sin^{-1}\left(\frac{H}{r}\right) - b\right)\right)} \right), \tag{8.3}$$

where r is the 3D distance between the UE and UAV, H is the UAV height, b and c are constants which depend on the environment. As can be seen in (8.3), probability of having a LOS connection increases as the height of the UAVs increases.

Since practical values for UAV height in certain applications is around 50∼100 meters, a more realistic LOS probability function proposed for 3GPP terrestrial communications is employed also for UAV networks in [115]. The height of a macrocell base station is usually around 32 m, which is comparable to the practical UAV height. Therefore, employment of the LOS probability function for 3GPP macrocell-to-UE communciation is also reasonable for the UAV networks in such relatively low-altitude scenarios. For the low-altitude model, LOS probability function is expressed as

$$\mathcal{P}_{\text{LOS}}^{\text{low}}(r) = \min\left(1, \frac{18}{r}\right)\left(1 - \exp\left(-\frac{r}{63}\right)\right) + \exp\left(-\frac{r}{63}\right). \tag{8.4}$$

Note that different from the high-altitude model, LOS probability function in (8.4) decreases with the increase in the 3D distance r, independent of the UAV height. In Fig. 8.2, LOS probability function is plotted using high-altitude and low-altitude models. Solid lines show the LOS probability as a function of the UAV height H when the 2D distance to the cluster center UAV is fixed at $d = 10$ m, and dashed lines display the LOS probability as a function of the 2D distance to the cluster center UAV d when the UAV height is $H = 50$ m. As shown in Fig. 8.2, LOS probability increases with increasing UAV height when the high-altitude model is used, and decreases when the low-altitude model is considered. We observe that the LOS probability decreases for both models as the 2D distance to the cluster center UAV increases. We also note that the analysis in the remainder of the chapter is general and is applicable to

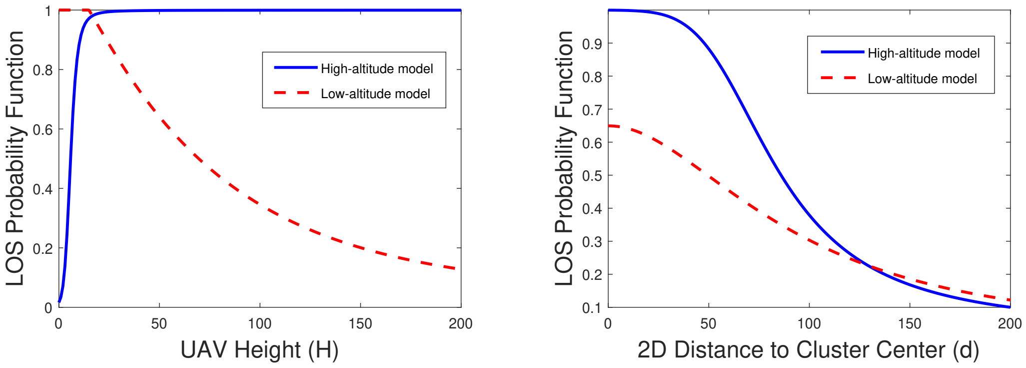

(a) (b)

Figure 8.2: LOS probability function for high-altitude and low-altitude models as a function of (a) UAV height H and (b) 2D distance to the cluster center UAV d.

any LOS probability function. Only in Section 8.5, we employ the LOS probability functions in (8.3) and (8.4) to obtain the numerical results.

Path loss in NLOS links is generally higher than the path-loss in LOS links due to the reflection and scattering of signals. Therefore, different path loss laws are applied to LOS and NLOS links. Thus, the path loss on each link in tier k for $k = 0, 1$ can be expressed as follows:

$$\begin{aligned} L_{k,\mathrm{LOS}}(r) &= r^{\alpha_{\mathrm{LOS}}} \\ L_{k,\mathrm{NLOS}}(r) &= r^{\alpha_{\mathrm{NLOS}}}, \end{aligned} \tag{8.5}$$

where α_{LOS} and α_{NLOS} are the LOS and NLOS path-loss exponents, respectively.

8.2.2 3D Antenna Modeling

In this chapter, we adopt the analytical model developed in [114] for the effect of 3D antenna radiation patterns on the received signal. UWB transmitter and receiver antennas with doughnut-shaped radiation patterns are placed at the UAV and UE, respectively, and air-to-ground channel measurements are carried out in order to characterize the impact of the 3D antenna radiation pattern on the received signal for different antenna orientations in [114]. As a result of these measurements, transmitter and receiver antenna gains are modeled analytically for horizontal-horizontal (HH), horizontal-vertical (HV) and vertical-vertical (VV) antenna orientations as follows:

$$G_k(\theta) = G_{\mathrm{TX}}(\theta)G_{\mathrm{RX}}(\theta) = \begin{cases} \sin(\theta)\sin(\theta) & \text{for} \quad \text{HH} \\ \sin(\theta)\cos(\theta) & \text{for} \quad \text{HV}, \\ \cos(\theta)\cos(\theta) & \text{for} \quad \text{VV} \end{cases} \tag{8.6}$$

where θ is the elevation angle between the transmitter at the UAV and the receiver at the UE on the ground. In this antenna model, radiation pattern is approximated by a circle in the vertical dimension, while it is assumed to be constant for all horizontal directions. In other words, antenna gains depend only on the elevation angle θ, and are considered as independent of the azimuth angle between the transmitter at the UAV and the receiver at the UE. Approximated antenna radiation patterns of UAV and UE are shown in Fig. 8.3 for HH antenna orientation. They can be plotted for HV and VV orientations as well by rotating the transmitter and/or receiver antennas by 90°. Note that for HH antenna orientation $G_{\mathrm{TX}}(\theta) = G_{\mathrm{RX}} \to 0$ as $\theta \to 0$ which happens when the UEs are located far away from the cluster center, i.e. as the σ_c increases, and $G_{\mathrm{TX}}(\theta) = G_{\mathrm{RX}} \to 1$ as $\theta \to 90^o$ which happens when the UEs get closer to the cluster center. Similar observations can be drawn for VH and VV antenna orientations. Effective antenna gain G_k as a function of r can be rewritten in terms of UAV height H and the path loss on each link in tier k for $k = 0, 1$ as follows:

$$G_k(r) = \begin{cases} H^2 L_{k,s}^{-\frac{2}{\alpha_s}}(r) & \text{for} \quad \text{HH} \\ H\left(\sqrt{L_{k,s}^{\frac{2}{\alpha_s}}(r) - H^2}\right) L_{k,s}^{-\frac{2}{\alpha_s}}(r) & \text{for} \quad \text{HV} \\ \left(L_{k,s}^{\frac{2}{\alpha_s}}(r) - H^2\right) L_{k,s}^{-\frac{2}{\alpha_s}}(r) & \text{for} \quad \text{VV}. \end{cases} \tag{8.7}$$

In the rest of the analysis, we assume that the typical UE and all UAVs in the

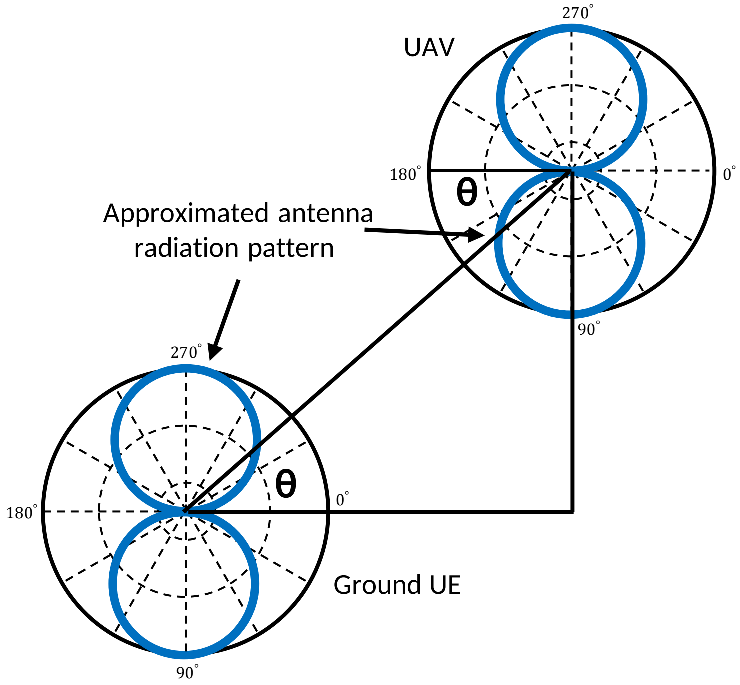

Figure 8.3: Approximated antenna radiation pattern for HH antenna orientation.

network have horizontal antenna orientation. Therefore, HH antenna orientation for the main link and interfering links are considered due to its analytical tractability. Moreover, UEs are considered to be clustered around the projections of UAVs on the ground and more UEs are encouraged to be associated with their cluster center UAV. As a result, the angle between the transmitter at the UAV and the receiver at the UE is expected to be large. Therefore, HH antenna orientation is more suitable than the other two orientations. However, in the numerical results section, simulation results for HV and VV orientations are also provided in order to compare their effect on the UAV association and energy coverage probabilities.

8.3 Path Loss and UAV Association

8.3.1 Statistical Characterization of the Path Loss

We first characterize the complementary cumulative distribution function (CCDF) and the probability density function (PDF) of the path loss in the following lemmas and corollaries.

Lemma 8.1 *The CCDF of the path loss from a typical UE to a* 0^{th} *tier UAV can be formulated as*

$$\begin{aligned}\bar{F}_{L_0}(x) &= \sum_{s\in\{LOS,NLOS\}} \bar{F}_{L_{0,s}}(x) \\ &= \sum_{s\in\{LOS,NLOS\}} \int_{\sqrt{x^{2/\alpha_s}-H^2}}^{\infty} \mathcal{P}_s(\sqrt{d^2+H^2}) f_D(d)\mathrm{d}d, \end{aligned} \tag{8.8}$$

where $f_D(d)$ *is given in (8.1),* $\mathcal{P}_s(\cdot)$ *is the LOS or NLOS probability depending on whether* $s = LOS$ *or* $s = NLOS$ [1]*.*

Proof: See Appendix M.

Lemma 8.2 *CCDF of the path loss from a typical UE to a* 1^{st} *tier UAV is given by*

$$\bar{F}_{L_1}(x) = \prod_{s\in\{LOS,NLOS\}} \bar{F}_{L_{1,s}}(x) = \prod_{s\in\{LOS,NLOS\}} \exp\big(-\Lambda_{1,s}([0,x))\big), \tag{8.9}$$

where $\Lambda_{1,s}([0,x))$ *is defined as follows:*

$$\Lambda_{1,s}([0,x)) = 2\pi\lambda_U \int_H^{x^{\frac{1}{\alpha_s}}} \mathcal{P}_s(r) r\mathrm{d}r. \tag{8.10}$$

---

[1] For instance, LOS probability is given by (8.3) and (8.4) for the high-altitude and low-altitude models, respectively, and NLOS probability is $P_{\text{NLOS}} = 1 - P_{\text{LOS}}$

Proof: See Appendix N.

Corollary 8.1 *The PDF of the path loss from a typical UE to a* 0^{th} *tier LOS/NLOS UAV can be computed by using the Leibniz integral rule as follows:*

$$\begin{aligned} f_{L_{0,s}}(x) &= -\frac{d\bar{F}_{L_{0,s}}(x)}{dx} \\ &= \frac{1}{\sigma_c^2}\frac{x^{\frac{2}{\alpha_s}-1}}{\alpha_s}\mathcal{P}_s\left(x^{\frac{1}{\alpha_s}}\right)\exp\left(-\frac{1}{2\sigma_c^2}\left(x^{\frac{2}{\alpha_s}}-H^2\right)\right). \end{aligned} \tag{8.11}$$

Corollary 8.2 *The PDF of the path loss from a typical UE to a* 1^{st} *tier LOS/NLOS UAV can be computed as*

$$f_{L_{1,s}}(x) = -\frac{d\bar{F}_{L_{1,s}}(x)}{dx} = \Lambda'_{1,s}([0,x))\exp\big(-\Lambda_{1,s}([0,x))\big), \tag{8.12}$$

where $\Lambda'_{1,s}([0,x))$ *is obtained as follows using the Leibniz integral rule:*

$$\Lambda'_{1,s}([0,x)) = 2\pi\lambda_U\frac{x^{\frac{2}{\alpha_s}-1}}{\alpha_s}\mathcal{P}_s\left(x^{\frac{1}{\alpha_s}}\right). \tag{8.13}$$

In the results above, we have determined the CCDFs and PDFs of the path loss for each tier. They depend on the key network parameters including the variance of the cluster process σ_c^2, UAV density λ_U, UAV LOS probability $\mathcal{P}_s(\cdot)$, UAV height H and path loss exponents α_s. In the following sections, these distributions are utilized in determining the association and energy coverage probabilities.

8.3.2 Cell Association

In this work, UEs are assumed to be associated with a UAV offering the strongest long-term averaged power. In other words, a typical UE is associated with its cluster center UAV, i.e., the 0th UAV, if

$$P_0 G_0(r) L_0^{-1}(r) \geq P_1 G_1(r) L_{\min,1}^{-1}(r), \tag{8.14}$$

where P_k and $G_k(r)$ denote the transmit power and antenna gain of the link, respectively, in tier $k \in (0, 1)$. $L_0(r)$ is the path loss from the 0th tier UAV, and $L_{\min,1}(r)$ is the path loss from 1st UAV providing the minimum path loss. In the following lemma, we provide the association probabilities using the result of Lemmas 8.1 and 8.2 and Corollaries 8.1 and 8.2.

Lemma 8.3 *The association probabilities with a* 0^{th} *tier LOS/NLOS UAV and* 1^{st} *tier LOS/NLOS UAV are given, respectively, as*

$$\mathcal{A}_{0,s} = \int_{H^{\alpha_s}}^{\infty} \prod_{m \in \{LOS, NLOS\}} \bar{F}_{L_{1,m}} \left(\left(\frac{P_1}{P_0} l_{0,s}^{\frac{2}{\alpha_s}+1} \right)^{\frac{\alpha_m}{\alpha_m+2}} \right) f_{L_{0,s}}(l_{0,s}) \mathrm{d}l_{0,s}, \tag{8.15}$$

$$\mathcal{A}_{1,s} = \int_{H^{\alpha_s}}^{\infty} \sum_{m \in \{LOS, NLOS\}} \bar{F}_{L_{0,m}} \left(\left(\frac{P_0}{P_1} l_{1,s}^{\frac{2}{\alpha_s}+1} \right)^{\frac{\alpha_m}{\alpha_m+2}} \right) \bar{F}_{L_{1,s'}}(l_{1,s}) f_{L_{1,s}}(l_{1,s}) \mathrm{d}l_{1,s}, \tag{8.16}$$

where $s, s' \in \{LOS, NLOS\}$ *and* $s \neq s'$.

Proof: See Appendix O.

8.4 Energy Coverage Probability Analysis

In this section, we develop a theoretical framework to analyze the energy coverage probability for a typical UE clustered around the 0th tier UAV (i.e., its own cluster-center UAV) using stochastic geometry.

8.4.1 Downlink Power Transfer

The total power received at a typical UE at a random distance r from its associated UAV in the k^{th} tier can be written as

$$P_{r,k} = S_k + \sum_{j=0}^{1} I_{j,k} \quad \text{for} \quad k = 0, 1, \tag{8.17}$$

where the received power from the serving UAV S_k and the interference power received from the UAVs in the j^{th} tier $I_{j,k}$ are given as follows:

$$S_k = P_k G_k(r) h_{k,0} L_k^{-1}(r), \tag{8.18}$$

$$I_{0,1} = P_0 G_0(r) h_{0,0} L_0^{-1}(r), \tag{8.19}$$

$$I_{1,k} = \sum_{i \in \Phi_U \setminus \mathcal{E}_{k,0}} P_1 G_i(r) h_{1,i} L_i^{-1}(r), \tag{8.20}$$

where $h_{k,0}$ and $h_{j,i}$ are the small-scale fading gains from the serving and interfering UAVs, respectively. Note that since only one UAV exists in the 0^{th} tier, $I_{0,0} = 0$. All links are assumed to be subject to independent Rayleigh fading, i.e., small-scale fading gains denoted by h have an exponential distribution. According to the UAV association policy, when a typical UE is associated with a UAV whose path loss is $L_k(r)$, there exists no UAV within a disc $\mathcal{E}_{k,0}$ centered at the origin. This region is referred to as the exclusion disc.

8.4.2 Energy Coverage Probability

The energy harvested at a typical UE in unit time is expressed as $E_k = \xi P_{r,k}$ where $\xi \in (0, 1]$ is the rectifier efficiency, and $P_{r,k}$ is the total received power given in (8.17). Since the effect of additive noise power is negligibly small relative to the total received power, it is omitted [99]. The conditional energy coverage probability $\mathrm{E}_k^{\mathrm{C}}(\Gamma_k)$ is defined as the probability that the harvested energy E_k is larger than the energy outage threshold $\Gamma_k > 0$ given that the typical UE is associated with a UAV from the k^{th} tier, i.e., $\mathrm{E}_k^{\mathrm{C}}(\Gamma_k) = \mathbb{P}(E_k > \Gamma_k | t = k)$ where t indicates the associated tier. Therefore, total energy coverage probability E^{C} for the typical UE can be computed as follows:

$$\mathrm{E}^{\mathrm{C}} = \sum_{k=0}^{1} \sum_{s \in \{\text{LOS,NLOS}\}} \left[\mathrm{E}_{k,s}^{\mathrm{C}}(\Gamma_k) \mathcal{A}_{k,s} \right], \tag{8.21}$$

where $\mathrm{E}_{k,s}^{\mathrm{C}}(\Gamma_k)$ is the conditional energy coverage probability given that the UE is associated with a k^{th} tier LOS/NLOS UAV, $\mathcal{A}_{k,s}$ is the association probability. In the following theorem, we provide the main result for the total energy coverage probability.

Theorem 8.1 *In a UAV network with practical antenna radiation patterns and clustered UEs, the total energy coverage probability for the typical UE is approximately given by*

$$\begin{aligned}
E^C \approx & \sum_{s \in \{LOS,NLOS\}} \sum_{n=0}^{N} (-1)^n \binom{N}{n} \\
& \times \Bigg[\int_{H^{\alpha_s}}^{\infty} \left(1 + \hat{a} P_0 H^2 l_{0,s}^{-\left(1+\frac{2}{\alpha_s}\right)} \right)^{-1} \mathcal{L}_{I_{1,0}}\left(\Gamma_0, \mathcal{E}_{0,0}\right) \\
& \qquad \times \prod_{m \in \{LOS,NLOS\}} \bar{F}_{L_{1,m}} \left(\left(\frac{P_1}{P_0} l_{0,s}^{\frac{2}{\alpha_s}+1} \right)^{\frac{\alpha_m}{\alpha_m+2}} \right) f_{L_{0,s}}(l_{0,s}) \mathrm{d}l_{0,s} \\
& + \int_{H^{\alpha_s}}^{\infty} \left(1 + \hat{a} P_1 H^2 l_{1,s}^{-\left(1+\frac{2}{\alpha_s}\right)} \right)^{-1} \left(\prod_{j=0}^{1} \mathcal{L}_{I_{j,1}}\left(\Gamma_1, \mathcal{E}_{1,0}\right) \right) \\
& \qquad \times \sum_{m \in \{LOS,NLOS\}} \bar{F}_{L_{0,m}} \left(\left(\frac{P_0}{P_1} l_{1,s}^{\frac{2}{\alpha_s}+1} \right)^{\frac{\alpha_m}{\alpha_m+2}} \right) \bar{F}_{L_{1,s'}}(l_{1,s}) f_{L_{1,s}}(l_{1,s}) \mathrm{d}l_{1,s} \Bigg]
\end{aligned} \tag{8.22}$$

where $\hat{a} = \frac{n\eta}{\Gamma_k/\xi}$, $\eta = N(N!)^{-\frac{1}{N}}$, *$N$ is the number of terms in the approximation and the Laplace transforms of the interference terms are given by*

$$\mathcal{L}_{I_{0,k}}(\Gamma_k, \mathcal{E}_{k,0}) = \sum_{s' \in \{LOS,NLOS\}} \int_{\mathcal{E}_{k,0}}^{\infty} \left(1 + \hat{a} P_0 H^2 x^{-\left(1+\frac{2}{\alpha_{s'}}\right)} \right)^{-1} f_{L_{0,s'}}(x) \mathrm{d}x, \tag{8.23}$$

$$\mathcal{L}_{I_{1,k}}(\Gamma_k, \mathcal{E}_{k,0}) =$$

$$\prod_{s' \in \{LOS,NLOS\}} \exp\left(-\int_{\mathcal{E}_{k,0}}^{\infty} \left(1 - \left(1 + \hat{a} P_1 H^2 x^{-\left(1+\frac{2}{\alpha_{s'}}\right)} \right)^{-1} \right) \Lambda'_{1,s'}([0,x))\mathrm{d}x \right). \quad (8.24)$$

Proof: See Appendix P.

Note that since 0^{th} tier consists of only one UAV, i.e., the cluster center UAV, Laplace transform expression $\mathcal{L}_{I_{0,0}}(\Gamma_0, \mathcal{E}_{0,0}) = 1$. General sketch of the proof is as follows. First, energy coverage probability is computed given that a UE is associated with a k^{th} tier LOS/NLOS UAV. Subsequently, each of the conditional probabilities are multiplied with their corresponding association probabilities, and are summed up to obtain the total energy coverage probability of the network. In order to determine the conditional energy coverage probabilities, Laplace transforms of interferences from each tier are obtained using tools from stochastic geometry. We also note that although the characterization in Theorem 8.1 involves multiple integrals, we explicitly see the dependence of the energy coverage on, for instance, UAV heights, path loss distributions, path loss exponents, transmission power levels. Moreover, the integrals can be computed relatively easily by using numerical integration tools, providing us with additional insight on the impact of key system/network parameters, as demonstrated in the next section.

8.5 Simulation and Numerical Results

In this section, we provide the numerical evaluations of theoretical expressions in addition to the simulation results in order to validate the accuracy of the proposed UAV network model as well as to confirm of the analytical characterizations. In the numerical evaluations and simulations, unless stated otherwise, the parameter values listed in Table 8.1 are used.

Table 8.1: System Parameters

Description	**Parameter**	**Value**
Path-loss exponents	α_{LOS}, α_{NLOS}	2, 4
Environment dependent constants	b, c	11.95, 0.136
Height of UAVs	H	50 m
Transmit power	$P_k\ \forall k$	37 dBm
Energy outage threshold	$\Gamma_k\ \forall k$	-30 dB
UAV density	λ_U	10^{-4} (1/m^2)
UE distribution's standard deviation	σ_c	10
Rectifier efficiency	ξ	1

8.5.1 Impact of Cluster Size

First, we investigate the effect of UE distribution's standard deviation σ_c on the association probability and the energy coverage probability using the LOS probability functions of high-altitude and low-altitude models of (8.3) and (8.4) in Figs. 8.4a and 8.4b. As the standard deviation increases, the UEs have a wider spread and the distances between the cluster-center 0^{th} tier UAV and UEs also increase. As a result, association probability with the 0^{th} tier UAV, $\mathcal{A}_0$, decreases, while the association probability with 1^{st} tier UAVs, $\mathcal{A}_1$, increases for both models. Also, for a fixed height, LOS probability of cluster center UAV decreases for both models with the increasing cluster size, and hence association probabilities exhibit similar trends. Therefore, the energy coverage probability of the 0^{th} tier UAV, $\mathrm{E}_0^{\mathrm{C}}$, increases while the energy coverage probability of the 1^{st} tier UAVs, $\mathrm{E}_1^{\mathrm{C}}$, decreases as the cluster size grows in both models. On the other hand, the increase in $\mathrm{E}_1^{\mathrm{C}}$ cannot compensate the decrease in $\mathrm{E}_0^{\mathrm{C}}$, and therefore the total energy coverage probability E^{C} diminishes. In other words, smaller cluster size, i.e., more compactly distributed UEs results in a higher E^{C}. Finally, we note that simulation results are also plotted in the figure with markers and there is a very good match between simulation and analytical results, further confirming our analysis.

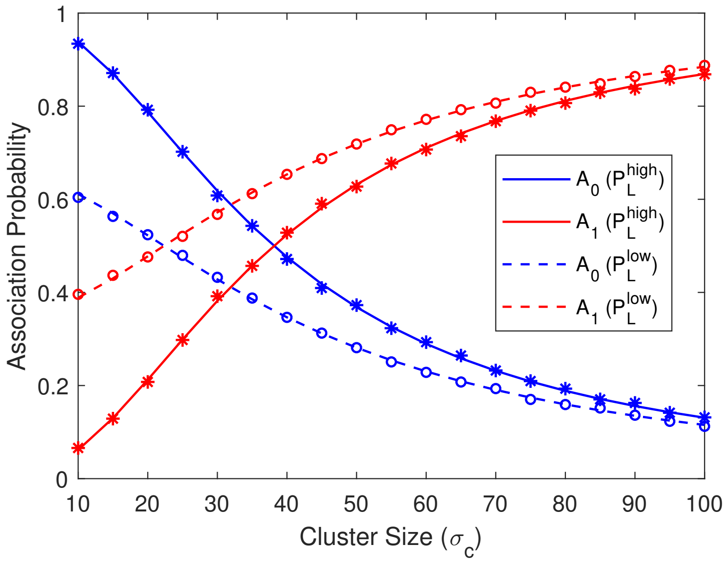

(a) Association probability.

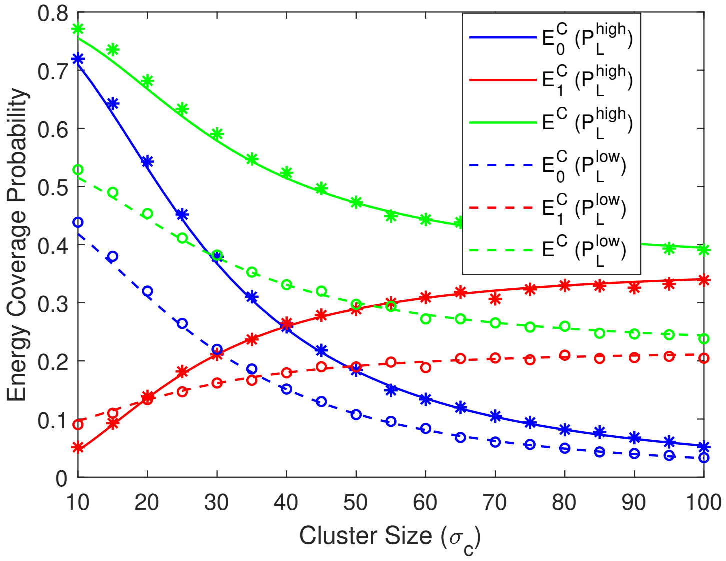

(b) Energy coverage probability.

Figure 8.4: (a) Association probability and (b) energy coverage probability as a function of UE distribution's standard deviation σ_c for LOS probability functions of high-altitude and low-altitude models when $H = 50$ m. Simulation results are plotted with markers while dashed/solid curves show theoretical results.

8.5.2 Impact of UAV Height

Next, in Figs. 8.5a and 8.5b, we plot the association probability and energy coverage probability as a function of UAV height considering the LOS probability functions of both high-altitude and low-altitude models. For the high-altitude model, since LOS probability increases with the increasing UAV height, association probability with the 0^{th} tier UAV increases slightly. On the other hand, LOS probability decreases as a result of the increase in the 3D distance with the increasing UAV height in the low-altitude model. Therefore, more UEs prefer to connect to 1^{st} tier UAVs (i.e., UAVs other than the cluster-center one) at higher values of the UAV height.

Energy coverage probability of the cluster center UAV, $\mathrm{E}_0^{\mathrm{C}}$, exhibits similar trends for both types of LOS functions. More specifically, $\mathrm{E}_0^{\mathrm{C}}$ increases first then it starts decreasing with the increasing UAV height. Since the effective antenna gain for HH antenna orientation is an increasing function of UAV height for a fixed cluster size, an initial increase in $\mathrm{E}_0^{\mathrm{C}}$ is expected. However, further increase in UAV height results in a decrease in $\mathrm{E}_0^{\mathrm{C}}$ of both high-altitude and low-altitude models due to the increase in the distance. Therefore, for a fixed cluster size, there exists an optimal UAV height maximizing the network energy coverage, E^{C}, for both models. On the other hand, optimal height maximizing the E^{C} in the low-altitude model is lower and E^{C} decreases faster than that in the high-altitude model because the LOS probability function of the low-altitude model is a decreasing function of distance while the LOS probability function of the high-altitude model is an increasing function of the UAV height (e.g., as seen in Fig. 8.2). Moreover, since UEs are more compactly distributed around the cluster center UAVs for $\sigma_c = 10$, energy coverage probability of the 1^{st} tier UAVs, $\mathrm{E}_1^{\mathrm{C}}$, is relatively small and changes only very slightly for both models.

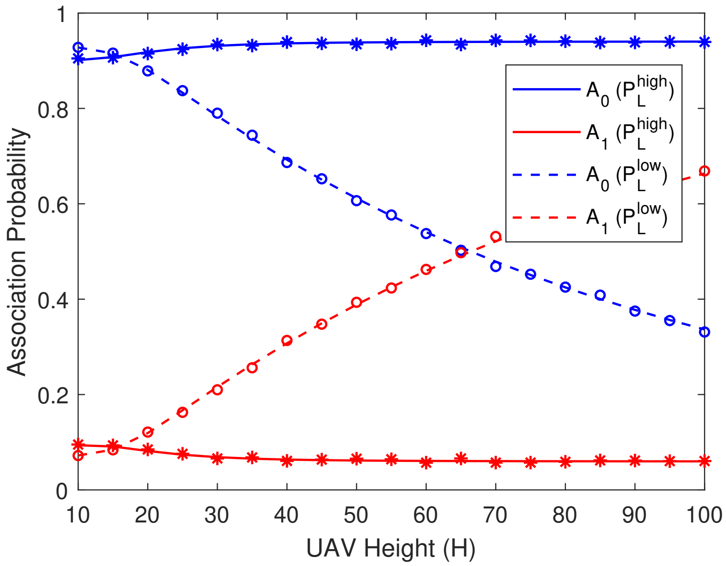

(a) Association probability.

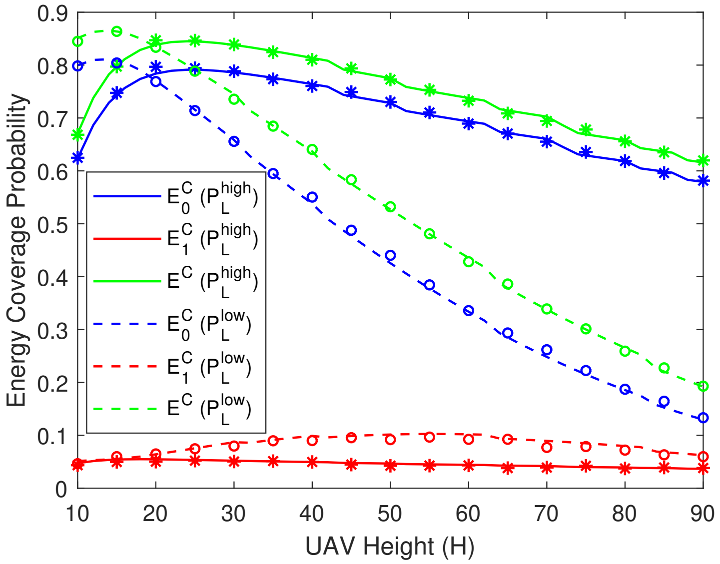

(b) Energy coverage probability.

Figure 8.5: (a) Association probability and (b) energy coverage probability as a function of UAV height H for LOS probability functions of high-altitude and low-altitude models when $\sigma_c = 10$. Simulation results are plotted with markers while dashed/solid curves show theoretical results.

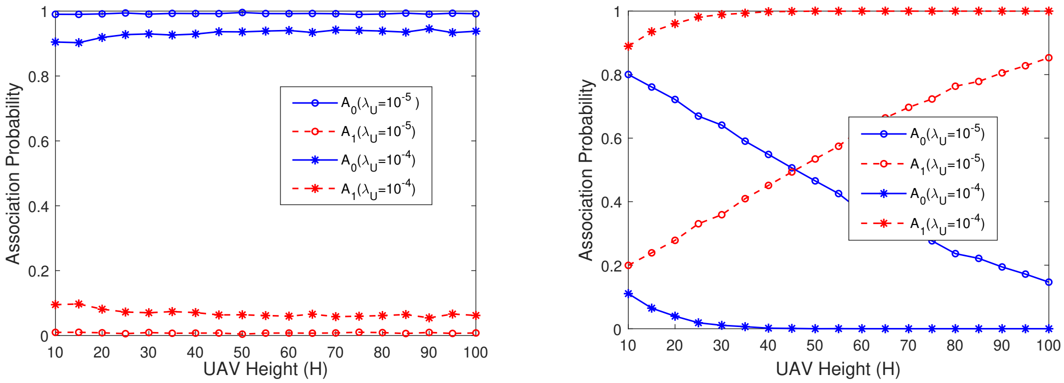

(a) HH orientation.

(b) VV orientation.

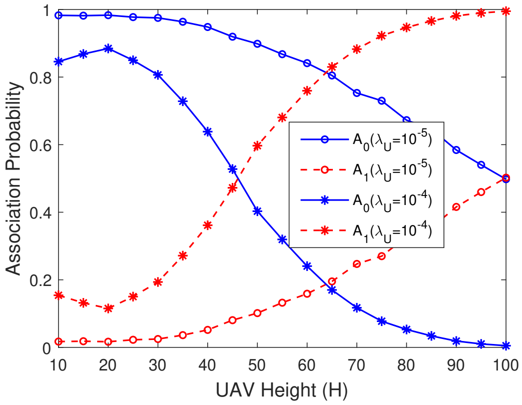

(c) HV orientation.

Figure 8.6: Association probability as a function of UAV height H for different values of UAV density λ_U for (a) HH, (b) VV and (c) HV antenna orientations when $\sigma_c = 10$.

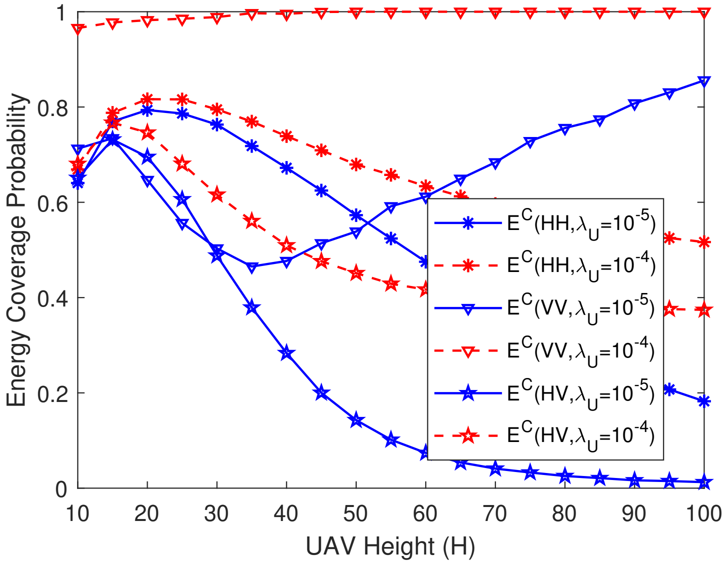

Figure 8.7: Energy coverage probability as a function of UAV height H for different values of UAV density λ_U for different antenna orientations when $\sigma_c = 10$.

8.5.3 Impact of Antenna Orientation

In Figs. 8.6a, 8.6b and 8.6c, we plot the association probability as a function of UAV height H for different values of UAV density λ_U for three different antenna orientations considering the high-altitude LOS probability model. Note that since the analysis for VV and HV antenna orientations seems to be intractable, only simulation results are plotted. Since effective antenna gain depends on the sine function of the angle between the UAVs and UEs for HH antenna orientation, UEs prefer to connect to their cluster center UAV, and hence $\mathcal{A}_0$ is much larger than $\mathcal{A}_1$ even when there is an increase in the number of UAVs (as seen when the UAV density is increased from $\lambda_U = 10^{-5}$ to $\lambda_U = 10^{-4}$) as shown in Fig. 8.6a. Also note that since both antenna gain and LOS probability is an increasing function with UAV height, increase in them can compensate the increasing path loss and the association probabilities remain almost constant.

For the VV case, effective antenna gain depends on the cosine function of the angle between the UAVs and UEs, and hence the links between the farther away UAVs and

UEs have a greater effective antenna gain than the closer links. As a result, UEs are more likely to be associated with 1^{st} tier UAVs than the cluster-center UAV in a denser UAV network (with UAV density $\lambda_U = 10^{-4}$) as shown in Fig. 8.6b. On the other hand, as the density of UAVs decreases, larger path loss of 1^{st} tier UAVs results in cluster-center UAV being preferred at lower UAV heights. However, as the height increases, $\mathcal{A}_1$ dominates $\mathcal{A}_0$.

Finally, for the HV case, effective antenna gain is a function of both cosine and sine of the angle between θ. For larger values of UAV density, association probability with the 0^{th} tier UAV, $\mathcal{A}_0$, slightly increases with increasing UAV height at first as a result of increase in both the LOS probability and the effective antenna gain. Subsequently, it starts decreasing because the increase in the LOS probability cannot compensate the rapid decrease in the effective antenna gain between the UE and the cluster center UAV. For a less dense network, UEs associate with the cluster-center UAV mostly at lower UAV heights. However, with the increasing height, antenna gain with the cluster-center UAV decreases and consequently, the association probability with 1^{st} tier UAVs, $\mathcal{A}_1$, increases.

We also plot the energy coverage probability for different UAV heights, antenna orientations, and UAV densities in Fig. 8.7. The performance with the HV antenna orientation exhibits similar behavior as that with the HH antenna orientation which is described in Section 8.5.2. The only difference is that increasing the UAV density improves the energy coverage performance for both HH and HV orientations as a result of the increase in the interference levels (which are indeed beneficial for energy harvesting purposes). On the other hand, performance with the VV antenna orientation is significantly different from that with other antenna orientations. For lower-density UAV networks, UEs are forced to connect with their cluster center UAV as shown in Fig. 8.6b at lower UAV height values, and hence the performance degrades initially with increasing UAV height, but then starts improving with the further increase in

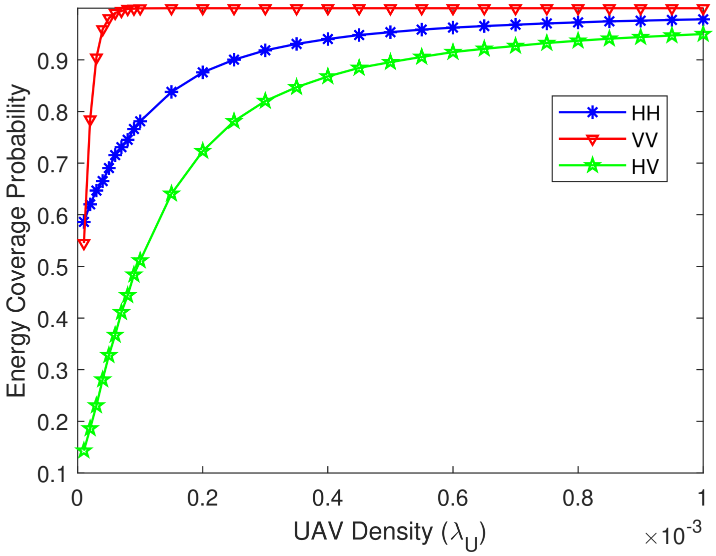

Figure 8.8: Energy coverage probability as a function of UAV density λ_U.

the height as a result of increase in the association with 1st tier UAVs which provide higher antenna gains. When the UAV density is higher, UEs are more likely to be associated with the 1st tier UAVs rather than the cluster-center UAV. In this case, better energy coverage probability is achieved. Therefore, energy coverage performance can be improved by changing the antenna orientations depending on the number of UAVs in the network and their height.

Furthermore, we plot the energy coverage probability as a function of UAV density for three different antenna orientations considering the high-altitude LOS probability model in Fig. 8.8. Energy coverage probability is an increasing function of UAV density irrespective of antenna orientation for a fixed UAV height. Adding more UAVs to the network results in an increase in the total power received at the typical UE, hence energy coverage performance of the network improves. We also note that VV antenna orientation generally leads to larger energy coverage probabilities when the UAV density is sufficiently large, due to the fact that one can harvest more energy from the dense 1st-tier UAVs with smaller elevation angles when this antenna orientation is used. .

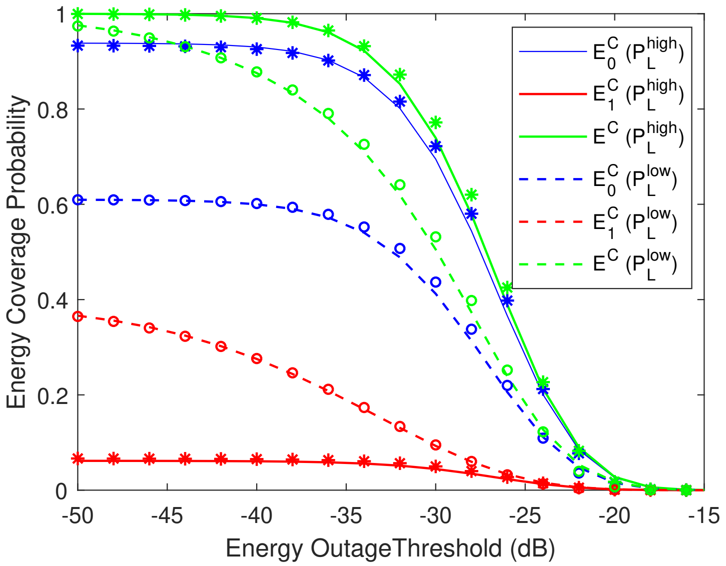

Figure 8.9: Energy coverage probability as a function of energy outage threshold in dB for LOS probability functions of high-altitude and low-altitude models when $\sigma_c = 10$ and $H = 50$ m. Simulation results are plotted with markers while dashed/solid curves show theoretical results.

8.5.4 Impact of Energy Outage Threshold

In Fig. 8.9, we plot the energy coverage probabilities of different tiers (i.e., E_0^C and E_1^C) and also the total energy coverage probability E^C as a function of the energy outage threshold for both high-altitude and low-altitude models. As seen in Fig. 8.4a and Fig. 8.5a, UEs are more likely to be associated with the 0th tier UAV rather than 1st tier UAVs in the high-altitude model when $\sigma_c = 10$, and hence E_0^C is much higher than E_1^C. On the other hand, for the low-altitude model, since association probabilities with each tier are not very different, more UEs can be covered by 1st tier UAVs compared to the high-altitude model. However, E_0^C is still greater than E_1^C due to the relatively smaller distance to the cluster-center UAV. We also observe that as a general trend, energy coverage probabilities expectedly diminish with increasing energy outage threshold.

8.6 Conclusion

In this chapter, we have provided an analytical framework to compute the energy coverage probability of a UAV network with clustered UEs. UAVs are assumed to be distributed according to an independent PPP, while locations of UEs are modeled as a PCP around the projections of UAVs on the ground, and UEs are assumed to be connected to the tier providing the strongest long-term averaged power. In this setting, we have determined the association probabilities and characterized the energy coverage probability. We have analyzed the effect of two different LOS probability functions on the network performance. We have also investigated the impact of practical 3D antenna radiation patterns on the energy coverage performance.

Using numerical results, we have shown that standard deviation of UE distribution σ_c, UAV height H, and antenna orientation have significant impacts on UAV association and energy coverage probabilities. For instance, less compactly located UEs result in a decrease in the total energy coverage probability of the network for both LOS probability models. While for a certain cluster size there exists an optimal UAV height that maximizes the network energy coverage, this optimal height depends on the type of the LOS probability model. We have also shown that antenna orientation greatly affects the energy coverage probability depending on the UAV density, and better performance can be achieved by changing the antenna orientations according to the number of UAVs in the network and their height.

Chapter 9

Conclusion

9.1 Summary

In this thesis, performance of mmWave cellular networks has been studied. Tools from stochastic geometry are employed to study the error probability, energy efficiency, coverage probability, outage probability of mmWave cellular networks. Additionally, performance of the UAV assisted cellular networks is analyzed. Specifically, the contributions of this thesis are summarized below.

In Chapter 2, we have analyzed the average error performance of downlink mmWave cellular networks, incorporating the distinguishing features of mmWave communication into the average error probability analysis. Sectored antenna and simplified ball-LOS models have been considered to simplify the analysis. Numerical results show that employing directional antennas improves the error performance. Also, we show that better ASEP values can be obtained by increasing BS density and main lobe gain.

In Chapter 3, we have analyzed the energy efficiency of relay-assisted downlink mmWave cellular networks by incorporating the distinguishing features of mmWave communication into the energy efficiency analysis. Directional beamforming with sectored antenna model and simplified ball-LOS models have been considered in the analysis. BSs and RSs are assumed to be distributed according to independent PPPs, and SINR coverage probabilities are derived using tools from stochastic geometry to characterize the energy efficiency. Numerical results demonstrate that employing directional antennas makes the mmWave cellular networks more energy efficient. In other words, increasing the main lobe gain and decreasing the main lobe beam width results in improved energy efficiency. We have also shown that BS density should be lowered to achieve the maximum energy efficiency when the LOS ball radius is larger. Moreover, we have observed that there is a tradeoff between the area spectral efficiency and energy efficiency depending on the RS density. Finally, the effect of alignment error on energy efficiency is quantified.

In Chapter 4, we have provided a general analytical framework to compute the SINR and rate coverage probabilities in heterogeneous downlink mmWave cellular networks composed of K tiers. Moreover, we have studied the energy efficiency metric and analyzed the effect of biasing on energy efficiency. Directional beamforming with sectored antenna model and D-ball approximation for blockage model have been considered in the analysis. BSs of each tier and UEs are assumed to be distributed according to independent PPPs, and UEs are assumed to be connected to the tier providing the maximum average biased-received power. Numerical results show that mmWave cellular networks can be approximated to be noise-limited rather than being interference-limited especially if the number of tiers is small. We have also shown that increasing main lobe gain results in higher SNR coverage. Moreover, we have observed the effect of biasing. Increase in the biasing factor of smaller cells has led to better coverage probability of smaller cells because of the higher number of UEs connected to them, while the overall network coverage probability has slightly diminished due to association with the BS not offering the strongest average received power. Furthermore, we have shown that smaller cells provide higher rate than larger cells. Additionally, it is verified that there is an optimal biasing factor to achieve the maximum energy efficiency. The effect of alignment error on coverage probability is also quantified. Finally, we have demonstrated that the proposed analytical framework is also applicable to μWave-mmWave hybrid networks, and gleaned interesting insight on the impact of interference when operating in μWave frequency bands.

In Chapter 5, we have provided an analytical framework to compute SINR outage probabilities for both cellular and D2D links in a D2D-enabled mmWave cellular network. Directional beamforming with sectored antenna model and modified LOS ball model for blockage modeling have been considered in the analysis. BSs and UEs are assumed to be distributed according to independent PPPs, and potential D2D UEs are allowed to choose cellular or D2D mode according to a flexible mode selection scheme. Numerical results show that probability of selecting D2D mode increases with increasing biasing factor T_d and decreasing $p_{L,c}$. We have also shown that increasing the main lobe gain and decreasing the beam width of the main lobe result in lower SINR outage. Moreover, we have observed that the type of spectrum sharing plays a crucial role in SINR outage performance of cellular UEs.

In Chapter 6, we have provided an analytical framework to compute the SINR outage probabilities for both cellular and D2D links in a D2D-enabled mmWave cellular network with clustered UEs. Distinguishing features of mmWave communications, such as directional beamforming with sectored antenna model, modified LOS ball model for blockage modeling and Nakagami fading, have been considered in the analysis. BSs and cellular UEs are assumed to be distributed according to independent PPPs, while potential D2D UEs locations' are modeled as a PCP. Potential D2D UEs in the clusters are allowed to choose cellular or D2D mode according to a flexible mode selection scheme. Under these assumptions, we have analyzed the interference experienced in cellular uplink and D2D links, and characterized the SINR outage probabilities. Numerical results show that probability of selecting D2D mode decreases with increasing UE distribution's standard deviation σ_d and increasing $p_{L,c}$, while increase in $p_{L,d}$ leads to higher D2D mode selection probability. We have also shown that more simultaneously transmitting potential D2D UEs and/or higher cluster center density result in higher outage probabilities for both cellular and D2D links due to the growing impact of interference. Moreover, the type of spectrum sharing plays a crucial role in the SINR outage performance of cellular UEs. Another interesting observation is that smaller LOS ball radius is preferred for small values of σ_d while the opposite is advantageous for large values of σ_d. Moreover, increasing the main lobe gain and decreasing the beam width of the main lobe result in lower SINR outage. Effect of alignment error on outage probability is also quantified and importance of beam alignment in improving the performance is noted. Finally, ASE of the cellular and D2D networks are analyzed for both underlay and overlay types of sharing. We have shown that there is an optimal number of simultaneously active D2D links, maximizing the ASE in the D2D network. This optimal number is independent of the cluster center density and spectrum partition factor. For overlay sharing, there exists an optimal spectrum partition factor if the optimal weighted proportional fair spectrum partition is considered.

In Chapter 7, we have provided an analytical framework to compute the SINR coverage probability of UAV assisted cellular networks with clustered UEs. Moreover, we have formulated the ASE, and investigated the effect of UAV density and standard deviation of the UE distribution on the ASE. Furthermore, we have presented SINR coverage probability expression for a more general model by considering that UAVs are located at different heights. UAVs and ground BSs are assumed to be distributed according to independent PPPs, while locations of UEs are modeled as a PCP around the projections of UAVs on the ground and UEs are assumed to be connected to the tier providing the maximum average biased-received power. Using numerical results, we have shown that standard deviation of UE distribution σ_c and UAV height H have significant impact on association probabilities. For instance, less compactly located UEs and higher UAV height lead to a decrease in the association with the cluster center UAV. We have also shown that total coverage probability can be improved by reducing the UAV height as a result of the decrease in the distances between cluster center UAV and UEs. Moreover, path-loss exponents play a crucial role in the coverage performance if the UAV height is high, and there exists an optimal value for path-loss exponents in which the coverage probability is maximized. Another important observation is that smaller number of UAVs results in a better coverage performance, while deployment of more UAVs lead to a higher ASE. Furthermore, a higher ASE can be achieved if the UES are located more compactly in each cluster.

In Chapter 8, we have provided an analytical framework to compute the energy coverage probability of a UAV network with clustered UEs. UAVs are assumed to be distributed according to an independent PPP, while locations of UEs are modeled as a PCP around the projections of UAVs on the ground, and UEs are assumed to be connected to the tier providing the strongest long-term averaged power. In this setting, we have determined the association probabilities and characterized the energy coverage probability. We have analyzed the effect of two different LOS probability functions on the network performance. We have also investigated the impact of practical 3D antenna radiation patterns on the energy coverage performance. Using numerical results, we have shown that standard deviation of UE distribution σ_c, UAV height H, and antenna orientation have significant impacts on UAV association and energy coverage probabilities. For instance, less compactly located UEs result in a decrease in the total energy coverage probability of the network for both LOS probability models. While for a certain cluster size there exists an optimal UAV height that maximizes the network energy coverage, this optimal height depends on the type of the LOS probability model. We have also shown that antenna orientation greatly affects the energy coverage probability depending on the UAV density, and better performance can be achieved by changing the antenna orientations according to the number of UAVs in the network and their height.

9.2 Future Research Directions

In this section, some promising directions are presented for future work related to the contributions in this thesis.

9.2.1 Simultaneous Information and Energy Transfer in UAV Networks with 3D Antenna Radiation Patterns

In Chapter 8, energy coverage probability of a UAV network with clustered users is studied. Impacts of different LOS probability functions and practical 3D antenna radiation on the network performance is analyzed. In this work, we consider only downlink power transfer. On the other hand, transmitted signal carry both energy and information simultaneously. Therefore, in order to make the best use of the RF spectrum and radiations, a joint transfer of information and power to the receiving node, which is known as simultaneous wireless information and power transfer (SWIPT), has attracted considerable attention in recent years. Employment of UAVs in SWIPT systems is another promising research direction. Therefore, it would be interesting to analyze the performance of a UAV network with SWIPT and practical 3D antenna radiation.

9.2.2 Visible Light Communication Energy Harvesting

As we have discussed in Chapter 8, energy consumption of wireless devices has been increasing tremendously and hence RF energy harvesting technology, where the energy content of incident signal from BSs/UAVs are exploited for energy harvesting, is one of the promising solutions to meet this increasing energy demand. However, currently utilized RF spectrum will not be sufficient to provide energy to the exponentially increasing number of wireless devices. Therefore, coexistence of RF and visible light communication (VLC) links for energy harvesting has been emerged as a promising technology. Hence, it would be interesting to study the energy harvesting in a network consisting of both UAVs and ground BSs.

Appendix A

Proof of Lemma 4.1

Intensity function for the D-ball path loss model can be computed as

$$\begin{aligned}
&\Lambda_k([0,x)) \overset{(a)}{=} \int_{\mathbb{R}^2} \mathbb{P}(L_k(r) < x) dr \\
&= 2\pi\lambda_k \int_0^{\infty} \mathbb{P}((\kappa(r) r)^{\alpha^k(r)} < x) r dr \\
&\overset{(b)}{=} 2\pi\lambda_k \bigg(\beta_{k1} \int_0^{R_{k1}} r \mathbb{1}(\kappa_1^L r^{\alpha_1^{k,L}} < x) dr + (1-\beta_{k1}) \int_0^{R_{k1}} r \mathbb{1}(\kappa_1^N r^{\alpha_1^{k,D}} < x) dr \\
&+ \beta_{k2} \int_{R_{k1}}^{R_{k2}} r \mathbb{1}(\kappa_2^L r^{\alpha_2^{k,L}} < x) dr + (1-\beta_{k2}) \int_{R_{k1}}^{R_{k2}} r \mathbb{1}(\kappa_2^N r^{\alpha_2^{k,N}} < x) dr \bigg) + \cdots \\
&+ \beta_{kD} \int_{R_{k(D-1)}}^{R_{kD}} r \mathbb{1}(\kappa_D^L r^{\alpha_D^{k,L}} < x) dr + (1-\beta_{kD}) \int_{R_{k(D-1)}}^{R_{kD}} r \mathbb{1}(\kappa_D^N r^{\alpha_D^{k,N}} < x) dr \bigg) \\
&\overset{(c)}{=} 2\pi\lambda_k \sum_{d=1}^{D} \bigg(\beta_{kd} \int_{R_{k(d-1)}}^{\min\{R_{kd}, (x/\kappa_d^L)^{\frac{1}{\alpha_d^{k,L}}}\}} r dr + (1-\beta_{kd}) \int_{R_{k(d-1)}}^{\min\{R_{kd}, (x/\kappa_d^N)^{\frac{1}{\alpha_d^{k,N}}}\}} r dr \bigg) \\
&= \pi\lambda_k \sum_{d=1}^{D} \bigg(\beta_{kd} \bigg(\left(R_{kd}^2 - R_{k(d-1)}^2\right) \mathbb{1}\left(x > \kappa_d^L R_{kd}^{\alpha_d^{k,L}} \right) \\
&+ \left((x/\kappa_d^L)^{\frac{2}{\alpha_d^{k,L}}} - R_{k(nd-1)}^2 \right) \mathbb{1}\left(\kappa_d^L R_{k(d-1)}^{\alpha_d^{k,L}} < x < \kappa_d^L R_{kd}^{\alpha_d^{k,L}} \right) \bigg) \\
&+ (1-\beta_{kd}) \bigg(\left(R_{kd}^2 - R_{k(d-1)}^2\right) \mathbb{1}\left(x > \kappa_d^N R_{kd}^{\alpha_d^{k,N}} \right) \\
&+ \left((x/\kappa_d^N)^{\frac{2}{\alpha_d^{k,N}}} - R_{k(d-1)}^2 \right) \mathbb{1}\left(\kappa_d^N R_{k(d-1)}^{\alpha_d^{k,N}} < x < \kappa_d^N R_{kd}^{\alpha_d^{k,N}} \right) \bigg) \bigg). \qquad \text{(A.1)}
\end{aligned}$$

where (a) follows from the definition of intensity function for the point process of the path loss $\mathcal{N}_k = \{L_k(r)\}_{r \in \phi_k}$; (b) is obtained when different values of distance dependent path loss exponent $\alpha_k(r)$ are inserted according to the D-ball model; and (c) follows from the definition of the indicator function. Finally, evaluating the integrals and rearranging the terms, we obtain the result in Lemma 4.1.

Appendix B

Proof of Lemma 4.3

Note that the association probability is

$$\begin{aligned}
\mathcal{A}_{k,s} &= \mathbb{P}\left(P_kG_kB_kL_{k,s}^{-1} \geq \max_{j,j\neq k} P_jG_jB_jL_j^{-1}\right)\mathbb{P}\left(L_{k,s'} > L_{k,s}\right) \\
&\overset{(a)}{=} \left(\prod_{j=1,j\neq k}^{K} \mathbb{P}\left(P_kG_kB_kL_{k,s}^{-1} \geq P_jG_jB_jL_j^{-1}\right)\right)\mathbb{P}(L_{k,s'} > L_{k,s}) \\
&= \int_0^\infty \prod_{j=1,j\neq k}^{K} \bar{F}_{L_j}\left(\frac{P_jB_j}{P_kG_kB_k} l_{k,s}\right) e^{-\Lambda_{k,s'}\left(\left[0,l_{k,s}\right)\right)} f_{L_{k,s}}(l_{k,s})dl_{k,s} \\
&\overset{(b)}{=} \int_0^\infty e^{-\sum_{\substack{j=1,\\ j\neq k}}^{K} \Lambda_j\left(\left[0,\frac{P_jB_j}{P_kG_kB_k}l_{k,s}\right)\right)} e^{-\Lambda_{k,s'}([0,l_{k,s}))}\Lambda'_{k,s}([0,l_{k,s}))e^{-\Lambda_{k,s}([0,l_{k,s}))}dl_{k,s} \\
&\overset{(c)}{=} \int_0^\infty e^{-\sum_{\substack{j=1,\\ j\neq k}}^{K} \Lambda_j\left(\left[0,\frac{P_jG_jB_j}{P_kG_kB_k}l_{k,s}\right)\right)} \Lambda'_{k,s}([0,l_{k,s}))e^{-\Lambda_k([0,l_{k,s}))}dl_{k,s} \\
&= \int_0^\infty \Lambda'_{k,s}([0,l_{k,s}))e^{-\sum_{j=1}^{K} \Lambda_j\left(\left[0,\frac{P_jG_jB_j}{P_kG_kB_k}l_{k,s}\right)\right)}dl_{k,s},
\end{aligned} \tag{B.1}$$

where $s, s' \in \{\mathrm{LOS}, \mathrm{NLOS}\}$, and $s \neq s'$. In (a), CCDF of L_j is formulated as a result of the first probability expression, and similarly $\mathbb{P}(L_{k,s'} > L_{k,s}) = \bar{F}_{L_{k,s'}}(l_{k,s}) = e^{-\Lambda_{k,s'}([0,l_{k,s}))}$; (b) follows from the definition of the CCDF of the path loss, and by plugging the PDF of the path loss $L_{k,s}$; and (c) follows from the fact that $\Lambda_{k,s}([0, l_{k,s})) + \Lambda_{k,s'}([0, l_{k,s})) = \Lambda_k([0, l_{k,s}))$.

Appendix C

Proof of Theorem 4.1

The coverage probability can be expressed as

$$\begin{aligned}\mathrm{P_C} &= \sum_{k=1}^{K} \sum_{s \in \mathrm{LOS,NLOS}} \left[\mathbb{P}\left(\mathrm{SINR}_{k,s} > \Gamma_k; t = k\right) \mathbb{P}\left(L_{k,s'} > L_{k,s}\right)\right], \\ &= \sum_{k=1}^{K} \sum_{s \in \mathrm{LOS,NLOS}} \Bigg[\underbrace{\mathbb{P}\left(\mathrm{SINR}_{k,s} > \Gamma_k\right)}_{\mathrm{P}_{\mathrm{C}}^{k,s}(\Gamma_k)} \\ &\qquad \underbrace{\mathbb{P}\left(P_k G_k B_k L_{k,s}^{-1} \geq \max_{j, j \neq k} P_j G_j B_j L_j^{-1}\right) \mathbb{P}(L_{k,s'} > L_{k,s})}_{\mathcal{A}_{k,s}}\Bigg],\end{aligned} \tag{C.1}$$

where the last step follows from the assumption that Φ_j and Φ_k are independent from each other for $j \neq k$. The expression to obtain the association probability, $\mathcal{A}_{k,s}$ was provided in Lemma 4.3. Given that the UE is associated with a BS in $\Phi_{k,s}$, the conditional coverage probability $\mathrm{P}_{\mathrm{C}}^{k,s}(\Gamma_k)$ can be computed as follows

$$\begin{aligned}\mathrm{P}_{\mathrm{C}}^{k,s}(\Gamma_k) &= \mathbb{P}(\mathrm{SINR}_{k,s} > \Gamma_k)\\ &= \mathbb{P}\bigg(\frac{P_k G_0 h_{k,0} L_{k,s}^{-1}}{\sigma_k^2 + \sum_{j=1}^{K} \sum_{i\in\Phi_j\setminus B_{k,0}} P_j G_{j,i} h_{j,i} L_{j,i}^{-1}(r)} > \Gamma_k\bigg)\\ &= \mathbb{P}\bigg(h_{k,0} > \frac{\Gamma_k L_{k,s}}{P_k G_0}\bigg(\sigma_k^2 + \sum_{j=1}^{K}\Big(I_{j,\mathrm{LOS}} + I_{j,\mathrm{NLOS}}\Big)\bigg)\bigg)\\ &\approx \sum_{n=1}^{N_s}(-1)^{n+1}\binom{N_s}{n} e^{-u\sigma_k^2}\prod_{j=1}^{K}\Big(\mathcal{L}_{I_{j,\mathrm{LOS}}}(u)\mathcal{L}_{I_{j,\mathrm{NLOS}}}(u)\Big), \end{aligned} \tag{C.2}$$

where $u = \frac{n\eta_s\Gamma_k L_{k,s}}{P_k G_0}$, $I_{j,s} = \sum_{i\in\Phi_{j,s}\setminus B_{k,0}} P_j G_{j,i} h_{j,i} L_{j,i}^{-1}(r)$ is the interference from the jth tier LOS and NLOS BSs, and $\mathcal{L}_{I_{j,s}}(u)$ is the Laplace transform of $I_{j,s}$ evaluated at u. The approximation in the last step is obtained using the same approach as in [9, Equation (22) Appendix C]. Tools from stochastic geometry can be applied to compute the Laplace transform $\mathcal{L}_{I_{j,s}}(u)$ for $s \in \{\mathrm{LOS}, \mathrm{NLOS}\}$. Using the thinning property, we can split $I_{j,s}$ into three independent PPPs as follows [32]:

$$I_{j,s} = I_{j,s}^{MM} + I_{j,s}^{Mm} + I_{j,s}^{mm} = \sum_{G\in\{MM,Mm,mm\}} I_{j,s}^{G} \tag{C.3}$$

where $I_{j,s}^{G}$ for $s \in \{\mathrm{LOS}, \mathrm{NLOS}\}$ denotes the interference from BSs with random antenna gain G defined in (4.1). According to the thinning theorem, each independent PPP has a density of $\lambda_j p_G$ where p_G is given in (4.1) for each antenna gain $G \in \{MM, Mm, mm\}$. Inserting (C.3) into the Laplace transform expression and using the definition of Laplace transform yield

$$\mathcal{L}_{I_{j,s}}(u) = \mathbb{E}_{I_{j,s}}[e^{-uI_{j,s}}] = \mathbb{E}_{I_{j,s}}\Big[e^{-u\left(I_{j,s}^{MM}+I_{j,s}^{Mm}+I_{j,s}^{mm}\right)}\Big] = \prod_{G}\mathbb{E}_{I_{j,s}^{G}}[e^{-uI_{j,s}^{G}}], \tag{C.4}$$

where $G \in \{MM, Mm, mm\}$, $u = \frac{n\eta_s\Gamma_k L_{k,s}}{P_k G_0}$, and the last step follows from the fact that $I_{j,s}^{G}$s are the interferences generated from independent thinned PPPs. Laplace transforms of the interferences from the LOS and NLOS interfering BSs with a generic antenna gain G can be calculated using stochastic geometry as follows:

$$\begin{aligned}\mathbb{E}_{I^G_{j,s}}\left[e^{-uI^G_{j,s}}\right] &= e^{-\int_{\frac{P_jB_j}{P_kB_k}l_{k,s}}^{\infty}\left(1-\mathbb{E}_{h,s}\left[e^{-uP_jGh_{j,s}x^{-1}}\right]\right)\Lambda'_{j,s}(dx)} \\ &\overset{(a)}{=} e^{-\int_{\frac{P_jB_j}{P_kB_k}l_{k,s}}^{\infty}\left(1-1/\left(1+uP_jGx^{-1}/N_s\right)^{N_s}\right)\Lambda'_{j,s}(dx)},\end{aligned} \tag{C.5}$$

where $\Lambda'_{j,s}(dx)$ is obtained by differentiating the equations in (4.6) and (4.7) with respect to x for $s \in \{\text{LOS}, \text{NLOS}\}$, respectively, (a) is obtained by computing the moment generating function (MGF) of the gamma random variable h, and the lower bound for the integral is determined using the fact that the minimum separation between the UE and the interfering BS from the jth tier is equal to $\frac{P_jG_jB_j}{P_kG_kB_k}l_{k,s}$. Finally, by combining (4.11), (C.1), (C.2), (C.4) and (C.5), SINR coverage probability expression given in Theorem 4.1 is obtained.

Appendix D

Proof of Lemma 6.1

Probability of selecting the D2D mode for a potential D2D UE located in a cluster $x \in \Phi_C$ can be computed as

$$\begin{aligned}
&P_{D2D} \\
&= \sum_{s\in\{L,N\}} \sum_{s'\in\{L,N\}} \mathbb{P}\left(T_d r_d^{-\alpha_{s',d}} \geq r_c^{-\alpha_{s,c}}\right) p_{s',d}(r_d)\mathcal{B}_{s,c} \\
&= \sum_{s\in\{L,N\}} \sum_{s'\in\{L,N\}} \mathbb{P}\left(r_c \geq r_d^{\alpha_{s',d}/\alpha_{s,c}} T_d^{-1/\alpha_{s,c}}\right) p_{s',d}(r_d)\mathcal{B}_{s,c} \\
&= \sum_{s\in\{L,N\}} \sum_{s'\in\{L,N\}} \int_0^\infty \int_0^\infty \bar{F}_s\left(\frac{r_d^{\alpha_{s',d}/\alpha_{s,c}}}{T_d^{1/\alpha_{s,c}}}\right) f_{R_d}(r_d|\omega) f_\Omega(\omega) p_{s',d}(r_d)\mathcal{B}_{s,c} dr_d d\omega \\
&\overset{(a)}{=} \sum_{s\in\{L,N\}} \sum_{s'\in\{L,N\}} \int_0^\infty \int_0^\infty e^{-2\pi\lambda_B \psi_s\left(r_d^{\alpha_{s',d}/\alpha_{s,c}}/T_d^{1/\alpha_{s,c}}\right)} f_{R_d}(r_d|\omega) f_\Omega(\omega) p_{s',d}(r_d) dr_d d\omega
\end{aligned} \tag{D.1}$$

where $\bar{F}_s(r_c) = e^{-2\pi\lambda_B \psi_s(r_c)}/\mathcal{B}_{s,c}$ is the complementary cumulative distribution function (ccdf) of the cellular link distance r_c to the nearest LOS/NLOS BS, $\mathcal{B}_{s,c} = 1 - e^{-2\pi\lambda_B \int_0^\infty x p_{s,c}(x)dx}$ is the probability that a UE has at least one LOS/NLOS BS, $p_{s',d}(r_d)$ is the LOS/NLOS probability function for the D2D link given in (6.4), and (a) follows by substituting the cdf of r_c into the expression.

Appendix E

Proof of Lemma 6.2

Laplace transform of the aggregate interference at the BS from cellular UEs transmitting in the same uplink channel in different cells can be calculated using (6.13) as follows:

$$\mathcal{L}_{I_{cc}}(v) = \prod_{G}\prod_{j}\mathcal{L}_{I_{cc,j}^{G}}(v), \tag{E.1}$$

where the Laplace transform for $I_{cc,j}^{G}$ can be computed using stochastic geometry as follows:

$$\begin{aligned}\mathcal{L}_{I_{cc,j}^{G}}(v) &\overset{(a)}{=} \exp\left(-2\pi\lambda_B p_G \int_0^\infty \left(1-\mathbb{E}_h\left[e^{-vP_cGht^{-\alpha_{j,c}}}\right]\right) Q(t^{\alpha_{j,c}}) p_{j,c}(t) t dt \right)\\ &\overset{(b)}{=} \exp\left(-2\pi\lambda_B p_G \int_0^\infty \left(1-\frac{1}{\left(1+vP_cGt^{-\alpha_{j,c}}/N_j\right)^{N_j}}\right) Q\left(t^{\alpha_{j,c}}\right) p_{j,c}(t) t dt \right),\end{aligned} \tag{E.2}$$

where (a) follows from computing the probability generating functional (PGFL) of PPP and h in (a) is a gamma random variable with parameter N_j, (b) is obtained by computing the MGF of the gamma random variable h, and $Q(y)$ is given in (6.3). By inserting (E.2) into (E.1) for $j \in \{L, N\}$ and $G \in \{M_{\mathrm{BS}_0}M_{\mathrm{UE}}, M_{\mathrm{BS}_0}m_{\mathrm{UE}}, m_{\mathrm{BS}_0}M_{\mathrm{UE}}, m_{\mathrm{BS}_0}m_{\mathrm{UE}}\}$, the Laplace transform expression can be obtained.

Appendix F

Proof of Lemma 6.3

Laplace transform of the aggregate interference at the BS from both intra-cluster and inter-cluster D2D UEs can be calculated using (6.13)

$$\mathcal{L}_{I_{dc}}(v) = \prod_{G} \prod_{j} \mathcal{L}_{I_{dc,j}^{G}}(v), \tag{F.1}$$

where the Laplace transform for $I^G_{dc,j}$ can be computed using stochastic geometry and following the similar steps as in [70]:

$$
\begin{aligned}
&\mathcal{L}_{I^G_{dc,j}}(v) \\
&\overset{(a)}{=} \mathbb{E}_{\Phi_C}\Bigg[\prod_{x\in\Phi_C}\mathbb{E}_{\mathcal{A}_d^x}\Bigg[\prod_{y\in\mathcal{A}_d^x}\mathbb{E}_{h_{yx}}\Big[e^{-vP_dGh_{yx}\|x+y\|^{-\alpha_{j,d}}}\Big]\Bigg]\Bigg] \\
&\overset{(b)}{=} \mathbb{E}_{\Phi_C}\Bigg[\prod_{x\in\Phi_C}\mathbb{E}_{\mathcal{A}_d^x}\Bigg[\prod_{y\in\mathcal{A}_d^x}\frac{1}{(1+vP_dG\|x+y\|^{-\alpha_{j,d}}/N_j)^{N_j}}\Bigg]\Bigg] \\
&\overset{(c)}{=} \mathbb{E}_{\Phi_C}\Bigg[\prod_{x\in\Phi_C}\sum_{k=0}^{\infty}\Bigg(\int_{\mathbb{R}^2}\frac{1}{(1+vP_dG\|x+y\|^{-\alpha_{j,d}}/N_j)^{N_j}}p_{j,d}(\|x+y\|)f_Y(y)dy\Bigg)^k\mathbb{P}(K=k)\Bigg] \\
&\overset{(d)}{=} \exp\Bigg(-\lambda_C\int_{\mathbb{R}^2}\Bigg(1-\sum_{k=0}^{\infty}\Bigg(\int_{\mathbb{R}^2}\frac{1}{(1+vP_dG\|x+y\|^{-\alpha_{j,d}}/N_j)^{N_j}}(\|x+y\|)f_Y(y)dy\Bigg)^k \\
&\qquad \times p_{j,d}\frac{(\bar{n}P_{D2D}p_G)^k e^{-(\bar{n}P_{D2D}p_G)}}{k!}\Bigg)dx\Bigg) \\
&\overset{(e)}{=} \exp\Bigg(-2\pi\lambda_C\int_0^{\infty}\Bigg(1-\sum_{k=0}^{\infty}\Bigg(\int_0^{\infty}\frac{1}{(1+vP_dGu^{-\alpha_{j,d}}/N_j)^{N_j}}p_{j,d}(u)f_U(u|w)du\Bigg)^k \\
&\qquad \times \frac{(\bar{n}P_{D2D}p_G)^k e^{-(\bar{n}P_{D2D}p_G)}}{k!}\Bigg)wdw\Bigg) \\
&\overset{(f)}{=} \exp\Bigg(-2\pi\lambda_C\int_0^{\infty}\Bigg(1-\exp\Bigg(-\bar{n}P_{D2D}p_G\int_0^{\infty}\Bigg(1-\frac{1}{(1+vP_dGu^{-\alpha_{j,d}}/N_j)^{N_j}}\Bigg) \\
&\qquad \times p_{j,d}(u)f_U(u|w)du\Bigg)\Bigg)wdw\Bigg) \qquad \text{(F.2)}
\end{aligned}
$$

where (a) follows from the assumption of independent fading gains across all interfering links, (b) is obtained by computing the moment generating function (MGF) of the gamma random variable h_{y_x} with parameter N_j, (c) follows from the fact that the locations of the cluster members in each cluster are independent when conditioned on $x \in \Phi_C$ and expectation over the number of interfering devices which are Poisson distributed, (d) is determined by computing the probability generating functional (PGFL) of PPP, (e) follows by applying a change of variables with $\|x + y\| \rightarrow u$, and converting the coordinates from Cartesian to polar by using the pdf of the distance distribution $f_{R_{yx}}(r_{yx}|\omega) = \mathrm{Ricepdf}(r_{yx}, \omega; \sigma_d^2)$ where $\{r_{yx} = \|x+y\|, \forall x \in \Phi_C, \forall y \in \mathcal{A}_d^x\}$ and $\omega = \|x\|$, (f) follows from the averaging kth power of $A = \int_0^\infty \frac{1}{\left(1+vP_dGu^{-\alpha_{j,d}}/N_j\right)^{N_j}} p_{j,d}(u) f_U(u|w)du$ over the Poisson distribution, i.e., $\sum_{k=0}^\infty (A)^k \frac{(\bar{n}P_{D2D}p_G)^k e^{-(\bar{n}P_{D2D}p_G)}}{k!} = e^{-(\bar{n}P_{D2D}p_G)(1-A)}$. By inserting (F.2) into (F.1) for $j \in \{L, N\}$ and $G \in \{M_{\mathrm{BS}_0}M_{\mathrm{UE}}, M_{\mathrm{BS}_0}m_{\mathrm{UE}}, m_{\mathrm{BS}_0}M_{\mathrm{UE}}, m_{\mathrm{BS}_0}m_{\mathrm{UE}}\}$, we obtain the Laplace transform expression in (6.15).

Laplace transform expression in (F.2) can be lower bounded by

$$\begin{aligned}
&\mathcal{L}_{I_{dc}}(v) \\
&\overset{(a)}{\geq} \exp\left(-2\pi\lambda_C\bar{n}P_{D2D}p_G \int_0^\infty \int_0^\infty \Psi\left(N_j, \frac{vP_dGu^{-\alpha_{j,d}}}{N_j}\right) f_U(u|w)p_{j,d}(u)duwdw \right) \\
&= \exp\left(-2\pi\lambda_C\bar{n}P_{D2D}p_G \int_0^\infty \Psi\left(N_j, \frac{vP_dGu^{-\alpha_{j,d}}}{N_j}\right) p_{j,d}(u)udu \right) \qquad \text{(F.3)}
\end{aligned}$$

where $\Psi(N, x) = 1 - 1/(1+x)^N$, (a) follows from the Taylor series expansion of exponential function, i.e. $1 - \exp(-x) \approx x$ for small x, and the last step follows from the Rician distribution property that $\int_0^\infty f_U(u|w)wdw = u$. By inserting (F.3) into (F.1) for $j \in \{L, N\}$ and $G \in \{M_{\mathrm{BS}_0}M_{\mathrm{UE}}, M_{\mathrm{BS}_0}m_{\mathrm{UE}}, m_{\mathrm{BS}_0}M_{\mathrm{UE}}, m_{\mathrm{BS}_0}m_{\mathrm{UE}}\}$, we obtain the lower bound in (6.16).

Appendix G

Proof of Lemma 6.5

Laplace transform of the intra-cluster interference at the typical UE $\in \mathcal{N}_r^{x_0}$ in the representative cluster can be calculated using (6.13) as follows:

$$\mathcal{L}_{I_{dd_{\text{intra}}}}(v|w_0)) = \prod_{G} \prod_{j} \mathcal{L}_{I^G_{dd_{\text{intra}},j}}(v), \tag{G.1}$$

where the Laplace transform for $I^G_{dd_{\text{intra}},j}$ conditioned on w_0 can be computed following similar steps as in the proof of Lemma F:

$$\begin{aligned}
&\mathcal{L}_{I^G_{dd_{\text{intra}},j}}(v)\\
&= \mathbb{E}_{\mathcal{A}_d^{x_0}}\left[\prod_{y\in\mathcal{A}_d^{x_0}\setminus y_0} \mathbb{E}_{h_{yx_0}}\left[e^{-vP_dGh_{yx_0}\|x_0+y\|^{-\alpha_{j,d}}}\right]\right]\\
&\overset{(a)}{=} \mathbb{E}_{\mathcal{A}_d^{x_0}}\left[\prod_{y\in\mathcal{A}_d^{x_0}\setminus y_0} \frac{1}{\left(1+vP_dG\|x_0+y\|^{-\alpha_{j,d}}/N_j\right)^{N_j}}\right]\\
&\overset{(b)}{=} \sum_{k=0}^{\infty}\left(\int_{\mathbb{R}^2} \frac{1}{\left(1+vP_dG\|x_0+y\|^{-\alpha_{j,d}}/N_j\right)^{N_j}} p_{j,d}(\|x_0+y\|) f_Y(y)dy\right)^k \mathbb{P}(K=k)\\
&= \sum_{k=0}^{\infty}\left(\int_{\mathbb{R}^2} \frac{1}{\left(1+vP_dG\|x_0+y\|^{-\alpha_{j,d}}/N_j\right)^{N_j}} p_{j,d}(\|x_0+y\|) f_Y(y)dy\right)^k\\
&\times \frac{((\bar{n}P_{D2D}-1)p_G)^k e^{-(\bar{n}P_{D2D}-1)p_G}}{k!}\\
&\overset{(c)}{=} \exp\left(-\left(\bar{n}P_{D2D}-1\right)p_G\int_0^{\infty}\left(1-\frac{1}{\left(1+vP_dGu^{-\alpha_{j,d}}/N_j\right)^{N_j}}\right) f_U(u|w_0)p_{j,d}(u)du\right)
\end{aligned} \tag{G.2}$$

where $(\bar{n}P_{D2D}-1)p_G$ is the mean number of the interfering D2D UEs in D2D mode in the representative cluster with random antenna gain G, i.e. total of $\bar{n}P_{D2D}$ D2D UEs in D2D mode are simultaneously transmitting on average in this cluster, (a) is obtained by computing the MGF of the gamma random variable h_{yx_0} with parameter N_j, (b) follows from the fact that the locations of the intra-cluster D2D UEs simultaneously transmitting in D2D mode are independent when conditioned on $x_0 \in \Phi_C$ and expectation over the number of interfering devices which are Poisson distributed, (c) follows by applying a change of variables with $\|x_0+y\| \rightarrow u$, and converting the coordinates from Cartesian to polar by using the pdf of the distance distribution $f_{R_{d_1}}(r_{d_1}|\omega) = \text{Ricepdf}(r_{d_1}, \omega_0; \sigma_d^2)$ where $\{r_{d1} = \|x_0+y\|, \forall y \in \mathcal{A}_d^{x_0}\setminus y_0\}$ and $\omega_0 = \|x_0\|$, and averaging the kth power of $A = \int_0^\infty \frac{1}{\left(1+vP_dGr_{d1}^{-\alpha_{j,d}}/N_j\right)^{N_j}} f_U(u|w_0)p_{j,d}(u)du$ over Poisson distribution, i.e., $\sum_{k=0}^{\infty}(A)^k \frac{((\bar{n}P_{D2D}-1)p_G)^k e^{-((\bar{n}P_{D2D}-1)p_G)}}{k!} = e^{-((\bar{n}P_{D2D}-1)p_G)(1-A)}$.

By inserting (G.2) into (G.1) for $j \in \{L, N\}$ and $G \in \{M_{\mathrm{UE}}M_{\mathrm{UE}}, M_{\mathrm{UE}}m_{\mathrm{UE}}, m_{\mathrm{UE}}M_{\mathrm{UE}}, m_{\mathrm{UE}}m_{\mathrm{UE}}\}$, we readily obtain the Laplace transform expression.

Appendix H

Proof of Theorem 6.1

The outage probability for a typical UE in cellular mode can be calculated as follows:

$$
\begin{aligned}
\mathrm{P}^{c}_{\text{out}}(\Gamma) &= \mathrm{P}^{c}_{\text{out},L}(\Gamma)\mathcal{B}_{L,c} + \mathrm{P}^{c}_{\text{out},N}(\Gamma)\mathcal{B}_{N,c} \\
\mathrm{P}^{c}_{\text{out}}(\Gamma) &= \sum_{s\in\{L,N\}} \mathbb{P}\left(\frac{P_c G_0 h_0 r_c^{-\alpha_{s,c}}}{\sigma_N^2 + I_{cc} + I_{dc}} \leq \Gamma\right)\mathcal{B}_{s,c} \\
&= \sum_{s\in\{L,N\}} \int_0^{\infty} \mathbb{P}\left(h_0 \leq \frac{\Gamma r_c^{\alpha_{s,c}}}{P_c G_0}\left(\sigma_N^2 + I_{cc} + I_{dc}\right)\middle| r_c\right) f_s(r_c)\mathcal{B}_{s,c} dr_c \\
&\approx \sum_{s\in\{L,N\}} \int_0^{\infty} \sum_{n=0}^{N_s} (-1)^n \binom{N_s}{n} e^{-v\sigma_N^2} \mathcal{L}_{I_{cc}}(v)\mathcal{L}_{I_{dc}}(\beta v) f_s(r_c)\mathcal{B}_{s,c} dr_c \qquad \text{(H.1)}
\end{aligned}
$$

where $v = \frac{n\eta_s \Gamma r_c^{\alpha_{s,c}}}{P_c G_0}$, h_0 is a gamma random variable with parameter N_s, $\mathcal{L}_{I_{cc}}(v)$ and $\mathcal{L}_{I_{dc}}(\beta v)$ are the Laplace transforms of interferences at the BS from cellular UEs and D2D UEs, respectively, and β is the spectrum sharing indicator. (H.1) is approximated using the same approach as in [9, Equation (22) Appendix C].

Appendix I

Proof of Lemma 7.1

The CCDF of the path-loss L_0 from the typical UE to a 0^{th} tier UAV can be computed as follows:

$$\begin{aligned}
\bar{F}_{L_0}(x) &= \sum_{s\in\{\text{LOS,NLOS}\}} \bar{F}_{L_{0,s}}(x) \\
&= \sum_{s\in\{\text{LOS,NLOS}\}} \mathbb{E}_r\left[\mathcal{P}_s(r)\mathbb{P}\left(L_{0,s}(r)\geq x\right)\right] \\
&= \sum_{s\in\{\text{LOS,NLOS}\}} \mathbb{E}_d\left[\mathcal{P}_s\left(\sqrt{d^2+H^2}\right)\mathbb{P}\left(\eta_s(d^2+H^2)^{\alpha_s/2}\geq x\right)\right] \qquad \text{(I.1)} \\
&= \sum_{s\in\{\text{LOS,NLOS}\}} \mathbb{E}_d\left[\mathcal{P}_s\left(\sqrt{d^2+H^2}\right)\mathbb{P}\left(d\geq\sqrt{\left(\frac{x}{\eta_s}\right)^{2/\alpha_s}-H^2}\right)\right] \\
&= \sum_{s\in\{\text{LOS,NLOS}\}} \int_{\sqrt{\left(\frac{x}{\eta_s}\right)^{2/\alpha_s}-H^2}}^{\infty} \mathcal{P}_s\left(\sqrt{d^2+H^2}\right) f_D(d)\mathrm{d}d \qquad \text{(I.2)}
\end{aligned}$$

where $f_D(d)$ is given in (7.1) and (I.1) follows from the definition of path-loss and noting that $r=d$ for 0^{th} tier.

Appendix J

Proof of Lemma 7.2

Intensity function for the path-loss model from the typical UE to a 1st tier UAV for $s \in \{\mathrm{LOS}, \mathrm{NLOS}\}$ can be computed as

$$\begin{aligned}
\Lambda_{1,s}([0,x)) &= \int_{\mathbb{R}^2} \mathbb{P}\left(L_1(r) < x\right) dr & \text{(J.1)}\\
&= 2\pi\lambda_U \int_0^\infty \mathbb{P}\left(\eta_s \left(r^2 + H^2\right)^{\alpha_s/2} < x\right) \mathcal{P}_s(r) r dr \\
&= 2\pi\lambda_U \int_0^\infty \mathbb{P}\left(r < \sqrt{(x/\eta_s)^{2/\alpha_s} - H^2}\right) \mathcal{P}_s(r) r dr \\
&= 2\pi\lambda_U \int_0^{\sqrt{(x/\eta_s)^{2/\alpha_s} - H^2}} \mathcal{P}_s(r) r dr & \text{(J.2)}
\end{aligned}$$

where (J.1) follows from the definition of intensity function for the point process of the path-loss. Intensity function for 2nd tier BSs can be also computed using the same approach. Since the link between the ground BSs and the typical UE has only one state, intensity function expression in (J.2) reduces to $\Lambda_2([0,x)) = \pi\lambda_B (x/\eta_B)^{2/\alpha_B}$.

Appendix K

Proof of Lemma 7.3

Association probability with a 0^{th} tier LOS/NLOS UAV can be computed as follows:

$$\mathcal{A}_{0,s} = \mathbb{P}(P_0 B_0 L_{0,s}^{-1} \geq P_j B_j L_{min,j}^{-1}) \tag{K.1}$$

$$= \left(\prod_{j=1}^{2} \mathbb{P}\left(P_0 B_0 L_{0,s}^{-1} \geq P_j B_j L_j^{-1} \right) \right)$$

$$= \int_{\eta_s H^{\alpha_s}}^{\infty} \prod_{j=1}^{2} \bar{F}_{L_j}\left(\frac{P_j B_j}{P_0 B_0} l_{0,s} \right) f_{L_{0,s}}(l_{0,s}) dl_{0,s} \tag{K.2}$$

$$= \int_{\eta_s H^{\alpha_s}}^{\infty} e^{-\sum_{j=1}^{2} \Lambda_j \left(\left[0, \frac{P_j B_j}{P_0 B_0} l_{0,s} \right) \right)} f_{L_{0,s}}(l_{0,s}) dl_{0,s} \tag{K.3}$$

where (K.1) follows from the definition of association probability, in (K.2)CCDF of L_j is formulated as a result of the probability expression, and (K.3) follows from the definition of the CCDF of the path-loss.

Association probability with a 1^{st} tier LOS/NLOS UAV can be computed as follows:

$$
\begin{aligned}
\mathcal{A}_{1,s} &= \mathbb{P}(P_1B_1L_{1,s}^{-1} \geq P_jB_jL_{min,j}^{-1})\mathbb{P}(L_{1,s'} > L_{1,s}) && \text{(K.4)}\\
&= \left(\prod_{j=0,j\neq 1}^{2} \mathbb{P}\left(P_1B_1L_{1,s}^{-1} \geq P_jB_jL_j^{-1}\right)\right)\mathbb{P}(L_{1,s'} > L_{1,s}) && \\
&= \int_{\eta_s H^{\alpha_s}}^{\infty} \prod_{j=0,j\neq 1}^{2} \bar{F}_{L_j}\left(\frac{P_jB_j}{P_1B_1}l_{1,s}\right) e^{-\Lambda_{1,s'}([0,l_{1,s}))} f_{L_{1,s}}(l_{1,s})dl_{1,s} && \text{(K.5)}\\
&= \int_{\eta_s H^{\alpha_s}}^{\infty} \bar{F}_{L_0}\left(\frac{P_0B_0}{P_1B_1}l_{1,s}\right) e^{-\Lambda_2\left(\left[0,\frac{P_2B_2}{P_1B_1}l_{1,s}\right)\right)} e^{-\Lambda_{1,s'}([0,l_{1,s}))}\Lambda'_{1,s}([0,l_{1,s}))e^{-\Lambda_{1,s}([0,l_{1,s}))}dl_{1,s} && \\
& && \text{(K.6)}\\
&= \int_{\eta_s H^{\alpha_s}}^{\infty} \Lambda'_{1,s}\left([0,l_{1,s})\right) \bar{F}_{L_0}\left(\frac{P_0B_0}{P_1B_1}l_{1,s}\right) e^{-\sum_{j=1}^{2}\Lambda_j\left(\left[0,\frac{P_jB_j}{P_1B_1}l_{1,s}\right)\right)} dl_{1,s}, && \text{(K.7)}
\end{aligned}
$$

where $s, s' \in \{\mathrm{LOS}, \mathrm{NLOS}\}$, and $s \neq s'$. (K.4) follows from the definition of association probability, in (K.5), CCDF of L_j is formulated as a result of the probability expression, and similarly $\mathbb{P}(L_{1,s'} > L_{1,s}) = \bar{F}_{L_{1,s'}}(l_{1,s}) = e^{-\Lambda_{1,s'}([0,l_{1,s}))}$; (K.6) follows from the definition of the CCDF of the path-loss, and by plugging the PDF of the path-loss $L_{1,s}$; and (K.7) follows from the fact that $\Lambda_{1,s}([0,l_{1,s})) + \Lambda_{1,s'}([0,l_{1,s})) = \Lambda_1([0,l_{1,s}))$. Since the minimum distance between UEs and UAVs is equal to H, integration starts from $l_{k,s} = \eta_s H^{\alpha_s}$. Association probability with a 2nd tier BS can be obtained following the similar steps. Note that, since the minimum distance between the typical UE and a ground BS is equal to 0, integration starts from 0.

Appendix L

Proof of Theorem 7.1

Given that the UE is associated with a UAV in $k = \{0, 1\}$, the conditional coverage probability $\mathrm{P}^{\mathrm{C}}_{k,s}(\Gamma_k)$ can be computed as follows

$$\begin{aligned}\mathrm{P}^{\mathrm{C}}_{k,s}(\Gamma_k) &= \mathbb{P}(\mathrm{SINR}_{k,s} > \Gamma_k)\\ &= \mathbb{P}\left(\frac{P_k h_{k,0} L_{k,s}^{-1}}{\sigma_k^2 + \sum_{j=0}^{2} I_{j,k}} > \Gamma_k\right)\\ &= \mathbb{P}\left(h_{k,0} > \frac{\Gamma_k L_{k,s}}{P_k}\left(\sigma_k^2 + \sum_{j=0}^{2} I_{j,k}\right)\right)\\ &= e^{-u\sigma_k^2}\prod_{j=0}^{2}\mathcal{L}_{I_{j,k}}(u), \end{aligned} \tag{L.1}$$

where $u = \frac{\Gamma_k L_{k,s}}{P_k}$, $\mathcal{L}_{I_{j,k}}(u)$ is the Laplace transform of $I_{j,k}$ evaluated at u, the last steps follows from $h_{k,0} \sim \exp(1)$, and by noting that Laplace transforms of interference at the UE from different tier UAVs and BSs are independent. $\mathrm{P}^{\mathrm{C}}_{2}(\Gamma_2)$ can be obtained using the similar steps. Tools from stochastic geometry can be applied to compute the Laplace transforms. Recall that 0^{th} is generated by the UAV at the cluster center of the typical UE. When the typical UE is associated with a UAV or a BS in tier-k for $k = 1, 2$, Laplace transform of the interference from 0^{th} tier UAV can be obtained as follows:

$$\begin{aligned}\mathcal{L}_{I_{0,k}}(u) &= \mathbb{E}_{I_{0,k}}\left[e^{-uI_{0,k}}\right]\\ &= \sum_{s'\in\{\text{LOS,NLOS}\}} \mathbb{E}_x\left[\mathbb{E}_{h_{0,0}}\left[\exp\left(-uP_0h_{0,0}x^{-1}\right)|x > \frac{P_0B_0}{P_kB_k}l_k\right]\right] &\text{(L.2)}\\ &= \sum_{s'\in\{\text{LOS,NLOS}\}} \mathbb{E}_x\left[\frac{1}{1+uP_0x^{-1}}|x > \frac{P_0B_0}{P_kB_k}l_k\right] &\text{(L.3)}\\ &= \sum_{s'\in\{\text{LOS,NLOS}\}} \int_{\mathcal{E}_{0,0}}^{\infty}\frac{1}{1+uP_0x^{-1}}f_{L_{0,s'}}(x)dx &\text{(L.4)}\end{aligned}$$

where conditioning in (L.2) is a result of the fact that interfering 0^{th} tier UAV lies outside the exclusion disc $\mathcal{E}_{0,0}$ with radius $\frac{P_0B_0}{P_kB_k}l_k$, and (L.3) follows from $h_{0,0} \sim \exp(1)$. Also note that, $\mathcal{L}_{I_{0,k}}(u)$ is equal to one, if the typical UE is associated with 0^{th} UAV. Laplace transform of the interference from 1^{st} tier UAVs can be calculated as

$$\begin{aligned}\mathcal{L}_{I_{1,k}}(u) &= \mathbb{E}_{I_{1,k}}\left[e^{-uI_{1,k}}\right] &\text{(L.5)}\\ &= \prod_{s'\in\{\text{LOS,NLOS}\}} \exp\left(-\int_{\mathcal{E}_{1,0}}^{\infty}\left(1-\mathbb{E}_{h_{1,i}}\left[e^{-uP_1h_{1,i}x^{-1}}\right]\right)\Lambda'_{1,s'}(dx)\right)\\ &= \prod_{s'\in\{\text{LOS,NLOS}\}} \exp\left(-\int_{\mathcal{E}_{1,0}}^{\infty}\left(\frac{uP_1x^{-1}}{1+uP_1x^{-1}}\right)\Lambda'_{1,s'}(dx)\right) &\text{(L.6)}\end{aligned}$$

where $\Lambda'_{1,s'}(dx)$ is obtained by differentiating $\Lambda_{1,s'}([0,x))$ given in (7.7) with respect to x for $s' \in \{\text{LOS}, \text{NLOS}\}$, respectively, interfering 1^{st} tier UAVs lie outside the exclusion disc $\mathcal{E}_{1,0}$ with radius $\frac{P_1B_1}{P_kB_k}l_k$, (L.5) is obtained by computing the PGFL of the PPP, and (L.6) follows from computing the MGF of the exponentially distributed random variable h. Laplace transform of the interference from 2^{nd} tier BSs, $\mathcal{L}_{I_{2,k}}(u)$, can be calculated following the same steps with the calculation of $\mathcal{L}_{I_{1,k}}(u)$. However, note that there are only LOS BSs for 2^{nd} tier. Finally, by inserting (7.14), (7.15), (7.16), (7.21), (7.22), (7.23) into (7.19), coverage probability expression in (7.20) can be obtained.

Appendix M

Proof of Lemma 8.1

The CCDF of the path loss $L_{0,s}$ from a typical UE to a 0^{th} tier LOS/NLOS UAV can be computed as follows:

$$\begin{aligned}
&\bar{F}_{L_{0,s}}(x) \\
&= \mathbb{E}_r \left[\mathbb{P}\left(L_{0,s}(r) \geq x \right) \mathcal{P}_s(r) \right] \\
&= \mathbb{E}_d \left[\mathbb{P}\left((d^2 + H^2)^{\alpha_s/2} \geq x \right) \mathcal{P}_s(\sqrt{d^2 + H^2}) \right] && \text{(M.1)} \\
&= \int_0^\infty \mathbb{P}\left(d \geq \sqrt{x^{2/\alpha_s} - H^2} \right) \mathcal{P}_s(\sqrt{d^2 + H^2}) f_D(d) \mathrm{d}d \\
&= \int_{\sqrt{x^{2/\alpha_s} - H^2}}^\infty \mathcal{P}_s(\sqrt{d^2 + H^2}) f_D(d) \mathrm{d}d && \text{(M.2)}
\end{aligned}$$

for$s \in \{\mathrm{LOS}, \mathrm{NLOS}\}$ where $f_D(d)$ is given in (8.1), $\mathcal{P}_s(\cdot)$ is the LOS or NLOS probability depending on whether $s = \mathrm{LOS1}$ or $s = \mathrm{NLOS}$, and (M.1) follows from the definition of path loss. Therefore, the CCDF of the path loss L_0 from a typical UE to a 0^{th} tier UAV given in (8.8) can be obtained by summing up over s.

Appendix N

Proof of Lemma 8.2

Intensity function for the path loss model from a typical UE to a 1st tier UAV for $s \in \{\mathrm{LOS}, \mathrm{NLOS}\}$ can be computed as

$$\begin{aligned}
\Lambda_{1,s}([0,x)) &= \int_{\mathbb{R}^2} \mathbb{P}\left(L_1(r) < x\right) \mathrm{d}r && \text{(N.1)}\\
&= 2\pi\lambda_U \int_H^\infty \mathbb{P}\left(r^{\alpha_s} < x\right) \mathcal{P}_s(r) r \mathrm{d}r && \text{(N.2)}\\
&= 2\pi\lambda_U \int_H^\infty \mathbb{P}\left(r < x^{1/\alpha_s}\right) \mathcal{P}_s(r) r \mathrm{d}r && \text{(N.3)}\\
&= 2\pi\lambda_U \int_H^{x^{1/\alpha_s}} \mathcal{P}_s(r) r \mathrm{d}r && \text{(N.4)}
\end{aligned}$$

where (N.1) follows from the definition of intensity function for the point process of the path loss. CCDF of the path loss L_1 from a typical UE to a 1st tier UAV given in 8.9 can be obtained by summing up $\Lambda_{1,s}([0,x))$ over s.

Appendix O

Proof of Lemma 8.3

Association probability with a 0th tier LOS/NLOS UAV can be computed as follows:

$$\begin{align}
\mathcal{A}_{0,s} &= \prod_{m\in\{\text{LOS},\text{NLOS}\}} \mathbb{P}(P_0 G_0(r) L_{0,s}^{-1} \geq P_1 G_1(r) L_{1,m}^{-1}) \tag{O.1}\\
&= \prod_{m\in\{\text{LOS},\text{NLOS}\}} \mathbb{P}\left(P_0 \frac{H^2}{L_{0,s}^{\frac{2}{\alpha_s}}} L_{0,s}^{-1} \geq P_1 \frac{H^2}{L_{1,m}^{\frac{2}{\alpha_L}}} L_{1,m}^{-1}\right) \tag{O.2}\\
&= \prod_{m\in\{\text{LOS},\text{NLOS}\}} \mathbb{P}\left(L_{1,m} \geq \left(\frac{P_1}{P_0} L_{0,s}^{\frac{2}{\alpha_s}+1}\right)^{\frac{\alpha_m}{\alpha_m+2}}\right) \nonumber\\
&= \int_{H^{\alpha_s}}^{\infty} \prod_{m\in\{\text{LOS},\text{NLOS}\}} \bar{F}_{L_m}\left(\left(\frac{P_1}{P_0} l_{0,s}^{\frac{2}{\alpha_s}+1}\right)^{\frac{\alpha_m}{\alpha_m+2}}\right) f_{L_{0,s}}(l_{0,s})\mathrm{d}l_{0,s} \tag{O.3}
\end{align}$$

where (O.1) follows from the definition of association probability and the fact that LOS and NLOS links in the 1st tier are independent, (O.3) follows from the definition of the CCDF of the path loss. Since the minimum distance between UEs and UAVs is equal to H, integration starts from $l_{0,s} = H^{\alpha_s}$.

Association probability with a 1st tier LOS/NLOS UAV can be computed as follows:

$$\begin{aligned}
\mathcal{A}_{1,s} &= \mathbb{P}(L_{1,s'} > L_{1,s}) \prod_{m\in\{\text{LOS,NLOS}\}} \mathbb{P}(P_1 G_1(r) L_{1,s}^{-1} \geq P_0 G_0(r) L_{0,m}^{-1}) && \text{(O.4)}\\
&= \mathbb{P}(L_{1,s'} > L_{1,s}) \prod_{m\in\{\text{LOS,NLOS}\}} \mathbb{P}\left(P_1 \frac{H^2}{L_{1,s}^{\frac{2}{\alpha_s}}} L_{1,s}^{-1} \geq P_0 \frac{H^2}{L_{0,m}^{\frac{2}{\alpha_m}}} L_{0,m}^{-1} \right)\\
&= \mathbb{P}(L_{1,s'} > L_{1,s}) \prod_{m\in\{\text{LOS,NLOS}\}} \mathbb{P}\left(L_{0,m} \geq \left(\frac{P_0}{P_1} L_{1,s}^{\frac{2}{\alpha_s}+1} \right)^{\frac{\alpha_m}{\alpha_m+2}} \right)\\
&= \int_{H^{\alpha_s}}^{\infty} \bar{F}_{L_{1,s'}}(l_{1,s}) \prod_{m\in\{\text{LOS,NLOS}\}} \bar{F}_{L_{0,m}} \left(\left(\frac{P_0}{P_1} l_{1,s}^{\frac{2}{\alpha_s}+1} \right)^{\frac{\alpha_m}{\alpha_m+2}} \right) f_{L_{1,s}}(l_{1,s}) \mathrm{d}l_{1,s}, && \text{(O.5)}
\end{aligned}$$

where $s, s' \in \{\text{LOS}, \text{NLOS}\}$, and $s \neq s'$. (O.4) follows from the definition of association probability and the fact that LOS and NLOS links in the 0^{th} tier are independent, and $\mathbb{P}(L_{1,s'} > L_{1,s}) = \bar{F}_{L_{1,s'}}(l_{1,s})$.

Appendix P

Proof of Theorem 8.1

Given that the UE is associated with a LOS/NLOS UAV in $k = \{0, 1\}$, the conditional energy coverage probability $\mathrm{E}^{\mathrm{C}}_{k,s}(\Gamma_k)$ can be computed as follows:

$$\begin{aligned}
\mathrm{E}^{\mathrm{C}}_{k,s}(\Gamma_k) &= \mathbb{P}(\xi\left(S_{k,s} + I_{tot}\right) > \Gamma_k) && \text{(P.1)}\\
&\approx \sum_{n=0}^{N}(-1)^n\binom{N}{n}\mathbb{E}_{S_{k,s},I_{tot}}\left[e^{-\hat{a}(S_{k,s}+I_{tot})}\right] && \text{(P.2)}\\
&= \sum_{n=0}^{N}(-1)^n\binom{N}{n}\mathbb{E}_{S_{k,s}}\left[e^{-\hat{a}S_{k,s}}\mathbb{E}_{I_{tot}|S_{k,s}}\left[e^{-\hat{a}I_{tot}}\right]\right]\\
&= \sum_{n=0}^{N}(-1)^n\binom{N}{n}\mathbb{E}_{L_{k,s}}\left[\left(1+\hat{a}P_kG_kL_{k,s}^{-1}\right)^{-1}\prod_{j=0}^{1}\mathbb{E}_{I_{j,k}|L_{k,s}}\left[e^{-\hat{a}I_{j,k}}\right]\right] && \text{(P.3)}\\
&= \sum_{n=0}^{N}(-1)^n\binom{N}{n}\mathbb{E}_{L_{k,s}}\left[\left(1+\hat{a}P_kH^2L_{k,s}^{-\left(1+\frac{2}{\alpha_s}\right)}\right)^{-1}\prod_{j=0}^{1}\mathcal{L}_{I_{j,k}}(\Gamma_k,\mathcal{E}_{k,0})\right] && \text{(P.4)}
\end{aligned}$$

where $\hat{a} = \frac{n\eta}{\Gamma_k/\xi}$, $\eta = N(N!)^{-\frac{1}{N}}$, N is the number of terms in the approximation, $\mathcal{L}_{I_{j,k}}(\Gamma_k, \mathcal{E}_{k,0})$ is the Laplace transform of $I_{j,k}$, (P.1) follows from the definition of energy coverage probability, (P.2) is approximated by following the similar steps in [99]. In (P.3) we inserted the antenna gain $G_k = H^2L_{k,s}^{\frac{2}{\alpha_s}}$, and the last step in (P.4) follows from $h_{k,0} \sim \exp(1)$ and by noting that Laplace transforms of interference at the UE from different tier UAVs are independent.

Tools from stochastic geometry can be applied to compute the Laplace transforms. Recall that 0^{th} is generated by the UAV at the cluster center of the typical UE. When the typical UE is associated with a UAV in the 1^{st} tier, Laplace transform of the interference from 0^{th} tier UAV can be obtained as follows:

$$\begin{aligned}
&\mathcal{L}_{I_{0,k}}(u) = \mathbb{E}_{I_{0,k}}\left[e^{-\hat{a}I_{0,k}}\right] \\
&= \sum_{s'\in\{\text{LOS,NLOS}\}} \mathbb{E}_x\left[\mathbb{E}_{h_{0,0}}\left[\exp\left(-\hat{a}P_0G_0h_{0,0}x^{-1}\right)|P_0G_0x^{-1} < P_kG_kl_k^{-1}\right]\right] && \text{(P.5)} \\
&= \sum_{s'\in\{\text{LOS,NLOS}\}} \mathbb{E}_x\left[\left(1+\hat{a}P_0H^2x^{-\left(1+\frac{2}{\alpha_{s'}}\right)}\right)^{-1}\middle| x > \left(\frac{P_0}{P_k}l_{k,s}^{1+\frac{2}{\alpha_s}}\right)^{\frac{\alpha_{s'}}{\alpha_{s'}+2}}\right] && \text{(P.6)} \\
&= \sum_{s'\in\{\text{LOS,NLOS}\}} \int_{\mathcal{E}_{k,0}}^{\infty}\left(1+\hat{a}P_0H^2x^{-\left(1+\frac{2}{\alpha_{s'}}\right)}\right)^{-1} f_{L_{0,s'}}(x)\mathrm{d}x && \text{(P.7)}
\end{aligned}$$

where conditioning in (P.5) is a result of the cell association policy, i.e., the received power from the interfering 0^{th} tier UAV is less than the received power from the associated UAV, (P.6) follows from $h_{0,0} \sim \exp(1)$ and inserting the antenna gains, in the last step the exclusion disc $\mathcal{E}_{k,0} = \left(\frac{P_0}{P_k}l_{k,s}^{1+\frac{2}{\alpha_s}}\right)^{\frac{\alpha_{s'}}{\alpha_{s'}+2}}$. Also note that $\mathcal{L}_{I_{0,k}}(u)$ is equal to one, if the typical UE is associated with 0^{th} tier UAV.

Laplace transform of the interference from 1^{st} tier UAVs can be calculated as

$$\begin{aligned}
&\mathcal{L}_{I_{1,k}}(u) = \mathbb{E}_{I_{1,k}}\left[e^{-\hat{a}I_{1,k}}\right] \\
&= \prod_{s'\in\{\text{LOS,NLOS}\}} \exp\left(-\int_{\mathcal{E}_{k,0}}^{\infty}\left(1-\mathbb{E}_{h_{1,i}}\left[e^{-\hat{a}P_1H^2h_{1,i}x^{-\left(1+\frac{2}{\alpha_{s'}}\right)}}\right]\right)\Lambda'_{1,s'}([0,x))\mathrm{d}x\right) && \text{(P.8)} \\
&= \prod_{s'\in\{\text{LOS,NLOS}\}} \exp\left(-\int_{\mathcal{E}_{k,0}}^{\infty}\left(1-\left(1+\hat{a}P_1H^2x^{-\left(1+\frac{2}{\alpha_{s'}}\right)}\right)^{-1}\right)\Lambda'_{1,s'}([0,x))\mathrm{d}x\right) && \text{(P.9)}
\end{aligned}$$

where (P.8) is obtained by computing the probability generating functional of the

PPP, and (P.9) follows by computing the moment generating function of the exponentially distributed random variable h. Note that the interfering 1^{st} tier UAVs lie outside the exclusion disc $\mathcal{E}_{k,0}$ with radius $\left(\frac{P_1}{P_k} l_{k,s}^{1+\frac{2}{\alpha_s}}\right)^{\frac{\alpha_{s'}}{\alpha_{s'}+2}}$. Finally, by inserting (8.15), (8.16), (8.23), (8.24) into (8.21), energy coverage probability expression in (8.22) can be obtained.

Bibliography

[1] "Mobile traffic forecasts: 2010-2020 report," in *Proc. UMTS Forum Rep.*, vol. 44, pp. 1-92, Zurich, Switzerland, 2011.

[2] Ericson, "More than 50 billion connected devices," Feb. 2011.

[3] T. Rappaport *et al.*, "Millimeter wave mobile cimmunications for 5G cellular: It will work!," *IEEE Access*, vol. 1, pp. 335-349, May 2013.

[4] W. Roh et al., "Millimeter-wave beamforming as an enabling technology for 5G cellular communications: Theoretical feasibility and prototype results," *IEEE Commun. Mag.*, vol. 52, no. 2, pp. 106-113, Feb. 2014.

[5] J. G. Andrews *et al.*, "What will 5G be?," *IEEE J. Sel. Areas Commun.*, vol. 32, no. 6, pp. 1065-1082, Jun. 2014.

[6] S. Rangan and T.S. Rappaport and E. Erkip, "Millimeter-wave cellular wireless networks: Potentials and challenges," *Proceedings of the IEEE*, vol. 102, no. 3, pp. 366-385, Mar. 2014.

[7] A. Ghosh and T. A. Thomas and M. C. Cudak and R. Ratasuk and P. Moorut and F. W. Vook and T. S. Rappaport and G. R. MacCartney and Shu Sun and Shuai Nie, "Millimeter wave enhanced local area systems: A high data rate approach for future wireless networks," *IEEE Journal on Sel. Areas in Comm.*, Special Issue on 5G, Jul., 2014.

[8] P. Wang, Y. Li, L. Song, and B. Vucetic,“Multi-gigabit millimeter wave wireless communications for 5G: From fixed access to cellular networks,” *IEEE Commun. Mag.*, vol. 53, no. 1, pp. 168-178, Jan. 2015.

[9] T. Bai, and R. W. Heath, “Coverage and rate analysis for millimeter wave cellular networks,” *IEEE Trans. Wireless Commun.*, vol. 14, no. 2, pp. 1100-1114, Feb. 2015.

[10] S. Singh, M. Kulkarni, A. Ghosh, and J. Andrews, “Tractable model for rate in self-backhauled millimeter wave cellular networks,” *IEEE Journal on Selected Areas in Communications*, vol. 33, no. 10, pp. 2196-2211, Oct. 2015.

[11] M. N. Kulkarni, S. Singh, and J. G. Andrews “Coverage and rate trends in dense urban mmWave cellular networks,” *IEEE Global Communications Conference (GLOBECOM)* pp. 3809-3814, Dec. 2014.

[12] M. Akdeniz, Y. Liu, M. Samimi, S. Sun, S. Rangan, T. Rappaport, and E. Erkip, “Millimeter wave channel modeling and cellular capacity evaluation,” *IEEE Journal on Selected Areas in Communications*, vol. 32, no. 6, pp. 1164-1179, Jun. 2014.

[13] M. Di Renzo, “Stochastic geometry modeling and analysis of multi-tier millimeter wave cellular networks,” *IEEE Trans. Commun.*, vol. 14, no. 9, pp. 5038-5057, Sep. 2015.

[14] H. ElSawy, E. Hossain, and M. Haenggi, “Stochastic geometry for modeling, analysis, and design of multi-tier and cognitive cellular wireless networks: A survey,” *IEEE Commun. Surveys Tutorials*, vol. 15, no. 3, pp. 996-1019, 2013.

[15] H. ElSawy, A. Sultan-Salem, M. S. Alouini, and M. Z. Win, “Modeling and analysis of cellular networks using stochastic geometry: A tutorial,” *IEEE Commun. Surveys Tutorials*, vol. 19, no. 1, pp: 167-203, First Quarter 2017.

[16] J. G. Andrews, T. Bai, M. N. Kulkarni, A. Alkhateeb, A. K. Gupta, and R. W. Heath, "Modeling and analyzing millimeter wave cellular systems," *IEEE Trans. on Commun.*, vol. 65, no. 1, pp. 403-430, Jan 2017.

[17] N. H. Motlagh, T. Taleb, and O. Arouk, "Low-altitude unmanned aerial vehicles-based internet of things services: comprehensive survey and future perspectives," *IEEE Internet of Things J.*, vol. 3, no. 6, pp. 899–922, Dec. 2016.

[18] A. Merwaday, A. Tuncer, A. Kumbhar, and I. Guvenc, "Improved throughput coverage in natural disasters: Unmanned aerial base stations for public-safety communications," *IEEE Veh. Techno. Mag.*, vol. 11, no. 4, pp. 53-60, Dec. 2016.

[19] R. I. Bor-Yaliniz, and H. Yanikomeroglu, "The new frontier in RAN heterogeneity: Multi-tier drone-cells," *IEEE Commun. Mag.*, vol. 54, no. 11, pp. 48–55, Nov. 2016.

[20] E. Turgut, and M. C. Gursoy, "Average error probability analysis in mmWave cellular networks," *Proc. IEEE Veh. Technol. Conf. (VTC-Fall)*, pp. 1–5, Sep. 2015.

[21] E. Turgut, and M. C. Gursoy, "Energy efficiency in relay-assisted mmwave cellular networks," *Proc. IEEE Veh. Technol. Conf. (VTC-Fall)*, pp. 1–5, Sep. 2016.

[22] E. Turgut and M. Cenk Gursoy, "Coverage in heterogeneous downlink millimeter wave cellular networks," *IEEE Trans. Commun.*, vol. 65, no. 10, pp. 4463-4477, Oct. 2017.

[23] E. Turgut and M. C. Gursoy, "Coverage in heterogeneous downlink millimeter wave cellular networks," *Proc. of IEEE Global Commun. Conf. (Globecom)*, pp. 1-6, Dec. 2016.

[24] E. Turgut, and M. C. Gursoy, “Uplink performance analysis in D2D-enabled millimeter wave cellular networks,” *Proc. IEEE Veh. Technol. Conf. (VTC-Fall)*, pp. 1–5, Sep. 2017.

[25] E. Turgut and M. Cenk Gursoy, “Uplink performance analysis in D2D-enabled mmwave cellular networks with clustered users,” *IEEE Trans. Wireless Commun.*, vol. 18, no. 2, pp. 1085-1100, Feb. 2019.

[26] E. Turgut, and M. C. Gursoy, “Outage probability analysis in D2D-enabled mmwave cellular networks with clustered users,” *Proc. IEEE Veh. Technol. Conf. (VTC-Fall)*, pp. 1–5, Aug. 2018.

[27] E. Turgut and M. Cenk Gursoy, “Downlink analysis in unmanned aerial vehicle (UAV) assisted cellular networks with clustered users,” *IEEE Access*, vol. 6, pp. 36313-36324, May 2018.

[28] M. Di Renzo and P. Guan, “Stochastic geometry modeling of coverage and rate of cellular networks using the Gil-Pelaez inversion theorem”, *IEEE Commun. Lett.*, vol. 18, no. 9, pp. 1575-1578, Sep. 2014.

[29] F. Baccelli and B. Blaszczyszyn, “Stochastic Geometry and Wireless Networks, Part I: Theory, Part II: Applications,” NOW: Foundations and Trends in Networking, 2010.

[30] M. Z. Win and P. C. Pinto and L. A. Shepp, “A mathematical theory of network interference and its applications,” *Proc. of the IEEE*, vol. 97, no. 2, pp. 205-230, Feb. 2009.

[31] P. Guan and M. Di Renzo, “Stochastic geometry analysis of the average error probability of downlink cellular networks,” *IEEE Int. Conf. Comput. Netw. Commun.*, pp. 649-655, Feb. 2014.

[32] A. Thornburg, T. Bai, and R. W. Heath, “Performance analysis of mmWave ad hoc networks,” *IEEE Trans. Signal Process.*, *IEEE Trans. Signal Processing.*, vol. 64, no. 15, pp. 4065-4079. Aug. 2016.

[33] Jeffrey G. Andrews and François Baccelli and Radha Krishna Ganti, “A Tractable approach to coverage and rate in cellular networks,” *IEEE Trans. Commun.*, vol. 59, no. 11, Nov. 2011.

[34] A. Hunter and J. Andrews and S. Weber, “Transmission capacity of ad hoc networks with spatial diversity,” *IEEE Trans. Wireless Commun.*, vol. 7, no. 12, pp. 5058-5071, Dec. 2008.

[35] T. Bai and R. Vaze and R. W. Heath Jr., “Analysis of blockage effects on urban cellular networks,” *IEEE Trans. Wireless Commun.*, vol. 13, no. 9, pp. 5070-5083, Sept. 2014.

[36] M. K. Simon and M. S. Alouini, *Digital Communication over Fading Channels*, 2nd ed. Hoboken, NJ, USA: Willey, 2005.

[37] G. Samoradnitsky and M.S. Taqqu, *Stable Non-Gaussian Random Processes*, Chapman and Hall, Jun. 1994.

[38] J. Gil-Pelaez, “Notes on the inversion theorem,” *Biometrika*, vol. 38, pp. 481-482, Dec. 1951.

[39] E. Biglieri and G. Caire and G. Taricco and J. Ventura-Traveset, “Computing error probabilities over fading channels: A unified approach,” *European Trans. Telecommun.*, vol. 9, no. 1, pp. 15-25, Jan.-Feb. 1998

[40] M. Haenggi and R. K. Ganti, “Interference in Large Wireless Networks,” Foundations and Trends in Networking, vol. 3, no. 2, pp. 127-248, 2009.

[41] I. S. Gradshteyn and I. M. Ryzhik, “Tables of Integrals, Series, and Products,” San Diego, CA: Academic, 7th ed., 2007.

[42] A. Goldsmith, *Wireless Communications*, Cambridge University Press, 2005.

[43] J. Wildman, P. H. J. Nardelli, M. Latva-aho, and Steven Weber, “On the joint impact of beamwidth and orientation error on throughput in directional wireless Poisson networks,” *IEEE Trans. Wireless Commun.*, vol. 13, no. 12, pp. 7072-7085, Dec. 2014.

[44] H. Yu, Y. Li, M. Kountouris, X. Xu, and J. Wang, “Energy efficiency analysis of relay-assisted cellular networks using stochastic geometry,” *12th International Symposium on Modeling and Optimization in Mobile, Ad Hoc, and Wireless Networks (WiOpt)*, pp. 667 - 671, 2014.

[45] H. Wei, N. Deng, M. Zhao, W. Zhou, and P. Dong, “Station density effect on energy efficiency of relay-assisted cellular networks,” *Proc. of the 1st IEEE International Conference on Communications in China (ICCC), Beijing, China*, vol. 411, pp. 415, 2012.

[46] T. S. Rappaport, and J. N. Murdock, “Power efficiency and consumption factor analysis for broadband millimeter-wave cellular networks,” *IEEE Global Communications Conference (GLOBECOM)*, pp.4518 - 4523, Dec. 2012.

[47] S. Yun, S. H. Jeon, J. K. Choi, and Ae-Soon Park, “Energy efficiency of relay operation in millimeter-wave mobile broadband systems,” *IEEE VTC-Spring*, pp. 1-5, May 2014.

[48] F. Richter, A. J. Fehske, and Gerhard P. Fettweis, “Energy efficiency aspects of base station deployment strategies for cellular networks,” *Proc. of IEEE VTC-Fall*, pp. 1-5, Sep. 2009.

[49] H. S. Dhillon, R. K. Ganti, F.Baccelli, and J. G. Andrews, “Modeling and analysis of K-Tier downlink heterogeneous cellular networks,” *IEEE Journal on Selected Areas in Communications*, vol. 30, no.3, pp.550-560, Apr. 2012.

[50] H.-S. Jo, Y. J. Sang, P. Xia, and J. G. Andrews, “Heterogeneous cellular networks with flexible cell association: A comprehensive downlink SINR analysis,” *IEEE Trans. Wireless Commun.*, vol. 11, no. 10, pp. 3484-3495, Oct. 2012.

[51] A. Damnjanovic, J. Montojo, Y. Wei, T. Ji, T. Luo, M. Vajapeyam, T. Yoo, O. Song, and D. Malladi, “A survey on 3GPP heterogeneous networks,” *IEEE Wireless Commun. Mag.*, vol. 18, no. 3, pp. 10-21, Jun. 2011.

[52] M. Di Renzo, A. Guidotti,and G. E. Corazza, “Average rate of downlink heterogeneous cellular networks over generalized fading channels: A stochastic geometry approach,” *IEEE Trans. on Commun.*, vol. 61, no. 7, pp. 3050-3071 Jul. 2013.

[53] H. Shokri-Ghadikolaei, C. Fischione, G. Fodor, P. Popovski, and M. Zorzi, “Millimeter wave cellular networks: A MAC layer perspective,” *IEEE Transactions on Communications*, vol. 63, no. 10, pp. 3437-3458, Oct. 2015.

[54] H. Elshaer, M. N. Kulkarni, F. Boccardi, J. G. Andrews, M. Dohler, “Downlink and uplink cell association with traditional macrocells and millimeter wave small cells,” *IEEE Trans. Wireless Commun.*, vol. 15, no. 9, pp. 6244- 6258, Sep. 2016.

[55] M. Rebato, F. Boccardi, M. Mezzavilla, S. Rangan, and M. Zorzi, “Hybrid spectrum access for mmWave networks,” *Proc. IEEE IFIP Annu. Medit. Ad Hoc Netw. Workshop (Med-Hoc-Net)*, pp. 1-7, 2016.

[56] D. Maamari, N. Devroye, and D. Tuninetti, “Coverage in mmWave cellular networks with base station cooperation,” *IEEE Trans. Wireless Commun.*, vol. 15, no. 4, pp. 2981-2994, Apr. 2016.

[57] M. Di Renzo, W. Lu, and P. Guan, "The intensity matching approach: A tractable stochastic geometry approximation to system-level analysis of cellular networks," *IEEE Trans. Wireless Commun.*, vol. 11, no. 9, pp. 5963-5983, Sep. 2016.

[58] W. Lu and M. Di Renzo, "Stochastic geometry modeling of cellular networks: analysis, simulation and experimental validation," *ACM MSWiM*, pp. 179-188, Nov. 2015.

[59] T. Bai and R. W. Heath, Jr, "Coverage in dense millimeter wave cellular networks," *Asilomar Conference on Signals, Systems and Computers*,pp. 2062-2066, Nov. 2013.

[60] M. Ding, P. Wang, D. López-Pérez, G. Mao, and Z. Lin, "Performance impact of LoS and NLoS transmissions in dense cellular networks," *IEEE Trans. Wireless Commun.*, vol. 15, no. 3, pp. 2365-2380, Mar. 2016.

[61] B. Blaszczyszyn, M. K. Karray, and H.P. Keeler, "Using Poisson processes to model lattice cellular networks," *IEEE International Conference on Computer Communications*, pp. 773-781, Apr. 2013.

[62] A. K. Gupta, J. G. Andrews, and R. W. J. Heath, "On the Feasibility of Sharing Spectrum Licenses in mmWave Cellular Systems," *IEEE Trans. Commun.*, vol. 64, no. 9, pp. 3981-3995, Sep. 2016.

[63] S. Singh, H. S. Dhillon, and J. G. Andrews, "Offloading in heterogeneous networks: Modeling, analysis, and design insights," *IEEE Trans. Wireless Commun.*, vol. 12, pp. 2484-2497, May 2013.

[64] Z. Hasan, H. Boostanimehr, and V. K. Bhargava, "Green cellular networks: A survey, some research issues and challenges," *IEEE Commun. Surveys Tuts.*, vol. 13, no. 4, pp. 524-540, 2011.

[65] J. Qiao, X. Shen, J. Mark, Q. Shen, Y. He, and L. Lei, "Enabling deviceto-device communications in millimeter-wave (5G) cellular networks," *IEEE Commun. Mag.*, vol. 53, no. 1, pp. 209-215, Jan. 2015.

[66] Z. Guizani and N. Hamdi, "mmWave E-Band D2D communications for 5G-Underlay networks: Effect of power allocation on D2D and cellular users throughputs," *IEEE Symposium on Computers and Communication*, June 2015.

[67] X. Lin, J. G. Andrews, and A. Ghosh, "Spectrum sharing for device-to-device communication in cellular networks," *IEEE Trans. Wireless Commun.*, vol. 13, no. 12, pp. 6727-6740, Dec. 2014.

[68] N. Eshraghi, B. Maham, and V. Shah-Mansouri, "Millimeter-wave device-to-device multi-hop routing for multimedia applications," *IEEE International Conference on Communications (ICC)*, May 2016.

[69] H. ElSawy and E. Hossain, "Analytical modeling of mode selection and power control for underlay D2D communication in cellular networks," *IEEE Trans. Commun.*, vol. 62, no. 11, pp. 4147-4161, Nov. 2014.

[70] M. Afshang, H. S. Dhillon, and P. H. J. Chong, "Modeling and performance analysis of clustered device-to-device networks," *IEEE Trans. Wireless Commun.*, vol. 15, no. 7, pp. 4957-4972, Jul. 2016.

[71] M. Afshang, H. S. Dhillon, and P. H. J. Chong, "Fundamentals of Cluster-Centric Content Placement in Cache-Enabled Device-to-Device Networks," *IEEE Trans. Commun.*, vol. 64, no. 6, pp. 2511-2526, Jun. 2016.

[72] M. Afshang and H. S. Dhillon, "Spatial modeling of device-to-device networks: Poisson cluster process meets Poisson hole process," *Proc. Annual Asilomar Conf. on Signals, Syst., Comp.*, pp. 317-321, Nov. 2015.

[73] B. Yu, S. Mukherjee, H. Ishii, and L. Yang “Dynamic TDD support in the LTE-B enhanced local area architecture,” *Proc. of the IEEE Globecom Workshops*, pp. 585-591, Dec. 2012.

[74] M. Haenggi, “User point processes in cellular networks,” *IEEE Wireless Commun. Letters*, vol. 6, no. 2, pp. 258-261, Apr. 2017.

[75] A. Al-Hourani, S. Kandeepan, and S. Lardner, “Optimal LAP altitude for maximum coverage,” *IEEE Wireless Commun. Letters*, vol. 3, no. 6, Dec. 2014.

[76] B. Galkin, J. Kibiłda, and L. A. DaSilva, “Coverage Analysis for Low-Altitude UAV Networks in Urban Environments,” *Proc. of IEEE Globecom*, Dec 2017.

[77] V. V. Chetlur, and H. S. Dhillon, “Downlink coverage analysis for a finite 3-D wireless network of unmanned aerial vehicles,” *IEEE Trans. Commun.*, vol. 65, no. 10, pp. 4543-4558, Oct. 2017.

[78] M. M. Azari, Y. Murillo, O. Amin, F. Rosas, M.-S. Alouini, and S. Pollin, “Coverage Maximization for a Poisson Field of Drone Cells,” Submitted, available at https://arxiv.org/pdf/1708.06598.pdf, 2017.

[79] C. Zhang, and W. Zhang, “Spectrum sharing for drone networks,” *IEEE J. Sel. Areas Commun.*, vol. 35, no. 1, pp. 136-144, Jan. 2017.

[80] R. I. Bor-Yaliniz, A. El-Keyi, and H. Yanikomeroglu, “Efficient 3-D placement of an aerial base station in next generation cellular networks,” *Proc. of IEEE Int. Conf. Commun. (ICC)*, pp. 1-5, May. 2016.

[81] M. Mozaffari, W. Saad, M. Bennis, and M. Debbah, “Efficient deployment of multiple unmanned aerial vehicles for optimal wireless coverage,” *IEEE Wireless Commun. Letters*, vol. 20, no. 8, Aug. 2016.

[82] M. Mozaffari, W. Saad, M. Bennis, and M. Debbah, “Optimal transport theory for power-efficient deployment of unmanned aerial vehicles,” *Proc. IEEE Int. Conf. Commun. (ICC)*, May. 2016.

[83] M. Mozaffari, W. Saad, M. Bennis, and M. Debbah, “Optimal transport theory for cell association in UAV-enabled cellular networks,” *IEEE Wireless Commun. Letters*, vol. 21, no. 9, Sep. 2017.

[84] M. Mozaffari, W. Saad, M. Bennis, and M. Debbah, “Unmanned aerial vehicle with underlaid device-to-device communications: Performance and tradeoffs,” *IEEE Trans. Wireless Commun.*, vol. 15, no. 6, Jun. 2016.

[85] A. Kumbhar, I. Guvenc, S. Singh, and A. Tuncer, “Exploiting LTE-advanced HetNets and FeICIC for UAV-assisted public safety communications,” *IEEE Access*, 2017.

[86] P.-V. Mekikis, A. Antonopoulos, E. Kartsakli, L. Alonso, and C. Verikoukis, “Communication recovery with emergency aerial networks,” *IEEE Trans. Consumer Electronics*, vol. 63, no. 3, pp. 291-299, Aug. 2017.

[87] X. Zhou, J. Guo, S. Durrani, and H. Yanikomeroglu, “Uplink coverage performance of underlay drone cell for temporary events,” Submitted, available at https://arxiv.org/pdf/1801.05948.pdf.

[88] R. K. Ganti and M. Haenggi, “Interference and outage in clustered wireless ad hoc networks,” *IEEE Trans. Info. Theory*, vol. 55, no. 9, pp. 4067-4086, Sept. 2009.

[89] M. Afshang, C. Saha, and H. S. Dhillon, “Nearest-neighbor and contact distance distributions for Thomas cluster process,” *IEEE Wireless Commun. Letters*, vol. 6, no. 1, Feb. 2017.

[90] M. Afshang, C. Saha, and H. S. Dhillon, “Nearest-neighbor and contact distance distributions for Matérn cluster process,” *IEEE Wireless Commun. Letters*, vol. 21, no. 12, Dec. 2017.

[91] M. Afshang, and H. S. Dhillon, “Poisson cluster process based analysis of HetNets with correlated user and base station locations,” *IEEE Trans. Wireless Commun.*, Jan. 2018.

[92] C. Saha, M. Afshang, and H. S. Dhillon, “3GPP-inspired HetNet model using Poisson cluster process: Sum-product functionals and downlink coverage,” *IEEE Trans. on Wireless Commun*, Dec. 2017.

[93] C. Saha, M. Afshang, and H. S. Dhillon, “Enriched K-Tier HetNet model to enable the analysis of user-centric small cell deployments,” *IEEE Trans. Wireless Commun.*, vol. 16, no. 3, Mar. 2017.

[94] X. Wang, E. Turgut and M. Cenk Gursoy, “Coverage in downlink heterogeneous mmWave cellular networks with user-centric small cell deployment,” *IEEE Trans. Vehicular Techno.*, Early Access, 2019.

[95] M. Haenggi, *Stochastic Geometry for Wireless Networks.* Cambridge, U.K.: Cambridge Univ. Press, 2012.

[96] A. Hourani, S. Kandeepan, and A. Jamalipour, “Modeling air-to-ground path loss for low altitude platforms in urban environments,” *Proc. of IEEE Global Comm. Conf. (GLOBECOM)*, Dec. 2014.

[97] Y. Zeng, B. Clerckx, and R. Zhang, “Communications and signals design for wireless power transmission,” *IEEE Trans. Commun.*, vol. 65, no. 5, pp. 2264–2290, May 2017.

[98] S. Bi, C. K. Ho, and R. Zhang, "Wireless powered communication: Opportunities and challenges," *IEEE Commun. Mag.*, vol. 53, no. 4, pp. 117–125, Apr. 2015.

[99] T. A. Khan, A. Alkhateeb, and R. W. Heath, "Millimeter wave energy harvesting," *IEEE Trans. Wireless Commun.*, vol. 15, no. 9, pp. 6048-6062, Sep. 2016.

[100] A. Sakr and E. Hossain, "Cognitive and energy harvesting-based D2D communication in cellular networks: Stochastic geometry modeling and analysis," *IEEE Trans. Commun.*, vol. 63, pp. 1867-1880, May 2015.

[101] K. Huang and V. Lau, "Enabling wireless power transfer in cellular networks: Architecture, modeling and deployment," *IEEE Trans. Wireless Commun.*, vol. 13, pp. 902-912, Feb. 2014.

[102] M. Di Renzo, and W. Lu, "System-level analysis and optimization of cellular networks with simultaneous wireless information and power transfer: Stochastic geometry modeling," *IEEE Trans. Veh. Techn.*, vol. 66, no. 3, pp. 2251-2275, Mar. 2017.

[103] J. Xu, Y. Zeng, and R. Zhang, "UAV-enabled wireless power transfer: Trajectory design and energy optimization," *IEEE Trans. Wireless Commun.*, vol. 17, no. 8, pp. 5092–5106, Aug. 2018.

[104] Y. Wu, J. Xu, and L. Qiu, "UAV-enabled wireless power transfer with directional antenna: A two-user case (invited paper)," *Intern. Symp. on Wireless Commun. Syst. (ISWCS)*, pp. 1–6, Aug. 2018.

[105] Y. Hu, X. Yuan, J. Xu, and A. Schmeink, "Optimal 1D trajectory design for UAV-enabled multiuser wireless power transfer," Available online at: https://arxiv.org/pdf/1811.00471.pdf, 2018.

[106] L. Xie, J. Xu, and R. Zhang, "Throughput maximization for UAV-enabled wireless powered communication networks," *IEEE Internet of Things J.*, Early Access, Oct. 2018.

[107] S. Cho, K. Lee, B. Kang, K. Koo, and I. Joe, "Weighted harvest-then-transmit: UAV-enabled wireless powered communication networks," *IEEE Access*, vol. 6, pp. 72212-72224, Nov. 2018.

[108] J. Lyu, Y. Zeng, and R. Zhang, "UAV-aided cellular offloading for cellular hotspot," *IEEE Trans. Wireless Commun.*, vol. 17, no. 6, pp. 3988-4001, Jun. 2018.

[109] P. Chandhar, D. Danev, and E. G. Larsson, "Massive MIMO for communications with drone swarms," *IEEE Trans. Wireless Commun.*, vol. 17, no. 3, pp. 1604-1629, Mar. 2018.

[110] G. Geraci, A. Garcia-Rodriguez, L. G. Giordano, D. Lopez-Perez, and E. Bjornson "Understanding UAV Cellular Communications: From Existing Networks to Massive MIMO," *IEEE Access*, vol. 6, pp. 67853-67865, Nov. 2018.

[111] W. Khawaja, I. Guvenc, D. Matolak, U.-C. Fiebig, and N. Schneckenberger, "A survey of air-to -ground propagation channel modeling for unmanned aerial vehicles," available online: arxiv.org/abs/1801.01656, 2018.

[112] E. Yanmaz, R. Kuschnig, and C. Bettstetter, "Channel measurements over 802.11a-based UAV-to-ground links," *Proc. IEEE GLOBECOM Workshops (GC Wkshps)*, pp. 1280–1284, Dec. 2011.

[113] E. Yanmaz, R. Kuschnig, and C. Bettstetter, "Achieving air-ground communications in 802.11 networks with three-dimensional aerial mobility," *Proc. IEEE INFOCOM*, pp. 120–124, Apr. 2013.

[114] J. Chen, D. Raye, W. Khawaja, P. Sinha, and I. Guvenc, “Impact of 3D UWB antenna radiation pattern on air-to-ground drone connectivity,” *Proc. of the IEEE Vehicular Techno. Conf. (VTC)-Fall*, Aug. 2018.

[115] C. Liu, M. Ding, C. Ma, Q. Li, Z. Lin, and Y.-C. Liang, “Performance analysis for practical unmanned aerial vehicle networks with LoS/NLoS transmissions,” *IEEE Inter. Conf. on Commun. Workshops (ICC Workshops)*, pp. 1–6, May 2018.

[116] S. Ulukus, A. Yener, E. Erkip, O. Simeone, M. Zorzi, P. Grover, and Kaibin Huang, “Energy harvesting wireless communications: A review of recent advances,” *IEEE J. Sel. Areas Commun.*, vol. 33, no. 3, pp. 360–381, Mar. 2015.

VITA

ESMA TURGUT: She received the B.S. degree in electrical and electronics engineering from the Middle East Technical University, Ankara, Turkey, in 2010 and the M.S. degree in electrical and electronics engineering from Bilkent University, Ankara, Turkey, in 2012. She has been a Ph.D. student at the Department of Electrical Engineering and Computer Science at Syracuse University since 2014. Her research interests include wireless communications, stochastic geometry, heterogeneous cellular networks, unmanned aerial vehicles, device-to-device cellular communications, statistical modeling, analysis of mmWave cellular networks, and energy harvesting.